



# THE UNIVERSITY *of* EDINBURGH

This thesis has been submitted in fulfilment of the requirements for a postgraduate degree (e.g. PhD, MPhil, DClinPsychol) at the University of Edinburgh. Please note the following terms and conditions of use:

This work is protected by copyright and other intellectual property rights, which are retained by the thesis author, unless otherwise stated.

A copy can be downloaded for personal non-commercial research or study, without prior permission or charge.

This thesis cannot be reproduced or quoted extensively from without first obtaining permission in writing from the author.

The content must not be changed in any way or sold commercially in any format or medium without the formal permission of the author.

When referring to this work, full bibliographic details including the author, title, awarding institution and date of the thesis must be given.

# Detection of Calcification in Atherosclerotic Plaques Using Optical Imaging

**Alisia Mara Sim**



THE UNIVERSITY  
*of* EDINBURGH

A thesis submitted for the degree of  
Doctor of Philosophy

The University of Edinburgh

2018

# Declaration

This thesis is submitted in part fulfilment of the requirement for the degree of Doctor of Philosophy at the University of Edinburgh. Unless otherwise stated, the work described in this thesis is original and has not been submitted previously in whole, or in part for any degree or qualification at this, or any other university.

In accordance with the dissertation regulations as specified by The University of Edinburgh, this thesis does not exceed 100,000 words in length.

Alisia Sim

# Acknowledgements

First and foremost, I would like to thank my PhD programme, OPTIMA CDT, for taking a chance on me, I wouldn't be writing this page if it wasn't for them. I would like to thank them for giving me the opportunity to pursue a career in science but also for allowing me to gain a basic understanding of business and entrepreneurship. This experience has definitely shaped my future career choices.

I would also like to thank my supervisors Professor Alison Hulme, Dr Fabio Nudelman and Dr Marc Dweck. Without their imagination this project would have never taken shape, thank you for all the help. A big thanks goes to Dr Vicky MacRae, although she's not one of my main supervisors, she has been a great support and has always considered me one of her own students. Her words have always been kind and this has pushed me to persevere during times when I needed the most guidance.

Special thanks go to the Hulme and MacRae group, past and present members as they have made my 4-year journey a great experience not only academically but also outside of work. Mention should go to my two 'work best friends': Sally and Fiona, they have kept me sane during the long and depressing days at work whether in Chemistry or at the Roslin. I should also thank the Skye crew (Annabel, Veronica, Piera, Lindsey, Pete, Sally, Stefan and Stefano); that long weekend away was one of the best weekends I've had, and I can only hope we can have many more in the future. Thanks to Nabil, Lucy and many of the Farquharson group who have helped me during my period in biology. I cannot forget Fergus, he's been my colleague, my line manager (as I like to call him) and my friend; he's helped me from day one.

Appreciations to Dr Junxi Wu from the Hadoke group who helped me with all the *ApoE*<sup>-/-</sup> work and Dr Alistair Moss who has helped me with human tissue work and PET/CT.

The biggest thank you should go to my family, my parents always allowed me to do what I wanted, apart from being a chef. They have supported me through all the ups and downs of my undergraduate and PhD. I thank my sisters for all the love they have given me. I have been distant and busy for the past 4 years and I am so happy to move closer to home now.

Lastly, because he's been cheesy in his acknowledgements, I want to thank my fiancé, Stefan who has supported me since the day we met. He has been a shoulder to cry on when I was upset and has always been able to cheer me up. *I swear I couldn't love you more than I do right now, and yet I know I will tomorrow.* You are my best friend, and my other half. Thank you.

# Abstract

PET imaging, using the bone tracer  $\text{Na}^{18}\text{F}$ , allows the non-invasive location of atherosclerotic plaques that are at risk of rupture. However, the spatial resolution of PET is only 4-5 mm, limiting the mechanistic information this technique can provide. In this thesis, the use of fluorescence and Raman imaging to elucidate the mechanism of micro-calcification within atherosclerotic plaques has been investigated.

A number of fluorescent probes to detect fluoride and calcium have been synthesised. One of the fluoride probes has been shown to be selective for fluoride however, the concentration of fluoride required to activate the probe is order of magnitudes higher than the amount of  $\text{Na}^{18}\text{F}$  used for PET imaging making it problematic to use for future studies. On the other hand, a calcium probe has been shown to: selectively bind to hydroxyapatite (HAP); permit visualisation and quantification of HAP in both vascular and bone cell models; and effectively stain cultured aortic sections and whole mouse aorta for OPT imaging. Building on these preliminary data, fluorescence imaging and immunohistochemistry (IHC) imaging of both healthy and atherosclerotic tissue that were previously subjected to PET imaging, were successfully carried out showing the ability of the probe to detect HAP in human vascular tissue. IHC staining for Osteoprotegerin (OPG) and Osteopontin (OPN), two bone proteins recently detected in vascular tissue, showed the co-localization of OPG with the probe. Conversely, the OPN was shown to localize in areas surrounding high OPG and probe signal.

To determine the exact composition of vascular calcification, Raman spectroscopy was also used. It is believed that the biosynthetic pathway to HAP passes through a series of transitional states; each of these has different structural characteristics which can be studied using Raman spectroscopy. In particular, HAP has a strong characteristic Raman peak at  $960\text{ cm}^{-1}$ . An increase in HAP concentration has been detected by Raman in both calcified cell models and aortic sections. When human vascular tissue was analysed, an additional peak at  $973\text{ cm}^{-1}$  was present suggesting the presence of whitlockite (WTK) in this tissue as well as HAP.

# Lay Abstract

Cardiovascular related deaths (CVD) are the second most common cause of death worldwide. It was estimated that around 17 million people died in 2015 due to a complication of heart disease. Atherosclerosis is one of the main causes of CVD and it consists of the build-up of plaques in the arteries. The arteries are highly inflamed and could rupture leading to infarcts and strokes. It is thought that the way the body tries to deal with the plaque formation is by creating a barrier between the plaque and the artery, this barrier, known as calcification, is formed of hydroxyapatite, a calcium mineral which is also present in bone. At the start, when the calcification is weak, it increases the chances of plaque rupture however, once the calcification is bigger it stabilizes the plaque.

Unfortunately, even though the field of cardiovascular diagnostic has advanced, there are only a limited way of detecting the smaller calcification deposits which could cause sudden acute death. Those that are currently available do not provide enough information into why calcification forms. In this project, two imaging techniques are used to study the formation of calcification in cells, rodent and human models. These imaging techniques have provided new and important information into the process of calcification.

# Table of Contents

Declaration	ii
Acknowledgements	iii
Abstract	iv
Lay Abstract	v
Table of Contents	vi
Chapter 1 - Atherosclerosis	1
1.1 Cardiovascular disease	1
1.1.1 Atherosclerosis	1
1.2 The pathology of calcification	3
1.3 The inflammatory response and its link with calcification	6
1.4 Current imaging techniques	9
1.4.1 Invasive techniques	10
1.4.2 Non-Invasive techniques	12
1.5 Conclusion	15
1.6 Approach	16
1.7 References	17
Chapter 2- Synthesis of Fluorescent Dyes for the <i>In Vitro</i> Detection of Calcification	23
2.1 Fluorophores	23
2.2 Approach for the detection of HAP	25
2.3 Fluoride probes	26
2.3.1 Probe selection	26
2.3.2 Naphthalene 2-cyanoacrylate	28
2.3.3 Imidazole bearing rhodamine 6G	29
2.3.4 Selectivity of fluoride probes	30
2.3.5 Conclusion	33
2.4 Calcium probes	35

2.4.1	Cyanine dyes	35
2.4.2	Fluorescein	36
2.4.3	Examples of HAP binding molecules	38
2.4.4	Synthesis of Cy dyes	40
2.4.5	Synthesis of quaternary heterocyclic ammonium salt precursors	40
2.4.6	Cyanine dye assembly	42
2.4.7	Coupling and synthesis of bisphosphonate protected alendronate	47
2.4.8	HAP binding peptide	51
2.4.9	Characterization of the calcium probes	53
2.4.10	Binding affinity of probes to calcium compounds	55
2.5	Conclusion	59
2.6	References	60
Chapter 3- Characterization of Fluorescein-BP in an <i>In Vitro</i> Model of Osteoblast Matrix Calcification		66
3.1	Importance of calcium	66
3.2	Gold standard methods of detecting calcification	67
3.2.1	Alizarin S	67
3.2.2	Von Kossa	68
3.2.3	HCl/DC assay	69
3.2.4	Calcein and other fluorescence methods	69
3.3	Models for calcification	70
3.3.1	Cells	70
3.3.2	<i>Ex vivo</i> rings	71
3.3.3	Genetically modified mouse models	71
3.4	Probe toxicity studies	73
3.5	Probe localization studies	74
3.6	Comparison of probe with Alizarin S and calcium leaching assay	76
3.6.1	MOVAS	76
3.6.2	VSMCs	78
3.6.3	MC3T3	80
3.7	Aortic rings	81
3.8	ApoE <sup>-/-</sup> mice	85
3.9	Conclusion	88
3.10	References	88



Chapter 4-	Human Tissue and Potential Biomarkers for Plaque Vulnerability	94
4.1	Carotid and coronary plaques	94
4.2	Rodent vs human models	95
4.3	Early detection of calcification, PET and Fluorescein-BP	96
4.4	Selectivity of Na <sup>18</sup> F PET tracer	96
4.5	PET/CT and Fluorescein-BP imaging of ex vivo coronary plaques	97
4.6	Fluorescein-BP imaging of ex vivo carotid plaques	99
4.7	Comparison of PET and Alizarin S with the upregulation of osteogenic markers	100
4.8	Comparison of Alizarin S with the upregulation of osteogenic markers	103
4.9	Comparison of Fluorescein-BP, OPG and OPN on coronary plaques	104
4.10	Conclusion	105
4.11	References	106
Chapter 5-	Chemical Composition of Vascular Calcification Deposits	110
5.1	Raman spectroscopy	110
5.2	Raman spectroscopy of biological samples	102
5.3	Raman spectroscopy of mineralized vascular tissue	113
5.4	Raman on Calcium species	114
5.5	Raman analysis on calcified cell pellet	115
5.6	Raman analysis of calcified cell monolayer	118
5.7	Raman analysis on calcified aortic rings	121
5.8	Raman on calcified human samples analysis and comparison to PET/CT	123
5.9	Conclusion	127
5.10	References	128
Chapter 6-	Conclusion and Future Work	132
Chapter 7-	Materials and Methods	135
7.1	Synthesis	135
7.1.1	General Information	135
7.1.2	Fluoride sensor	136
7.1.3	Cy dye building blocks	140
7.1.4	Solution phase approach	146

7.1.5	On resin approach	150
7.1.6	Fluorescein compounds	152
7.1.7	Azide alendronate synthesis	154
7.1.8	Peptide synthesis	156
7.1.9	Incorporation of probes in calcium minerals	158
7.2	Biology	159
7.2.1	General procedures	159
7.2.2	Tissue culture	159
7.2.3	Imaging of cell and tissue cultures	162
7.2.4	Biochemical assays	165
7.2.5	Raman Spectroscopy	166
7.3	References	167
Chapter 8- Abbreviations		170
Chapter 9- Permissions		175
1.1	Chapter 1	175
1.2	Chapter 2	182
1.3	Chapter 3	186
1.4	Chapter 5	187
Appendix 1- Cyanine dyes		188
Appendix 2- Patient information		189
Appendix 2.1 Coronary tissue samples		189
Appendix 2.2 Carotid tissue samples		189
Appendix 3- IGG control		190
Appendix 4- Staining solutions		191

# Chapter 1 - Atherosclerosis

## 1.1 Cardiovascular disease

Cardiovascular disease (CVD) is a global concern which was responsible for taking more than 17 million lives in 2015.<sup>1-8</sup> In 2012, CVD was classed as the second main cause of death in the UK (28%), behind cancer (29%) (Table 1).<sup>6,9</sup> CVDs are a group of disorders of the heart and blood vessels which are caused by the formation of atherosclerotic plaques within the arteries. Atherosclerotic plaques containing calcific lesions are reported in more than 65% of the population over the age of 45.<sup>6</sup>

**Table 1: Cause of death in the UK in 2014.** All values obtained from the British Heart Foundation (BHF) 2014 statistics.

<b>Cause</b>	<b>Number of people affected</b>
<b>CVDs</b>	161,252
<b>Cancer</b>	165,818
<b>Respiratory disease</b>	79,899
<b>Neurodegenerative diseases</b>	49,899
<b>Diabetes</b>	7,638

### 1.1.1 Atherosclerosis

Atherosclerosis is a progressive disease characterized by macrophage infiltration within the vessel and by the accumulation of lipids and fibrous elements in the large arteries. This is frequently accompanied by inflammation and vascular remodelling of the vessel wall.<sup>3,8,10-13</sup> Plaques are made up of various substances such as; fat, cholesterol, calcium and a wide range of other entities commonly found in the blood.<sup>14</sup> They are characterized histologically as an atheroma with a fibrous cap, consisting of smooth muscle cells (VSMCs), extracellular matrix,<sup>10,11</sup> and a lower lipid-rich necrotic core.<sup>8,10</sup> Over time, with the progression of the disease, the accumulation of lipids and fibrous elements will harden making the arteries narrower (*Figure 1.1*) which result in myocardial ischaemia and angina.<sup>8,10,11,15</sup>

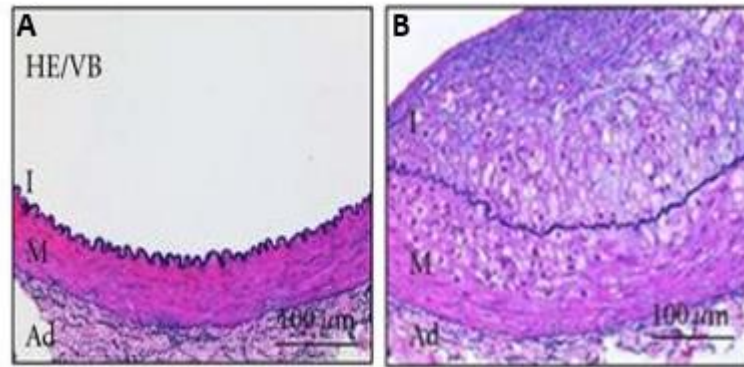


**Figure 1.1:** H&E of a normal (A) and atherosclerotic (B) coronary artery. H&E showing the adventitia (Ad), media (M) and intimal layers (I) of the coronary artery with the positive remodelling of the artery wall. Reproduced with permission.<sup>16</sup>

The most important clinical complication is caused by sudden plaque rupture or erosion of the lesions, resulting in thrombosis or myocardial infarction.<sup>8,10,11,13,15,17-20</sup> The chance of rupture is determined by the plaque composition and vulnerability.<sup>7,11</sup> Vulnerable plaques generally have a thin fibrous caps and an increased number of inflammatory cells.<sup>2,10,11,21,22</sup>

The plaques can become progressively more complex, with calcification, ulceration and neovascularisation affecting their stability (Figure 1.2).<sup>10,23</sup>

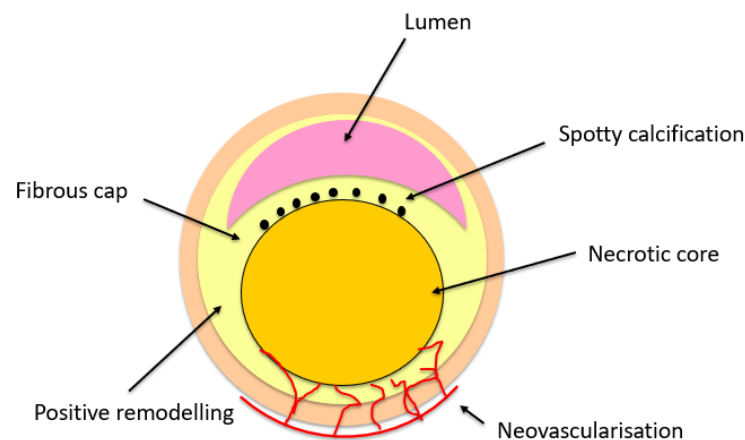


**Figure 1.2:** Schematic representation of an atherosclerotic plaque which has caused positive remodelling of the vessel. Neovascularisation and spotty calcification start appearing around the necrotic core.

Vascular calcification, a hallmark of atherosclerosis, is a complex biological process that involves the deposition of calcium and phosphate.<sup>21,24-26</sup> Calcification was only realised to be important in vascular disease in 1990s.<sup>20,27</sup> Research discovered osteogenic morphogens present in calcifying blood vessels as well as the presence of bone matrix proteins (BMP) in cardiovascular tissue. These findings established the ‘osteogenic hypothesis’ which suggested

that vascular and valvular calcification is an active process regulated by a process similar to the one in bone mineralization.<sup>6,23,25–33</sup> This hypothesis has been strengthened by the observation of events such as the production of matrix vesicles, apoptotic bodies and hydroxyapatite (HAP).<sup>10,25,34,35</sup> Small calcified HAP micronodules (*Figure 1.3 A*) appear first in the vessel and subsequently grow into much larger macroscopic deposits (*Figure 1.3 B*).<sup>24</sup>

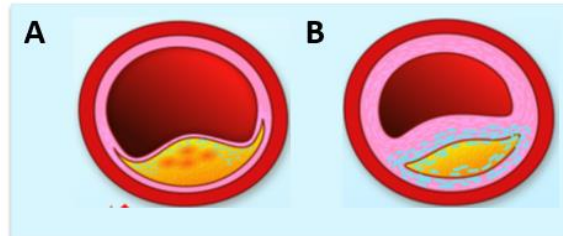


**Figure 1.3 Micro-calcification (A) and Macro-calcification (B).** HAP crystal (blue) deposits on the fibrous cap of the plaque. At the start, HAP is only small but with time it will grow and stabilize the plaque. Reproduced with permission.<sup>22</sup>

The size of the deposits is very important in assessing the vulnerability of the plaque. The presence of large deposits,  $>50\ \mu\text{m}$ ,<sup>24</sup> known as macro-calcification (*Figure 1.3 B*),<sup>22</sup> stabilize the plaque while the occurrence of smaller deposits,  $<50\ \mu\text{m}$ ,<sup>24</sup> known as micro-calcification (*Figure 1.3 A*), the beginning of the mineralization of the vessel wall, is known to be involved in plaque rupture.<sup>10,22,24–26</sup> Micro-calcification is therefore associated with high risk lesions,<sup>13,17</sup> and directly weakens the fibrous cap.<sup>13</sup>

Currently there are little to no methods for assessing the degree of vulnerability of the plaques. As a consequence, developing techniques to identify micro-calcification is a major research goal with the potential of improving patient outcome.

## 1.2 The pathology of calcification

An artery consists of three distinct layers: the intima, the media and the adventitia (*Figure 1.1* and *Figure 1.4*).<sup>36</sup> The intima is the inner layer which consists of extracellular matrix and is surrounded by a layer of endothelial cells on the luminal side and a layer of elastic fibres on the peripheral side. The adventitia is the outer layer which consists mainly of connective tissue with fibroblasts and VSMCs. Between the two, the media is located, which mainly consists of VSMCs.<sup>11,36–38</sup>

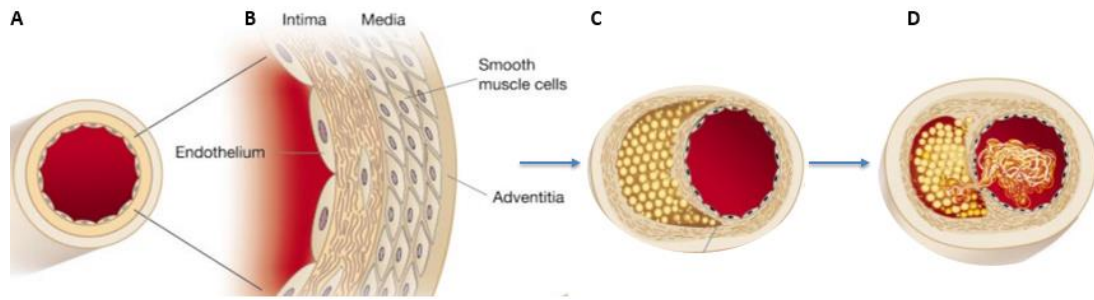


**Figure 1.4:** Schematic cross-sections showing the difference between a normal artery (A), an atherosclerotic one where plaque deposits between the media and the endothelium of the vessel wall (C) and a ruptured one (D). Over time the plaque will harden and cause obstruction to the blood flow causing patients to have cardiac events. Reproduced with permission.<sup>39</sup>

Vascular calcification can occur at different locations within the vessel wall, either in the intima or in the media (Figure 1.4). Intimal calcification is mainly associated with atherosclerosis while medial calcification is largely associated with chronic kidney disease (CKD) and was also recently shown to be the main type of mineralisation in valve calcification.<sup>20,22,23,29,32,34,40–42</sup>

Vascular calcification, as mentioned previously, is very similar to the physiological bone formation process.<sup>23,26,28–30,43</sup> Under stress, VSMCs can differentiate into different mesenchymal-derived cell types such as osteoblasts, adipocytes and chondrocytes. This in turn leads to calcification, altering lipid accumulation and matrix production.<sup>6,11,20,23,25,28,29,37,44,45</sup> There are at least three key aspects to be considered regarding the role of VSMCs in the pathogenesis of vascular calcification;<sup>25,45</sup>

- endocytosis and toxicity of HAP crystals,
- transformation into osteochondrogenic phenotype,
- generation of nucleating structures for HAP deposition.

*Endocytosis and cell death phase:*

In order to activate osteogenic gene expression, HAP crystals need to be endocytosed and accumulated in the lysosomes, where the calcium and phosphate crystals are then dissolved (Figure 1.5). The release of calcium causes either apoptosis or osteogene expression which causes the release of HAP-filled matrix vesicles.<sup>46</sup>

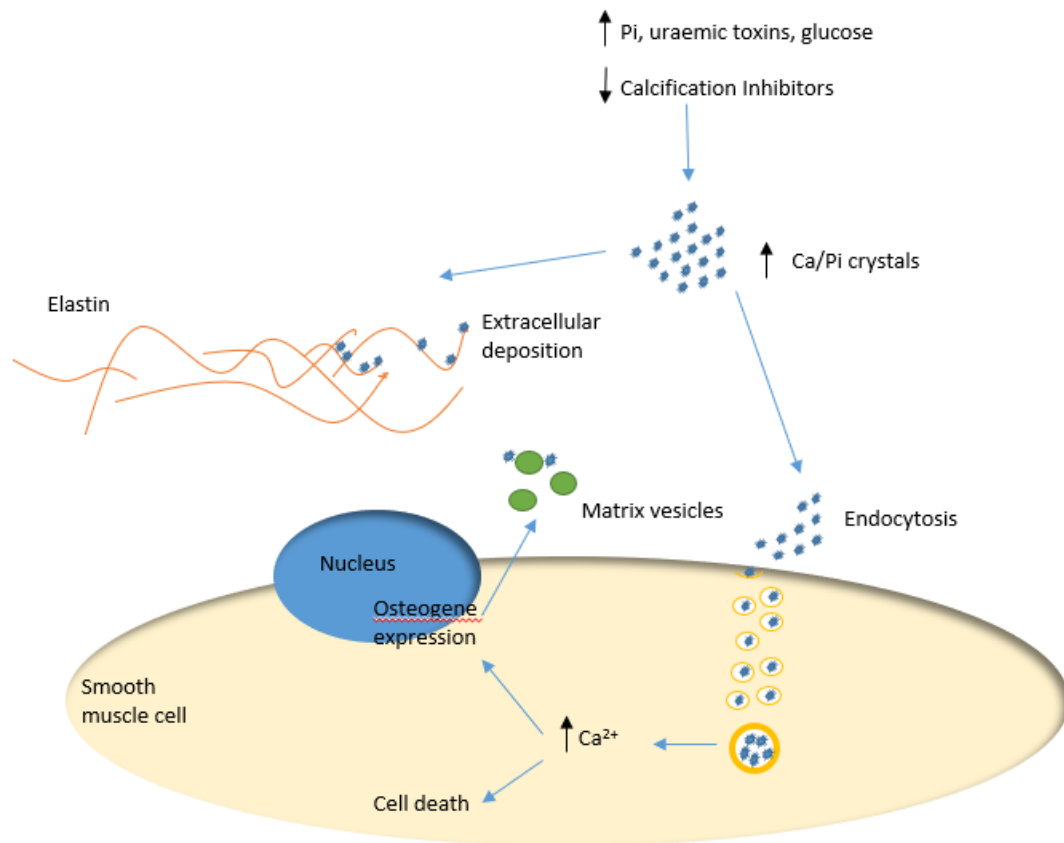


**Figure 1.5** The role of calcium and phosphate crystals in HAP deposition. Crystals of calcium and phosphate in VSMC's can be nucleated and either deposited on extracellular elastin or endocytosed and directed to lysosomes where they are then dissolved, and free calcium ions are released in the cytosol. Here, cell death or cell differentiation takes place.

*Transformation phase:*

At the sites where HAP nanocrystals are depositing, VSMCs undergo an osteochondrogenic phenotypic change and increase the expression of mineralization-regulating proteins that would otherwise only be found in bones and cartilage. Runx, Osterix, Osteopontin (OPN) and Osteoprotegerin (OPG) are just a few.<sup>20,23,26,33,34,47</sup> The upregulation of osteochondrogenic genes concurrently downregulates smooth muscle cell genes. The transcription factor that is responsible for this process is Runx2.<sup>26</sup> It is the Bone Morphogenic Protein (BMP) that activates the transcription activity of Runx2. Upon vascular injury, the differentiated VSMCs increase osteogenic signalling through BMP and upregulate HAP deposition.<sup>26,29,48</sup> The deposition of HAP on the matrix has also been shown to upregulate not only BMP but also OPN which in turn accelerates the calcification process (*Figure 1.5*).

*Nucleation site formation phase:*

In order to create an environment that tolerates calcification, matrix vesicles are used as nucleation sites for HAP.<sup>6,26,46</sup> Normally, VSMCs do not calcify as they are loaded with mineralization inhibitors such as Matrix Gla Protein (MGP), Fetuin-A and Pyrophosphate.<sup>23,31,33,37,43,45</sup> However, when the cells undergo a phenotypic change and there are high levels of calcium and calcification inhibitors are low, VSMCs produce mineralization-competent vesicles that contain already synthesised HAP.<sup>6,25,31,46</sup> To permit the growth of the crystals, the vesicles contain alkaline phosphate (ALK) which creates a phosphate source by degrading pyrophosphate.

Over time the HAP sediments grow and eventually stabilize the plaque, however, at the beginning when smaller deposits are being laid down, the plaque is very fragile and the HAP deposits will weaken the plaque and cause its rupture.<sup>10,22,24-26</sup> A new understanding is required to appreciate the mechanism behind HAP deposition and to distinguish weakened plaques before they rupture.

### 1.3 The inflammatory response and its link to calcification

Although significant progress has been achieved over recent years, the exact role and process of calcification in atherosclerosis remains to be defined.<sup>22,26</sup> Emerging evidence suggests that intimal calcification occurs as a healing response to intense inflammation and cell death within the atherosclerotic plaque.<sup>22,23,31,49</sup> Aiwaka *et al.* were able to demonstrate the association of inflammation and calcification in mouse atherosclerotic models, showing that macrophage infiltration takes place before the osteogenic conversion of VSMCs and subsequently followed by the release of matrix vesicles.<sup>30</sup> This is one of the first studies that provides evidence that inflammation is a powerful initiator of calcification. Recently, vesicles have been shown to not only be released by VSMCs but also by inflammatory macrophages, suggesting that macrophages are also a potential source of calcification.<sup>22</sup> Pro-inflammatory cytokines, produced as an immune response to inflammation, are also shown to promote the differentiation of VSMCs to osteoblastic and/or chondrocytic cells which will then provide HAP and lead to a more stabilized plaque with macro-calcification (*Figure 1.6*).<sup>22,36,50,51</sup>



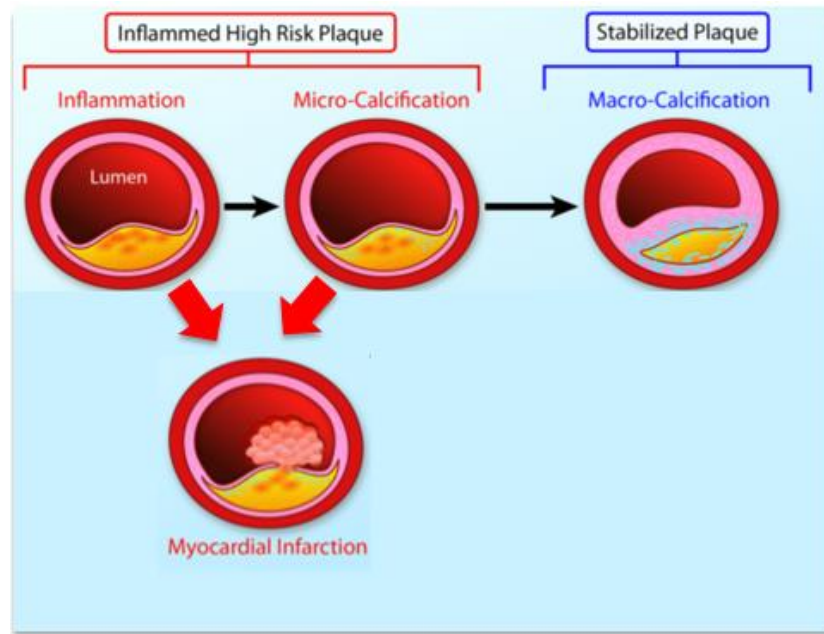


**Figure 1.6 Relationship between inflammation, calcification and infarction.** A large necrotic core, thin fibrous cap and intense inflammation are key players in plaque rupture. Calcification occurs as a healing process, however, at the early stages the calcification is microscopic (blue) and causes increased stress on the cap, increasing the chance of plaque rupture. However, once a large amount of calcification is deposited, the plaque is considered clinically stable and therefore not at risk of rupture. Reproduced with permission.<sup>22</sup>

The continuous process of atherosclerosis and atheroma formation can be divided in six stages. These are classified into pre-lesional stages (stages I, II, III) and progressive plaque formation stages (stages IV, V, VI) (Figure 1.7).<sup>36</sup>

*Stage I start of plaque formation:*

In arterial lesion-prone areas, the initial event that takes place in response to a change in body homeostasis is the alteration of endothelial cells (ECs). There are two main functions that are affected: modification of EC permeability to allow for Low Density Lipoprotein (LDL) deposition and change in EC phenotype.<sup>8,15,26,36,52-54</sup> The LDLs that enter the vessel via the modification of the EC permeability are then confined in the intima. Here, they interact with the proteoglycans and matrix proteins converting them into modified lipoproteins (MLp), rich in cholesterol (Figure 1.7). When the ECs allow the accumulation of MLp within the intima, major changes to the biosynthetic capacity of ECs takes place. This change causes the proliferation of the basal lamina (BL) and the disruption of the myo-endothelial junctions and in turn leads to gaps between the neighbouring VSMCs.<sup>36</sup>

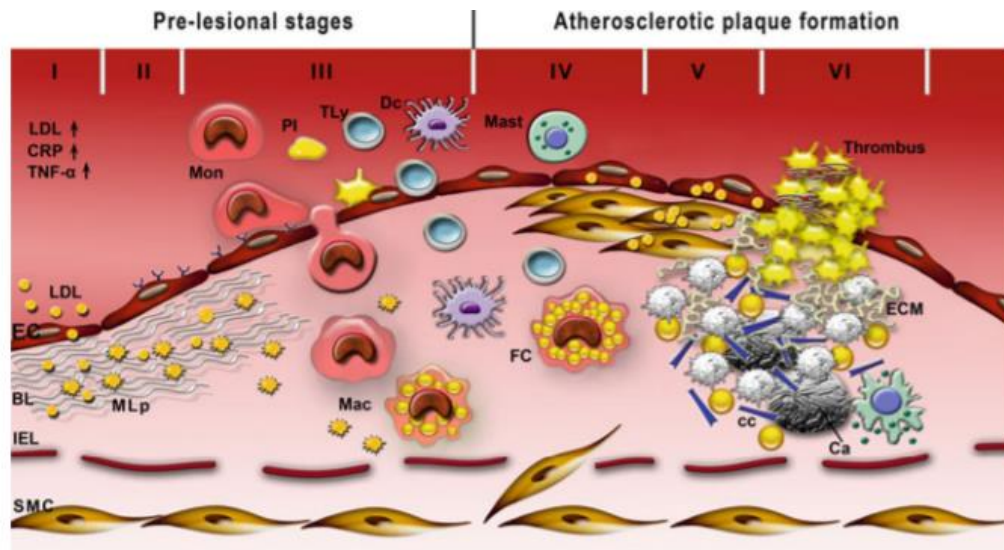


**Figure 1.7: Atheroma formation and its phases.** Phase I, start of plaque formation; phase II, disruption of the EC; phase III, inflammatory reaction; phase IV, formation of fibrous plaque; phase V, formation of calcified atherosclerotic plaque; phase VI thrombus formation. LDL: low density lipoproteins, EC: endothelial cells, MLp: modified lipoproteins, (V)SMC: smooth muscle cells, BL: basal lamina, Mon: monocytes, Mac: macrophages, FC: foam cells, ECM: extracellular matrix, Ca: hydroxyapatite crystals, cc: cholesterol crystals. Reproduced with permission.<sup>36</sup>

#### *Phase II disruption of the EC:*

The alteration of the plasma lipid and the sub-endothelial build-up of MLp initiate a defence mechanism which causes an inflammatory response by recruiting blood inflammatory cells (Figure 1.7).<sup>8,36,53,54</sup>

#### *Phase III inflammatory reaction:*

There are eight main immune cells that are responsible for the inflammatory process.<sup>36</sup> Monocytes, being one of them, undergo a coordinated process which causes their adhesion to the endothelium lining and they then progress through the EC junctions to the sub-endothelium.<sup>36</sup> Platelets, T-cells, dendritic cells, neutrophils, mast cells and B-cells also play an important role in the inflammatory process. Platelets specifically aid in the recruitment of blood monocytes (Mon), therefore playing an important role in plaque formation.<sup>36,55</sup> Dendritic cells instead activate the T-cells which are important for the expression and secretion of cytokines; these are in turn responsible for the differentiation of macrophages (Mac) from monocytes.<sup>20,26,36,50,55,56</sup> The activated macrophages, also known as macrophage-derived foam cells (FC), take up MLp and loads the latter with cholesterol (Figure 1.7). Accumulation of foam cells is what characterises fatty-streak type lesions, which may then evolve into advanced

plaques.<sup>8,26,36,55</sup> The cytokines also convert the VSMCs to the osteoblastic phenotype which initiates the start of the calcification pathway allowing the VSMCs to produce HAP.<sup>26,32,52</sup>

*Stage IV formation of fibrous plaque:*

The inflammatory cells send molecular messages which direct the plaque development, specifically the build-up of VSMCs within the intima (*Figure 1.7*). This is known as intimal thickening.<sup>36,51</sup>

*Stage V and VI Calcified atherosclerotic plaque and thrombus formation:*

The progression of the plaques is characterized by accumulation of extracellular lipid droplets, macrophage foam cells, VSMC-derived foam cells and calcification mini clusters which will then develop into macro-calcification.<sup>36,54</sup> The accumulation of cholesterol in the plaque causes apoptosis of both the macrophage-derived foam cells and the VSMCs. Upon cell death, the cells release their content forming the necrotic core (*Figure 1.7*).<sup>8,23,26,36,51,54</sup> Plaque inflammation triggers VSMC loss and the production of Matrix Metalloproteinases (MMP) that weaken the fibrous cap and lead to thrombus formation (stage VI).<sup>8,36</sup> Calcification is thought to be the healing response to intense necrotic plaque inflammation and when macro-calcification is deposited it results in the separation of inflammatory regions from the lumen, making the plaque less likely to rupture.

## 1.4 Current imaging techniques

Imaging inflammatory and calcific processes that take place in the arteries has the potential to improve the understanding of the pathways that lead to CVD, and consequently to improve patient outcomes.<sup>7</sup> Advances have occurred in a variety of both invasive and non-invasive imaging modalities.<sup>3,7,8,57</sup> Invasive imaging relies on accessing the arteries with specifically designed catheters *via* the coronary vessels and then administering contrast media. Novel advances in the design and technology of such catheters allow for a selection of different invasive approaches which can be coupled to the standard angiographic assessment. Examples of these additional imaging technologies are intravascular ultrasonography (IVUS), optical coherence tomography (OCT), near-infrared spectroscopy (NIRS) as well as near-infrared fluorescence (NIRF). In the field of non-invasive modalities, developments in computed tomography (CT), magnetic resonance imaging (MRI) and positron emission tomography (PET) have taken place. Each approach provides complementary information and allows for a comprehensive, multidimensional evaluation of coronary atherosclerosis.<sup>7,8,22</sup>

The main assessment focus of coronary artery disease using imaging has been the detection of luminal stenosis or obstruction to blood flow. However, the capacity of the angiography results to prevent myocardial infarction leaves somewhat to be desired.<sup>3,58</sup> Studies have shown that the majority of lesions that go on to rupture and cause myocardial infarction are in fact non-obstructive on previous angiographies.<sup>7,22,59,60</sup>

Plaque burden however can provide a powerful prognostic on the basis that the more plaques a patient has, the greater the likelihood that one will rupture and cause myocardial infarction. The wide range of invasive and non-invasive imaging techniques that are available are described below.

### 1.4.1 Invasive techniques

#### 1.4.1.1 Angiography

Angiography is the most commonly used and reproducible technique to accurately assess the lesion severity and is therefore used to diagnose coronary artery disease (*Figure 1.8*). An angiogram is an X-ray of the blood vessels after they are filled with a contrast material, such as gadolinium or iodine, which will reveal the extent and severity of a blockage. The technique involves the selective intubation of the patient with a catheter, allowing for high spatial resolution (0.1-0.2 mm)<sup>7,59</sup> of the vessel wall. However, detailed analysis of the plaque cannot be obtained.<sup>7</sup> Angiography has been combined with IVUS, OCT and NIRS to provide more information on the coronary plaque composition.<sup>7</sup>

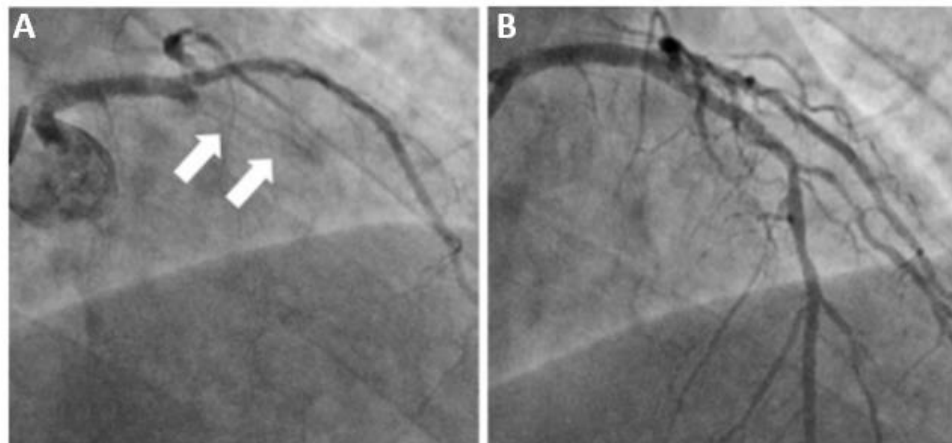


**Figure 1.8: Coronary angiography of the left coronary artery.** (A) Total occlusion (white arrow) of the mid left anterior descending artery. (B) After balloon angioplasty distal flow was obtained. Reproduced with permission.<sup>61</sup>

### 1.4.1.2 IVUS

IVUS involves using a small ultrasound transducer to record the reflection of high frequency sound waves and therefore generating greyscale cross-sectional images of the arterial wall (*Figure 1.9*).<sup>3</sup> The transducer itself has limited ability to differentiate the individual plaque components but virtual histology on the backscattered radiofrequency allows features such as the necrotic core, the calcium fibrous density and the fatty plaques to be detected at an exceptionally high spatial resolution (150-200  $\mu\text{m}$ ).<sup>7</sup> IVUS can be used to accurately assess the luminal dimensions and the volume of the plaque. By doing so it allows for an accurate quantification of plaque burden and therefore acts as a powerful predictor of disease progression.<sup>3,8</sup> However, a major limitation of this technology is the low signal-to-noise ratio and the increased number of artefacts making which render interpretation difficult. In addition, the spatial resolution is too low to accurately and reliably detect the fibrous cap.<sup>7</sup>

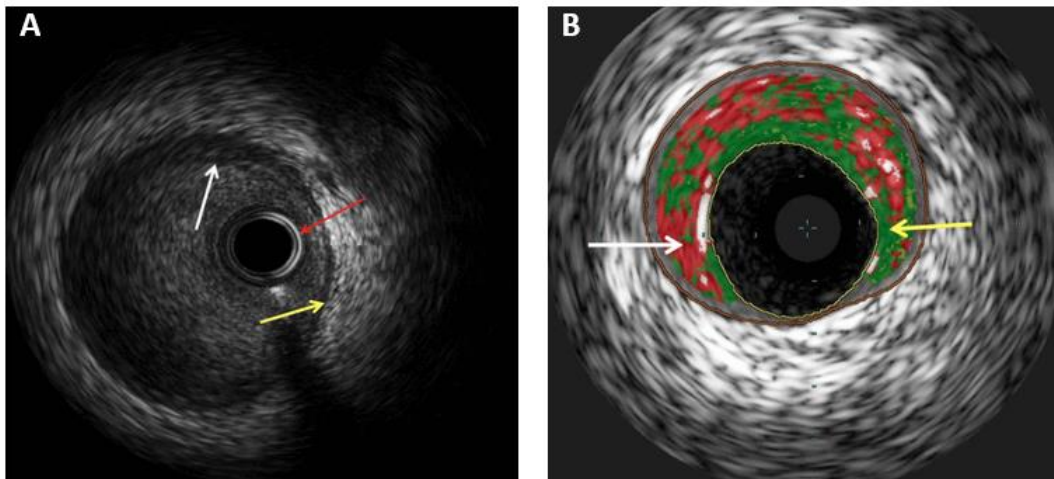


**Figure 1.9: Normal IVUS (A) and virtual histology IVUS (B).** (A) shows three layers; intima (white arrow), external elastic membrane that represents interface between media and adventitia (yellow arrow). IVUS catheter shown with the red arrow. (B) virtual reconstruction of the artery. Image shows necrotic core shown in red (white arrow) and fibrous plaque shown in green (yellow arrow). Reproduced with permission.<sup>21</sup>

### 1.4.1.3 OCT

OCT uses a near-infrared (NIR) fibre-optic wire within the catheter which, by emitting light in the NIR area is able to measure the backscatter signal from tissues while still inside the artery.<sup>3,7</sup> The fibre-optic wire is set with a rotating lens and thus allows high spatial resolution, up to 10-15  $\mu\text{m}$ , permitting accurate measurements of the thickness of the fibrous cap.<sup>3,7,21</sup> In contrast to IVUS, OCT is able to image the thrombus, plaque rupture and superficial plaque erosion with improved sensitivity and definition.<sup>3,62</sup> Measurement of the fibrous cap thickness not only allows the assessment of the plaque vulnerability, but also disease progression and

plaque stabilization in response to therapy.<sup>3,63</sup> The major limitation of OCT is the lack of penetration, 1-3 mm, which makes assessment of the entire plaque volume impossible.<sup>3,7,64</sup>

#### 1.4.1.4 NIRS

NIRS works on the phenomenon that organic molecules absorb and reflect light differently at specific wavelengths. When light is emitted onto the vessel wall, a chemogram based on the absorption and emission pattern of the vessel wall components is created. This technique is extremely useful in the detection of lipids within the plaque, thus allowing the identification of areas of lipid-rich lesions and quantification of the lipid core.<sup>3,7,65,66</sup> Apart from the ability to provide information on lipid content, NIRS is not able to offer any structural information on the plaque. This can be overcome by the development of NIRS-IVUS hybrids which have been shown, in preclinical studies, to discriminate between vulnerable and non-vulnerable plaques.<sup>67</sup>

In the research environment, NIR-OCT catheters have been used with an indocyanine green (ICG) fluorophore to enhance the signal of *in vivo* lipid-rich inflamed plaques in rabbits and of *ex-vivo* human atheroma specimens.<sup>68</sup> This technology could not only be used to provide read-outs of high risk plaques, but also to examine the mechanism and efficacy of atherosclerosis therapeutics.<sup>7,68-70</sup> Other NIRS tracers are undergoing preclinical evaluation and include agents activated by proteases that localize inflamed plaques,<sup>3,71,72</sup> tracers that target fibrin,<sup>73</sup> and expensive HAP specific tracers such as Osteosense.<sup>17,30,74-76</sup> Unfortunately, the cost of the HAP specific tracer has limited its use in a research environment resulting in the synthesis of novel probes. Nonetheless, due to the higher spatial resolution, NIRS and molecular imaging are already well positioned to further elucidate the first steps of calcification and the role of inflammation in myocardial infarction.<sup>68-70</sup>

### 1.4.2 Non-Invasive techniques

#### 1.4.2.1 Coronary artery calcium scoring (CAC) using CT

CAC scoring uses electrocardiogram-gated CT, providing an accurate and simple measure of the overall atherosclerotic burden, plaque morphology and composition (*Figure 1.10*). Without the need for contrast agents, CAC scoring quantifies the macroscopic calcium within the vessels.<sup>3,7,22,24,26,35</sup> It can also provide some information on the less stable adjacent plaques. However, as for IVUS, the spatial resolution is low and overall this technique underestimates the size of non-calcified plaques and overestimates the size of calcified plaques due to 'booming artefacts'.<sup>7,12,13,22</sup>

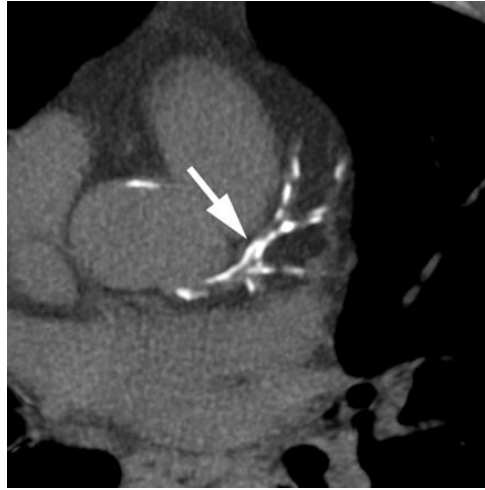


**Figure 1.10: Imaging of coronary calcification by CT.** Coronary macro-calcification deposits (white arrow) have high attenuation and are therefore clearly visible by CT. Reproduced with permission.<sup>77</sup>

This makes the technique unsuitable for detecting micro-calcification as it is not able to identify calcium deposits smaller than 200  $\mu\text{m}$  in diameter.<sup>7,13</sup> When compared to IVUS, CAC is better for the detection of fibrous plaques and to a lesser extent the necrotic core and fibrofatty tissues.<sup>7</sup> However, unstable lesions tend to be very sparsely calcified and therefore tend to be unnoticed on CAC images.<sup>8</sup>

#### 1.4.2.2 PET

PET in contrast to CAC can detect molecular signals at picomolar concentrations. Unfortunately, the spatial resolution of this technology is low, 4-5 mm, which only allows it to be used together with either CT or MRI for precise anatomical localization of the PET signal (Figure 1.11).

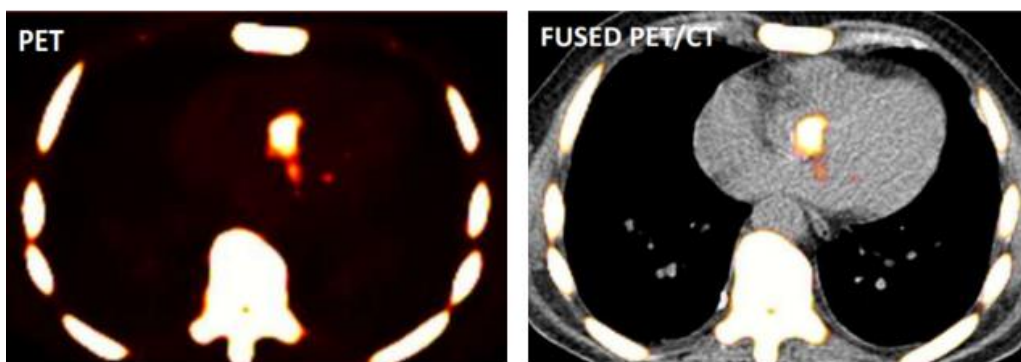


**Figure 1.11: PET and Fused PET/CT of the aortic valve.** Image downloaded.<sup>78</sup>

PET relies on using tracers which will localize in specific areas, allowing biological processes to be measured in vivo.<sup>3,8,22,79,80</sup> To date, the most commonly used tracer is fluorodeoxyglucose

( $^{18}\text{F}$ -FDG) which has been routinely used to image inflammation.<sup>22,35,54,57</sup>  $^{18}\text{F}$ -FDG localizes in areas with high metabolic rate and within the vascular tissue it will accumulate in the macrophages.<sup>7,8,13,35</sup>  $^{18}\text{F}$ -FDG has been used to characterize atherosclerotic burden and inflammation in vessels as well as being used to monitor therapy.<sup>12,22,74,79</sup> However, high levels of inflammation within the plaques are not always associated with vulnerable plaques (*Figure 1.12*).

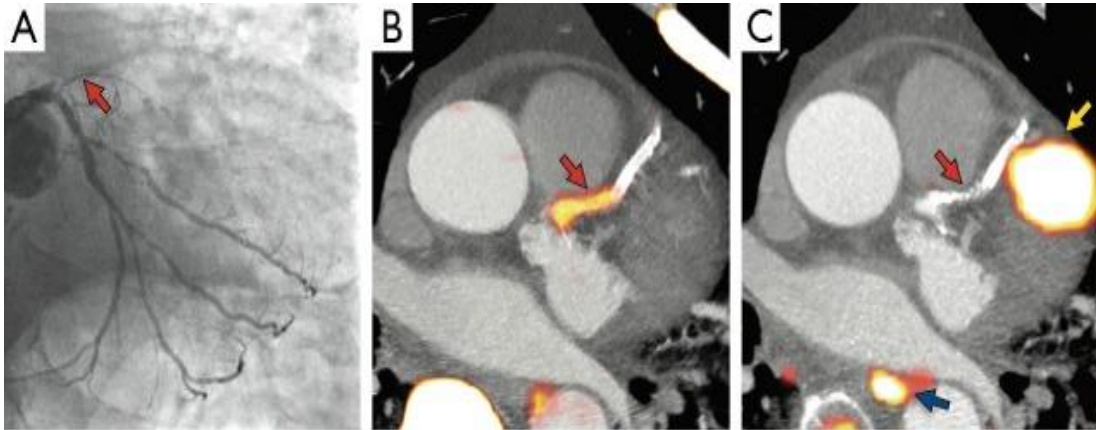


**Figure 1.12: Focal  $^{18}\text{F}$ -sodium fluoride and  $^{18}\text{F}$ -fluorodeoxyglucose uptake in patients with myocardial infarction and stable angina.** (A) invasive coronary angiography of a proximal occlusion (red arrow) of the left anterior descending artery (B) Fused PET/CT image using  $^{18}\text{F}$ -NaF showing intense fluoride uptake at the site of the vulnerable plaque (red arrow). (C) Fused PET/CT using  $^{18}\text{F}$ -FDG showing no uptake at the site of the plaque (red arrow). Blue and yellow arrows indicative of other areas where  $^{18}\text{F}$ -FDG has been taken up (yellow-coronary artery, blue-oesophagus). Reproduced with permission.<sup>13</sup>

On the other hand, another recently repurposed tracer, which had previously been used in bones, is  $^{18}\text{F}$ -NaF. In contrast to  $^{18}\text{F}$ -FDG,  $^{18}\text{F}$ -NaF binds to HAP via an exchange process between the hydroxyl groups in HAP with the fluoride ions on  $^{18}\text{F}$ -NaF.<sup>8,13,24,35,54,80</sup> This exchange process had been reported by Volker *et al.* in 1972. In the first instance, the fluoride, associates rapidly with the HAP surface and within hours the exchange process occurs before converting HAP into fluorinated apatite (f-HAP).<sup>81–85</sup> It appears that the tracer binds preferentially to regions of newly developing vascular micro-calcification, with calcium deposits which are beyond the resolution of CT (*Figure 1.13*). The binding appears to be dependent upon the surface area of the calcification.<sup>3,13,24,26,35,84</sup>



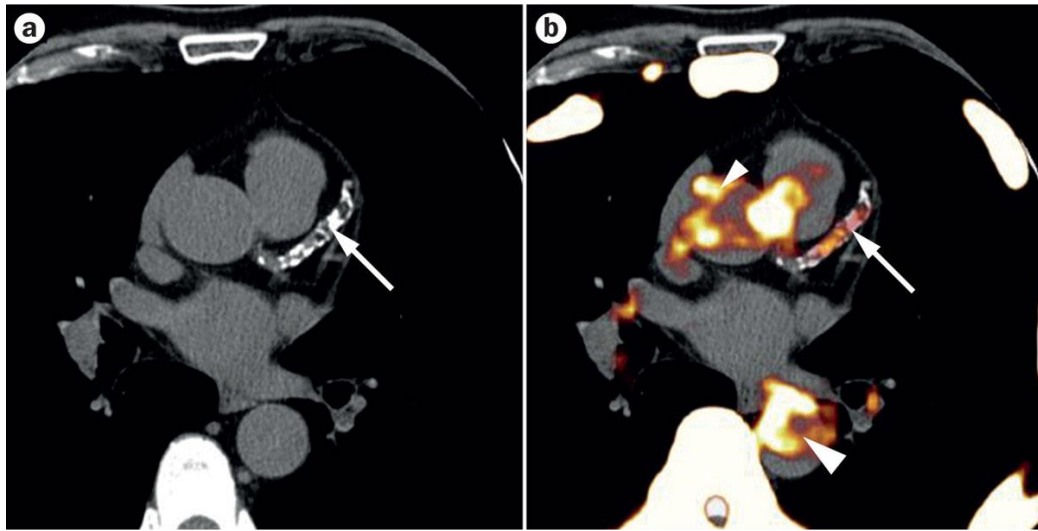


**Figure 1.13** Transaxial images of a patient with chronic stable angina. (A) CAC showing high volume calcium in the left anterior artery (white arrow). (B) Intense  $^{18}\text{F}$ -NaF uptake on fused PET–CT image (white arrows). Larger arrows show area where only  $^{18}\text{F}$ -NaF is picked up with no CAC signal being observed. Reproduced with permission.<sup>86</sup>

A recent study by Irkle *et al.* shows that in patients with stable coronary artery disease  $^{18}\text{F}$ -NaF uptake correlates with CAC, although nearly half the patients with a high CAC score do not present any  $^{18}\text{F}$ -NaF signal and high  $^{18}\text{F}$ -NaF signal can be seen in areas with a low CAC score.<sup>13,24</sup> This is indicative that  $^{18}\text{F}$ -NaF can be used to identify high-risk coronary lesions and hence plaques that are at high risk of rupture.<sup>24</sup>  $^{18}\text{F}$ -NaF has proven promising in the identification of high risk plaques but lacks the resolution required to determine the specific calcification that may contribute to plaque rupture. One strategy to access this is to use molecular imaging techniques to study plaque and calcification morphology with higher resolution than PET.<sup>68,70</sup>

## 1.5 Conclusion

Vulnerable atherosclerotic plaques are an important topic in cardiology as CVD is the second highest cause of death and currently there is little understanding of the mechanism behind the disease. Another major issue is the lack of imaging techniques that are able to assess the vulnerability of the plaque. As a consequence, the development of techniques that can identify micro-calcification and therefore plaque vulnerability is a major research goal with the potential to improve the understanding of the disease pathology and also to reduce morbidity and mortality rates. The emerging technique that has proven the most promising required for the identification of plaques at high risk of rupture is  $^{18}\text{F}$ -NaF. However, it lacks the resolution required to provide anatomical information on the vulnerability of the plaque. One strategy to access this additional information is to use molecular imaging techniques such as fluorescence

and Raman which have a much higher resolution and can provide us with additional molecular and anatomical information about the plaque.

## 1.6 Approach

The focus of this thesis is on the development of optical probes to better understand the mechanism behind plaque formation, looking specifically at calcification with the hope to develop an improved and more suitable approach to detect micro-calcification at an early stage before plaque rupture.

Two types of fluorescent probes were synthesized; a fluoride-specific probe to detect the fluoride PET tracer, upon localization of the fluoride anions around the surface of the HAP, and a calcium-specific probe to bind directly to HAP. It was anticipated that both probes would provide a better understanding of the binding of NaF to calcified deposits and additional information on the mechanism behind calcification and plaque formation.

Fluorescent fluoride and calcium probes were synthesized and their selectivity was tested against different types of anions (fluoride probe) and calcium minerals (calcium probe) (Chapter 2). For the fluoride probe to be valuable, its limit of detection (LOD) needed to be in the pM concentration range for it to be able to detect Na<sup>18</sup>F, unfortunately, this did not appear to be the case and therefore the fluoride probe was set aside. Upon examining the specificity of the calcium probes for HAP, only one was shown to be selective for HAP and this was taken forward into cell and *ex vivo* mouse studies (Chapter 3). At this point, the focus was on proving that the probe was nontoxic at the concentration used and it was compared to the current gold standard laboratory techniques used for the detection of calcification (Alizarin S, calcium leaching assay and von Kossa).

Once cell and *ex vivo* models proved satisfactory, the probe was tested on calcified vascular tissue (Chapter 4). Again, similarly to the previous chapter, the probe was compared to Alizarin S and von Kossa stains.

In the final results chapter (Chapter 5) of this thesis, the focus was shifted on analyzing calcified tissue (cells, *ex vivo* rat aortic tissue and human vascular tissue) by Raman spectroscopy in order to understand the crystal form of the calcified deposits.

Together, fluorescence and Raman spectroscopy have provided us with additional scientific knowledge that will hopefully shape the future of cardiovascular research.

## 1.7 References

- 1 J. D. Hutcheson, M. C. Blaser and E. Aikawa, *Circ. Res.*, 2017, **120**, 270–273.
- 2 G. Anwaier, C. Chen, Y. Cao and R. Qi, *Int. J. Nanomedicine*, 2017, **12**, 7681–7693.
- 3 M. R. Dweck, M. K. Doris, M. Motwani, P. D. Adamson, P. Slomka, D. Dey, Z. A. Fayad, D. E. Newby and D. Berman, *Nat. Rev. Cardiol.*, 2016, **13**, 533–548.
- 4 W. Liu, Y. Zhang, C.-M. Yu, Q.-W. Ji, M. Cai, Y.-X. Zhao and Y.-J. Zhou, *J. Geriatr. Cardiol.*, 2015, **12**, 668–75.
- 5 T. Benedek, I. Rodean, M. Ratiu, N. Rat, L. Y. Eremie, C. Biriş, L. Lazăr, M. Păcurar and I. Benedek, *J. Cardiovasc. Emergencies*, 2018, **22**, 40–265.
- 6 S. Bertazzo, E. Gentleman, K. L. Cloyd, A. H. Chester, M. H. Yacoub and M. M. Stevens, *Nat. Mater.*, 2013, **12**, 576–583.
- 7 J. M. Tarkin, M. R. Dweck, N. R. Evans, R. A. P. Takx, A. J. Brown, A. Tawakol, Z. A. Fayad and J. H. F. Rudd, *Circ. Res.*, 2016, **118**, 750–69.
- 8 J. P. M. Andrews, Z. A. Fayad and M. R. Dweck, *Atherosclerosis*, 2018, **272**, 118–128.
- 9 N. Townsend, J. Williams, P. Bhatnagar, K. Wickramasinghe and M. Rayner, *Cardiovascular disease statistics, 2014*, 2014.
- 10 A. J. Lusis, *Nature*, 2000, **407**, 233–241.
- 11 I. Tabas, G. Garcia-Cardena and G. K. Owens, *J. Cell Biol.*, 2015, **209**, 13–22.
- 12 F. A. Jaffer, *Methods Mol. Biol.*, 2011, **680**, 131–40.
- 13 P. D. Adamson, A. T. Vesey, N. V. Joshi, D. E. Newby and M. R. Dweck, *Cardiovasc. Diagn. Ther.*, 2015, **5**, 150–155.
- 14 L. Cui, N. A. Rashdan, D. Zhu, E. M. Milne, P. Ajuh, G. Milne, M. H. Helfrich, K. Lim, S. Prasad, D. A. Lerman, A. T. Vesey, M. R. Dweck, W. S. Jenkins, D. E. Newby, C. Farquharson and V. E. Macrae, *J. Cell. Physiol.*, 2017, **232**, 2985–2995.
- 15 S. Gargiulo, M. Gramanzini and M. Mancini, *Int. J. Mol. Sci.*, , DOI:10.3390/ijms17091511.
- 16 A. Yamashita and Y. Asada, *J. Biomed. Biotechnol.*, 2011, **2011**, 424929.
- 17 J. D. Hutcheson, N. Maldonado and E. Aikawa, *Curr. Opin. Lipidol.*, 2014, **25**, 327–

- 32.
- 18 D. Cheng, X. Li, C. Zhang, H. Tan, C. Wang, L. Pang and H. Shi, *ACS Appl. Mater. Interfaces*, 2015, **7**, 2847–55.
- 19 C. Liu, S. Boydston-White, A. Weisberg, W. Wang, L. A. Sordillo, A. Perotte, V. P. Tomaselli, P. P. Sordillo, Z. Pei, L. Shi and R. R. Alfano, *J. Biomed. Opt.*, 2016, **21**, 127006.
- 20 A. L. Durham, M. Y. Speer, M. Scatena, C. M. Giachelli and C. M. Shanahan, *Cardiovasc. Res.*, 2018, 114, 590–600.
- 21 M. Asrar ul Haq, J. Layland, V. Mutha and P. Barlis, *Heart Asia*, 2013, **5**, 154–161.
- 22 M. R. Dweck, E. Aikawa, D. E. Newby, J. M. Tarkin, J. H. F. Rudd, J. Narula and Z. A. Fayad, *Circ. Res.*, 2016, 119, 330–340.
- 23 T. M. Doherty, K. Asotra, L. A. Fitzpatrick, J.-H. Qiao, D. J. Wilkin, R. C. Detrano, C. R. Dunstan, P. K. Shah and T. B. Rajavashisth, *Proc. Natl. Acad. Sci.*, 2003, **100**, 11201–11206.
- 24 A. Irkle, A. T. Vesey, D. Y. Lewis, J. N. Skepper, J. L. E. Bird, M. R. Dweck, F. R. Joshi, F. A. Gallagher, E. A. Warburton, M. R. Bennett, K. M. Brindle, D. E. Newby, J. H. Rudd and A. P. Davenport, *Nat. Commun.*, 2015, **6**, 7495.
- 25 P. Lanzer, M. Boehm, V. Sorribas, M. Thiriet, J. Janzen, T. Zeller, C. S. Hilaire and C. Shanahan, *Eur. Heart J.*, 2014, **35**, 1–14.
- 26 L. Bessueille and D. Magne, *Cell. Mol. Life Sci.*, 2015, **72**, 2475–2489.
- 27 M. R. Rubin and S. J. Silverberg, *J. Clin. Endocrinol. Metab.*, 2004, 89, 4243–4245.
- 28 R. Kramann, C. Goettsch, J. Wongboonsin, H. Iwata, R. K. Schneider, C. Kuppe, N. Kaesler, M. Chang-Panesso, F. G. Machado, S. Gratwohl, K. Madhurima, J. D. Hutcheson, S. Jain, E. Aikawa and B. D. Humphreys, *Cell Stem Cell*, 2016, **19**, 628–642.
- 29 R. Shroff, D. A. Long and C. Shanahan, *J. Am. Soc. Nephrol.*, 2013, **24**, 179–189.
- 30 E. Aikawa, M. Nahrendorf, J. L. Figueiredo, F. K. Swirski, T. Shtatland, R. H. Kohler, F. A. Jaffer, M. Aikawa and R. Weissleder, *Circulation*, 2007, **116**, 2841–2850.
- 31 C. M. Shanahan, *Circulation*, 2007, 116, 2782–2785.

- 32 L. Hortells, S. Sur and C. St. Hilaire, *Front. Cardiovasc. Med.*, 2018, **5**, 27.
- 33 M. Abedin, Y. Tintut and L. L. Demer, *Arterioscler. Thromb. Vasc. Biol.*, 2004, **24**, 1161–1170.
- 34 M. R. Dweck, N. A. Boon and D. E. Newby, *J. Am. Coll. Cardiol.*, 2012, **60**, 1854–1863.
- 35 T. A. Pawade, D. E. Newby and M. R. Dweck, *J. Am. Coll. Cardiol.*, 2015, **66**, 561–577.
- 36 M. Simionescu and A. V. Sima, *Inflammation and Atherosclerosis*, Springer, 2012.
- 37 N. Reznikov, J. A. M. Steele, P. Fratzl and M. M. Stevens, *Nat. Rev. Mater.*, 2016, **1**, 16041.
- 38 M. R. Bennett, S. Sinha and G. K. Owens, *Circ. Res.*, 2016, **118**, 692–702.
- 39 P. Libby, *Nature*, 2002, **420**, 868–874.
- 40 P. A. McCullough, K. R. Sandberg, F. Dumler and J. E. Yanez, *J. Nephrol.*, 2004, **17**, 205–215.
- 41 M. M. Izquierdo-Gómez, I. Hernández-Betancor, J. García-Niebla, B. Marí-López, I. Laynez-Cerdeña and J. Lacalzada-Almeida, *Biomed Res. Int.*, 2017, **2017**, 5178631.
- 42 N. M. Rajamannan, F. J. Evans, E. Aikawa, K. J. Grande-Allen, L. L. Demer, D. D. Heistad, C. A. Simmons, K. S. Masters, P. Mathieu, K. D. O'Brien, F. J. Schoen, D. A. Towler, A. P. Yoganathan and C. M. Otto, *Circulation*, 2011, **124**, 1783–91.
- 43 T. Akiyoshi, H. Ota, K. Iijima, B. K. Son, T. Kahyo, M. Setou, S. Ogawa, Y. Ouchi and M. Akishita, *Atherosclerosis*, 2016, **244**, 51–58.
- 44 J. S. Lee, J. D. Morrisett and C.-H. Tung, *Atherosclerosis*, 2012, **224**, 340–7.
- 45 K. Johnson, M. Polewski, D. Van Etten and R. Terkeltaub, *Arterioscler. Thromb. Vasc. Biol.*, 2005, **25**, 686–691.
- 46 S. Boonrungsiman, E. Gentleman, R. Carzaniga, N. D. Evans, D. W. McComb, A. E. Porter and M. M. Stevens, *Proc. Natl. Acad. Sci.*, 2012, **109**, 14170–14175.
- 47 J. L. Hunt, R. Fairman, M. E. Mitchell, J. P. Carpenter, M. Golden, T. Khalapyan, M. Wolfe, D. Neschis, R. Milner, B. Scoll, A. Cusack and E. R. Mohler, *Stroke*, 2002, **33**, 1214–9.

- 48 C. F. T. van der Ven, P.-J. Wu, M. W. Tibbitt, A. van Mil, J. P. G. Sluijter, R. Langer and E. Aikawa, *Clin. Sci.*, 2017, **131**, 181–195.
- 49 D. E. Andreou and I. Andreadou, *Pharmakeftiki*, 2009, **22**, 83–96.
- 50 M. Rattazzi and M. E. Rosenfeld, *Atherosclerosis*, 2018, **270**, 193–195.
- 51 F. Otsuka, K. Sakakura, K. Yahagi, M. Joner and R. Virmani, *Arterioscler. Thromb. Vasc. Biol.*, 2014, **34**, 724–736.
- 52 A. Ferreira Mendes, J. D. Hutcheson, C. García-Rodríguez, I. Parra-Izquierdo, I. Castaños-Mollor, J. López, J. A. San Román and M. S. Crespo, *Front. Physiol. Front. Physiol*, 2018, **9**, 201.
- 53 M. J. Goumans, A. Zwijsen, P. ten Dijke and S. Bailly, *Cold Spring Harb. Perspect. Biol.*, 2018, **10**, a031989.
- 54 T. Nakahara, J. Narula and H. W. Strauss, *J. Am. Coll. Cardiol.*, 2016, **67**, 79–80.
- 55 E. P. C. van der Vorst, R. J. de Jong and M. M. P. C. Donners, *Front. Cardiovasc. Med.*, 2018, **5**, 2.
- 56 R. Arvizo, R. Bhattacharya and P. Mukherjee, *Expert Opin. Drug Deliv.*, 2010, **7**, 753–63.
- 57 J. H. F. Rudd, K. S. Myers, S. Bansilal, J. Machac, M. Woodward, V. Fuster, M. E. Farkouh and Z. A. Fayad, *Circ. Cardiovasc. Imaging*, 2009, **2**, 107–115.
- 58 P. J. Harris, K. L. Lee, F. E. Harrell, V. S. Behar, R. A. Rosati, J. A. Cabico, J. Friedman and G. A. Diamond, *Circulation*, 1980, **62**, 718–26.
- 59 J. A. Ambrose, M. A. Tannenbaum, D. Alexopoulos, C. E. Hjendahl-Monsen, J. Leavy, M. Weiss, S. Borrico, R. Gorlin and V. Fuster, *J. Am. Coll. Cardiol.*, 1988, **12**, 56–62.
- 60 E. Falk, P. K. Shah and V. Fuster, *Circulation*, 1995, **92**, 657–671.
- 61 H.-S. Shin and T. S. Kang, *Korean Circ. J.*, 2012, **42**, 54.
- 62 F. Prati, S. Uemura, G. Souteyrand, R. Virmani, P. Motreff, L. Di Vito, G. Biondi-Zoccai, J. Halperin, V. Fuster, Y. Ozaki and J. Narula, *JACC Cardiovasc. Imaging*, 2013, **6**, 283–287.
- 63 K. Hattori, Y. Ozaki, T. F. Ismail, M. Okumura, H. Naruse, S. Kan, M. Ishikawa, T.

- Kawai, M. Ohta, H. Kawai, T. Hashimoto, Y. Takagi, J. Ishii, P. W. Serruys and J. Narula, *JACC Cardiovasc. Imaging*, 2012, **5**, 169–177.
- 64 G. J. Tearney, H. Yabushita, S. L. Houser, H. T. Aretz, I. K. Jang, K. H. Schlendorf, C. R. Kauffman, M. Shishkov, E. F. Halpern and B. E. Bouma, *Circulation*, 2003, **107**, 113–119.
- 65 C. M. Gardner, H. Tan, E. L. Hull, J. B. Lissauskas, S. T. Sum, T. M. Meese, C. Jiang, S. P. Madden, J. D. Caplan, A. P. Burke, R. Virmani, J. Goldstein and J. E. Muller, *JACC Cardiovasc. Imaging*, 2008, **1**, 638–648.
- 66 S. Waxman, S. R. Dixon, P. L’Allier, J. W. Moses, J. L. Petersen, D. Cutlip, J. C. Tardif, R. W. Nesto, J. E. Muller, M. J. Hendricks, S. T. Sum, C. M. Gardner, J. A. Goldstein, G. W. Stone and M. W. Krucoff, *JACC Cardiovasc. Imaging*, 2009, **2**, 858–868.
- 67 R. D. Madder, J. A. Goldstein, S. P. Madden, R. Puri, K. Wolski, M. Hendricks, S. T. Sum, A. Kini, S. Sharma, D. Rizik, E. S. Brilakis, K. A. Shunk, J. Petersen, G. Weisz, R. Virmani, S. J. Nicholls, A. Maehara, G. S. Mintz, G. W. Stone and J. E. Muller, *JACC Cardiovasc. Interv.*, 2013, **6**, 838–846.
- 68 C. Vinegoni, I. Botnaru, E. Aikawa, M. A. Calfon, Y. Iwamoto, E. J. Folco, V. Ntziachristos, R. Weissleder, P. Libby and F. A. Jaffer, *Sci. Transl. Med.*, 2011, **3**, 84ra45.
- 69 D. M. Mizrahi, O. Ziv-Polat, B. Perlstein, E. Gluz and S. Margel, *Eur. J. Med. Chem.*, 2011, **46**, 5175–83.
- 70 F. A. Jaffer, C.-H. Tung, R. E. Gerszten and R. Weissleder, *Arterioscler. Thromb. Vasc. Biol.*, 2002, **22**, 1929–35.
- 71 F. A. Jaffer, C. Vinegoni, M. C. John, E. Aikawa, H. K. Gold, A. V Finn, V. Ntziachristos, P. Libby and R. Weissleder, *Circulation*, 2008, **118**, 1802–1809.
- 72 F. A. Jaffer, M. A. Calfon, A. Rosenthal, G. Mallas, R. N. Razansky, A. Mauskapf, R. Weissleder, P. Libby and V. Ntziachristos, *J. Am. Coll. Cardiol.*, 2011, **57**, 2516–2526.
- 73 T. Hara, G. J. Ughi, J. R. McCarthy, S. S. Erdem, A. Mauskapf, S. C. Lyon, A. M. Fard, E. R. Edelman, G. J. Tearney and F. A. Jaffer, *Eur. Heart J.*, 2017, **38**, 447–455.
- 74 A. Zaheer, M. Murshed, A. M. De Grand, T. G. Morgan, G. Karsenty and J. V Frangioni, *Arterioscler. Thromb. Vasc. Biol.*, 2006, **26**, 1132–1136.

- 75 E. Aikawa, M. Aikawa, G. Rusanescu, Y. Iwamoto, G. P. Shi, F. A. Jaffer, P. Libby, J. L. Figueiredo, D. Fukuda, R. H. Kohler and R. Weissleder, *Circulation*, 2009, **119**, 1785–1794.
- 76 H. Maeda, T. Kowada, J. Kikuta, M. Furuya, M. Shirazaki, S. Mizukami, M. Ishii and K. Kikuchi, *Nat. Chem. Biol.*, 2016, **12**, 579–585.
- 77 S. Achenbach and P. Raggi, *Eur. Heart J.*, 2010, **31**, 1442–1448.
- 78 M. Dweck, Imaging Vascular Calcification and Inflammation Using PET/CT, [https://www.pathsoc.org/files/meetings/edinburghpresthurs/1000 Thurs Fintry Dweck.pdf%0A](https://www.pathsoc.org/files/meetings/edinburghpresthurs/1000_Thurs_Fintry_Dweck.pdf%0A).
- 79 W. Chen and V. Dilsizian, *Curr. Cardiol. Rep.*, 2013, **15**, 364.
- 80 T. Nakahara and H. W. Strauss, *Eur. J. Nucl. Med. Mol. Imaging*, 2017, **44**, 858–860.
- 81 T. Gomwe, S. E. Both and J. W. Nicholson, *Ceram. - Silikaty*, 2012, **56**, 85–88.
- 82 T. Aoba, *Crit. Rev. Oral Biol. Med.*, 1997, **8**, 136–53.
- 83 M. Braun and C. Jana, *Chem. Phys. Lett.*, 1995, **245**, 19–22.
- 84 M. Blau, R. Ganatra and M. A. Bender, *Semin. Nucl. Med.*, 1972, **2**, 31–37.
- 85 M. Blau, W. Nagler and M. A. Bender, *J. Nucl. Med.*, 1962, **3**, 332–334.
- 86 J. M. Tarkin, F. R. Joshi and J. H. F. Rudd, *Nat. Rev. Cardiol.*, 2014, **11**, 443–57.



# Chapter 2- Synthesis of Fluorescent Dyes for the *In Vitro* Detection of Calcification

## 2.1 Fluorophores

Fluorescence has long been used to visualize biological processes at many levels, from single molecules to complete organisms.<sup>1,2</sup> In the past, fluorescence imaging was achieved by the attachment of small organic dyes attached to antibodies or proteins of interest (*Figure 2.1*).

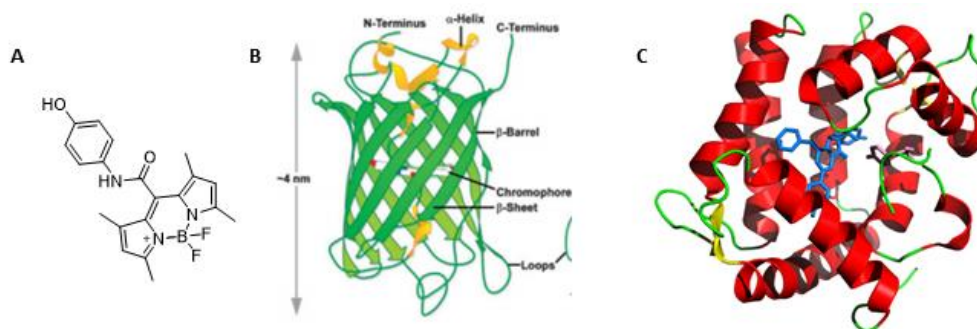


**Figure 2.1:** A fluorophore, can be: (A) small molecules; (B) genetically encoded material (e.g. GFP) and (C) genetically encoded hybrid system (e.g. aequorin).

The use of fluorescent proteins has enabled non-invasive imaging in living cells and organisms, protein trafficking and numerous dynamic biochemical signals.<sup>3,4</sup> Hybrid systems in which fluorescent proteins are genetically encoded are filling other useful niches in identifying cancer, cardiovascular and neurodegenerative diseases.<sup>5,6</sup>

Fluorophores (*Figure 2.2*), for covalently labelling macromolecules, have undergone intensive optimization in wavelength range, brightness, photostability and reduction in self-quenching.<sup>1,7</sup> Molecular strategies have included extension of double-bond conjugation, rigidification through addition of extra ring systems and decoration with electron-withdrawing or charged substituents such as fluorine and/or sulfonates.<sup>8</sup> Fluorophores can be compared by assessing the brightness, a product of the extinction coefficient and the quantum yield ( $\epsilon \times \Phi$ ) which accounts for both the amount of light absorbed and the quantum efficiency of the

fluorophore.<sup>9</sup> Hundreds of such dyes are commercially available and further progress is likely to be incremental.<sup>1</sup>

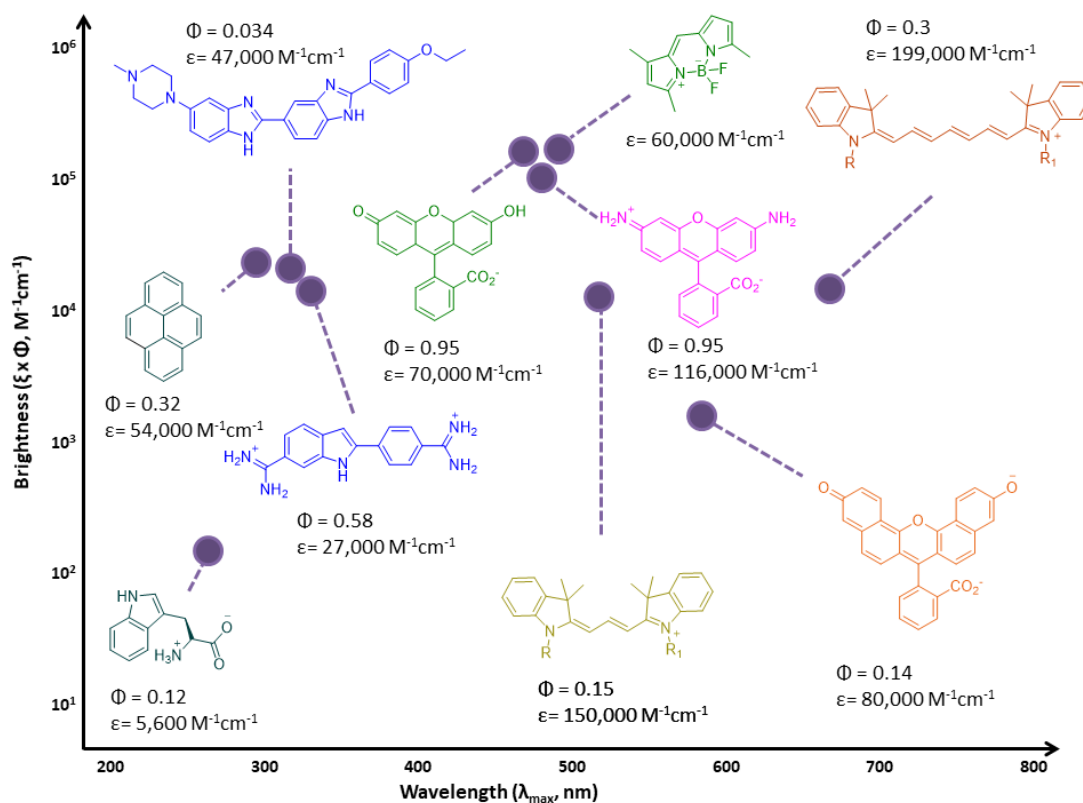


**Figure 2.2: Commonly used fluorophores.** Fluorophores are reported in a graph plotting brightness against emission wavelength.

Over the last several decades there has been a remarkable growth in the use of small-molecule fluorescent probes in the field of biological sciences (Figure 2.3). Non-fluorescent molecules of interest can be tagged with a fluorescent moiety using well established protocols, thus allowing the visualisation of specific biological pathways. In addition to aiding imaging, functional fluorescent probes have become indispensable tools in modern biology because they provide dynamic information concerning the localization and a number of molecules of interest.<sup>10</sup>

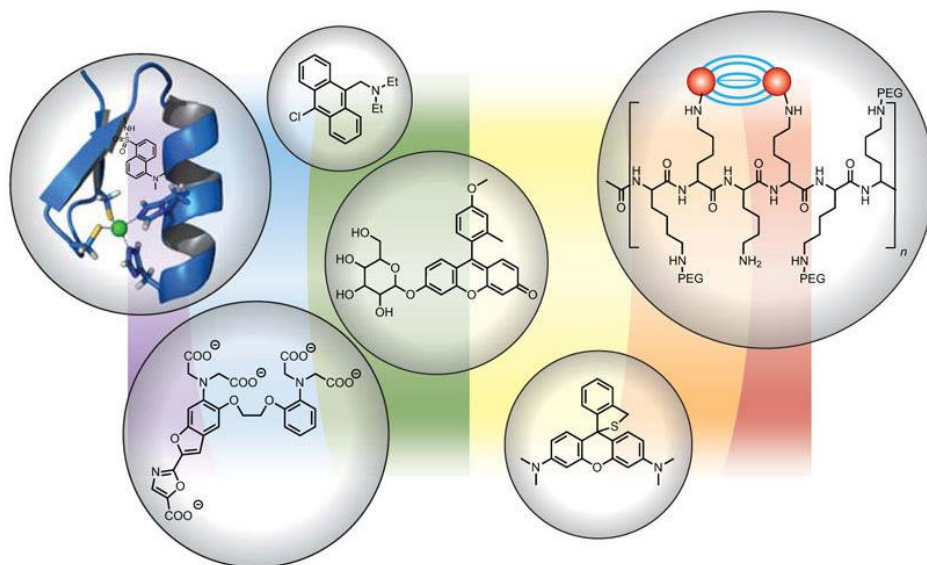


**Figure 2.3: Small molecule probes.** Illustrated are a zinc finger-small molecule probe (top left), pH probe (top middle), protease probe for in vivo imaging (top right),  $\beta$ -galactosidase probe (middle),  $\text{Ca}^{2+}$  probe (bottom left) and a hypochlorite specific reactive-oxygen species probe (bottom right). Image reproduced with permission.<sup>10</sup>

Fluorescent dyes, in comparison to absorbance-based probes often used by researchers in the nineteenth century, provide nearly infinite contrast, this arises from the release of light on a dark background when illuminated with shorter-wavelength light.<sup>10</sup> Fluorescent dyes can provide single-molecule sensitivity, real time quantification and molecule localization.<sup>11</sup> The great potential utility for fluorescence visualisation of biomolecules, has led to the development of a wide range of fluorophores for labelling biological molecules.<sup>10</sup>

## 2.2 Approach for the detection of HAP

As mentioned in Chapter 1, two different approaches have been identified to study vascular calcification; one involving fluoride probes (section 2.3) and the other involving calcium probes (section 2.4).

The fluoride probes, will allow the presence of  $\text{Na}^{18}\text{F}$  localized around the HAP crystals to be detected and will be correlated with PET while the calcium probes will bind directly to HAP and will therefore allow for a more direct study of the calcification process.

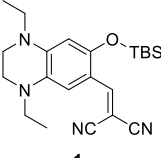
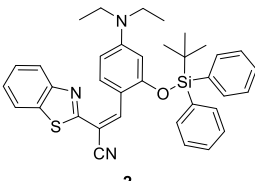
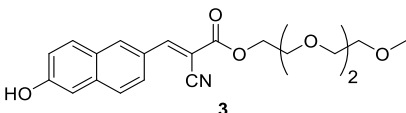
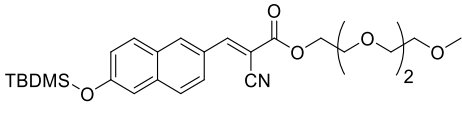
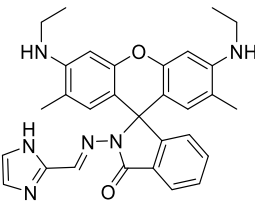
## 2.3 Fluoride probes

### 2.3.1 Probe selection

The design and synthesis of fluorescent probes that allow for a selective and sensitive detection of anions has gained a large amount of attention the past few years.<sup>12-14</sup> Anions are known to play an important role in a wide range of chemical and biological processes and have been the target of investigations into these processes for the past decade.<sup>15</sup> Effort has been put into the development of rapid, selective and sensitive chemical sensors for the detection and imaging of the location of fluoride ions by exploiting the unique reactivity of fluoride.<sup>13</sup> These are based on cleavage reactions, nucleophilic additions and molecular interactions. Most of them have been proven to work only in anhydrous organic media, with slow response times and low sensitivity. Very few have been reported to be tolerated in biological systems for cell imaging applications.<sup>15,16</sup>

To investigate the Na<sup>18</sup>F PET tracer, a number of published fluoride sensors were analysed for their potential application to this target. The selected fluorophore should: be cell permeable; have high sensitivity for fluoride; and have excellent properties for fluorescent microscopy.<sup>13,17-19</sup> Five probes with the above characteristics were inspected further (*Table 2.1*), one of which is based on a tetrahydroquinoxaline motif (**1**) which had previously been investigated by the Song group.<sup>15</sup> The probe (**1**) was described to have excellent water solubility, photostability properties and emission in the NIR region. However, the synthetic approach to obtain the tetrahydroquinoxaline (**1**) involved several laborious synthesis and purification steps making the other probes more appealing.

Table 2.1: Potential fluoride probes and their advantages.

Fluoride probes	# Synthetic steps	Advantages
 <p><b>1</b></p> <p><math>\lambda_{ex} = 511 \text{ nm}</math> <math>\lambda_{em} = 616 \text{ nm}</math></p>	Multi-step	Reported to present excellent water solubility and photostability properties.
 <p><b>2</b></p> <p><math>\lambda_{ex} = 465 \text{ nm}</math> <math>\lambda_{em} = 535 \text{ nm}</math></p>	2 step	Reported to show high sensitivity for fluoride.
 <p><b>3</b></p> <p><math>\lambda_{ex} = 388 \text{ nm}</math> <math>\lambda_{em} = 490 \text{ nm}</math></p>	3 step	Reported to demonstrate excellent cell permeability.
 <p><b>4</b></p>	4 step	Parent compound <b>3</b> reported to demonstrate excellent cell permeability.
 <p><b>5</b></p> <p><math>\lambda_{ex} = 500 \text{ nm}</math> <math>\lambda_{em} = 557 \text{ nm}</math></p>	1 step	Reported to be highly sensitive and selective for fluoride.

Another probe explored was (*E*)-2-(benzo[*d*]thiazol-2-yl)-3-(2-*tert*-butyl-(diphenylsilyloxy)-4-diethylaminophenyl)acrylonitrile (**2**). In the presence of fluoride this probe is reported to cyclize and form a highly fluorescent cyclic coumarin.<sup>19</sup> In contrast to the tetrahydroquinoxaline (**1**), to acquire **2**, only a two-step synthesis was required making the

probe of interest in investigating the role of the Na<sup>18</sup>F PET tracer. However, upon close inspection of the fluorescent characteristics of probe (2), a very strong background fluorescence signal was observed even before the addition of NaF and therefore this probe was also set aside.

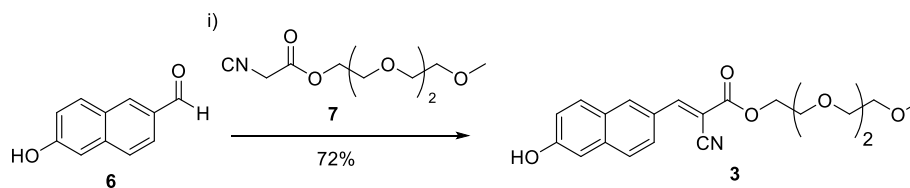
Two other fluorophores, based on the naphthalene cyanoacrylate motif, were considered excellent candidates for detecting fluoride. The naphthalene cyanoacrylate motif (3 and 4) has been previously shown to have excellent cell permeability properties,<sup>13</sup> in addition, the synthesis appeared straightforward with only 3-4 steps required.

Rhodamine-based probe (5) was yet another probe with interesting properties and was recently reported to detect fluoride in biological systems with high sensitivity and selectivity.<sup>20</sup> Another advantage of this probe was the rapid one-step reaction required to synthesise the probe, making it very appealing for our application.

These three most biologically relevant fluoride sensors (3-5) were explored in more detail for their potential to be used to analyse the mechanism underlying the uptake of the tracer.

### 2.3.2 Naphthalene 2-cyanoacrylate

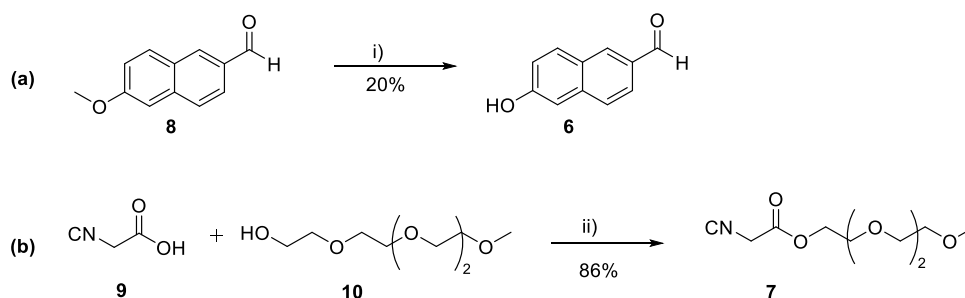
One of the two probes that were selected was reported by Qu's group whose focus was on synthesizing new water soluble fluorescent dyes containing a phenol group based on naphthalene 2-cyanoacrylate.<sup>13</sup> Cyanoacrylate dyes have previously been used for amyloid fluorescent detection due to their excellent cell permeability. Cyanoacrylate probe (3) was prepared by reacting 6-hydroxy-2-naphthaldehyde (6) with 2-(2-(2-methoxyethoxy)ethoxy)-ethyl 2-cyanoacetate (7) (Scheme 2.1). These two starting materials had to be synthesised as they were not commercially available.



**Scheme 2.1:** Synthesis of cyanoacrylate probe (3). Reagents and conditions: i) 7, DMAP, THF, 60 °C, 24 h.

Thus 6-hydroxy-2-naphthaldehyde (6) was synthesised by the cleavage of the methyl ether moiety of 6-methoxy-2-naphthaldehyde (8) using AlCl<sub>3</sub> in chlorobenzene at 130 °C for 4 hours with 20% yield (Scheme 2.2 (a)). 2-(2-(2-Methoxyethoxy)ethoxy)-ethyl 2-cyanoacetate (7)

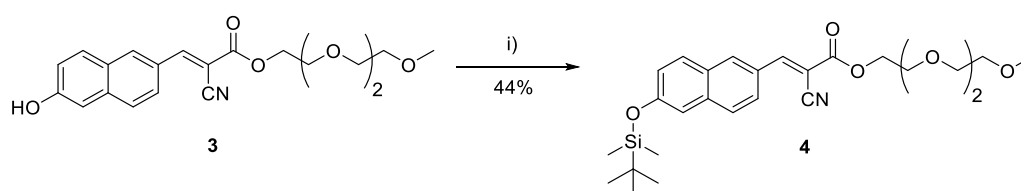
was also synthesised as it is not commercially available by coupling 2-cyanoacetic acid (**9**) triethylene glycol monomethyl ether (**10**) using DCC and DMAP at 0 °C for 6 hours. The product was obtained in 86% yield (*Scheme 2.2 (b)*).



**Scheme 2.2 Synthesis of the two precursors for the assembly of the cyanoacrylate probe (3).** (a) Synthesis of 6-hydroxy-2-naphthaldehyde (**6**). Reagents and conditions: i)  $\text{AlCl}_3$ , chlorobenzene, 130 °C, 4 h. (b) Synthesis of 2-(2-(2-methoxyethoxy)ethoxy)-ethyl 2-cyanoacetate (**7**). Reagents and conditions: ii) DMAP, DCC, DCM, 0 °C, 6 h.

The reaction of the two fragments was then carried out using catalytic amounts of DMAP to give naphthalene 2-cyanoacrylate (**3**) in 72% yield (*Scheme 2.1*).

A TBDMS protected naphthalene 2-cyanoacrylate probe (**4**) was also synthesised as it was proposed that a silyl protecting group would be more selective towards fluoride than to any other anions. Having a free hydroxyl group, it was suspected that naphthalene 2-cyanoacrylate could also be deprotonated by other anions, and thus its selectivity solely for fluoride had to be proven. TBDMS protected naphthalene 2-cyanoacrylate (**4**) was synthesised by reacting naphthalene 2-cyanoacrylate (**3**) with *tert*-butyldimethylsilyl chloride (TBDMS-Cl) using DMAP and imidazole to obtain the TBDMS product in 44% yield (*Scheme 2.3*).

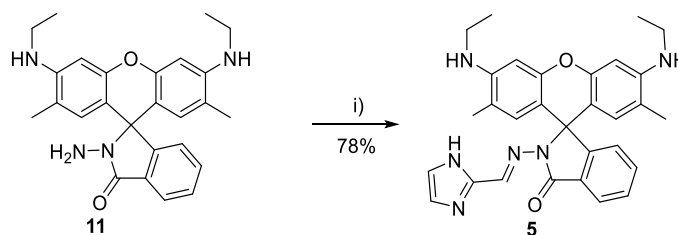


**Scheme 2.3: Synthesis of TBDMS protected cyanoacrylate (4).** Reagents and conditions: i) TBDMS-Cl, DMAP, imidazole, DMF, rt, 1 h.

### 2.3.3 Imidazole bearing rhodamine 6G

Another fluoride probe (**5**) which was synthesised by the Chellappa group was also considered. Here, the development of a rhodamine based sensor for the detection of fluoride ions in live cell imaging was investigated.<sup>20</sup> The imidazole bearing rhodamine 6G (**5**) was readily

synthesised using a one-step reaction involving two commercially available starting materials. The synthesis involved the reaction between rhodamine 6G with 2-formyl imidazole to obtain a colourless solid in a 78% yield (Scheme 2.4) which was then used for selectivity studies.

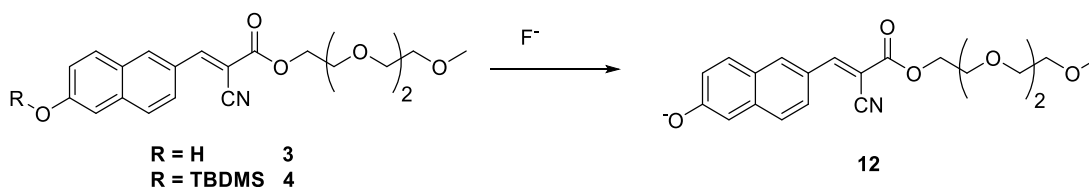


**Scheme 2.4: Synthesis of imidazole bearing Rhodamine 6 G.** Reagents and conditions: i) 2-formyl imidazole, EtOH, 90 °C, 24 h.

### 2.3.4 Selectivity of fluoride probes

The 2,2-cyanoacrylate probes (**3**, **4**) and the imidazole bearing rhodamine 6G (**5**) were studied to determine their reactivity and selectivity toward fluoride ions.

For the 2,2-cyanoacrylate probes, UV/VIS was used as a first line of assessment to determine both the absorption of the probes and the reproducibility of the data presented in the literature. Upon addition of NaF to both probe **3** and **4**, deprotonation of the hydroxyl group was expected (Scheme 2.5).



**Scheme 2.5: Deprotonation or deprotection of the hydroxyl group on the cyanoacrylate probes (3 and 4) upon addition of fluoride.**

It had been reported in the literature that the addition of NaF to naphthalene 2-cyanoacrylate (**3**) would lead to a change in the absorption spectra (Figure 2.4 A); with a decrease in peaks at 290 and 382 nm and the rapid appearance of a peak at 548 nm. However, when UV/VIS tests were carried out on both naphthalene 2-cyanoacrylate probes (**3** and **4**) the change in spectra did not take place as established (Figure 2.4 B, C). Peaks at 290 nm and 382 nm did indeed decrease with increased addition of NaF however, no additional peak appeared at 548 nm, even when a large excess of the fluoride source was added. This test was carried out using phosphazene base (P<sub>2</sub>-Et). Upon addition of the basic solution to the probe there was an immediate change in colour; from light yellow to bright red however, the UV spectra did not



provide the same data reported in the literature. These results suggest that fluoride ions are not able to deprotonate or deprotect the hydroxyl group therefore making this probe ineffective for the study of Na<sup>18</sup>F PET tracer.

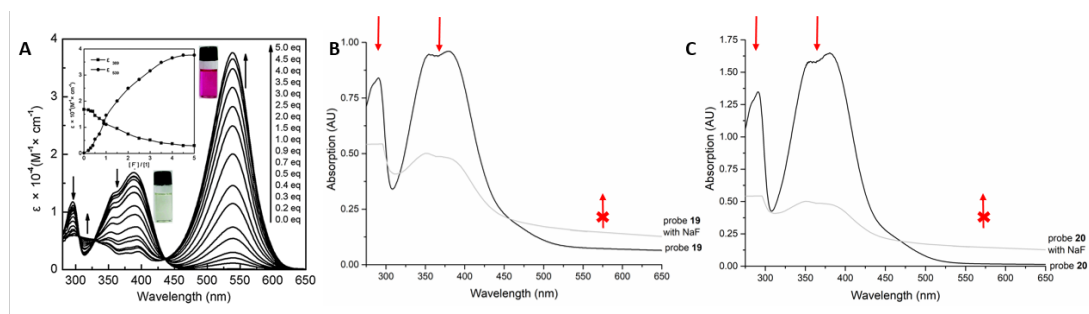
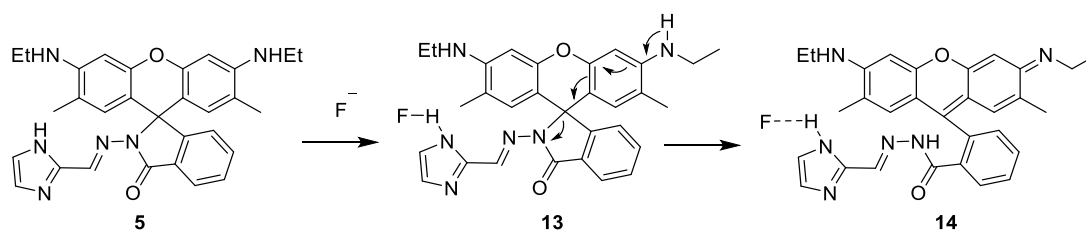


**Figure 2.4: UV/VIS spectra of cyanoacrylate probes.** (A) Reported absorption spectrum of 2-cyanoacrylate probe (3) reproduced with permission.<sup>13</sup> UV/VIS spectra of (B) 2-cyanoacrylate (3) and (C) TBDMS protected 2-cyanoacrylate (4) (30  $\mu\text{M}$ ) upon addition of excess NaF (5 mM) in PBS buffer (10 mM, pH 7.4, with 1% DMSO).

Chellappa *et al.* reported that when the imidazole bearing Rhodamine 6G (5) was incubated with different concentrations of NaF an increase in fluorescence intensity was recorded. The increase in fluorescence is associated with the conversion of the rhodamine spiro form (5) to the amide form (14) stimulated by the fluoride (Scheme 2.6).



**Scheme 2.6: Proposed mechanism of fluoride incorporation in imidazole bearing rhodamine 6G (5).**

Similar data to those presented by the Chellappa lab were achieved: on titrating the imidazole-bearing Rhodamine 6G (5) with increasing equivalents of fluoride ions, the probe showed a gradual increase in the intensity of the peak at 557 nm (Figure 2.5). However, it was noticeable that there was a weak fluorescent signal which was present prior to the addition of the NaF (Figure 2.5), suggesting that the starting material 5 is weakly fluorescent.

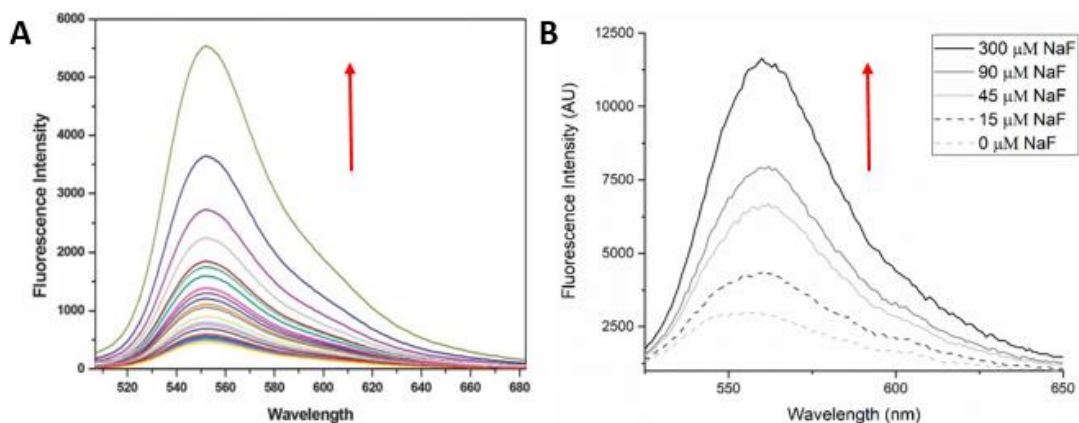


**Figure 2.5:** Fluorescence response of imidazole bearing rhodamine 6G (5  $\mu\text{M}$ ) toward different concentrations of NaF (0-300  $\mu\text{M}$ ) in HEPES buffer (20 mM, pH 7.4) solution in acetonitrile:water (3:7). (A) Literature reported data, reproduced with permission.<sup>20</sup> (B) Data from the synthesised imidazole bearing rhodamine 6G.  $\lambda_{\text{ex}} = 500 \text{ nm}$ . Data points for 30, 120 and 150  $\mu\text{M}$  removed for clarity. Data shown is from 3 repeats and is shown as the mean.

The fluorescence response was shown to increase linearly upon increasing of concentration of NaF (15-150  $\mu\text{M}$ ) indicating that the probe could be used accurately to determine fluoride ion concentration up to 150  $\mu\text{M}$  (Figure 2.6).

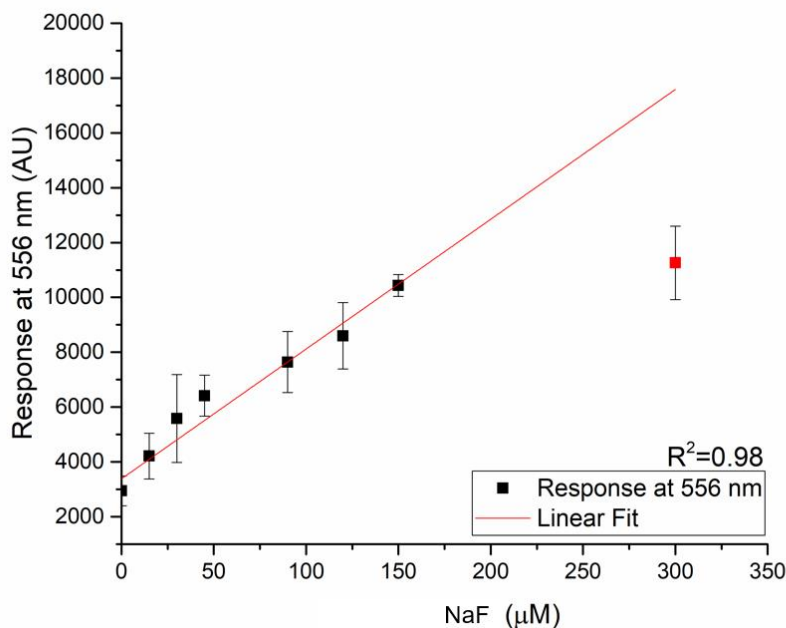


**Figure 2.6:** Change of fluorescence intensity of imidazole bearing rhodamine 6G upon addition of fluoride at  $\lambda_{\text{em}} = 556 \text{ nm}$ . Graph plotting response at 556 nm against concentration of fluoride ions in HEPES buffer (20 mM, pH 7.4) solution in acetonitrile:water (3:7) when 5  $\mu\text{M}$  of probe was used. 300  $\mu\text{M}$  data point reported in red as it does not fit with the linear fit. Data shown is from 3 repeats and shown as the mean  $\pm$  S.E.M.

The limit of detection (LOD) of the probe was calculated using the formula mean blank + 3\* SD of blank. This suggests that 2.9  $\mu\text{M}$  of NaF is required in order to detect any fluorescence signal when 5  $\mu\text{M}$  of rhodamine probe (**5**) is used. The LOD would have been lower if the rhodamine probe (**5**) did not show any fluorescent signal prior to incubation with NaF.

Additional studies on the selectivity of the probe to NaF were carried out. The imidazole-bearing rhodamine 6G (**5**) was incubated with a range of anions including  $\text{F}^-$ ,  $\text{AcO}^-$ ,  $\text{Cl}^-$ ,  $\text{I}^-$ ,  $\text{Br}^-$  and  $\text{HPO}_4^-$ . The other anions did not produce any colour change nor an increase in fluorescence which was only visible upon addition of NaF (Figure 2.7).

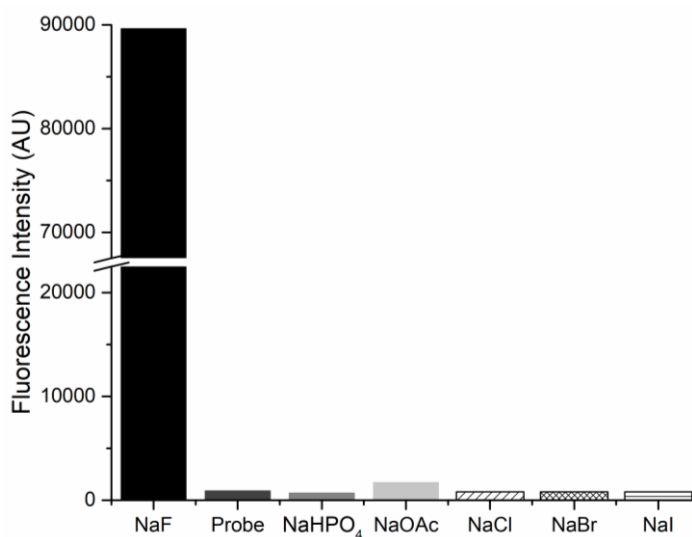


Figure 2.7: Fluorescence response of imidazole bearing rhodamine 6G (5  $\mu\text{M}$ ) in the presence of various anions (5 equivalents) in HEPES buffer (20 mM, pH 7.4) solution in acetonitrile:water (3:7).  $\lambda_{ex} = 500 \text{ nm}$ .

### 2.3.5 Conclusion

A number of fluoride probes were considered for their potential utility to detect the  $\text{Na}^{18}\text{F}$  PET tracer in clinical studies and their limitations are discussed in Table 2.2.

Table 2.2: Pros and cons of selected fluoride sensors

Probe	Pros	Cons
<b>1</b>	Reported to present excellent water solubility and photostability properties.	Numerous reaction steps
<b>2</b>	Reported to show high sensitivity for fluoride.	Highly fluorescent starting material
<b>3</b>	Reported to demonstrate excellent cell permeability. Product synthesised with a two-step reaction	Fluoride ions do not deprotonate the hydroxyl group
<b>4</b>	Product synthesised with a four-step reaction	Fluoride ions do not deprotect the silyl group
<b>5</b>	Reported to be highly sensitive and selective for fluoride. Product synthesised with a one-step reaction	LOD is in the $\mu\text{M}$ range rather than $\text{pM}$ required for PET imaging

Probe **1** and **2** were discarded due to the labour intensive synthetic approach and the high fluorescence signal of the starting material, respectively. Unfortunately, the cyanoacrylate probes (**3** and **4**) were also not taken forward as upon addition of NaF no peak at 548 nm appeared, while the imidazole bearing Rhodamine 6G (**5**) showed great sensitivity and selectivity towards fluoride ions.

However, for the fluorescence signal for 5  $\mu\text{M}$  of probe **5** to be intense enough to be detected over the background signal, concentrations of NaF of 2.9  $\mu\text{M}$  or above are required. This suggests that the ratio between the probe and the NaF is of 1: 0.6 approximately. For the probe to be used in a PET imaging setting,  $\text{pM}$  concentration of  $\text{Na}^{18}\text{F}$  are required,<sup>21</sup> suggesting that the probe should also be in the  $\text{pM}$  range. However, the fluorescence signal of the probe is not intense enough to be visualised at those concentrations, therefore even this probe was rejected.

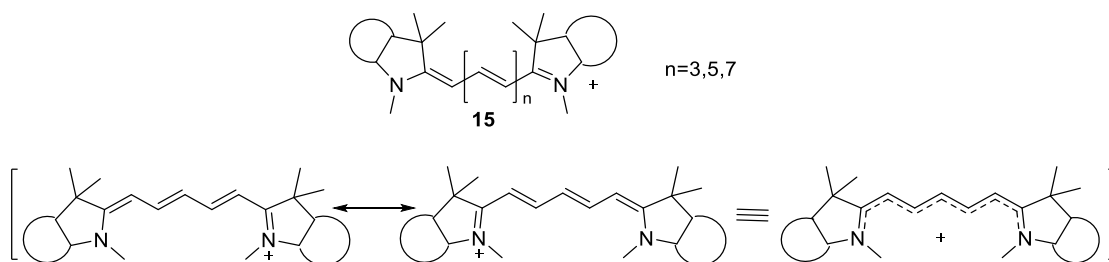
## 2.4 Calcium probes

A range of calcium probes precursors were examined and, two fluorophores and calcium binding molecules were selected for coupling. For the fluorophore entity, cyanine dyes and fluorescein were selected and these are discussed in more detail below, while as a binding motif, bisphosphonates and a calcium binding peptide were carefully chosen due to their ability to bind to HAP.

### 2.4.1 Cyanine dyes

The cyanine (Cy) dyes are a class of highly fluorescent compounds that possess the key requirements necessary for highly sensitive multicolour detection, with wavelengths which are tuneable upon the addition of specific functional groups, across the visible spectrum.<sup>22</sup> They also display excellent photophysical properties that include high extinction coefficients and moderate quantum yields, while possessing fluorescent wavelengths removed from the natural autofluorescence of biomolecules.<sup>22-24</sup>

Cy dyes are photosensitive structures composed of two heterocycles, one of which is a quaternary ammonium salt, that are linked together through a polymethine bridge (**15**) which allows for delocalization of the positive charge (Scheme 2.7).<sup>24,25</sup> The absorbance and fluorescence wavelengths can be controlled by a choice of the polymethine bridge length: Cy dyes with a longer bridge possess higher absorbance and emission wavelengths up to the near infrared region.



**Scheme 2.7:** *Cy dye polymethine bridge structure. Polymethine bridge and delocalization of the double bonds within the system.*

There are a variety of Cy dyes which have been reported in the literature (*Figure 2.8*): non-sulfonated (**16-21**) or sulfonated (sulfo; **22**) being two key classes. For many applications they are interchangeable, this is due to their spectral properties being nearly identical. Both can be used for labelling biomolecules however, critically, sulfo-dyes are water soluble and do not require organic co-solvent for the labelling of molecules in aqueous environments.

Inopportunately, the synthesis and purification of sulfo-Cy dyes is more challenging. Common Cy dye core structures include Cy3 (**16**), Cy3.5 (**19**), Cy5 (**17**), Cy5.5 (**20**), Cy7 (**18**) and Cy7.5 (**21**) (Figure 2.8), where the number identifies the number of carbons between the two indolenine groups. The suffix .5 is added for cyanine dyes which contain a benzo-fused indole motif as part of the cyanine dyes.

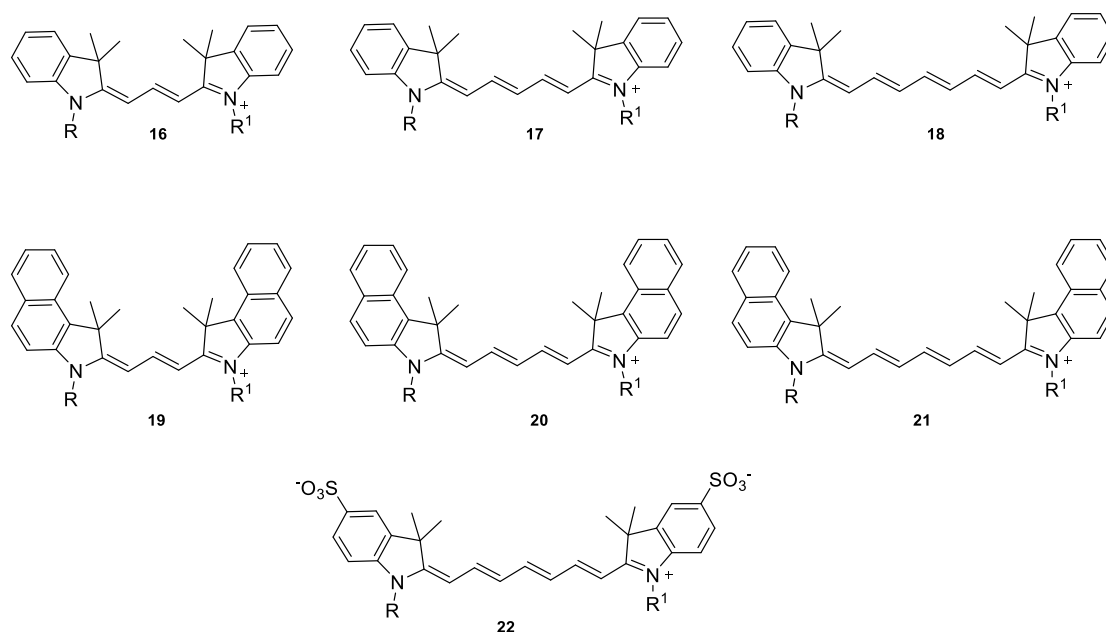
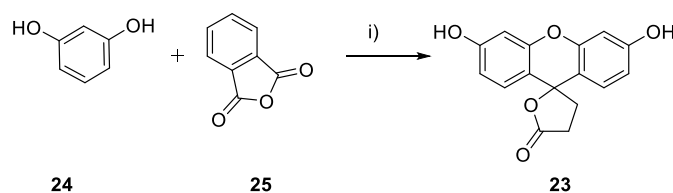


**Figure 2.8: Library of Cy dyes.** Cy3 (**16**), Cy5 (**17**), Cy7 (**18**) all possess two indole groups while Cy3.5 (**19**), Cy5.5 (**20**), Cy7.5 (**21**) contain two benzo-fused indoles. Sulfo-Cy7 (**22**) contains sulfo groups.

In recent years cyanine dyes have been used as fluorescent probes in biomedical screening techniques,<sup>22,23,26</sup> as luminescent materials for labelling<sup>27</sup> and as analyte-responsive fluorescent probes in optoelectronic applications.<sup>14,28</sup>

### 2.4.2 Fluorescein

Fluorescein (**23**) is a common fluorophore used in microscopy with an absorption maximum at 494 nm and emission maximum of 515 nm. Fluorescein (**23**) was first synthesised by Adolph Von Baeyer in 1871 who reacted resorcinol (**24**) with phthalic anhydride (**25**).<sup>29,30</sup> Scheme 2.8 shows a modern adaptation of this reaction.



**Scheme 2.8: Synthesis of fluorescein via a modified Friedel-Craft acylation.** Reagents and conditions: i)  $ZnCl_2$ ,  $H_2O$ , MW,  $200\text{ }^\circ\text{C}$ , 1 h.

To demonstrate the sensitivity of fluorescein (**23**), 10 kg of sodium fluorescein were placed in the Danube and 60 hours later green fluorescence was detected in the river Rhine, 200 km from where it was first introduced. In 1942, Albert Coons labelled antibodies with fluorescein (**23**) thus giving birth to the field of immunofluorescence.<sup>31,32</sup> Since then, it has been widely used as a fluorophore bound to antibodies but also to other molecules of interest, allowing scientists to utilise fluorescence immunocytochemical techniques to visualise cellular mechanisms. Fluorescein (**23**) has many uses in the fields of biochemical and medical research. In cellular biology, it is used to label and track cells in fluorescence microscopy, specifically in flow cytometry.

Ten years later, in 1953, the use of sodium fluorescein (**9**) to assess *in vivo* circulation was reported by Paul Ehrlich, who detected fluorescein in a rabbit eye following parenteral administration.<sup>30,33</sup> Once the nontoxic properties of fluorescein (**23**) were demonstrated it started being used in human subjects mainly in the field of ophthalmology and especially in the analysis of corneal abrasion and surface irregularities (*Figure 2.9*).<sup>30,34,35</sup> This work was pioneered by MacLean and Maumenee in the late 1950s where they injected fluorescein in a patient's eye and then observed a vascular anomaly under a lamp providing cobalt blue illumination.<sup>30,35,36</sup>

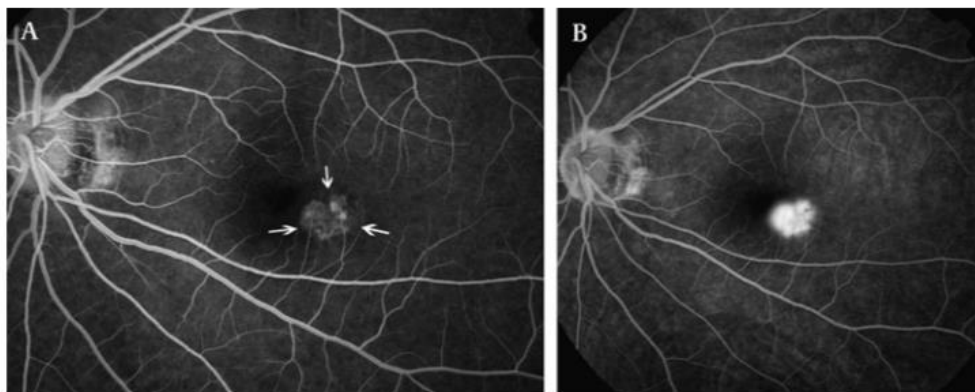


**Figure 2.9** *Fluorescein angiography. (A) Early and (B) late phase of angiography of a patient with multifocal choroiditis. Arrows indicate an area of fluorescein localization. Image reproduced with permission.*<sup>37</sup>

Another medical application is seen in the field of angiography, where it is used intravenously, or orally, to diagnose and categorize vascular disorders including: retinal disease; macular degeneration; diabetic retinopathy; and intraocular tumours. Most recently, it has discovered an application in surgery for brain tumours,<sup>38</sup> as well as in open heart surgery.<sup>39</sup>

### 2.4.3 Examples of HAP binding molecules

Bisphosphonates (BPs) are a class of drugs that are used to treat adult disease of high bone turnover such as Paget's, osteoporosis myeloma and metastatic bone disease.<sup>40-42</sup> Alendronate (**26**) is part of the bisphosphonate family together with pamidronate (**27**) and risedronate (**28**), as well as numerous others (*Figure 2.10*).<sup>40,43,44</sup>

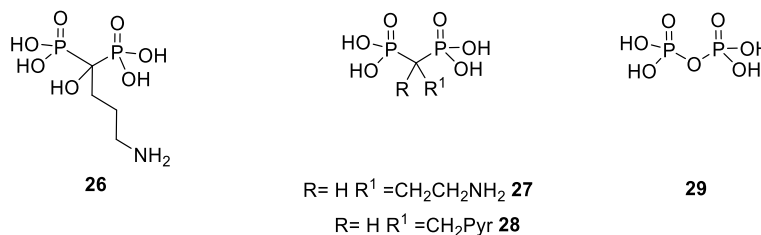


**Figure 2.10:** *Bisphosphonates. Alendronate (26) pamidronate (27), risedronate (28) and pyrophosphate (29).*

BPs are structurally similar to pyrophosphate (**29**) which is a normal product of human metabolism. BPs inhibit the farnesyl pyrophosphate synthase enzyme (*Figure 2.11*) and eventually induce osteoclast apoptosis.<sup>45,46</sup>



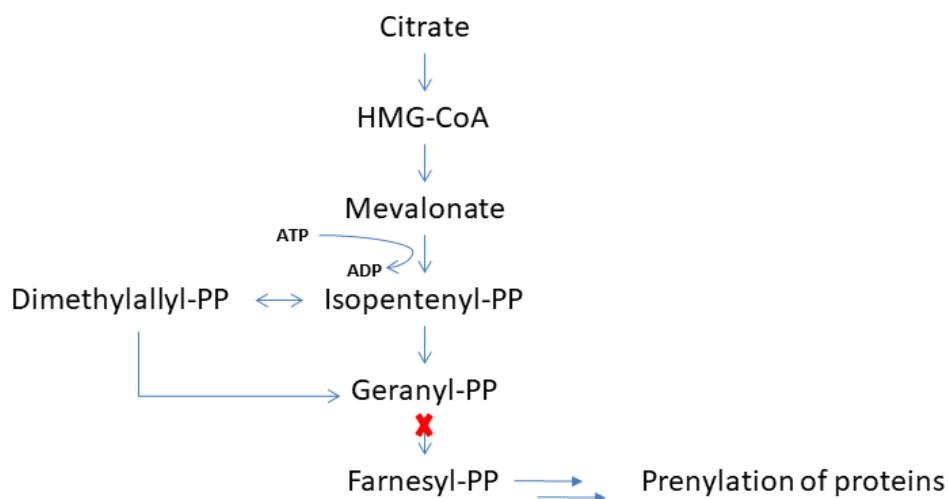


**Figure 2.11:** Systematic diagram of the mevalonate pathway for cholesterol synthesis. BPs inhibit farnesyl pyrophosphate synthase, preventing the synthesis of Farnesyl-PP from Geranyl-PP which is required for the prenylation of a number of key proteins essential for cell survival. Cross indicates where BPs inhibit the synthase enzyme.

The bisphosphonate moieties bind directly to mineralized bone surfaces where they are then taken up by osteoclasts and therefore inhibit osteoclast activity, this in turn leads to the reduction of bone resorption and a net positive bone balance.<sup>47-51</sup> Recently BPs have been used in both animal and human studies and have been shown to accumulate in the arterial wall and to suppress macrophage activity in atheromatous lesions as well as suppressing arterial calcification.<sup>49,50</sup> Previous data has shown that alendronate (**26**) is readily able to bind to bulk calcium mineral, in the micromolar range ( $K_i = 61 \mu\text{M}$ ),<sup>52</sup> even in the presence of free calcium ions.<sup>41,53,54</sup> The ready availability of the FDA-approved drug makes it a particularly attractive candidate for the development of probes for the detection of calcification.

Other molecules that have shown selectivity towards HAP are short 12-16mer peptides.<sup>55-57</sup> The Becker lab discovered a variety of short peptide sequences with strong affinity,<sup>55</sup> in the micromolar range, and specificity for binding to HAP. The sequence SVSVGMPKSPRP (**30**) was reported to have the greatest affinity for HAP, therefore was analysed further. Studies on the selectivity of peptide **30** towards other solids, specifically calcium carbonate ( $\text{CaCO}_3$ ) and calcium phosphate (CaPi) were conducted and the group concluded that there was little adhesion of the peptide to  $\text{CaCO}_3$  or to CaPi, demonstrating that the peptide was only binding to calcium phosphate. It was shown to be selective towards the more crystalline HAP (*Figure 2.12*).<sup>55</sup>

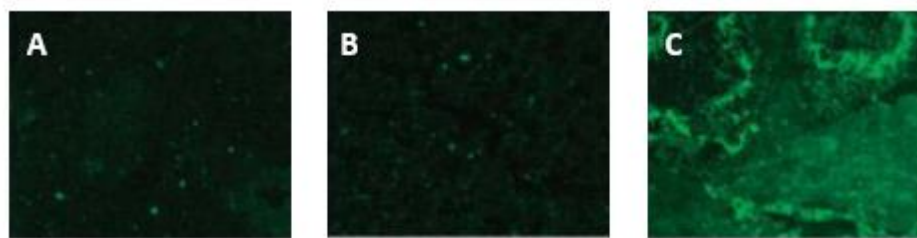


**Figure 2.12** Binding specificity of peptide 30 to  $\text{CaCO}_3$  (A),  $\text{CaPi}$  (B) and HAP (C). Image reproduced with permission.<sup>55</sup>

Due to the selectivity of both alendronate (**26**) and the SVSVGMPKSPRP-peptide (**30**) to HAP; these were considered excellent candidates to conjugate to selected fluorophores to study cardiovascular calcification.

#### 2.4.4 Synthesis of Cy dyes

A range of Cy dyes were synthesised in order to create a range of fluorophores that could be linked to the different calcification markers. Cy dyes, as discussed in 2.4.1, are compounds that are made up of two heterocyclic rings such as those found in the indolium ions (**31-35**) and a polymethine chain.<sup>24</sup> Their synthesis can be divided into two main parts: synthesis of the quaternary heterocyclic ammonium salt precursors (Section 2.4.5) and cyanine dye assembly (Section 2.4.6).

#### 2.4.5 Synthesis of quaternary heterocyclic ammonium salt precursors

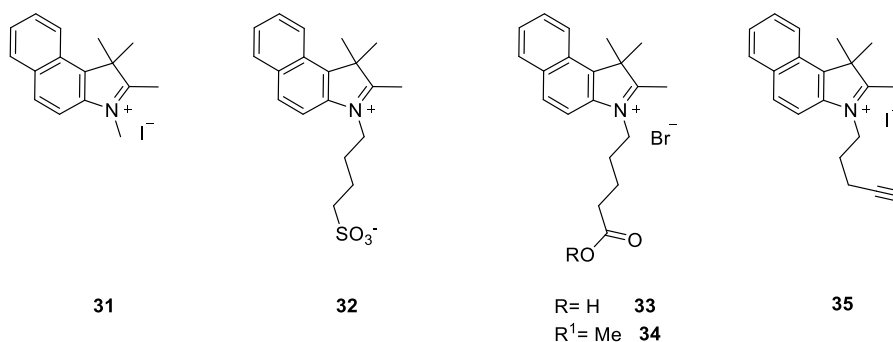
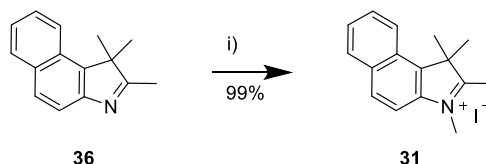


**Figure 2.13:** Selection of heterocyclic ammonium salts.

The heterocyclic ammonium salts (**31-35**) (Figure 2.13) were synthesized by quaternization of the corresponding heteroaromatic base, 2,3,3-trimethylindolenine (**36**), with suitable alkyl halides. This can be performed in the presence or absence of solvent.<sup>22,58</sup>

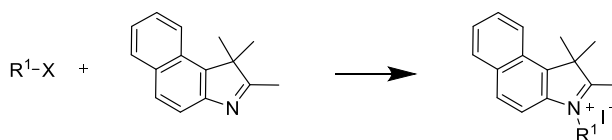
For example, *N*-methyl-2,3,3-trimethylindoleninium iodide (**31**) was prepared by the alkylation reaction between 2,3,3-trimethylindolenine (**36**) with 2 equivalents of methyl iodide at 100 °C in MeCN for 2 hours (Scheme 2.9). The resulting benzindolium salt was readily separated from the crude reaction mixture, in high purity, by precipitation upon the addition of Et<sub>2</sub>O and was isolated in 99% yield.



**Scheme 2.9:** Synthesis of *N*-methyl-2,3,3-trimethylindoleninium. Reagents and conditions: i) MeI, MeCN, 100 °C, 2 h.

The other quaternary heterocyclic ammonium salt precursors (**32-35**) were synthesised in a similar manner to the example above as reported in Table 2.3.

**Table 2.3:** Conditions for benzindolium salt synthesis.



Entry #	R <sup>1</sup> -X	Time (h)	Temp. (°C)	Product	% Yield
1	Mel	24	110 <sup>(a)</sup>	<b>31</b>	68
2	Mel	10	50 <sup>(b)</sup>	<b>31</b>	75
3	(CH <sub>2</sub> ) <sub>3</sub> CH <sub>2</sub> SO <sub>3</sub> <sup>-a</sup>	24	120 <sup>(a)</sup>	<b>32</b>	98
4	Br(CH <sub>2</sub> ) <sub>4</sub> CO <sub>2</sub> H	5	145 <sup>(a)</sup>	<b>33</b>	0
5	Br(CH <sub>2</sub> ) <sub>4</sub> CO <sub>2</sub> H	24	145 <sup>(a)</sup>	<b>33</b>	0
6	Br(CH <sub>2</sub> ) <sub>4</sub> CO <sub>2</sub> Me, KI	1	120 <sup>(b)</sup>	<b>34</b>	0
7	Br(CH <sub>2</sub> ) <sub>4</sub> CO <sub>2</sub> Me, KI	4 days	80 <sup>(b)</sup>	<b>34</b>	82
8	Cl(CH <sub>2</sub> ) <sub>3</sub> C≡CH, KI	24	Reflux <sup>(b)</sup>	<b>35</b>	72

\* Reactions were carried out in either DCB (a) or MeCN (b). All reactions were purified by trituration with Et<sub>2</sub>O. <sup>a</sup> Butane sultone was used.

Most quaternary heterocyclic ammonium salt precursors (Table 2.3 entry 1-3 and 8; **31**, **32**, **35**) were synthesised following a one-step reaction and obtained in good yield. Only 3-(4-carboxybutyl)-1,1,2-trimethyl-1*H*-Benzo[*e*]indolium (**33**) required a two-step reaction (Table 2.3 entry 7) involving the alkylation of 2,3,3-trimethylindolenine (**34**) with ethyl

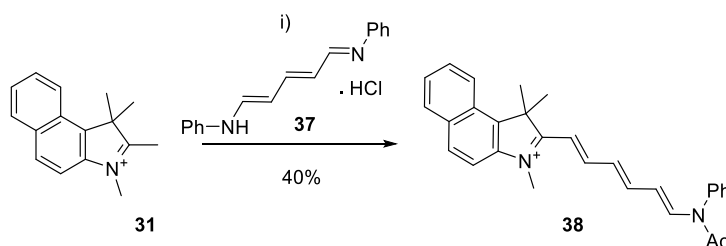
bromovalerate, which was achieved in a 82% yield, followed by hydrolysis to the acid (**33**) using HCl (5 N aq.) in a quantitative yield.

## 2.4.6 Cyanine dye assembly

A synthetic route to symmetrical and unsymmetrical Cy dyes involves the alkylation of quaternary heterocyclic ammonium salt precursors containing an activated methyl group (**31-35**) with derivatives of *N*-[5-(phenylamino)-2,4-pentadienyldiene]aniline monohydrochloride (**37**). This reaction can be carried out both in solution and using a solid support resin, with both routes described below.

### 2.4.6.1 Off resin approach

Unsymmetrical cyanine dyes are synthesized in two steps from benzindolium salt (**31-35**) through activated hemicyanine intermediates, such as 2-[6-(acetylphenylamino)-1,3,5-hexatrien-1-yl]-1,1-dimethyl-3-(methyl)-1*H*-Benz[*e*]indolium **38** as shown in *Scheme 2.10*.

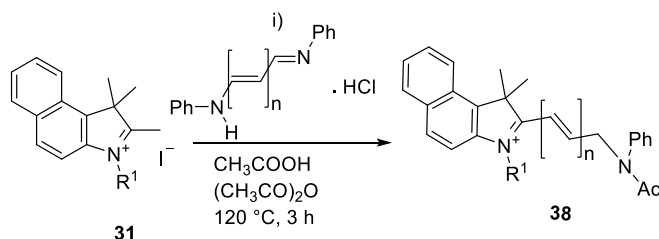


**Scheme 2.10: Synthesis of the acetylated hemicyanine dye activated intermediate (38).** Reagents and conditions: i) *N*-[5-(Anilino)-2,4-pentadienyldiene]aniline hydrochloride (**37**), acetic acid, acetic anhydride, 120 °C, 3 h.

The acetylated precursors were prepared by the reaction of equimolar amounts of the corresponding benzindolium salt (**31**) and *N*-[5-(phenylamino)-2,4-pentadienyldiene]aniline monohydrochloride (**37**) under reflux in Ac<sub>2</sub>O over 3 hours. The clean product was obtained by trituration of the reaction mixture with Et<sub>2</sub>O and water in a 1:1 mixture in 40% yield. Scheme 2.10 describes the synthesis of one of the four activated hemicyanine intermediates **38**, while Table 2.4 reports the yield for the synthesised compounds. The two benzindolium salts selected were 1,1,2,3-tetramethyl-1*H*-benzo[*e*]indolium (**31**) and 1,1,2-trimethyl-3-(4-sulfobutyl)-1*H*-Benzo[*e*]indolium (**32**) as their synthesis was more straightforward and took less time in comparison to the carbonyl (**33**) and the alkyne (**35**) benzindolium salts. From the two benzindolium salts, only four intermediates were synthesised, two using *N*-[5-(phenylamino)-2,4-pentadienyldiene]aniline monohydrochloride and two using

malondialdehyde bis(phenylimine)monohydrochloride to produce hemicyanine intermediates for Cy7.5 and Cy5.5, respectively.

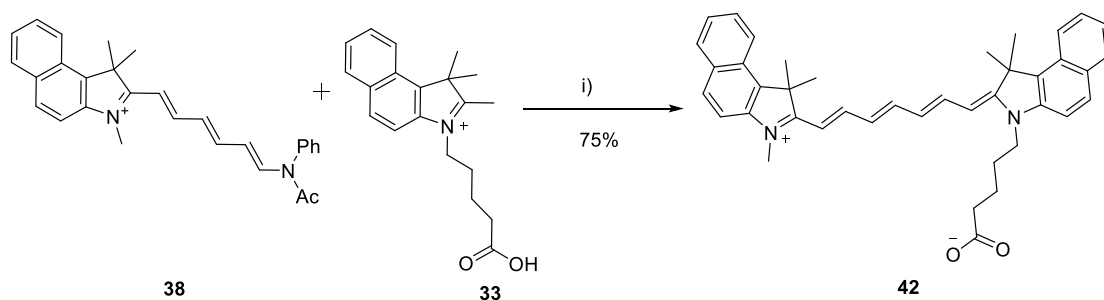
**Table 2.4: Activated hemicyanine intermediates synthesis.**



Entry #	R <sup>1</sup>	Polymethine bridge	Intermediate	Yield %
1	Me	n=3	38	40%
2	(CH <sub>2</sub> ) <sub>3</sub> CH <sub>2</sub> SO <sub>3</sub> <sup>-</sup>	n=3	39	38%
3	Me	n=2	40	(a)
4	(CH <sub>2</sub> ) <sub>3</sub> CH <sub>2</sub> SO <sub>3</sub> <sup>-</sup>	n=2	41	(a)

\*for n=3 N-[5-(phenylamino)-2,4-pentadienylidene]aniline monohydrochloride is used while for n=2 malondialdehyde bis(phenylimine) monohydrochloride is used. (a) Intermediates taken directly to the next reaction without purification.

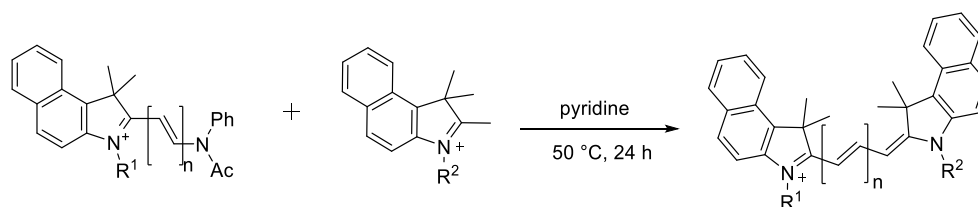
The hemicyanine intermediates were obtained by the reaction of the benzindolium salts with malondialdehydes in the presence of acetic acid and acetic anhydride for 2 hours to afford the activated intermediates in around 40% yield, this reaction provided as side products unwanted symmetrical cy dyes and unreacted benzindolium salts. The completed Cy dye (an example reported in *Scheme 2.11*) was obtained by reaction of the purified activated intermediate, such as **38-41**, and 1 equivalent of another benzindolium salt (**31-33** and **35**), in the presence of pyridine and under reflux for 24 hours. This afforded the unsymmetrical Cy dyes, such as **42**, in satisfactory yields after purification by column chromatography.



**Scheme 2.11:** Synthesis of 4-(2-(1E,3E,5E,7Z)-7-(3-(4-carboxybutyl)-1,1-dimethyl-1H-benzo[e]indol-2(3H)-ylidene)hepta-1,3,5-trienyl)-1,1-dimethyl-1H-benzo[e]indolinium-3-yl (39). Reagents and conditions: i) Pyridine, 50 °C, 24 h.

The standard reaction conditions as described above were used for the attempted synthesis of Cy7.5 (Table 2.5 entries 1-4; **42**, **43**, **44**, **45**) and Cy5.5 (Table 2.5 entries 5-7; **46**, **47**, **48**) dyes and the yields are reported in Table 2.5.

**Table 2.5:** Building blocks and yields for the solution phase synthesis of Cy7.5 and Cy5.5 library.



Entry #	R <sup>1</sup>	Polymethine bridge	R <sup>2</sup>	Cy dye	Yield
1	Me	n=3	(CH <sub>2</sub> ) <sub>4</sub> CO <sub>2</sub> H	<b>42</b>	75%
2	Me	n=3	(CH <sub>2</sub> ) <sub>3</sub> C≡CH	<b>43</b>	69%
3	(CH <sub>2</sub> ) <sub>3</sub> CH <sub>2</sub> SO <sub>3</sub> <sup>-</sup>	n=3	Me	<b>44</b>	n.d.
4	(CH <sub>2</sub> ) <sub>3</sub> CH <sub>2</sub> SO <sub>3</sub> <sup>-</sup>	n=3	(CH <sub>2</sub> ) <sub>4</sub> CO <sub>2</sub> H	<b>45</b>	n.d.
5	Me	n=2	(CH <sub>2</sub> ) <sub>4</sub> CO <sub>2</sub> H	<b>46</b>	70%
6	Me	n=2	(CH <sub>2</sub> ) <sub>3</sub> C≡CH	<b>47</b>	71%
7	(CH <sub>2</sub> ) <sub>3</sub> CH <sub>2</sub> SO <sub>3</sub> <sup>-</sup>	n=2	(CH <sub>2</sub> ) <sub>4</sub> CO <sub>2</sub> H	<b>48</b>	n.d.

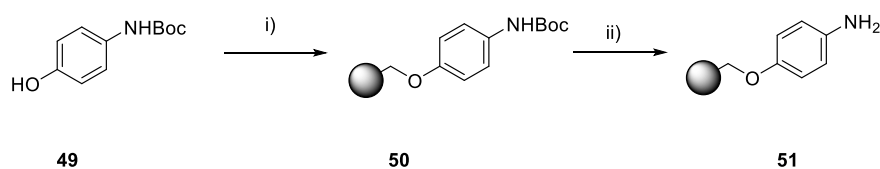
\*for n=3 *N*-(5-Anilino-2,4-pentadienylidene)aniline hydrochloride is used, while for n=2 malondialdehyde bis(phenylimine)monohydrochloride is used.

When 1,1,2-trimethyl-3-(4-sulfobutyl)-1H-Benz[e]indolinium (**32**) was used as the starting benzindolium salt and was coupled to either *N*-[5-(phenylamino)-2,4-pentadienylidene]aniline monohydrochloride or malondialdehyde bis(phenylimine) monohydrochloride to produce hemicyanine intermediates, the latter were not able to couple to the additional benzindolium salt. To overcome this, on resin approach was attempted as it had previously reported in the

literature of being a suitable method of overcoming the problem of unreacted hemicyanine production.

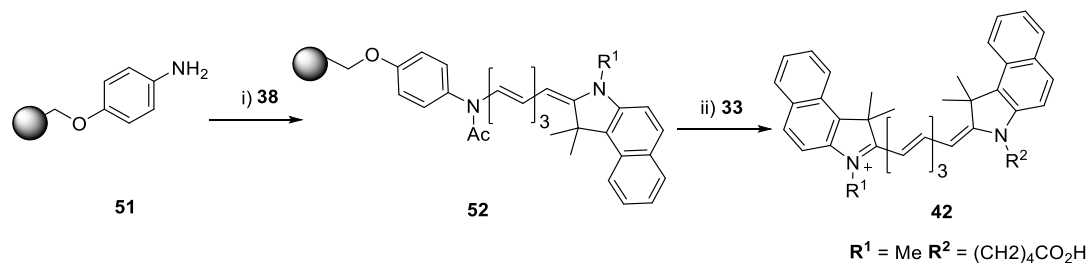
#### 2.4.6.2 On resin approach

Conventional synthetic methods for the preparation of unsymmetrical Cy dyes are based on the condensation of benzindolium salts with malondialdehydes and typically afford mixtures of the desired compounds along with unreacted hemicyanine and undesired symmetrical analogues. To avoid time consuming purifications and allow enhanced access to a broad range of Cy dyes, solid-phase synthesis methods have been reported.<sup>22,24</sup> The synthesis of benzindolium salts was carried out as described for the solution phase reactions previously discussed. The solid support is functionalised (Scheme 2.12) by reacting a *N*-Boc-4-hydroxyaniline handle (**49**) with 1% DVB cross-linked chloromethyl polystyrene (PS) to afford (4-hydroxyphenyl)carbamic acid *tert*-butyl ester PS (**50**) from which the Boc group could be removed to reveal the free amine (**51**).



**Scheme 2.12: Solid support synthesis.** Reagents and conditions (i) 1% DVB crossed-linked chloromethyl polystyrene,  $C_2CO_3$ , KI, acetone, 70 °C, 16 h; (ii) 20% TFA in DCM, rt, 2 h.

To synthesise the Cy dyes the hemicyanine intermediate, such as **38-41**, was synthesised in solution, as described in section 2.4.6.1, and loaded onto the aniline-functionalised solid support **52** using DCM as a solvent for 1 hour to give intermediates of the type (**51**) (Scheme 2.13). The reactions were monitored by IR. Cleavage from the solid support was then accomplished using a benzindolium salt (**31-33** and **35**) in a mixture of pyridine and  $Ac_2O$  (10:1) to afford the unsymmetrical cyanine dye (Table 2.5; **42**) in good yield.

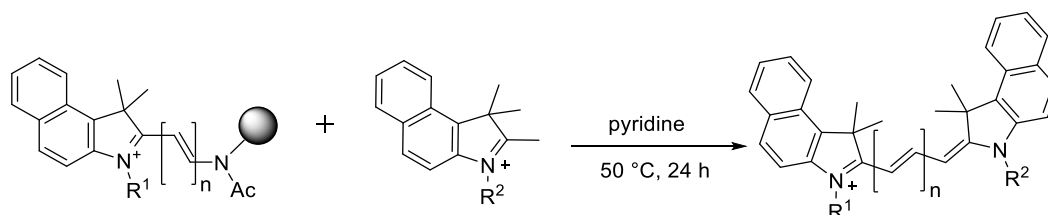


**Scheme 2.13: On resin approach for the synthesis of 4-(2-(1E,3E,5E,7Z)-7-(3-(4-carboxybutyl)-1,1-dimethyl-1H-benzo[e]indol-2(3H)-ylidene)hepta-1,3,5-trienyl)-1,1-dimethyl-1H-benzo[e]indolinium-3-yl (**42**).** Reagents and conditions: (i) 4-aminophenol PS,

DCM (51), rt, 1 h; (ii) 3-(4-carboxybutyl)-1,1,2-trimethyl-1H-Benz[e]indolium (33), pyridine, rt, 3 h.

A number of compounds (Table 2.6 entries 1-7; **42-48**) were synthesised using the on resin approach and obtained in the yields reported in Table 2.6, differently from the in solution approach cy dyes synthesised on resin did not require any purification after the second benzindolium salt was added.

**Table 2.6: Building blocks and yields for the on resin synthesis of Cy7.5 and Cy5.5 compounds.**



Entry #	R <sup>1</sup>	Polymethine bridge	R <sup>2</sup>	Cy dye	Yield
1	Me	n=3	(CH <sub>2</sub> ) <sub>4</sub> CO <sub>2</sub> H	<b>42</b>	64%
2	Me	n=3	(CH <sub>2</sub> ) <sub>3</sub> C≡CH	<b>43</b>	60%
3	(CH <sub>2</sub> ) <sub>3</sub> CH <sub>2</sub> SO <sub>3</sub> <sup>-</sup>	n=3	Me	<b>44</b>	n.d.
4	(CH <sub>2</sub> ) <sub>3</sub> CH <sub>2</sub> SO <sub>3</sub> <sup>-</sup>	n=3	(CH <sub>2</sub> ) <sub>4</sub> CO <sub>2</sub> H	<b>45</b>	n.d.
5	Me	n=2	(CH <sub>2</sub> ) <sub>4</sub> CO <sub>2</sub> H	<b>46</b>	73%
6	Me	n=2	(CH <sub>2</sub> ) <sub>3</sub> C≡CH	<b>47</b>	81%
7	(CH <sub>2</sub> ) <sub>3</sub> CH <sub>2</sub> SO <sub>3</sub> <sup>-</sup>	n=2	(CH <sub>2</sub> ) <sub>4</sub> CO <sub>2</sub> H	<b>48</b>	n.d.

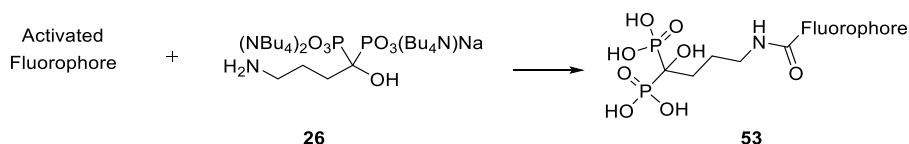
\*for n=3 *N*-(5-Anilino-2,4-pentadienylidene)aniline hydrochloride is used, while for n=2 malondialdehyde bis(phenylimine)monohydrochloride is used.

In conclusion, both methods were able to provide some of the Cy dyes required. The solution phase approach (Table 2.5) was able to provide Cy7.5 and Cy5.5 (Table 2.5 entries 1, 4, 6, 7; **42, 43, 46, 47**) with reasonable yield (69-75%) while the solid phase method (Table 2.6) was able to provide the Cy dyes (Table 2.6 entries 1, 4, 6, 7; **42, 43, 46, 47**) with similar yields (60-83%), however, an additional step was required in order to functionalise the resin support. Nevertheless, for both solution and solid approach, when indoles with sulfonated side chains were used, no cyanine dye product was observed.



## 2.4.7 Coupling and synthesis of bisphosphonate protected alendronate

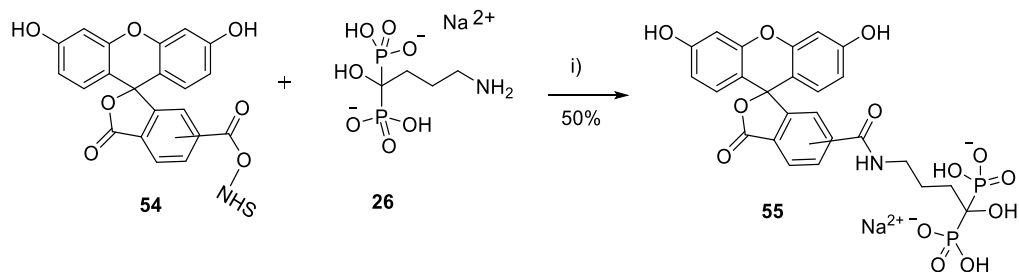
Two fluorophore-alendronate complexes, *Scheme 2.14*, were required; one that had high brightness and a relatively moderate emission wavelength as well as one that would emit at a region closer to the near infrared (NIR) region, as this would allow for potential *in vivo* experiments.



*Scheme 2.14: Fluorophore coupling to alendronate.*

Because of these requirements, 5/6-carboxy-fluorescein NHS ester (**54**) was selected as the fluorophore with high brightness and the Cy7.5 (**42**) and Cy5.5 (**46**) dyes were chosen as possible NIR fluorophores.

The coupling of 5/6-carboxy-fluorescein NHS ester (**54**) to alendronate (**26**) was facile (*Scheme 2.15*). Different conditions were examined including PBS buffer (pH 7.4) and TRIS buffer (pH 7.6) however, NaHCO<sub>3</sub> (sat.) gave the best conversion to fluorescein-alendronate (Fluorescein-BP, **55**) in a 50% yield.



*Scheme 2.15: Fluorescein coupling to alendronate. Reagents and conditions: i) HNaCO<sub>3</sub> (sat.), rt, 2 days.*

However, when the coupling of alendronate (**26**) to the mixed Cy7.5 (**42**) or the mixed Cy5.5 (**46**) was attempted and conditions such as NaHCO<sub>3</sub> (sat.), PBS buffer (pH 7.4), NHS with EDCI and DCC with Oxyma were used, none of the conjugated dye-alendronate systems were observed.

To define where the problem lies in the fluorophore-conjugation, a number of reactions with either the Cy dyes (**46**, **42**) or alendronate (**26**) were carried out. To do this, small organic molecules that had either amine groups or a carboxylic acid motif were chosen to act as

models. The data using the cyanine dyes are reported below in Table 2.7 while those using the alendronate are reported in Table 2.8.

**Table 2.7: Different conditions for the coupling of Cy 5.5 (46) and Cy 7 (42) dyes with *n*-butylamine.**

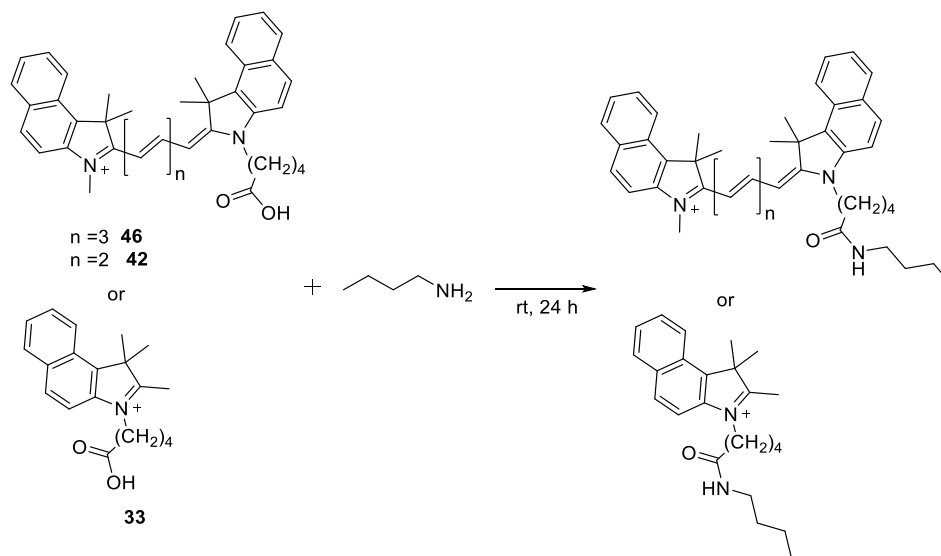
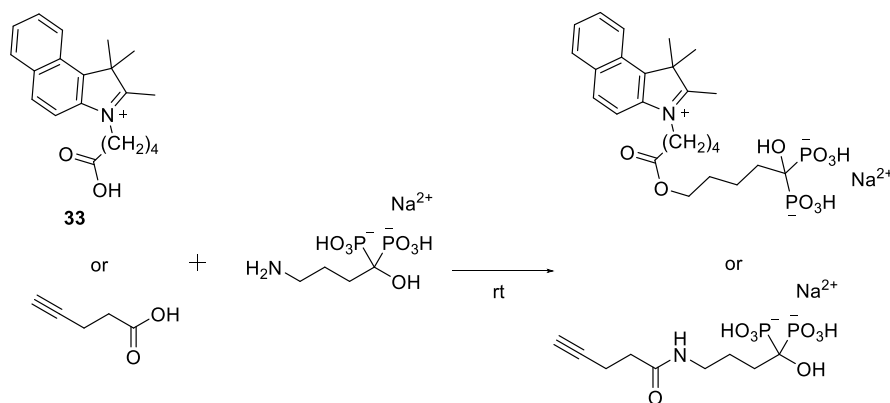


Table #	Reagent	Coupling Conditions	Yield
1	Cy5.5 (46)	NHS, EDCI	<i>n.r.</i>
2	Cy5.5 (46)	DCC, Oxyma	<i>n.r.</i>
3	Cy7.5 (42)	NHS, EDCI	<i>n.r.</i>
4	Cy7.5 (42)	DCC, Oxyma	<i>n.r.</i>
5	H (33)	NHS, EDCI	56%

\*All reactions were performed at room temperature for 24 hours.

When either Cy5.5 (46) or Cy7.5 (42) were reacted with *n*-butylamine (Table 2.7 entry 1-4), under different reaction conditions, neither cyanine dye afforded the coupled product. Conversely, coupling of 3-(4-carboxybutyl)-1,1,2-trimethyl-1H-Benz[e]indolium (33) with *n*-butylamine (Table 2.7, entry 5) yielded the coupled product in a 56% yield. This suggests that the problem with the coupling reaction might be related to the strong ion pairing between the iminium and the carboxybutyl chain of Cy5.5 (46) or Cy7.5 (42), and therefore might make the carboxybutyl chain unreactive.

Table 2.8: Different conditions for the coupling of alendronate (26) with acid (33).



Entry #	Coupling Conditions	R <sup>1</sup>	Time (h)	Yield
1	NHS (1.5 eq), EDCI (1 eq)	H	24	n.r.
2	PBS buffer (pH 7.4)	Benzo-fused indole (33)	8	n.r.
3	NHS (1.5 eq), EDCI (1eq)	Benzo-fused indole (33)	24	n.r.
4	HNaCO <sub>3</sub> (sat)	Benzo-fused indole (33)	24	n.r.

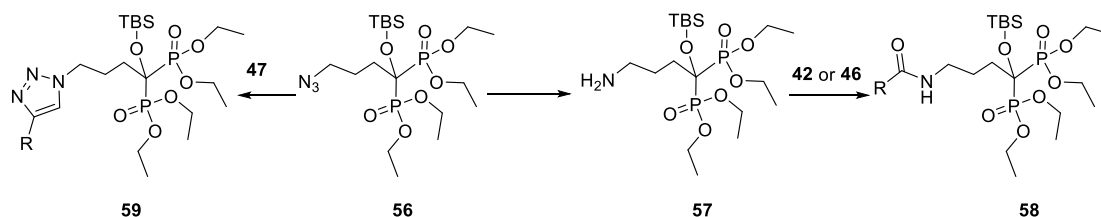
\*All reactions were performed at room temperature.

The reaction of alendronate (26) with pentynoic acid or 3-(4-carboxybutyl)-1,1,2-trimethyl-1H-Benz[e]indolium salt (33) was trialed under a range of conditions (Table 2.8 entry 1-4), however, no coupled product was obtained. It can therefore be supposed that the phosphate group is directly interfering with the coupling reaction.

With the lack of success in amide coupling reactions, it was decided that the phosphonate groups on the alendronate would be protected in order to remove any potential interaction between them and the cyanine dye itself. It was decided to attempt the synthesis of an azido-alendronate substrate with protected phosphate groups (56) and to then: either (a) convert the azide to the amine functionality required for amide bond formation; or (b) to attempt a copper mediated 1,3-dipolar cycloaddition reaction (click) with the alkyne substituted Cy5.5 dye (47) (Scheme 2.16). Triazoles have recently attracted a lot of attention as a bioisostere of the amide bond moiety due to their similarity in size, dipole moment and H bond acceptor capacity. In contrast to amide bonds, triazoles, offer the advantage of being extremely stable to hydrolysis which therefore make them potential surrogates of the amide bonds.<sup>59</sup>

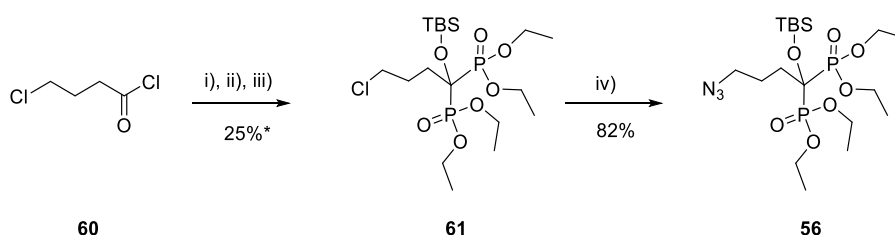
The azido-alendronate substrate with protected phosphate groups (56) could be used for both click coupling to the Cy5.5 dye (47) to obtain the triazole linked protected product (59)

(Scheme 2.16) as well as reduction of the azide to a amine (**57**) to allow for amide bond formation between the protected phosphate alendronate and the Cy7.5 dye (**42**) or Cy5.5 dye (**46**) giving product **58** (Scheme 2.16).



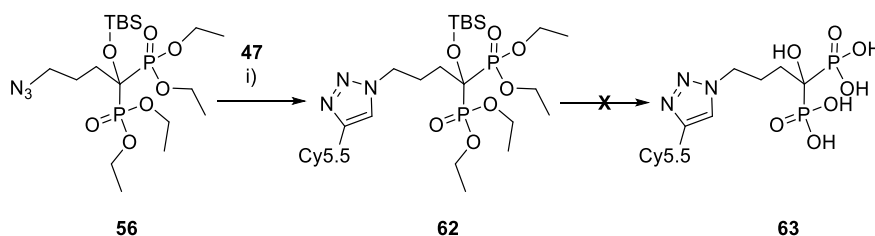
**Scheme 2.16:** Proposed pathways to obtain click coupled Cy-alendronate and amide coupled Cy-alendronate from the intermediate azide (**56**).

The synthesis of the azide protected bisphosphonate alendronate (**56**) was carried out using a two-step reaction involving a two stage Michaelis-Arbuzov reaction from 4-chlorobutyryl chloride (**60**) with triethylphosphite and diethylphosphite followed by a hydroxyl group protection step with *tert*-butyl silyl chloride to obtain **61** followed by the substitution of the chloride by an azide to obtain **56** in a 55% yield (Scheme 2.17).



**Scheme 2.17:** Synthesis of phosphate-protected azido alendronate. Reagents and conditions: (i) triethyl phosphite, DCM, rt, 15 minutes; (ii) diethylphosphite, DMAP, DCM, rt, 2 h; (iii) *tert*-butyldimethylsilyl chloride, rt, 24 h; (iv)  $\text{NaN}_3$ , DMF, 75 °C, 3 h. \* Yield over 3 steps.

After purification of **56**, click chemistry was attempted with the alkyne substituted Cy5.5 dye (**47**) (Scheme 2.18) using conditions previously reported in the Hulme group to give the protected triazoles (**62**).<sup>60</sup>



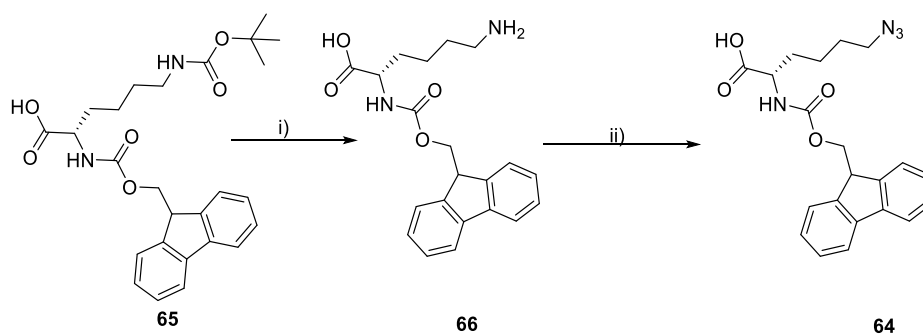
**Scheme 2.18:** Click and deprotection. Reagents and Conditions i) 0.2 mol %  $\text{CuSO}_4$ , 4 mol% sodium ascorbate, rt, 24 h.

After successful triazole formation, the protected phosphate groups were submitted to deprotection conditions to provide the free phosphate groups (**63**) (Scheme 2.18). The deprotection was attempted using a number of conditions;  $\text{Me}_3\text{BrSi}$ ,<sup>61,62</sup> TMS-I,<sup>61</sup> and  $\text{NH}_4\text{OH}$ ,<sup>63</sup> however, under these conditions the ether groups did not cleave and only starting material was observed when the reaction mixtures were analysed.

Unfortunately, since the deprotection of the triazoles intermediate could not be carried out, Fluorescein-BP (**55**) was the only alendronate probe that was taken forward into selectivity and animal studies.

## 2.4.8 HAP binding peptide

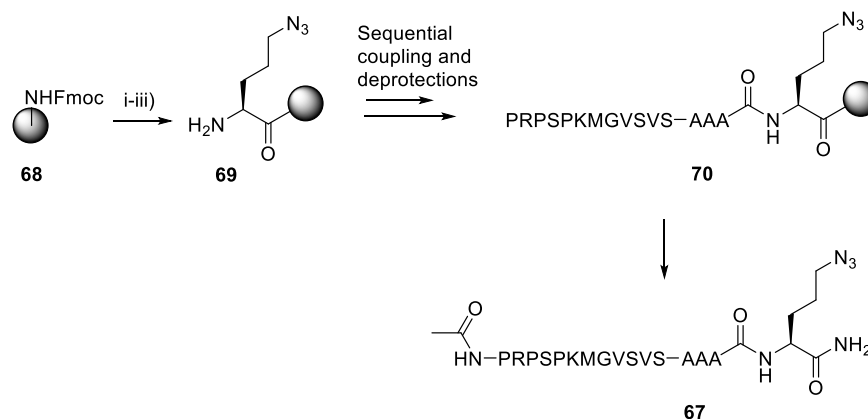
As mentioned in section 2.4.3, a range of short peptides were also considered as calcium probes due to their ability to selectively bind to specific minerals. Becker et al. showed that the peptide SVSVGMKPSRP (**30**) binds with both high specificity and high affinity to HAP. In order to obtain a more stable peptide, the click chemistry approach between the peptide and the Cy5.5 dye (**47**) was selected. To do so, a small 4 amino acid long linker, the same as the one used by the Becker lab was included in the peptide sequence. The linker was composed of AAK and in our instance, instead of lysine, a modified azido-lysine (Az-Lys) was incorporated in the linker. Az-Lys (**64**) was synthesised from Fmoc-Lys(OtBu)-OH (**65**) by a deprotection step to afford the free amine (**66**) and then a diazo transfer to afford Az-Lys (**64**) (Scheme 2.19). The unnatural amino acid Az-Lys (**64**) was then incorporated into the linker in place of the natural lysine.



**Scheme 2.19: Synthesis of Az-Lysine.** Reagents and conditions: i) TFA, DCM, rt, 1 h ii)  $\text{CuSO}_4 \cdot 5\text{H}_2\text{O}$ , imidazole-1-sulfonyl azide HCl,  $\text{NaHCO}_3$ , MeOH/ $\text{H}_2\text{O}$ , rt, 16 h.

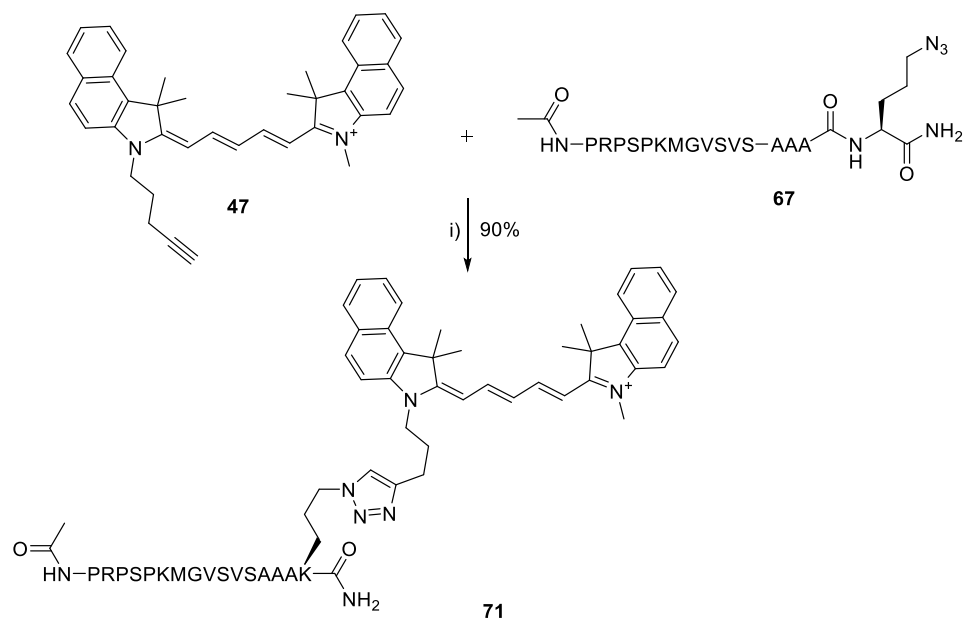
Peptide synthesis can occur both in solution and on solid support with both techniques affording peptides with excellent coupling efficiencies and facile scalability. However, the large number of couplings required when synthesising larger peptides in solution leads to

prolonged processes where isolating and recoupling the synthesised peptides offsets the benefits of solution phase synthesis.<sup>64-66</sup> On the other hand, solid phase synthesis (SPPS),<sup>67</sup> involving a solid support resin to restrain and grow the peptide can fast-track the process and it is for this reason that peptide **30** with Az-lysine (**67**) was synthesised on resin. An Fmoc/<sup>t</sup>Bu protection strategy was used as the Fmoc protecting group is orthogonal to an array of protecting groups. Rink amide resin was selected firstly for its compatibility with the Fmoc strategy and secondly because the resin releases a neutral C-terminal amide. SPPS synthesis also allows facile peptide capping at the N-terminus with an N-acetyl cap at the end of the synthesis. Capping at both the C and N termini ensures that charges on the peptide originate from the residue side chains only. These charges are responsible for the interaction with HAP, and removing any potential additional charges on the peptide will decrease the chances of unselective interactions between the peptide and the HAP. The SPPS synthesis of peptide **67** was carried as shown below in *Scheme 2.20*.



**Scheme 2.20: Synthesis of peptide 16 via SPPS. Reagents and conditions:** i) 20% piperidine, DMF, rt, 20 minutes; ii) Az-Lys, DIC, Oxyma, DMF, rt, 45 minutes; iii & deprotection) 20% piperidine, DMF, rt, 20 minutes; coupling) a.a., DIC, Oxyma, DMF, rt, 45 minutes.

A number of conditions were tested for the coupling of the peptide to the Cy5.5 (**47**) with 5% TBTA, 5% Cu(MeCN)<sub>4</sub>BF<sub>4</sub> proving optimal coupling conditions to obtained Cy-Pep (**71**) (*Scheme 2.21*).



**Scheme 2.21: Coupling of Cy5.5 and HAP selective peptide by click chemistry approach.** Reagents and conditions: i) 5% TBTA, 5% Cu(MeCN)<sub>4</sub>BF<sub>4</sub>, rt, 24 h.

#### 2.4.9 Characterization of the calcium probes

In H<sub>2</sub>O:DMF mix, Fluorescein-BP (**55**) and Cy-Pep (**71**) showed absorption maxima at 490 nm and 660 nm respectively. Upon excitation, Fluorescein-BP (**55**) showed maximum fluorescence intensity at 515 nm with Cy-Pep (**71**) at 695 nm.

Upon increasing concentration of Fluorescein-BP (**55**) (Figure 2.14 A) there was an increase in fluorescence signal when the fluorophore was excited at 488 nm. The signal response at 515 nm (Figure 2.14 B) also shows linear growth with increasing concentration (0.5-5 μM) suggesting that, under these specific conditions, Fluorescein-BP (**55**) could be detected at a concentration of 0.0065 μM. However, above 3 μM the response is not linear suggesting that there might be some quenching taking place.

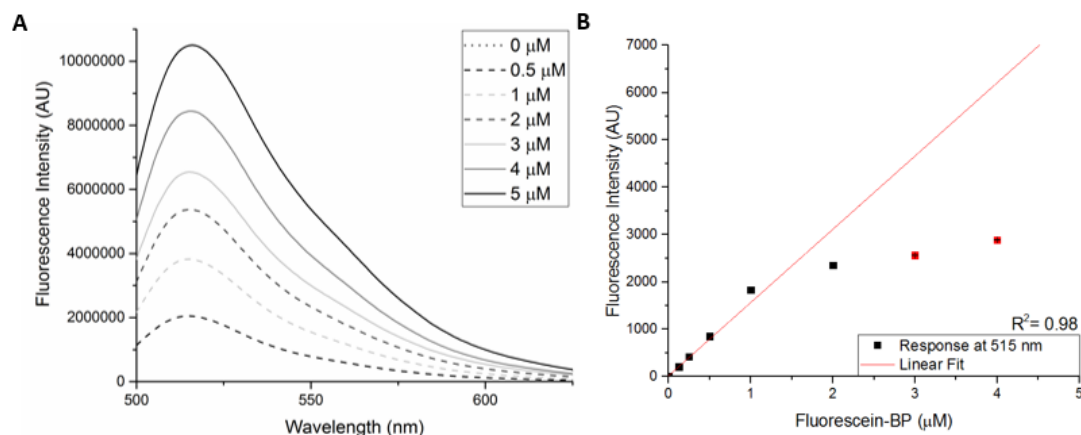


**Figure 2.14: Fluorescent signal of Fluorescein-BP.** (A) Fluorescence spectrum of increasing fluorescence signal upon increasing concentration (0-5  $\mu\text{M}$ ) ( $\lambda_{\text{ex}} = 488 \text{ nm}$ ). (B) Change of fluorescence intensity at  $\lambda_{\text{em}} = 515 \text{ nm}$  vs concentration of Fluorescein-BP probe (0-4  $\mu\text{M}$ ). 3 and 4  $\mu\text{M}$  data points reported in red as they do not fit with the linear fit. Data shown is from 3 repeats (A) and 6 repeats (B) and shown as the mean  $\pm$  S.E.M.

For Cy-Pep (**71**) upon increasing concentration, there was an increase of fluorescence at 660 nm, signal from 1  $\mu\text{M}$  to 10  $\mu\text{M}$  after which, at 20  $\mu\text{M}$  the fluorescence intensity still increased but a small shift in wavelength was noticeable ( $\lambda_{\text{em}} = 708 \text{ nm}$ ) (Figure 2.15 A). When a 50  $\mu\text{M}$  solution is used, a similar wavelength shift was apparent ( $\lambda_{\text{em}} = 717 \text{ nm}$ ) and there was a large decrease in fluorescence intensity to a value closer to that seen for probe concentrations of 10  $\mu\text{M}$ . The high concentration of Cy-Pep (**71**) in solution leads to clustering, which in turn leads to significant quenching of the fluorescence signal, a phenomenon that has already been shown to take place with cyanine dyes.<sup>68</sup> However, between 1  $\mu\text{M}$  to 10  $\mu\text{M}$  of Cy-Pep, a linear response at 695 nm was visible (Figure 2.15 B) suggesting the lowest concentration for detection is 0.025  $\mu\text{M}$ .



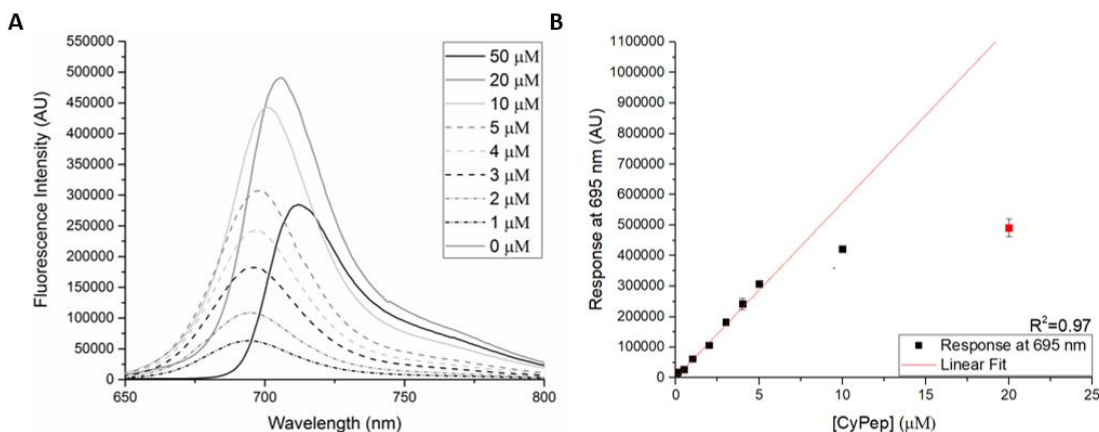


**Figure 2.15: Fluorescence signal of Cy-Pep.** (A) Fluorescence spectrum of increasing fluorescence signal upon increasing concentration (0-50  $\mu\text{M}$ ) ( $\lambda_{em} = 660 \text{ nm}$ ). (B) Change of fluorescence intensity at  $\lambda_{em} = 695 \text{ nm}$  vs concentration of Cy-Pep probe. 50  $\mu\text{M}$  removed for clarity as, together with 20  $\mu\text{M}$ , it does not give a linear response. Data shown in (A) and (B) is from 3 repeats and shown as the mean  $\pm$  S.E.M.

$\Phi$  by  $\epsilon$  (Table 2.9) are also easily calculated and show that Fluorescein-BP (**55**) is brighter than Cy-Pep (**71**). This can also be deduced from the fluorescence intensity of the probe at 5  $\mu\text{M}$  (Figure 2.14 A and Figure 2.15 A) showing that the signal for Fluorescein-BP (**55**) and Cy-Pep (**71**) are 10,000,000 and 300,000 AU respectively.

**Table 2.9: Absorbance and fluorescence maximum wavelength, quantum yield and extinction coefficient of Fluorescein-BP (55) and Cy-Pep (71).**

Compound	$\lambda_{abs} \text{ (nm)}$	$\lambda_{em} \text{ (nm)}$	$\Phi$	$\epsilon \text{ (M}^{-1}\text{cm}^{-1})$
Fluorescein-BP ( <b>55</b> )	491	515	0.83	41,100
Cy-Pep ( <b>71</b> )	660	695	0.73	110,000

\*quantum yields were measured in  $\text{H}_2\text{O}:\text{DMF}$  mix using: 5/6-carboxy-fluorescein NHS ester (**54**) as a standard ( $\Phi$  0.79) for Fluorescein-BP (**55**) and Cy5.5 NHS ester ( $\Phi$  0.2) for Cy-Pep (**71**).

#### 2.4.10 Binding affinity of probes to calcium compounds

As many calcium compounds are present in animal and human models, the ability of Fluorescein-BP (**55**) and Cy-Pep (**71**) to bind specifically to HAP needed to be assessed. To study the affinity of the probes to HAP, a range of other calcium based compounds were selected; calcium oxalate (CaOx) present in benign cancer,<sup>69-72</sup> calcium pyrophosphate (CaPyr) present in Pseudogout,<sup>73-77</sup> and calcium phosphate (CaPi) which is a precursor to the more crystalline HAP.

Two methods were explored to determine the selectivity of the probe towards calcium compounds. The first method used an aqueous suspension of these minerals, while the second method used calcium minerals embedded into an agarose phantom.

Method 1 involved an aqueous suspension of the calcium minerals, at fixed w/v, which were incubated with Fluorescein-BP (**55**) or Cy-Pep (**71**) for 2 hours, before removing any un-bound probe from the solids through a series of centrifugation and washing steps. Fluorescence analysis of the combined aqueous extracts (*Figure 2.16*) allowed the levels of un-bound probe to be quantified and hence a direct comparison could be made between the levels of Fluorescein-BP (**55**) or Cy-Pep (**71**) binding to each of the different calcium-containing minerals. These data showed that Fluorescein-BP (**55**) exhibited almost an order of magnitude higher selectivity towards HAP than any other calcium species tested. In contrast, when Cy-Pep (**71**), was incubated with the calcium minerals it showed a very similar fluorescent intensity for all of them indicating non-specific binding. There was also a sharp difference in fluorescence intensity obtained from both probes where Fluorescein-BP (**55**) displays a fluorescence intensity of around 32,500 AU upon binding to HAP while Cy-Pep (**71**) only displays an intensity of 7,625 AU upon the same binding, proving that Fluorescein-BP is more sensitive in comparison to Cy-Pep.

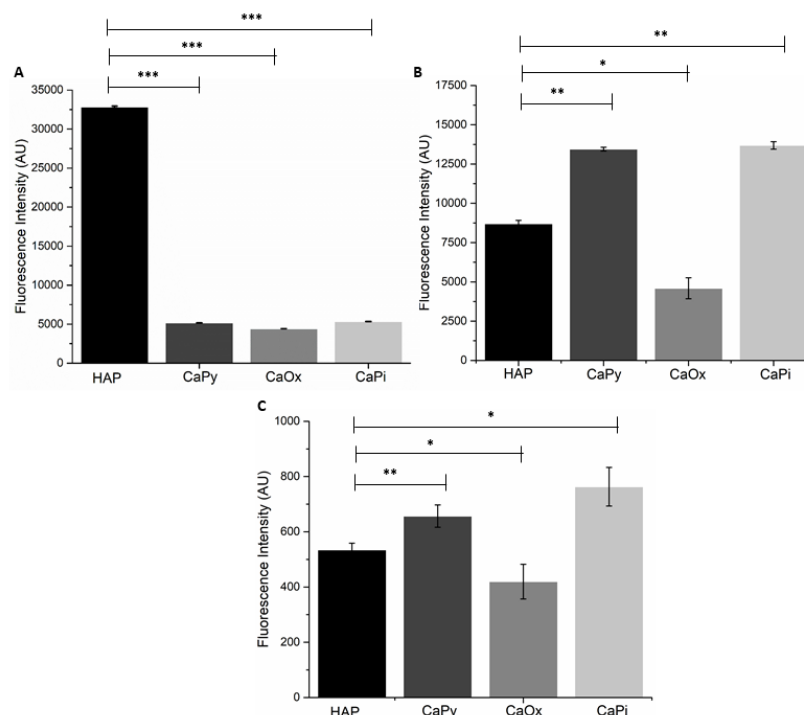


**Figure 2.16: Selectivity of Fluorescein-BP (55) (A), Cy-Pep (71) (B) towards Calcium minerals in comparison to Alizarin S stain (C).** Calcium minerals were incubated with Fluorescein-BP (5  $\mu$ M)  $\lambda_{em/ex}$  = 491/515 nm (A) or Cy-Pep (5  $\mu$ M)  $\lambda_{em/ex}$  = 660/695 nm (B) or 1% w/w Alizarin S  $\lambda_{em/ex}$  = 530/560 nm (C) in water for 2 hours and the un-bound probe was removed and quantified. The histograms show the relative amounts of bound probe for each of the calcium minerals. (A-C) show data that is representative of at least 3 independent experiments yielding comparable results. \*  $P < 0.05$ , \*\*  $P < 0.01$ , \*\*\*  $P < 0.001$ .

Non-specific binding was also observed when Alizarin S was incubated with the same minerals. Alizarin S is one of the most common staining methods for calcification together with von Kossa,<sup>77,78</sup> but comes with its own limitations. The colourimetric stain Alizarin S detects calcium, and not phosphate, thus it can also interact with calcium binding proteins and proteoglycans without discriminating for the presence of HAP.<sup>79</sup>

In order to achieve effective visualisation of the Alizarin S stain by fluorescence, millimolar concentrations of the stain were required which is in sharp contrast to the low micromolar concentrations required of Fluorescein-BP (55) and Cy-Pep (71). This reflects the relative brightness of the signal for each fluorophore which is proportional to its quantum yield ( $\Phi = 0.79$  for fluorescein,<sup>80-82</sup>  $\Phi = 0.30$  for Cy5.5,<sup>83-85</sup> and  $\Phi = 0.001$  for Alizarin S<sup>82,86</sup>). Not only  $\Phi$  is low for Alizarin S, it is also known that its binding affinity to HAP is 10-fold lower than the bisphosphonates which have a  $\mu$ M affinity.<sup>52,87</sup>

Method 2, the ‘phantom method’ involves creating a phantom substrate by mixing calcium compounds in an agarose hydrogel. The phantoms were then incubated with Fluorescein-BP (**55**), Cy-Pep (**71**) and Alizarin S (*Figure 2.17*). After 2 hours, the supernatant was removed and the phantoms were washed twice with water to remove excess un-bound probe and then imaged.

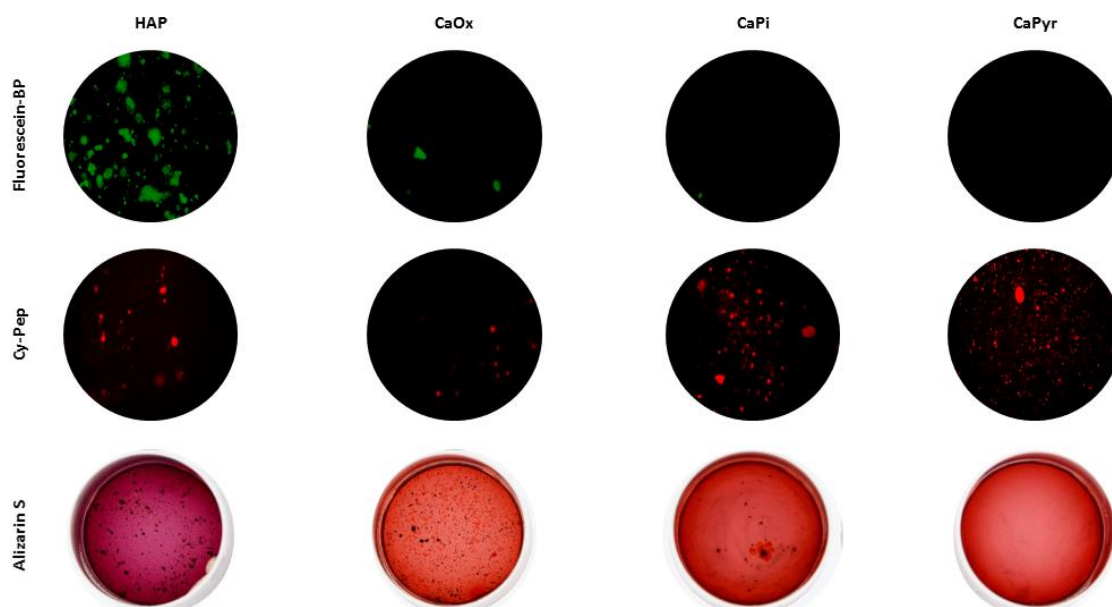


*Figure 2.17: Phantom models showing binding of Fluorescein-BP (**55**), Cy-Pep (**71**) and Alizarin S to different calcium species. Calcium minerals were embedded in agarose and then incubated with Fluorescein-BP ( $5 \mu\text{M}$ ) or Cy-Pep ( $5 \mu\text{M}$ ) or 1% w/w Alizarin S in water for 2 hours. The agarose phantoms were then washed with water and imaged. All data are representative of at least 3 independent experiments yielding comparable results.*

The phantom method initially appeared advantageous as it measured directly bound Fluorescein-BP (**55**) and Cy-Pep (**71**); however when combining the agarose and the calcium crystals, it became apparent that specific minerals disperse in different manners when in contact with the agarose. HAP and CaOx, being very crystalline in structure, form clusters while CaPi and CaPyr being powder-like dispersed evenly. Furthermore, when staining with Alizarin S, using powder-like materials was not easily differentiated from the unselective staining of the agarose gel itself. The addition of HAP caused the agarose to become basic, and when interacting with Alizarin S there was a colour change from bright red to a purple which this does not allow direct comparison with the other calcium compounds.

It was for the above reasons that the aqueous suspension method was selected as the most appropriate method to determine selectivity of the probes towards the different calcium

minerals. Due to the high selectivity of the Fluorescein-BP (**55**) probe towards HAP, it was selected for the next step involving *in vitro* and *ex vivo* studies.

## 2.5 Conclusion

Several fluorescent probes with different optical properties were synthesised. Three fluoride probes, two based on the cyanoacrylate motif; one with a free hydroxyl group (**3**) and one with a TBDS protected group (**4**), as well as a rhodamine-based probe (**5**) were synthesised and their selectivity towards NaF was tested. Upon addition of fluoride ions, a decrease in absorption was visible for both the cyanoacrylate probes, however no novel peak appeared as expected from the literature. On the other hand, when the imidazole bearing rhodamine 6G probe (**5**) was incubated with NaF an increase in the fluorescence peak was observed and when incubated with a range of anions the probe showed selectivity towards fluoride ions only, suggesting that it could be a respectable probe to examine the mechanism of NaF uptake in calcified models. However, for the fluorescence signal of probe **5** at 5  $\mu\text{M}$  concentration to be intense enough to be detected over the background signal, concentrations of NaF of 2.9  $\mu\text{M}$  or above are required; as previously mentioned, this suggests that the required ratio between the probe and NaF is 1:0.6. For PET imaging, pM concentrations of NaF are used suggesting that the probe will also need to be in the same concentration range. Unfortunately, the fluorescence signal of the probe is not intense enough to be visualised at those concentrations, therefore even this probe was rejected.

A number of fluorophores were synthesised and their coupling to calcium targeting molecules was investigated. Once synthesised, the Cy7.5 (**42**) and Cy5.5 (**47**) were reacted with alendronate (**26**), however, the conjugated cyanine-alendronate system was never observed. Cy5.5 bearing an alkyne group (**48**) was also synthesised and its coupling to the phosphate-protected azido alendronate (**56**) was successful, however, the deprotection of the phosphate protecting groups was never obtained. Cy5.5 (**48**) was nonetheless, coupled to a HAP selective peptide (**30**) which was then studied further to characterise the fluorophore and assess the selectivity of the probe. In contrast, Fluorescein-BP (**55**) was successfully synthesised without any complication. Fluorophore characterisation showed that although the Cy5.5-pep (**71**) emits in the NIR region, it is lacking in characteristics that the Fluorescein-BP (**55**) can provide; high quantum yields and extinction coefficient. When selectivity studies were carried out on different calcium minerals, Fluorescein-BP (**55**) provided a stronger fluorescence response when bound to HAP in comparison to the other minerals. When the same experiment was performed with Cy-Pep (**71**), although not using the same fluorophore, it was shown that

the peptide motif lacked the same selectivity and provided the roughly the same fluorescence signal for all the calcium minerals. For this reason, Fluorescein-BP (**55**) was selected as a robust selective calcium probe for application in biological systems.

## 2.6 References

- 1 B. N. G. Giepmans, S. R. Adams, M. H. Ellisman and R. Y. Tsien, *Science*, 2006, **312**, 217–24.
- 2 L. E. Morrison, *Methods Mol. Biol.*, 2008, **429**, 3–19.
- 3 S. Gross and D. Piwnica-Worms, *Cancer Cell*, 2005, **7**, 5–15.
- 4 H. Hong, Y. Yang and W. Cai, *Cold Spring Harb. Protoc.*, 2011, **2011**, pdb.top103.
- 5 M. Whitaker, *Methods Cell Biol.*, 2010, **99**, 153–182.
- 6 K. P. Carter, A. M. Young and A. E. Palmer, *Chem. Rev.*, 2014, **114**, 4564–4601.
- 7 M. Sauer, J. Hofkens and J. (Jörg) Enderlein, *Handbook of fluorescence spectroscopy and imaging : from single molecules to ensembles*, Wiley-VCH, 2011.
- 8 A. Chevalier, P.-Y. Renard and A. Romieu, *Chemistry*, 2014, **20**, 8330–7.
- 9 L. D. Lavis and R. T. Raines, *ACS Chem. Biol.*, 2008, **3**, 142–155.
- 10 T. Ueno and T. Nagano, *Nat. Methods*, 2011, **8**, 642–645.
- 11 C. Greb, *Handbook of Textile and Industrial Dyeing: Principles, Processes and Types of Dyes*, 2012, 564-567.
- 12 C. Saravanan, S. Easwaramoorthi, C. Y. Hsiow, K. Wang, M. Hayashi and L. Wang, *Org. Lett.*, 2014, **16**, 354–357.
- 13 R. Liu, Y. Gao, Q. Zhang, X. Yang, X. Lu, Z. Ke, W. Zhou and J. Qu, *New J. Chem.*, 2014, **38**, 2941.
- 14 Y. Jiao, B. Zhu, J. Chen and X. Duan, *Theranostics*, 2015, **5**, 173–87.
- 15 P. Hou, S. Chen, H. Wang, J. Wang, K. Voitchovsky and X. Song, *Chem. Commun. (Camb)*, 2013, **2**, 1–3.
- 16 J. Gui, B. Liu, G. Cao, A. M. Lipchik, M. Perez, Z. Dekan, M. Mobli, N. L. Daly, P. F. Alewood, L. L. Parker, G. F. King, Y. Zhou, S. E. Jordt and M. N. Nitabach, *Curr.*

- Biol.*, 2014, **24**, 473–483.
- 17 C. Delpivo, G. Micheletti and C. Boga, *Synthesis (Stuttg.)*, 2013, **45**, 1546–1552.
- 18 M. Kaur, M. J. Cho and D. H. Choi, *Dye. Pigment.*, 2014, **103**, 154–160.
- 19 J.-T. Yeh, P. Venkatesan and S.-P. Wu, *New J. Chem.*, 2014, **38**, 6198–6204.
- 20 G. Sivaraman and D. Chellappa, *J. Mater. Chem. B*, 2013, **1**, 5768.
- 21 C. S. Levin, *Proc. IEEE*, 2008, **96**, 439–467.
- 22 M. Lopalco, E. N. Koini, J. K. Cho and M. Bradley, *Org. Biomol. Chem.*, 2009, **7**, 856–9.
- 23 D. M. Mizrahi, O. Ziv-Polat, B. Perlstein, E. Gluz and S. Margel, *Eur. J. Med. Chem.*, 2011, **46**, 5175–83.
- 24 D. S. Pisoni, L. Todeschini, A. C. A. Borges, C. L. Petzhold, F. S. Rodembusch and L. F. Campo, *J. Org. Chem.*, 2014, **79**, 5511–5520.
- 25 H. A. Shindy, M. A. El-Maghraby and F. M. Eissa, *Eur. J. Chem.*, 2014, **5**, 451–456.
- 26 S. Luo, E. Zhang, Y. Su, T. Cheng and C. Shi, *Biomaterials*, 2011, **32**, 7127–7138.
- 27 M. S. T. Gonçalves, *Chem. Rev.*, 2009, **109**, 190–212.
- 28 F. Kong, L. Ge, X. Pan, K. Xu, X. Liu and B. Tang, *Chem. Sci.*, 2016, **7**, 1051–1056.
- 29 A. C. Morosanu, A. Gritco, D. G. Dimitriu, D. O. Dorohoi and C. Cheptea, *E-Health and Bioengineering Conference (EHB)*, IEEE, 2017, pp. 619–622.
- 30 J. F. Arevalo, *Retinal angiography and optical coherence tomography*, Springer, 2009.
- 31 A. H. Coons, *J. Immunol.*, 1961, **87**, 499–503.
- 32 A. H. Coons and M. H. Kaplan, *J. Exp. Med.*, 1950, **91**, 1–13.
- 33 F. Bosch and L. Rosich, *Pharmacology*, 2008, **82**, 171–179.
- 34 N. Efron and N. Efron, in *Contact Lens Complications*, Elsevier, 2012, pp. 102–112.
- 35 B. R. Hurley and C. D. Regillo, in *Retinal Angiography and Optical Coherence Tomography*, 2009, pp. 27–42.
- 36 A. L. MacLean and A. E. Maumenee, *Trans. Am. Ophthalmol. Soc.*, 1959, **57**, 171–94.

- 37 A. I. Kotsolis, F. A. Killian, I. D. Ladas and L. A. Yannuzzi, , DOI:10.1136/bjo.2009.159913.
- 38 K. Minkin, E. Naydenov, K. Gabrovski, P. Dimova, M. Penkov, R. Tanova, S. Nachev and K. Romanski, *Clin. Neurol. Neurosurg.*, 2016, **149**, 22–26.
- 39 T. Mathew, S. Kundan, M. I. Abdulsamad, S. Menon, B. S. Dharan and K. Jayakumar, *Ann. Thorac. Surg.*, 2014, **97**, e27–e28.
- 40 N. Li, J. Song, G. Zhu, X. Shi and Y. Wang, *Colloids Surfaces B Biointerfaces*, 2016, **142**, 344–350.
- 41 A. Swami, M. R. Reagan, P. Basto, Y. Mishima, N. Kamaly, S. Glavey, S. Zhang, M. Moschetta, D. Seevaratnam, Y. Zhang, J. Liu, M. Memarzadeh, J. Wu, S. Manier, J. Shi, N. Bertrand, Z. N. Lu, K. Nagano, R. Baron, A. Sacco, A. M. Roccaro, O. C. Farokhzad and I. M. Ghobrial, *Proc. Natl. Acad. Sci.*, 2014, **111**, 10287–10292.
- 42 T. Kowada, J. Kikuta, A. Kubo, M. Ishii, H. Maeda, S. Mizukami and K. Kikuchi, *J. Am. Chem. Soc.*, 2011, **133**, 17772–17776.
- 43 M. L. Lolli, B. Rolando, P. Tosco, S. Chaurasia, A. Di Stilo, L. Lazzarato, E. Gorassini, R. Ferracini, S. Oliaro-Bosso, R. Fruttero and A. Gasco, *Bioorganic Med. Chem.*, 2010, **18**, 2428–2438.
- 44 F. P. Coxon, K. Thompson, A. J. Roelofs, F. H. Ebetino and M. J. Rogers, *Bone*, 2008, **42**, 848–860.
- 45 M. A. Lawson, Z. Xia, B. L. Barnett, J. T. Triffitt, R. J. Phipps, J. E. Dunford, R. M. Locklin, F. H. Ebetino and R. G. G. Russell, *J. Biomed. Mater. Res. B. Appl. Biomater.*, 2010, **92**, 149–55.
- 46 V. Chandrasekaran, S. Kalyan, V. Biel, M. Lettau, P. T. Nerdal, H.-H. Oberg, D. Wesch, T. K. Lindhorst and D. Kabelitz, *Med. Chem. Commun.*, 2015, **6**, 919–925.
- 47 P. Vachal, J. J. Hale, Z. Lu, E. C. Streckfuss, S. G. Mills, M. MacCoss, D. H. Yin, K. Algayer, K. Manser, F. Kesisoglou, S. Ghosh and L. L. Alani, *J. Med. Chem.*, 2006, **49**, 3060–3063.
- 48 K. M. Kozloff, L. I. Volakis, J. C. Marini and M. S. Caird, *J. Bone Miner. Res.*, 2010, **25**, 1748–58.



- 49 M. P. Yavropoulou, M. Pikilidou and J. G. Yovos, *J. Vasc. Res.*, 2014, **51**, 37–49.
- 50 R. Ylitalo, *Gen. Pharmacol. Vasc. Syst.*, 2000, **35**, 287–296.
- 51 A. Jung, S. Bisaz and H. Fleisch, *Calcif. Tissue Res.*, 1973, **11**, 269–80.
- 52 C. T. Leu, E. Luegmayr, L. P. Freedman, G. A. Rodan and A. A. Reszka, *Bone*, 2006, **38**, 628–636.
- 53 J. Zhao, Y. Liu, W. Sun and X. Yang, *J. Dent. Sci.*, 2012, **7**, 316–323.
- 54 J. Zhao, Y. Liu, W.-B. Sun and H. Zhang, *Chem. Cent. J.*, 2011, **5**, 40.
- 55 M. D. Roy, S. K. Stanley, E. J. Amis and M. L. Becker, *Adv. Mater.*, 2008, **20**, 1830–1836.
- 56 Y.-H. Yang, R. Rajaiah, E. Ruoslahti and K. D. Moudgil, *Proc. Natl. Acad. Sci. U. S. A.*, 2011, **108**, 12857–62.
- 57 G. Mamone, G. Picariello, P. Ferranti and F. Addeo, *Proteomics*, 2010, **10**, 380–393.
- 58 A. J. Winstead, R. Williams, Y. Zhang, C. McLean and S. Oyaghire, *J. Microw. Power Electromagn. Energy*, 2010, **44**, 207–12.
- 59 H. Li, R. Aneja and I. Chaiken, *Molecules*, 2013, **18**, 9797–817.
- 60 R. C. Brewster, G. C. Gavins, B. Günthardt, S. Farr, K. M. Webb, P. Voigt and A. N. Hulme, *Chem. Commun.*, 2016, **52**, 12230–12232.
- 61 Y. Xu, S. A. Lee, T. G. Kutateladze, D. Sbrissa, A. Shisheva and G. D. Prestwich, *J. Am. Chem. Soc.*, 2006, **128**, 885–897.
- 62 T. Eisner, Charles University, Prague, 2014.
- 63 A. C. Spivey and D. Leese, *Annu. Rep. Prog. Chem., Sect. B Org. Chem.*, 2002, **98**, 41–60.
- 64 K. Hofmann, H. Yajima, T.-Y. Liu and N. Yanaihara, *J. Am. Chem. Soc.*, 1962, **84**, 4475–4480.
- 65 K. Hofmann, N. Yanaihara, S. Lands and H. Yajima, *J. Am. Chem. Soc.*, 1962, **84**, 4470–4474.
- 66 L. A. Carpino, S. Ghassemi, D. Ionescu, M. Ismail, D. Sadat-Aalae, G. A. Truran, E.

- M. E. Mansour, G. A. Siwruk, J. S. Eynon and B. Morgan, *Org. Process Res. Dev.*, 2003, **7**, 28–37.
- 67 R. B. Merrifield, *J. Am. Chem. Soc.*, 1963, **85**, 2149–2154.
- 68 N. G. Zhegalova, S. He, H. Zhou, D. M. Kim and M. Y. Berezin, *Contrast Media Mol. Imaging*, 2014, **9**, 355–362.
- 69 G. H. Wilson, J. C. Gore, T. E. Yankeelov, S. Barnes, T. E. Peterson, J. M. True, S. Shokouhi, J. O. McIntyre, M. Sanders, V. Abramson, T.-Q. Ngyuen, A. Mahadevan-Jansen, M. N. Tantawy and M. N. Tantawy, *J. Nucl. Med.*, 2014, **55**, 1138–43.
- 70 J. E. Gonzalez, R. G. Caldwell and J. Valaitis, *Am. J. Surg. Pathol.*, 1991, **15**, 586–91.
- 71 R. F. Cox, A. Hernandez-Santana, S. Ramdass, G. McMahon, J. H. Harmey and M. P. Morgan, *Br. J. Cancer*, 2012, **106**, 525–537.
- 72 R. D. Motrich, G. M. Castro, B. L. Caputto, H. Ferreyra, B. L. Caputto, O. A. Pucci, G. A. Gil, J. Bruha, O. Vycital and J. Finek, *PLoS One*, 2013, **8**, e53211.
- 73 D. Resnick, G. Niwayama, T. G. Goergen, P. D. Utsinger, R. F. Shapiro, D. H. Haselwood and K. B. Wiesner, *Radiology*, 1977, **122**, 1–15.
- 74 L. Carpenter, N. Juliano and R. Herb, *J. Am. Osteopath. Assoc.*, 2017, **117**, 199.
- 75 A. Di Matteo, E. Filippucci, F. Salaffi, M. Carotti, D. Carboni, E. Di Donato and W. Grassi, *Clin. Exp. Rheumatol.*, 2017, **35**, 647–652.
- 76 A. Williamson, *J. Educ. Teach. Emerg. Med.*, 2017, **2**, 8–9.
- 77 H. Paul, A. J. Reginato and H. R. Schumacher, *Arthritis Rheum.*, 1983, **26**, 191–200.
- 78 J. Rungby, M. Kassem, E. F. Eriksen and G. Danscher, *Histochem. J.*, 1993, **25**, 446–451.
- 79 L. F. Bonewald, S. E. Harris, J. Rosser, M. R. Dallas, S. L. Dallas, N. P. Camacho, B. Boyan and A. Boskey, in *Calcified Tissue International*, Springer-Verlag, 2003, vol. 72, pp. 537–547.
- 80 R. Sjöback, J. Nygren and M. Kubista, *Spectrochim. Acta Part A Mol. Biomol. Spectrosc.*, 1995, **51**, L7–L21.
- 81 X. F. Zhang, J. Zhang and L. Liu, *J. Fluoresc.*, 2014, **24**, 819–826.

- 82 M. Neumann, S. Földner, B. König and K. Zeitler, *Angew. Chemie - Int. Ed.*, 2011, **50**, 951–954.
- 83 V. E. Shershov, M. A. Spitsyn, V. E. Kuznetsova, E. N. Timofeev, O. A. Ivashkina, I. S. Abramov, T. V. Nasedkina, A. S. Zasedatelev and A. V. Chudinov, *Dye. Pigment.*, 2013, **97**, 353–360.
- 84 J.-F. Ge, Q.-Q. Zhang, J.-M. Lu, M. Kaiser, S. Wittlin, R. Brun and M. Ihara, *Medchemcomm*, 2012, **3**, 1435.
- 85 K. Rurack, in *Standardization and Quality Assurance in Fluorescence Measurements I*, Springer Berlin Heidelberg, Berlin, Heidelberg, 2008, pp. 101–145.
- 86 L. Zhang, S. Dong and L. Zhu, *Chem. Commun. (Camb)*., 2007, 1891–3.
- 87 W. Jahnke and C. Henry, *ChemMedChem*, 2010, **5**, 770–776.

# Chapter 3- Characterization of Fluorescein-BP in an *in vitro* model of osteoblast matrix calcification

## 3.1 Importance of calcium

Calcium is a crucial intracellular element that is responsible for regulating many cellular processes across every cell type in biological organisms.<sup>1-5</sup> Calcium is found in either the free ion form or as a mineral phase. An example of this is hydroxyapatite (HAP) which makes up bone and teeth. Numerous physiological processes, including: muscle contraction; cell adhesion; hormone/neurotransmitter release; glycogen metabolism; cell proliferation/differentiation; blood clotting and nerve or sympathetic impulse transmission are regulated by calcium signalling.<sup>6-10</sup> Defects in the integrity of cell-specific calcium signalling systems are associated with a number of human diseases including neurodegenerative and kidney diseases.<sup>1,11,12</sup>

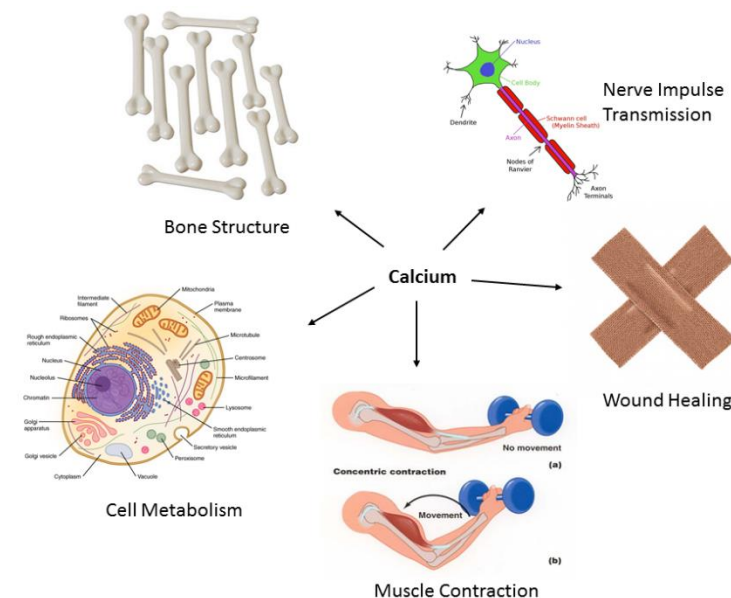


**Figure 3.1: Role of calcium ions.** Calcium plays an important role in bone structure, nerve impulse transmission, wound healing, muscle contraction and in cell metabolism. Images downloaded.

Moreover, pathological calcification is also a critical component of a wide range of diseases such as cancer, arthritis and CVD.<sup>13</sup> One example of this is the presence of two types of calcium species in breast cancer: calcium oxalate (CaOx) which is associated with benign breast disease; and HAP which is associated with malignant breast cancer.<sup>14–18</sup> As described in Chapter 1, HAP is also present in a range of CVD disorders.<sup>19,20</sup> Microscopic deposits of HAP, present in atherosclerotic lesions, can weaken the fibrous cap of an atherosclerotic plaque, leading to rupture of the plaque and vessel occlusion.<sup>21–25</sup> Thus, the development of a calcium assay which is able to selectively detect HAP with high sensitivity and specificity could both improve our pathophysiological understanding and the diagnosis of a range of clinical disorders including vascular calcification.

### 3.2 Gold standard methods of detecting calcification

The most common assays for calcium phosphate calcification are calcium leaching by hydrochloric acid (HCl); and staining with Alizarin S and von Kossa (*Figure 3.2*).<sup>26,27</sup> Each comes with their own advantages and limitations and will be briefly discussed below.

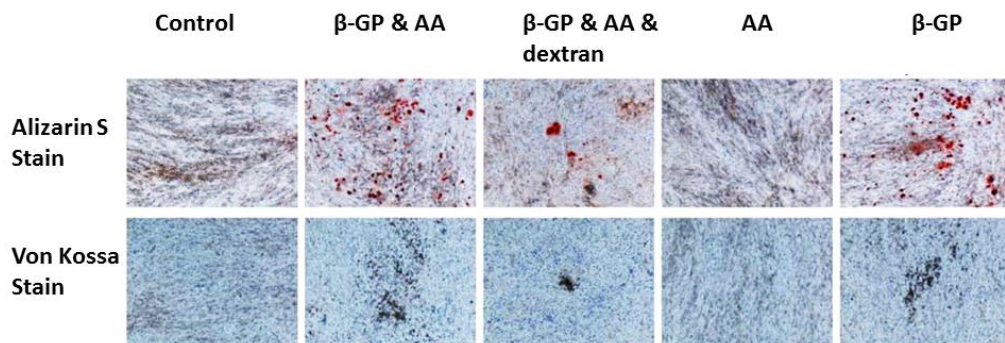


*Figure 3.2: Alizarin S and von Kossa stain of murine mammary adenocarcinoma 4T1 cell calcification under a range of different conditions which induce ( $\beta$ -glycerolphosphate ( $\beta$ -GP) & ascorbic acid (AA),  $\beta$ -GP & AA & dextran,  $\beta$ -GP) or inhibit calcification (AA). Image reproduced with permission.<sup>18</sup>*

#### 3.2.1 Alizarin S

Alizarin S staining has been used for decades as a staining tool to evaluate calcium rich deposits in cell culture (*Figure 3.2*) as well as a bone marker by staining calcification in red.<sup>28–30</sup> After staining with Alizarin S, the dye can be extracted from the cell monolayer or tissue sample and can be quantified by carrying out a colourimetric assay.<sup>31</sup> Alizarin S functions by forming a chelate ring around calcium, specifically the hydroxyl groups on the alizarin which

are adjacent to each other are capable of forming a ring structure (Figure 3.3) with metals such as aluminium, iron and other metal cations as well as calcium.<sup>28,30,32</sup>

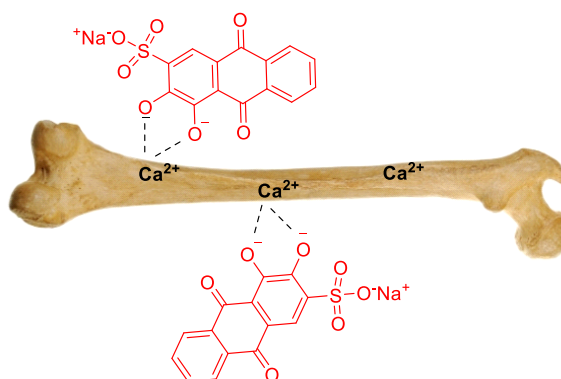


**Figure 3.3:** Mechanism of binding of Alizarin S to calcium present in bones.

However, even though it binds to calcific lesions, Alizarin S cannot discriminate between different calcium forms thus making it hard to confirm specifically the presence of HAP.<sup>33</sup>

### 3.2.2 Von Kossa

In contrast to Alizarin S, the colourimetric von Kossa stain reacts with phosphates but only in acidic environments (Figure 3.4). In von Kossa staining, sections are placed in a silver nitrate solution and exposed to light. Once exposed, the sections are then treated with sodium thiosulfate which removes unreacted silver. Silver nitrate reacts with phosphate, upon exposure to light the silver phosphate is then reduced to its metallic form.<sup>34</sup>

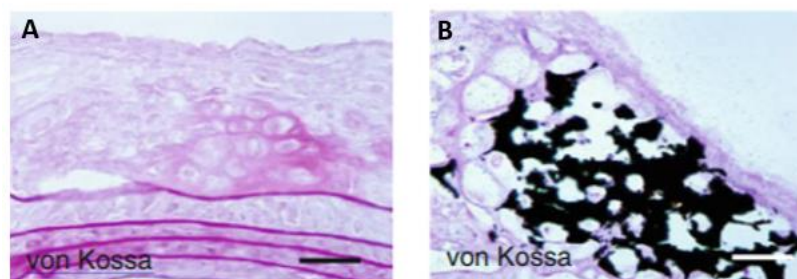


**Figure 3.4:** Von Kossa staining of atherosclerotic plaques. (A) Unobserved calcification in early lesion and (B) prominent calcification in advanced plaque. Image reproduced with permission.<sup>35</sup>

However, the presence of phosphate does not necessarily imply the presence of calcification or even specifically HAP as CaPi can also provide a positive stain.<sup>26,33,36</sup> Moreover, high phosphate levels are also associated with other components in the cell and the high level of free phosphate in the cytosol which could also display positive von Kossa staining.<sup>31,34</sup>

Both Alizarin S and von Kossa stains are used to indicate calcium depositions but at best give only semi-quantitative calcium readings and often stain in different areas due to the different binding abilities (*Figure 3.2*).<sup>37</sup>

### 3.2.3 HCl/DC assay

The calcium leaching assay is a further method used to determine calcium concentrations and has been used in laboratory settings to determine the presence of calcification in vascular and bone cell models.<sup>38-41</sup> The assay involves treating cell monolayers with HCl which allows the extraction of free calcium ions from the cells. The calcium content is then detected using a colorimetric assay, typically using o-cresolphthalein complexone, and normalised against the total number of cells per sample.<sup>42</sup> However, the assay presents major disadvantages when a large volume of cells are used as the HCl is not able to dissolve all the cell content and therefore an accurate reading of the total protein concentration is not obtained which makes the normalisation step hard. Furthermore, the calcium leaching assay is time intensive as it takes around 24-48 hours, making it unsuitable for high-throughput applications.

### 3.2.4 Calcein and other fluorescence methods

The discrepancies between the amounts of calcium visualized by Alizarin S and von Kossa has led scientists to develop novel calcium imaging probes that are more selective and more sensitive.

An example of this is calcein, this probe has routinely been used as a tool for imaging calcium, with higher sensitivity to Alizarin S and von Kossa. However, similarly to Alizarin S, calcein interacts with calcium (*Figure 3.5*) as well as a range of other metals including aluminium and zinc.<sup>43,44</sup> Nonetheless, even though it is able to bind to a range of cations, it has mainly been used for cell viability studies due to its ability to penetrate the cells and if alive fluoresce.

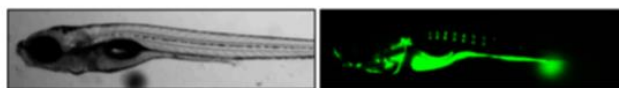
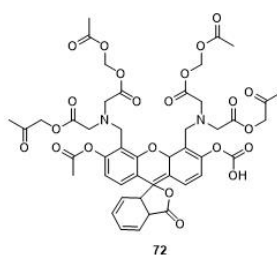


**Figure 3.5: Calcein staining of zebrafish embryos.** Calcein localization in the vertebrate column which is mainly composed of calcium. Image reproduced with permission.<sup>45</sup>

Another recently reported probe used in animal bone and vascular disease models is Osteosense (680 and 750), an expensive commercially available, near infrared (NIR) probe conjugated to a bisphosphonate.<sup>35,46–48</sup> This probe has been shown to be specifically selective for HAP and more sensitive than the current gold standard imaging techniques such as Alizarin S and von Kossa. However, the benefits offered by a NIR probe for *in vivo* studies, are negated by the need for non-standard filters for plate readers and microscopes in laboratory-based experiments which is why the development of new and more accessible imaging tools are necessary.

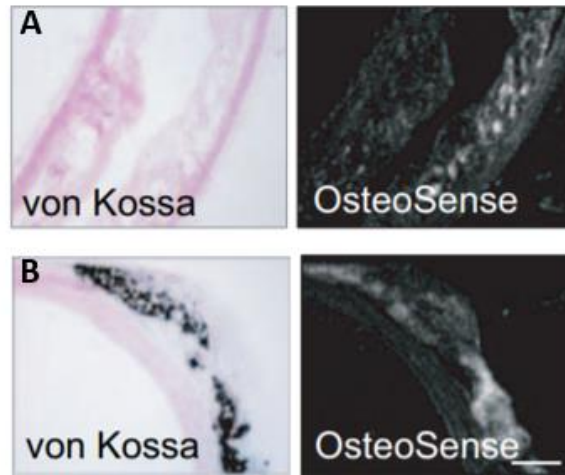


**Figure 3.6: Von Kossa and OsteoSense staining of atherosclerotic plaques.** (A) Early stage plaque formation showing no von Kossa staining but OsteoSense staining is visible in areas of micro-calcification. (B) Calcified plaque showing both von Kossa and OsteoSense staining of macro-calcification. Image reproduced with permission.<sup>35</sup>

### 3.3 Models for calcification

*In vitro* and *in vivo* models are important for underpinning the pathogenesis of human disease with the drive of developing novel therapies and imaging tools.<sup>49</sup> A number of models to address cardiovascular complications such as atherosclerosis have been recreated in different animal species and have been crucial in advancing the understanding of the disease mechanisms.

#### 3.3.1 Cells

Cells cultures are the first line of study. Specifically, primary vascular smooth muscle cells (VSMCs) which are the principal cell type involved in vascular calcification. They have been reported to provide respectable models to study calcification as they can undergo a phenotypic transition to calcifying osteoblastic cells.<sup>50</sup> Cell lines can also be used and, in contrast to



primary cells, offer a reliable, convenient and economical system in which to investigate vascular calcification *in vitro*.<sup>50</sup> The mouse VSMC cell line MOVAS-1 exhibits a smooth muscle cell phenotype and has also been previously employed to investigate the VSMC cell cycle and vascular calcification.<sup>50,51</sup>

### 3.3.2 *Ex vivo* rings

Cell monolayers only offer limited information of CVD due to their 2D structure which therefore does not provide the correct architecture and matrix structure which you would expect from normal vessels. They reach confluence over a short timeframe; they rapidly convert to a proliferative, secretory phenotype.<sup>52</sup> Morphological and phenotypic changes also occur at high passage numbers which lead to false results. In contrast, cultured aortae which have a 3D structure, are able to bridge the gap between 2D cultures and animal models using *in vivo* conditions.<sup>52,53</sup> Previous studies have cultured sectioned thoracic aortas dissected from mice and estimated the status of calcification under  $P_i$  stimulation at 2.6-3 mM  $P_i$  (Figure 3.7);<sup>53</sup> these phosphate concentrations correlate with myocardial infarction in human studies.<sup>53</sup>

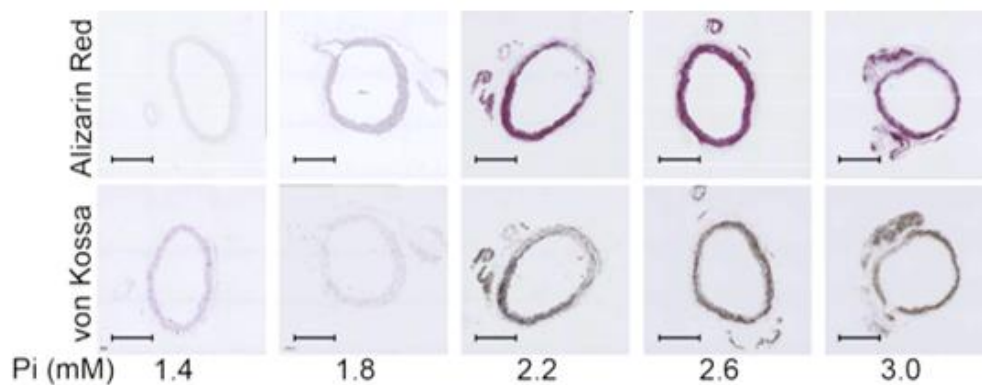


**Figure 3.7:** Thoracic aortic sections cultured under different phosphate concentrations (1.4, 1.8, 2.2, 2.6, 3.0 mM  $P_i$ ) for 7 days and stained with Alizarin S and von Kossa. Both Alizarin S and von Kossa show an increase in calcification present with increasing phosphate concentrations. Image reproduced with permission.<sup>52</sup>

### 3.3.3 Genetically modified mouse models

Another method for studying disease progression is by using animal models. Currently the use of small rodents, explicitly mice, as the main model of human disease is extensive. Their popularity is due to cost effectiveness and the ease with which a litter can be maintained. Other advantages include the large number of litters that provides a larger n value for studies as well as the ease in genetically modifying mice in order to either ablate, or overexpress, genes of

interest which can then provide useful information underpinning the mechanisms of CVD.<sup>49,54–56</sup>

In atherosclerosis murine models offer an additional advantage which is the development of the plaque in a very short time frame.<sup>56</sup> The two most commonly used mouse models are: apolipoprotein E knockout mouse (*ApoE*<sup>-/-</sup>) and low density lipoprotein receptor deficient mouse (*LDLR*<sup>-/-</sup>).<sup>49,54,55,57,58</sup> *ApoE*<sup>-/-</sup> is the most widely used as it develops atherosclerosis spontaneously (*Figure 3.8*),<sup>59</sup> and this development can be accelerated if the mice are placed on a high fat western type diet. These mice provide excellent models to study atherosclerosis as similarly to humans, they exhibit various phases of the disease including; early stage fatty streaks, accumulation of foam cells and the development of a fibrous cap and calcification nodules.<sup>56</sup> However, in contrast to humans where atherosclerotic plaques manifest in carotid and coronary arteries, mice predominantly develop plaques in the aortic arch.<sup>54,55</sup>

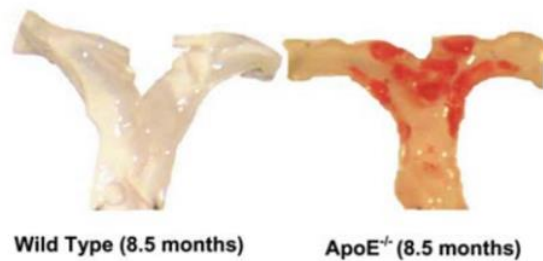


**Figure 3.8:** Wild type and *ApoE*<sup>-/-</sup> mice on a normal diet. *ApoE*<sup>-/-</sup> mice spontaneously develop atherosclerotic plaque over time. Image reproduced with permission.<sup>60</sup>

Several other murine knockout models have been created, where genes that regulate bone formation have been ablated, and these have led to new insight in the pathogenesis of arterial calcification. MGP knockout mice have shown extensive calcification in the aorta while OPG knockout mice developed medial and subintimal calcification in sites where endogenous OPG expression would be found suggesting that OPG may have a specific role in protecting the arteries from calcification.<sup>61</sup>

Another model that provides vascular calcification is the ENPP1 knockout mouse. ENPP1 is a key regulator of biomineralization and vascular calcification, however these knockout mice are mainly used in the study of generalised arterial calcification in infancy (GACI).<sup>39,40</sup> Due to the inhibition of pyrophosphate in constraining calcium deposition in ENPP1 mice, they could provide a potential therapeutic understanding on calcification deposition.<sup>62</sup>

### 3.4 Probe toxicity studies

Before any cell and *ex vivo* experiments could be carried out with the new probe, toxicity study to determine the optimum concentration of the probe that would not kill the cells had to be determined. To do this, MOVAS-1 cells were treated with a range of different concentrations of Fluorescein-BP (**55**) together with Alamar blue (*Figure 3.9*). Alamar blue is an accurate and rapid indicator of cellular health which has been used for the past 50 years in studies on cell viability and cytotoxicity.<sup>63</sup> Cells were incubated with both probes for 4 hours. Two controls were required, one which included cells with only Alamar Blue (positive control) and the other containing cells, Alamar Blue and DTT (identified in *Figure 3.9* as lysis buffer) which in turn causes cell lysis. It was found that, high concentrations of the Fluorescein-BP probe (5 and 10  $\mu\text{M}$ ) would cause the cells to die, while lower concentrations (0.5, 1, 2  $\mu\text{M}$ ) caused reduced levels of cell death. It was decided to use 1  $\mu\text{M}$  in subsequent studies as this provides a higher fluorescence signal when incubated with a cell monolayer in comparison to 0.5  $\mu\text{M}$ .

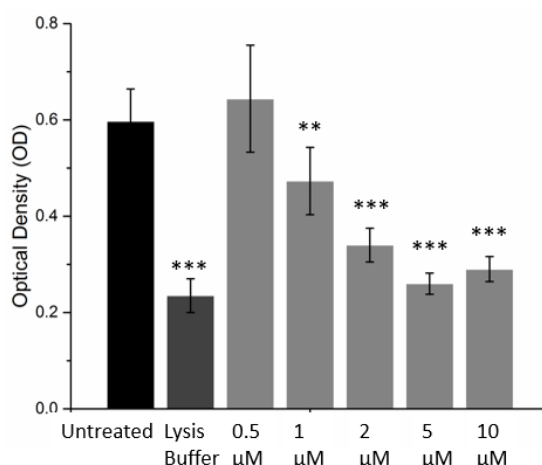


**Figure 3.9:** MOVAS-1 cell viability assay using Alamar Blue for different concentrations of Fluorescein-BP (**55**). Cells were seeded and grown until confluent. Cells were either: left untreated, treated with DTT to cause cell lysis, or treated with different concentrations of the probe to determine the optimum concentration of probe. Alamar blue was added to the cells for 4 hours before measuring the absorbance ( $\lambda_{ex} = 570 \text{ nm}$ ). Data shown is from at least 6 repeats and shown as the mean  $\pm$  S.E.M. \*  $p < 0.05$ , \*\*  $p < 0.01$ , \*\*\*  $p < 0.001$

Another cytotoxicity study with Alamar Blue assay was performed to determine whether the  $\text{Ca}^{2+}$  concentrations used to induce calcification were too high and were leading to cell apoptosis. 2.4 mM  $\text{Ca}^{2+}$  and 1.4 mM  $\text{P}_i$  and 2.7 mM  $\text{Ca}^{2+}$  and 2.5 mM  $\text{P}_i$  calcification conditions were selected as they are reported to induce calcification in VSMCs and resonance on real hypercalcemia and hyperphosphatemia conditions in patients.<sup>64</sup> Control and calcified

cell samples were incubated with, or without, Fluorescein-BP (**55**). Cells were also incubated with Fluorescein-BP (**55**) to determine whether incubation with the probe and the calcification conditions could have a negative synergistic effect on the cell monolayer and then lead to cell death. Both calcifying conditions ((i) 2.4 mM Ca and 1.4 mM P<sub>i</sub>, and (ii) 2.7 mM Ca and 2.5 mM P<sub>i</sub>) and control cell monolayers were grown for 7 days after which Fluorescein-BP (**55**) and Alamar Blue were added (*Figure 3.10*). Upon fluorescence examination, it was visible that neither calcification conditions, with or without Fluorescein-BP (**55**), had any negative effect on the cell monolayer as the optical density reading was equivalent within experimental error.

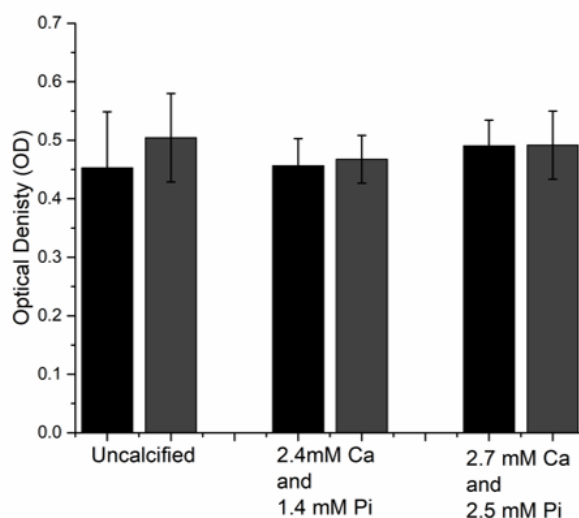


**Figure 3.10** MOVAS-1 cell viability assay using Alamar Blue for different calcification conditions. Cells were seeded and treated with calcification media ((i) 2.4 mM Ca and 1.4 mM P<sub>i</sub>, or (ii) 2.7 mM Ca and 2.5 mM P<sub>i</sub>) for 7 days. Cells were then incubated with Fluorescein-BP (1 μM, 2 hours) followed by Alamar blue (10 μL, 4 hours) reported in black or Alamar blue (10 μL, 4 hours) alone reported in grey. After incubation, the absorbance ( $\lambda_{ex}$  = 570 nm) was measured. Data shown is from at least 6 repeats and shown as the mean  $\pm$  S.E.M.

Together these data show that conditions such as 2.4 mM Ca and 1.4 mM P<sub>i</sub>, or 2.7 mM Ca and 2.5 mM P<sub>i</sub>, were appropriate for further studies.

### 3.5 Probe localization studies

Localisation studies were also carried out on MOVAS-1 cell monolayers. A monolayer of MOVAS-1 cells was incubated with 2.4 mM Ca and 1.4 mM P<sub>i</sub> for 7 days, then treated with Fluorescein-BP (**55**) for 2 hours. Once treated, the monolayer was imaged using confocal microscopy (*Figure 3.11*) which showed extracellular localisation of probe (**55**). This is indicative of the presence of HAP in the extracellular matrix which is in agreement with previous reports.<sup>65–68</sup>

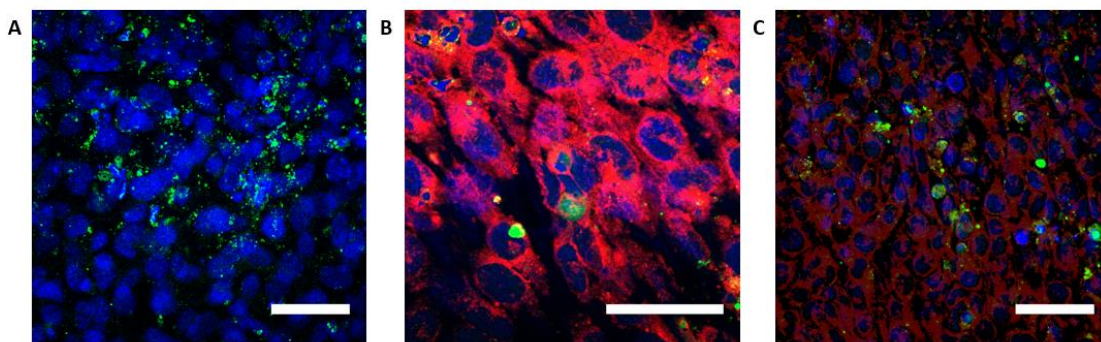


**Figure 3.11: Confocal imaging of calcified MOVAS-1 monolayers.** Monolayers of MOVAS-1 cells were grown to confluence (day 0) and then switched to calcification media (2.4 mM Ca and 1.4 mM P<sub>i</sub>) for 7 days, changing media on alternate days. The cell monolayers were treated sequentially with Fluorescein-BP (1 μM, 2 hours; green); CellMask Orange (500 nM, 10 minutes, pink); NBF (10%, 15 minutes); Triton X (0.05%, 3 x 5 minutes); DAPI (300 nM, 5 minutes, blue); then imaged on an Zeiss Confocal LSM710 microscope ( $\lambda_{ex}$  = 488 nm, 554 nm and 350 nm). Images are representative of at least 3 repeats. Scale bars = 100 μm. (A) Incubation with Fluorescein-BP and DAPI. (B, C) Incubation with Fluorescein-BP, CellMask Orange and DAPI.

In contrast to Fluorescein-BP (**55**) when the cells were incubated with Fluorescein-amino-1-pentol (Fluorescein-OH, **73**), a control fluorescein-based probe which lacks the bisphosphonate motif, no signal was observed (Figure 3.12). This demonstrated that the bisphosphonate motif was responsible for the Fluorescein-BP (**55**) binding to HAP in a cellular environment.

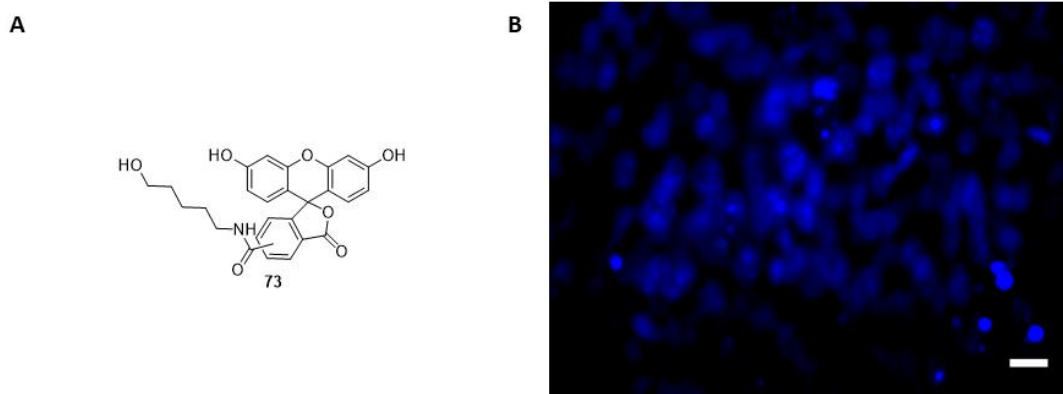


**Figure 3.12: Structure of Fluorescein-OH (73) (A) and fluorescence image of Calcified MOVAS-1 cells incubated with Fluorescein-OH (B).** A monolayer of MOVAS-1 cells was grown to confluence (day 0) and then switched to calcification media (2.4 mM Ca and 1.4 mM P<sub>i</sub>) for 7 days, changing media on alternate days. The cell monolayer was incubated with Fluorescein-OH (1 μM, 2 hours), fixed with NBF (10%, 15 minutes) and mounted using ProLong Gold Antifade with DAPI. Scale bar = 100 μm.

## 3.6 Comparison of probe with Alizarin S and calcium leaching assay

To investigate the range of conditions under which the Fluorescein-BP (**55**) probe can be used and to compare its efficacy with the calcium leaching assay and Alizarin S stain a supplementary series of calcification assays were conducted with both the MOVAS-1 cell line and primary VSMC cells.

### 3.6.1 MOVAS

Monolayers of the MOVAS-1 cell line were incubated in both phosphate-enriched (3 mM and 5 mM  $P_i$ ) and both phosphate and calcium-enriched (2.4 mM Ca and 1.4 mM  $P_i$  and 2.7 mM Ca and 2.5 mM  $P_i$ ) growth media. Both, the calcium leaching assay (4-fold,  $p < 0.001$ ) (*Figure 3.13 A*) and the fluorescence assay (4-fold,  $p < 0.001$ ) (*Figure 3.13 B*) demonstrated significant levels of calcium deposition when incubated in calcium enriched media. A comparison of the fluorescence images obtained for well plates with images of Alizarin S staining of equivalent plates (*Figure 3.13 C*), suggest that both fail to distinguish calcification in media only enriched with phosphate. Nevertheless, when cells are incubated in the presence of both calcium and phosphate enriched media, the fluorescent probe can detect the deposition of microcrystalline HAP with greater sensitivity than the Alizarin S stain. This is most notable when using commonly applied *in vitro* vascular calcification conditions, where the growth media have been enriched with 2.4 mM Ca and 1.4 mM  $P_i$ .<sup>38</sup>

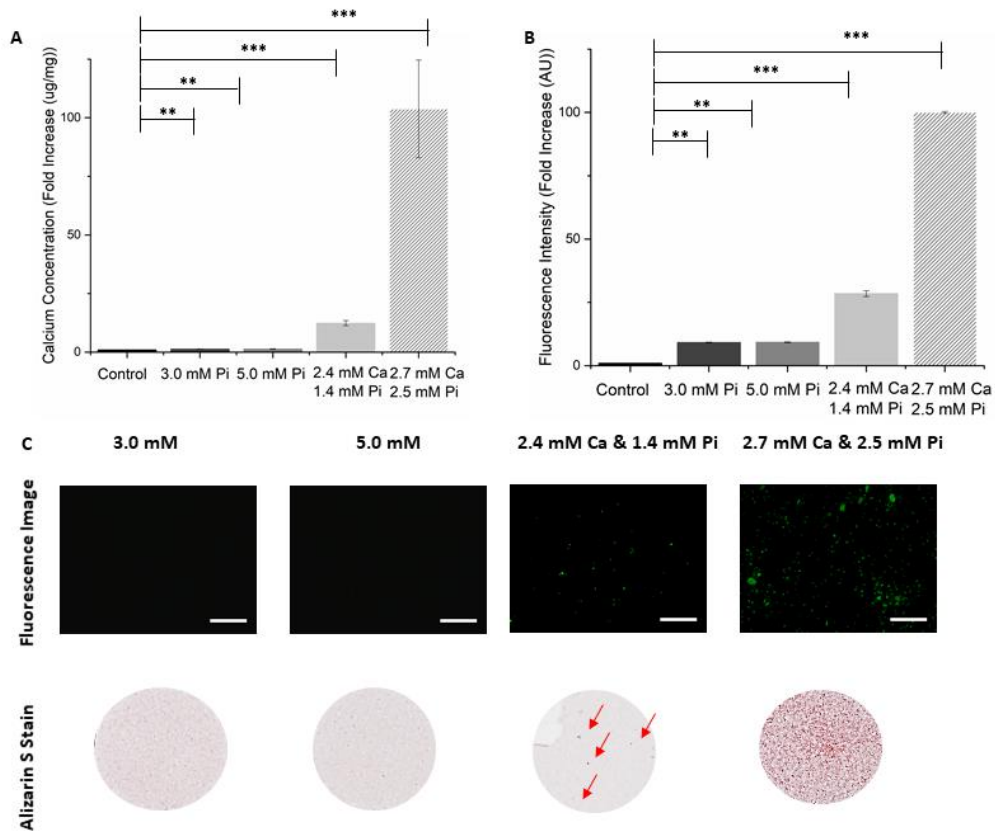


**Figure 3.13: Determination of calcification in the MOVAS cell line at various concentrations (3.0 mM  $P_i$ , 5.0 mM  $P_i$ , 2.4 mM Ca and 1.4 mM  $P_i$ , 2.7 mM Ca and 2.5 mM  $P_i$ ).** Monolayers of MOVAS-1 cells were grown to confluence (day 0) and then switched to calcification media. The monolayers were incubated in calcification media (3.0 mM  $P_i$ , 5.0 mM  $P_i$ , 2.4 mM Ca and 1.4 mM  $P_i$ , 2.7 mM Ca and 2.5 mM  $P_i$ ) for 7 days, changing media on alternate days. **(A)** Calcium leaching assay: *o*-cresolphthalein complexone. **(B)** Fluorescence assay: cell monolayers were incubated with Fluorescein-BP (1  $\mu$ M, 2 hours); NBF (10%, 15 minutes). **(C)** Fluorescence images and Alizarin S stain images: cell monolayers were either: incubated with Fluorescein-BP (1  $\mu$ M, 2 hours) and then fixed with NBF (10%, 15 minutes), or fixed with NBF (10%, 15 minutes) and then incubated with Alizarin S (2%, 500  $\mu$ L, 10 minutes). Data shown in **(A)** and **(B)** are from at least 6 repeats and shown as the mean  $\pm$  S.E.M., \*  $P < 0.05$ , \*\*  $P < 0.01$ , \*\*\*  $P < 0.001$  compared to control. Images shown in **(C)** are representative of at least 3 independent experiments yielding comparable results. Arrows indicate the location of calcium deposits within the well. Scale bars = 250  $\mu$ m.

In further experiments, MOVAS-1 cells (Figure 3.14) were incubated under the standard vascular calcification conditions (2.4 mM Ca and 1.4 mM  $P_i$ ) and the calcification on days 3, 5 and 7 was detected using Fluorescein-BP probe (55) (2.5-fold,  $p < 0.001$ ). These results were then compared with calcium leaching assay (5-fold,  $p < 0.001$ ) and staining by Alizarin S. Again in this instance, the fluorescent probe was shown to be more sensitive than both the other assays.

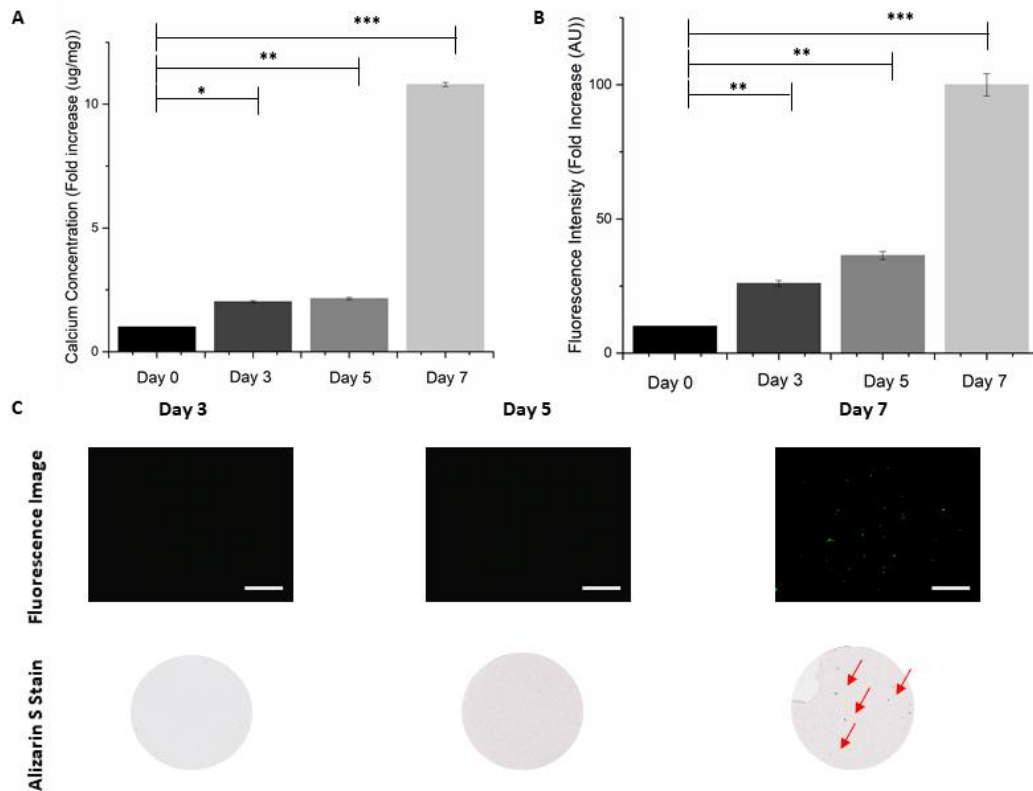


**Figure 3.14: Determination of calcification in the MOVAS-1 cell line at various days incubation (3, 5 and 7).** A monolayer of MOVAS-1 cells was grown to confluence (day 0) and then switched to calcification media (2.4 mM Ca and 1.4 mM  $P_i$ ) for 3, 5, or 7 days, changing media on alternate days. (A) Calcium leaching: *o*-cresolphthalein complexone. (B) Fluorescence assay; the cell monolayer was incubated with Fluorescein-BP (1  $\mu$ M, 2 hours); NBF (10%, 15 minutes). (C) Fluorescence images and Alizarin S stain images: cell monolayers were either: incubated with Fluorescein-BP (1  $\mu$ M, 2 hours) and then fixed with NBF (10%, 15 minutes), or fixed with NBF (10%, 15 minutes) and then incubated with Alizarin S (2%, 500  $\mu$ L, 10 minutes). Data shown in (A) and (B) are from at least 6 repeats and shown as the mean  $\pm$  S.E.M., \*  $P < 0.05$ , \*\*  $P < 0.01$ , \*\*\*  $P < 0.001$  compared to day 0 (control). Images shown in (C) are representative of at least 3 independent experiments yielding comparable results. Scale bars = 250  $\mu$ m.

### 3.6.2 VSMCs

When equivalent studies were completed using primary mouse VSMCs (Figure 3.15) where the monolayers were incubated with increasing levels of phosphate to induce calcification (1.8 mM  $P_i$ , 2.6 mM  $P_i$  and 3 mM  $P_i$ ), the fluorescent probe (5-fold,  $p < 0.001$ ) was once more shown to be more sensitive than both the Alizarin S or calcium leaching assays (1.2-fold,  $p < 0.001$ ).



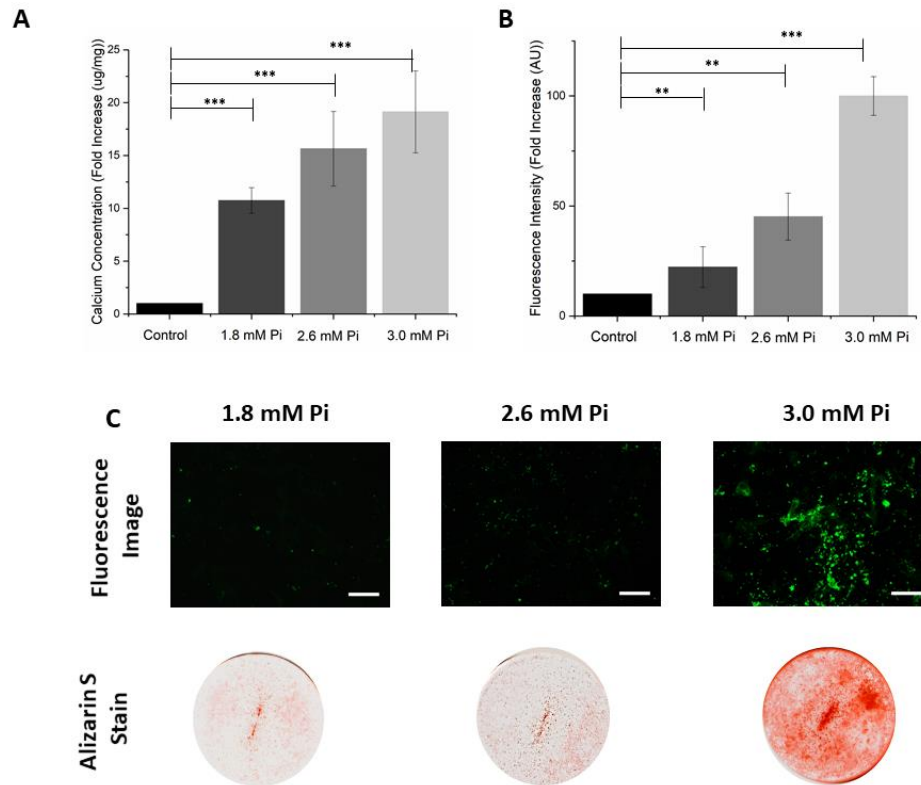


**Figure 3.15: Determination of calcification in primary mouse VSMCs at various concentrations (1.8 mM Pi, 2.6 mM Pi, 3.0 mM Pi).** Monolayers of primary mouse VSMCs were grown to confluence (day 0) and then switched to calcification media. The monolayers were incubated in calcification media (1.8 mM Pi, 2.6 mM Pi, 3.0 mM Pi) for 7 days, changing media on alternate days. (A) Calcium leaching assay: *o*-cresolphthalein complexone. (B) Fluorescence assay: cell monolayers were incubated with Fluorescein-BP (1  $\mu$ M, 2 hours); NBF (10%, 15 minutes). (C) Fluorescence images and Alizarin S stain images: cell monolayers were either incubated with Fluorescein-BP (1  $\mu$ M, 2 hours) and then fixed with NBF (10%, 15 minutes) or fixed with NBF (10%, 15 minutes) and then incubated with Alizarin S (2%, 500  $\mu$ L, 10 minutes). Data shown in (A) and (B) are from at least 6 repeats and shown as the mean  $\pm$  S.E.M., \*  $P < 0.05$ , \*\*  $P < 0.01$ , \*\*\*  $P < 0.001$  compared to control. Images shown in (C) are representative of at least 3 independent experiments yielding comparable results. \*  $P < 0.05$ , \*\*  $P < 0.01$ , \*\*\*  $P < 0.001$  compared to control,  $n = 6$ . Scale bars = 250  $\mu$ m.

Additional experiments were carried out where VSMCs were calcified for different times (Figure 3.16). VSMCs were incubated under standard calcification conditions (3.0 mM Pi)<sup>69</sup> and the calcification was detected on days 3, 5 and 7 using Fluorescein-BP (55) (2.5-fold,  $p < 0.001$ ) and compared with calcium leaching assay (2.5-fold,  $p < 0.001$ ) and staining by Alizarin S. As for the MOVAS-1 cell line, the fluorescent probe was revealed to be more sensitive than both other assays.

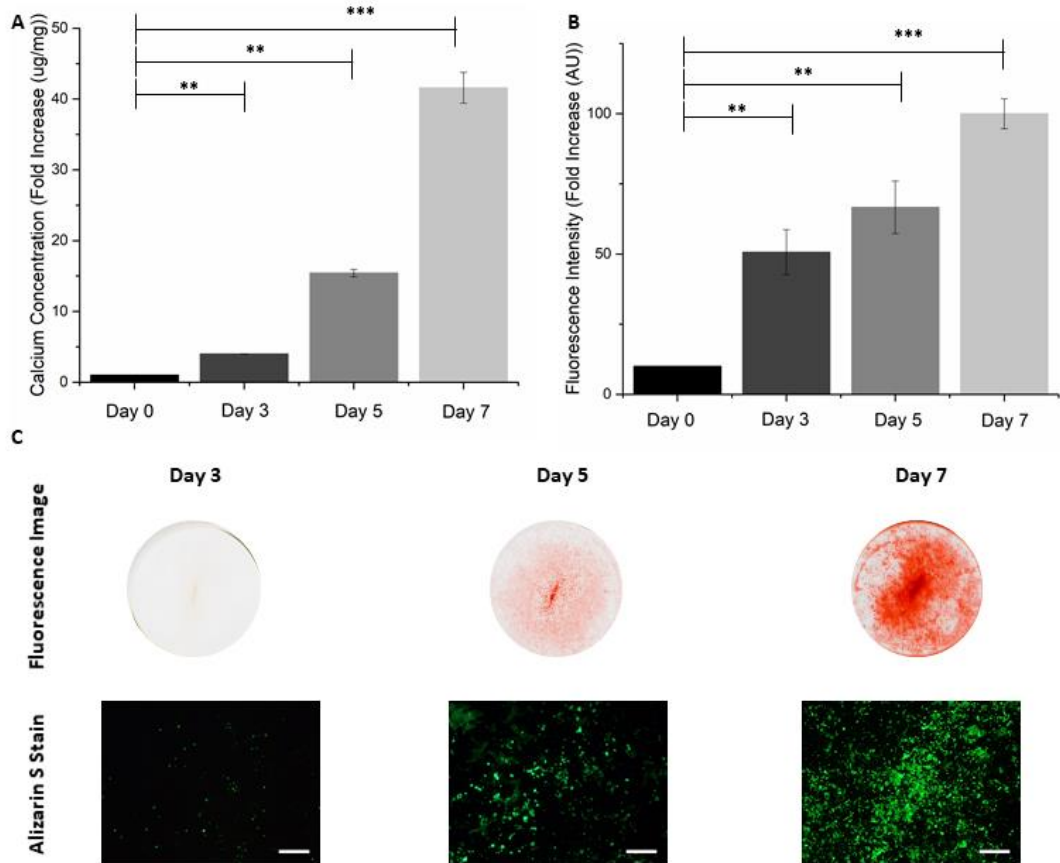


**Figure 3.16: Determination of calcification in VSMCS at various days incubation (3, 5 and 7).** A monolayer of VSMCS cells was grown to confluence (day 0) and then switched to calcification media (3.0 mM  $P_i$ ) for 3, 5, or 7 days, changing media on alternate days. (A) Calcium leaching assay: *o*-cresolphthalein complexone. (B) Fluorescence assay; the cell monolayer was incubated with Fluorescein-BP (1  $\mu$ M, 2 hours); NBF (10%, 15 minutes). (C) Fluorescence images and Alizarin S stain images: cell monolayers were either incubated with Fluorescein-BP (1  $\mu$ M, 2 hours) and then fixed with NBF (10%, 15 minutes) or fixed with NBF (10%, 15 minutes) and then incubated with Alizarin S (2%, 500  $\mu$ L, 10 minutes). Data shown in (A) and (B) are from at least 6 repeats and shown as the mean  $\pm$  S.E.M., \*  $P < 0.05$ , \*\*  $P < 0.01$ , \*\*\*  $P < 0.001$  compared to day 0 (control). Images shown in (C) are representative of at least 3 independent experiments yielding comparable results. Scale bars = 250  $\mu$ m.

### 3.6.3 MC3T3

Parallel experiments using MC3T3 cells (Figure 3.17) were performed. MC3T3 are an osteoblast derived cell line which is commonly used for studies in the field of bone and skeletal calcification.<sup>70,71</sup> Since both vascular, bone and skeletal calcification comprises of HAP deposits a comparative study between the different cell lines would allow the versatility of the probe to be determined. MC3T3 cells were incubated with Fluorescein-BP (55), and calcium

mineralisation was readily detected (2-fold,  $p < 0.001$ ). Differently from vascular calcification which occurs within 7 days, bone mineralization can take up to 21 days.

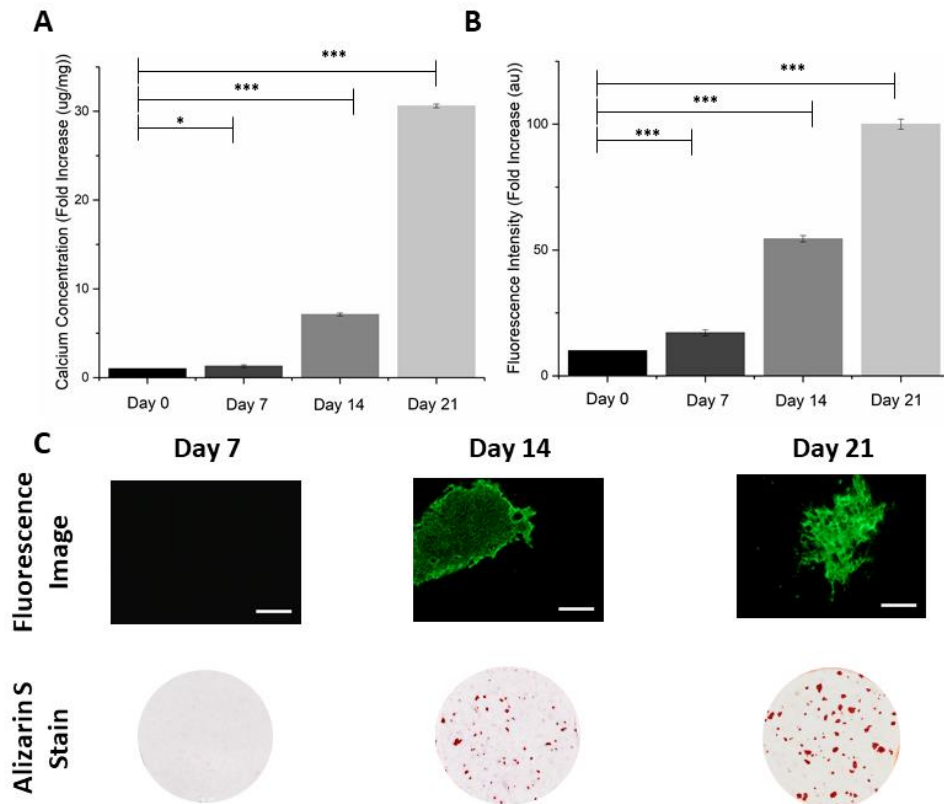


**Figure 3.17: Determination of calcification in MC3T3 at various days incubation (7, 14 and 21).** MC3T3 cells were grown to confluence (day 0) and switched to calcification media (2.5 mM  $\beta$ -GP and 50  $\mu$ g/ml AA). Cells were incubated for 7, 14, or 21 days, changing media on alternate days. (A) Calcium leaching assay: o-cresolphthalein complexone. (B) Fluorescence assay: cell monolayers were incubated with Fluorescein-BP (1  $\mu$ M, 2 hours); NBF (10%, 15 minutes). (C) Fluorescence images and Alizarin S stain images: cell monolayers were either incubated with Fluorescein-BP (1  $\mu$ M, 2 hours) and then fixed with NBF (10%, 15 minutes), or fixed with NBF (10%, 15 minutes) and then incubated with Alizarin S (2%, 500  $\mu$ L, 10 minutes). Data shown in (A) and (B) are from at least 6 repeats and shown as the mean  $\pm$  S.E.M., \*  $P < 0.05$ , \*\*  $P < 0.01$ , \*\*\*  $P < 0.001$  compared to day 0 (control). Images shown in (C) are representative of at least 3 independent experiments yielding comparable results. Scale bars = 250  $\mu$ m.

### 3.7 Aortic rings

To have a better understanding of the 3D structure of the mineral deposits in vascular tissue, *ex vivo* aortic rings from wild type (WT) rats were used. These were incubated under different calcification conditions (1.8 mM  $P_i$ , 2.6 mM  $P_i$  and 3.0 mM  $P_i$ ) for 7 days and subsequently incubated with Fluorescein-BP (55) followed by Alizarin S (Figure 3.18). From both staining methods, it is apparent that with increasing calcification conditions there is an increase in

signal in both the Alizarin S and Fluorescein channel. When the two channels are merged, it is clear that the Alizarin S and Fluorescein-BP (**55**) stains co-localize in most areas. However, the Alizarin S stain appears more intense at the edges of the sections in comparison to the Fluorescein-BP (**55**) probe suggesting a different calcium mineral content at the edges. This is perhaps not surprising as *in vitro* experiments show that a supersaturated solution of calcium phosphate initially forms a precipitate of amorphous calcium phosphate (ACP) which is then converted into the thermodynamically more stable crystalline form, HAP; a process which is also known to take place in biological calcification.<sup>72</sup> These different staining patterns might thus reflect the relative stages of mineralisation in the sections, with the most recently deposited calcium phosphate appearing at the edges in contact with the phosphate-enriched calcification media.

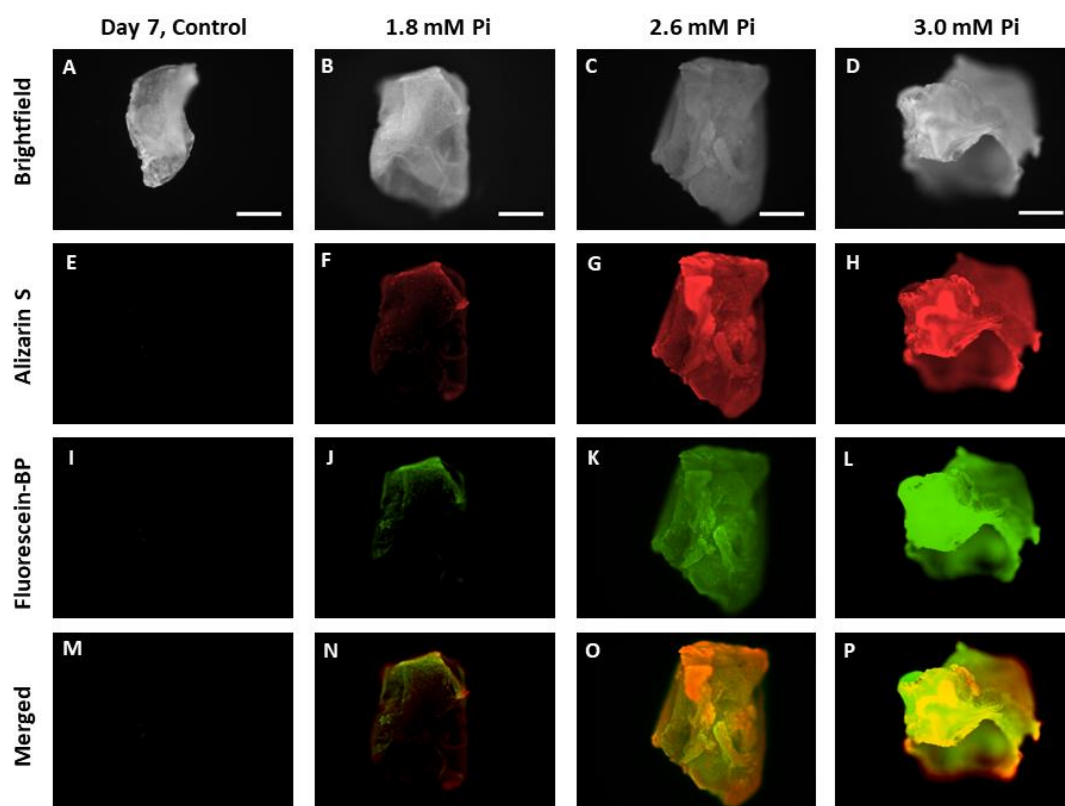


**Figure 3.18:** Determination of calcification in rat aorta incubated under different calcification conditions (1.8 mM  $P_i$ , 2.6 mM  $P_i$  and 3.0 mM  $P_i$ ). Rat aortic rings were incubated for 2 days in fresh control media followed by calcification media (1.8 mM  $P_i$ , 2.6 mM  $P_i$  and 3.0 mM  $P_i$ ) for 7 days. The rings were subsequently incubated with Fluorescein-BP (1  $\mu$ M, 2 hours), fixed with NBF (10%, 15 minutes), permeabilised in KOH (1%, 1 hour) and then incubated with Alizarin S (0.00005% Alizarin S in 1% KOH, 24 hours). Brightfield (A, B, C, D), Fluorescence (I, J, K, L), Alizarin S (E, F, G, H). Merged images (M, N, O, P) recorded using both Alizarin S and Fluorescein-BP channels. Images shown are representative of at least 3 independent experiments yielding comparable results. Scale bars = 250  $\mu$ m. Fluorescein-BP  $\lambda_{ex/em}$  = 491/515 nm; Alizarin S  $\lambda_{ex/em}$  = 530/560 nm.

A series of control experiments (*Figure 3.19*) to confirm that: no autofluorescence was present on the tissue samples that were not incubated with either Fluorescein-BP (**55**) (*Figure 3.19; B, F, J, N*) or Alizarin S stain (*Figure 3.19; C, G, K, O*) and that no Fluorescein-BP (**55**) or Alizarin S staining was bleeding into the other channel (*Figure 3.19*). Imaging aortic rings which were not stained didn't show any background autofluorescence in either channel suggesting that the fluorescence signal we obtain when the aortic rings are stained are due to the dye and only to the dye which emits in that specific channel.

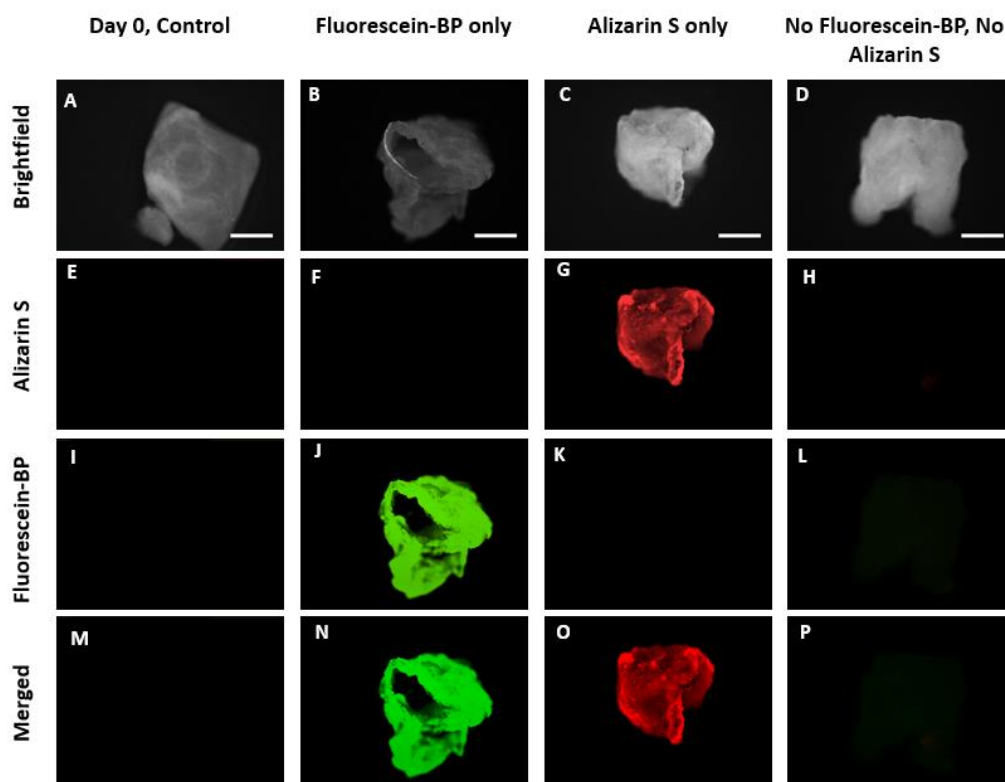


**Figure 3.19: Ex-vivo aorta sections controls.** Rat aortic rings were incubated for 2 days in fresh control media followed by calcification media (3.0 mM  $P_i$ ) for 7 days. The rings were subsequently incubated with either Fluorescein-BP (1  $\mu$ M, 2 hours) and then fixed with NBF (10%, 15 minutes) or fixed with NBF (10%, 15 minutes), permeabilised in KOH (1%, 1 hour) and then incubated with Alizarin S (0.00005% Alizarin S in 1% KOH, 24 hours). Brightfield (A, B, C, D), Fluorescence (I, J, K, L), Alizarin S (E, F, G, H). Merged images (M, N, O, P) recorded using both Alizarin S and Fluorescein-BP channels. Data shown are representative of at least 3 independent experiments yielding comparable results. Scale bars = 250  $\mu$ m.

Next, a more detailed analysis of the calcification in the aortic rings as well as their location was conducted using 5  $\mu$ m sections (*Figure 3.20*). Calcified aortic rings, which were derived from eight week old male Fischer rats, were fixed and cryosectioned on day 7. The sections were then incubated with Fluorescein-BP (**55**) followed by Alizarin S. Fluorescent imaging confirmed differences in calcification between the control and 3 mM  $P_i$  specimens.

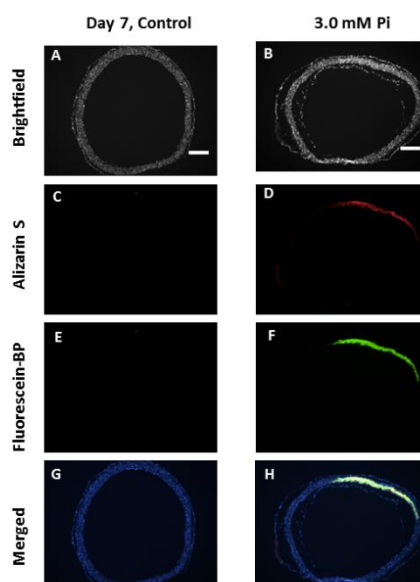


**Figure 3.20: Determination of calcification in rat aortic ring sections.** Rat aortic rings were incubated for 2 days in fresh control media followed by calcification media (3.0 mM  $P_i$ ) for 7 days and fixed with NBF (10%, 15 minutes). Rings were cryosectioned into 5  $\mu$ m sections. Sections were incubated with Fluorescein-BP (1  $\mu$ M, 2 hours), permeabilised in KOH (1%, 1 hour), incubated with Alizarin S (0.00005% Alizarin S in 1% KOH, 24 hours), followed by DAPI (500 nM, 5 minutes). Brightfield (A, B), Fluorescence (E, F), Alizarin S (C, D). Merged images (G, H) recorded using Alizarin S, Fluorescein-BP and DAPI channels. Images shown are representative of at least 3 independent experiments yielding comparable results. Scale bar = 250  $\mu$ m.

It is clear from the sections in Figure 3.20 that the calcification is present in the medial layer of the aorta. The Fluorescein-BP (55) probe appears to have a stronger signal in comparison to the Alizarin S as well as being more defined. This also allows the location of the calcification to be determined; which in this rat model occurs as in the medial layer of the aorta. To confirm the location of calcification within the ring sections,  $\alpha$ -smooth muscle actin (SMA) immunofluorescence (IF) staining was performed.  $\alpha$ -SMA is a stain for smooth muscle cells restricted to the vascular system.<sup>73,74</sup> The calcified aortic ring sections were stained with both  $\alpha$ -SMA and DAPI and when the two images were compared, Figure 3.21 A and B, is evident that the Fluorescein-BP is localised in areas which have a large concentration of  $\alpha$ -SMA.

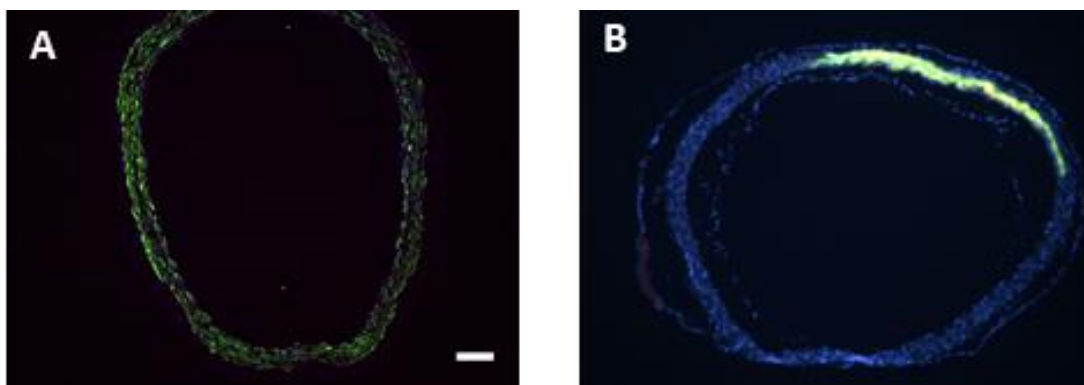


**Figure 3.21: IF of calcified aortic rings with  $\alpha$ -SMA (A) and Fluorescein-BP (B).** Rings were incubated for 2 days in fresh control media followed by calcification media 3 mM  $P_i$  for 7 days and fixed with NBF (10%, 15 minutes). Rings were cryosectioned into 5  $\mu$ m sections.  $\alpha$ -SMA IF (A): Sections were incubated with  $\alpha$ -SMA (1:100, 24 hours) followed by Alexa Fluor® 496 (1:250, 1 hour). Sections were washed and then stained with DAPI (500 nM, 5 minutes). Fluorescein-BP fluorescence (B): Sections were incubated with Fluorescein-BP (1  $\mu$ M, 2 hours) followed by DAPI (500 nM, 5 minutes). Data shown are representative of at least 3 independent experiments yielding comparable results. Scale bars = 100  $\mu$ m.

### 3.8 ApoE<sup>-/-</sup> mice

As mentioned in section 3.3.3 another method for studying disease progression is to use models obtained from genetically modified mice. ApoE<sup>-/-</sup> mice which were obtained from a collaboration with Dr P. Hadoke (University of Edinburgh); mice were fed a high fat diet until 22 weeks of age whereupon they were culled, and the aortae dissected. Dr Junxi Wu from the Hadoke group performed the von Kossa staining and the OPT imaging.

Serial sections of ApoE<sup>-/-</sup> mice were stained with both von Kossa and Fluorescein-BP (55) (Figure 3.22). Von Kossa staining showed calcification in sections 50, 60 and 70 with no sign of calcification in sections 30, 40 and 80. When fluorescence imaging was carried out on the subsequent sections (31, 41, 51, 61, 71 and 81) a similar staining pattern was observed in sections 51, 61 and 71 while sections 41 and 81 showed additional staining, <50  $\mu$ m, at much lower levels which were not detected when stained with von Kossa.

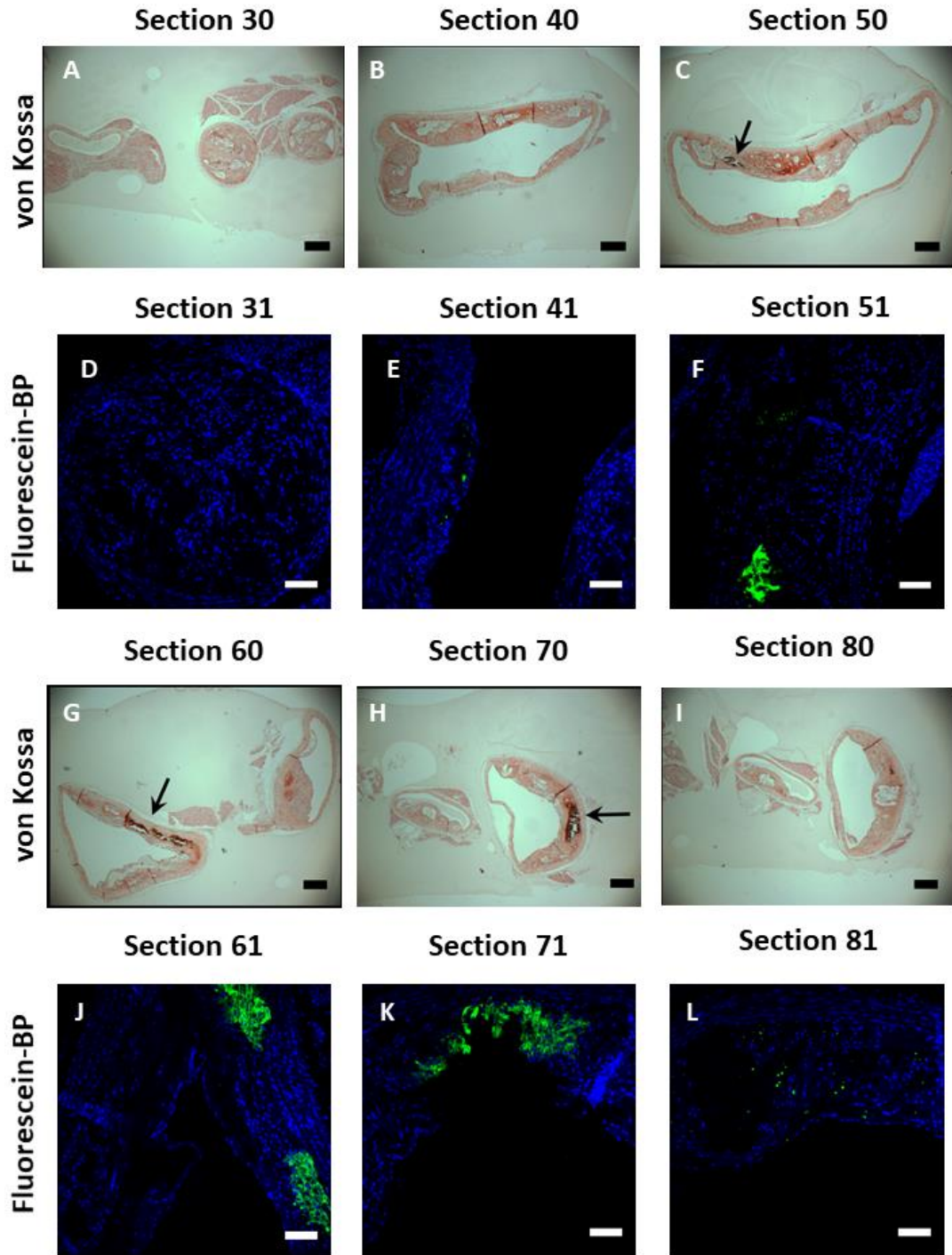


**Figure 3.22:** Von Kossa (A-C and G-I) and fluorescence (D-F and J-L) imaging of aortic sections of a 22 week old *ApoE*<sup>-/-</sup> mice fed a high fat diet. Sequential sections were stained with either von Kossa (silver nitrate, 20 minutes; 5% sodium thiosulfate, 5 minutes; 0.1% neutral red 2 minutes) or Fluorescein-BP (1  $\mu$ M, 2 hours) and DAPI (500 nM, 5 minutes). Scale bars = 0.1 cm for von Kossa and 100  $\mu$ m for fluorescence. Von Kossa staining and images were performed by Dr Junxi Wu.



It appears that the von Kossa stain although able to detect macrocalcific lesions, is not likely to detect smaller micro-calcification deposits. On the other hand, the Fluorescein-BP (**55**) probe is more sensitive, as also shown in the previous experiments, and was able to detect both macro-calcification and micro-calcification.

A second study conducted with *ApoE*<sup>-/-</sup> mice involved optical projection tomography (OPT) of whole aorta. OPT is a technique that images biological samples in 3D and provides similar information to standard confocal microscopy techniques without the need for taking physical sections from the sample. The specimen is rotated and optical images are captured.<sup>75,76</sup> Different excitation wavelengths can be chosen when using fluorescent probes but anatomical information can also be obtained by imaging the tissue autofluorescence. The *ApoE*<sup>-/-</sup> aorta were incubated with Fluorescein-BP (**55**) and then embedded in low melting point agarose for OPT imaging. Tissue was excited at both 475 nm and 425 nm to visualise probe localization and tissue autofluorescence, specifically elastin, respectively (*Figure 3.23*). Sections of the whole aorta were also obtained from the OPT imaging where signal from the Fluorescein-BP (**55**) (*Figure 3.23 A*) and the tissue autofluorescence (*Figure 3.23 B*) were merged.

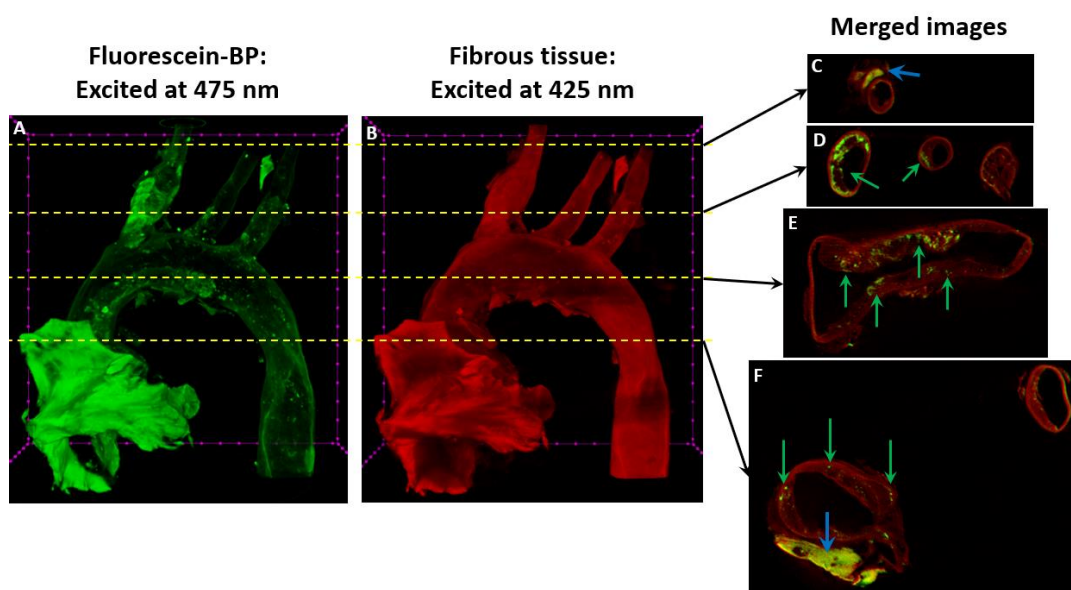


**Figure 3.23:** OPT of whole *ApoE*<sup>-/-</sup> mice aorta. Aortae was incubated with Fluorescein-BP (**55**) (1  $\mu$ M, 24 hours) followed by embedding in low melting agarose, dehydrated (100% EtOH, 3 times) and cleared (BABB, 48 hours). Green arrows indicate intraplaque calcification while blue arrow indicates tissue autofluorescence. (A) and (B) show whole aorta imaging at 475 nm (Fluorescein-BP) and 425 nm (autofluorescence) respectively; (C-D) cross-section of aorta at a number of different sites.

In this instance, sections provide information of the localization of the macro-calcification,  $\geq 50$   $\mu$ m, (*Figure 3.23 D*) with other areas presenting macro-calcification as well as micro-

calcification deposits (Figure 3.23 E) and other locations in the aortae that only show smaller micro-calcification deposits (Figure 3.23 F) which would have perhaps not been identified by conventional Alizarin S and von Kossa staining.

### 3.9 Conclusion

Fluorescein-BP (**55**) gives a dramatically enhanced signal output over more conservative imaging methods such as Alizarin S and von Kossa stains for the detection of calcium phosphate in a range of *in vitro* studies. It has been shown to be non-toxic and low  $\mu\text{M}$  concentrations has been used in both condition-specific and temporal studies of calcification in cell-based models of CVD and bone disease. In contrast to the calcium leaching assay which is not suitable for high-throughput applications, Fluorescein-BP (**55**) can be applied to experiment carried out in a 96-384 well plate which would allow for high-throughput multi-well analysis of calcification. When applied to *ex vivo* WT aortic sections and *ApoE*<sup>-/-</sup> sections, Fluorescein-BP (**55**) shows binding to intraplaque calcification. In *ApoE*<sup>-/-</sup> tissue, two different scales of calcium-based deposits are visible which suggest that the Fluorescein-BP (**55**) probe can detect both macro- and micro-calcification. When compared with von Kossa staining of comparable sections, the latter is unable to detect the microcalcification suggesting that Fluorescein-BP (**55**) can be used as a method for the detection of calcification in animal models and has the potential to translate into human models. Furthermore, the employment of this probe may enable the elucidation of key mechanisms underpinning these pathological processes involved in CVD.

### 3.10 References

- 1 M. J. Berridge, P. Lipp and M. D. Bootman, *Nat. Rev. Mol. Cell Biol.*, 2000, **1**, 11–21.
- 2 R. Nair, S. Raina, T. Keshavarz and M. J. P. Kerrigan, *Fungal Biol.*, 2011, **115**, 326–334.
- 3 G. Nelson, O. Kozlova-Zwinderman, A. J. Collis, M. R. Knight, J. R. S. Fincham, C. P. Stanger, A. Renwick, J. G. M. Hessing, P. J. Punt, C. A. M. J. J. Van Den Hondel and N. D. Read, *Mol. Microbiol.*, 2004, **52**, 1437–1450.
- 4 M. J. P. Kerrigan and A. C. Hall, *Osteoarthr. Cartil.*, 2008, **16**, 312–322.
- 5 E. A. Permyakov and R. H. Kretsinger, *J. Inorg. Biochem.*, 2009, **103**, 77–86.
- 6 A. F. Dulhunty, *Clin. Exp. Pharmacol. Physiol.*, 2006, **33**, 763–772.

- 7 K. P. Lu and A. R. Means, *Endocr. Rev.*, 1993, **14**, 40–58.
- 8 S. Orrenius, B. Zhivotovsky and P. Nicotera, *Nat. Rev. Mol. Cell Biol.*, 2003, **4**, 552–565.
- 9 C. Grienberger and A. Konnerth, *Neuron*, 2012, **73**, 862–885.
- 10 L. B. Bailey and J. F. Gregory, *J. Nutr.*, 1999, **129**, 779–782.
- 11 I. Bezprozvanny, *Trends Mol. Med.*, 2009, **15**, 89–100.
- 12 F. T. Chebib, C. R. Sussman, X. Wang, P. C. Harris and V. E. Torres, *Nat. Rev. Nephrol.*, 2015, **11**, 451–464.
- 13 S. M. Moe, *Prim. Care*, 2008, **35**, 215–37, v–vi.
- 14 G. H. Wilson, J. C. Gore, T. E. Yankeelov, S. Barnes, T. E. Peterson, J. M. True, S. Shokouhi, J. O. McIntyre, M. Sanders, V. Abramson, T.-Q. Ngyuen, A. Mahadevan-Jansen, M. N. Tantawy and M. N. Tantawy, *J. Nucl. Med.*, 2014, **55**, 1138–43.
- 15 J. E. Gonzalez, R. G. Caldwell and J. Valaitis, *Am. J. Surg. Pathol.*, 1991, **15**, 586–91.
- 16 R. F. Cox, A. Hernandez-Santana, S. Ramdass, G. McMahon, J. H. Harmey and M. P. Morgan, *Br. J. Cancer*, 2012, **106**, 525–537.
- 17 R. D. Motrich, G. M. Castro, B. L. Caputto, H. Ferreyra, B. L. Caputto, O. A. Pucci, G. A. Gil, J. Bruha, O. Vycital and J. Finek, *PLoS One*, 2013, **8**, e53211.
- 18 R. F. Cox, A. Jenkinson, K. Pohl, F. J. O’Brien and M. P. Morgan, *PLoS One*, 2012, **7**, e41679.
- 19 A. Zaheer, M. Murshed, A. M. De Grand, T. G. Morgan, G. Karsenty and J. V. Frangioni, *Arterioscler. Thromb. Vasc. Biol.*, 2006, **26**, 1132–1136.
- 20 J. S. Lee, J. D. Morrisett and C.-H. Tung, *Atherosclerosis*, 2012, **224**, 340–7.
- 21 J. D. Hutcheson, N. Maldonado and E. Aikawa, *Curr. Opin. Lipidol.*, 2014, **25**, 327–32.
- 22 M. Sakaguchi, T. Hasegawa, S. Ehara, K. Matsumoto, K. Mizutani, T. Iguchi, H. Ishii, M. Nakagawa, K. Shimada and M. Yoshiyama, *Heart Vessels*, 2016, **31**, 1915–1922.
- 23 F. Otsuka, K. Sakakura, K. Yahagi, M. Joner and R. Virmani, *Arterioscler. Thromb. Vasc. Biol.*, 2014, **34**, 724–736.

- 24 B. Wu, X. Pei and Z.-Y. Li, *ScientificWorldJournal.*, 2014, **2014**, 417324.
- 25 A. Irkle, A. T. Vesey, D. Y. Lewis, J. N. Skepper, J. L. E. Bird, M. R. Dweck, F. R. Joshi, F. A. Gallagher, E. A. Warburton, M. R. Bennett, K. M. Brindle, D. E. Newby, J. H. Rudd and A. P. Davenport, *Nat. Commun.*, 2015, **6**, 7495.
- 26 J. Rungby, M. Kassem, E. F. Eriksen and G. Danscher, *Histochem. J.*, 1993, **25**, 446–451.
- 27 H. Paul, A. J. Reginato and H. R. Schumacher, *Arthritis Rheum.*, 1983, **26**, 191–200.
- 28 H. M. Myers, *Am. J. Phys. Anthropol.*, 1968, **29**, 179–182.
- 29 A. Bensimon-Brito, J. Cardeira, G. Dionísio, A. Huysseune, M. L. Cancela and P. E. Witten, *BMC Dev. Biol.*, 2016, **16**, 2.
- 30 D. Rigueur and K. M. Lyons, *Methods Mol. Biol.*, 2014, **1130**, 113–121.
- 31 C. A. Gregory, W. G. Gunn, A. Peister and D. J. Prockop, *Anal. Biochem.*, 2004, **329**, 77–84.
- 32 H. Puchtler, S. N. Meloan and M. S. Terry, *J. Histochem. Cytochem.*, 1969, **17**, 110–124.
- 33 L. F. Bonewald, S. E. Harris, J. Rosser, M. R. Dallas, S. L. Dallas, N. P. Camacho, B. Boyan and A. Boskey, in *Calcified Tissue International*, Springer-Verlag, 2003, vol. 72, pp. 537–547.
- 34 H. Puchtler and S. N. Meloan, *Histochemistry*, 1978, **56**, 177–185.
- 35 E. Aikawa, M. Nahrendorf, J. L. Figueiredo, F. K. Swirski, T. Shtatland, R. H. Kohler, F. A. Jaffer, M. Aikawa and R. Weissleder, *Circulation*, 2007, **116**, 2841–2850.
- 36 L. M. Schäck, S. Noack, R. Winkler, G. Wißmann, P. Behrens, M. Wellmann, M. Jagodzinski, C. Krettek and A. Hoffmann, *PLoS One*, 2013, **8**, e65943.
- 37 L. V Hale, Y. F. Ma and R. F. Santerre, *Calcif. Tissue Int.*, 2000, **67**, 80–4.
- 38 L. Cui, N. A. Rashdan, D. Zhu, E. M. Milne, P. Ajuh, G. Milne, M. H. Helfrich, K. Lim, S. Prasad, D. A. Lerman, A. T. Vesey, M. R. Dweck, W. S. Jenkins, D. E. Newby, C. Farquharson and V. E. Macrae, *J. Cell. Physiol.*, 2017, **232**, 2985–2995.
- 39 C. Huesa, K. A. Staines, J. L. Millan and V. E. MacRae, *Int J Mol Med*, 2015, **36**, 159–165.

- 40 N. C. W. Mackenzie, C. Huesa, F. Rutsch and V. E. MacRae, *Bone*, 2012, **51**, 961–968.
- 41 J. Stern and W. H. P. Lewis, *Clin. Chim. Acta*, 1957, **2**, 576–580.
- 42 S. Jono, Y. Nishizawa, A. Shioi and H. Morii, *Arterioscler. Thromb. Vasc. Biol.*, 1997, **17**, 1135–42.
- 43 J. Furry, 1985.
- 44 H. Diehl and J. L. Ellingboe, *Anal. Chem.*, 1956, **28**, 882.
- 45 J. R. Chen, Y. H. Lai, J. J. Tsai and C. Der Hsiao, *Molecules*, 2017, **22**, 2068.
- 46 M. Garland, J. J. Yim and M. Bogoyo, *Cell Chem. Biol.*, 2016, **23**, 122–136.
- 47 D. Vonwil, J. Christensen, S. Fischer, O. Ronneberger and V. P. Shastri, *Mol. Imaging Biol.*, 2014, **16**, 350–61.
- 48 K. M. Harmatys, E. L. Cole and B. D. Smith, *Mol. Pharm.*, 2013, **10**, 4263–71.
- 49 H. G. Tsang, N. A. Rashdan, C. B. A. Whitelaw, B. M. Corcoran, K. M. Summers and V. E. MacRae, *Cell Biochem. Funct.*, 2016, **34**, 113–132.
- 50 MacRae, *Int. J. Mol. Med.*, 2011, **27**, 663–8.
- 51 T. Afroze, L. L. Yang, C. Wang, R. Gros, W. Kalair, A. N. Hoque, I. N. Mungrue, Z. Zhu and M. Husain, *AJP Cell Physiol.*, 2003, **285**, C88–C95.
- 52 T. Akiyoshi, H. Ota, K. Iijima, B. K. Son, T. Kahyo, M. Setou, S. Ogawa, Y. Ouchi and M. Akishita, *Atherosclerosis*, 2016, **244**, 51–58.
- 53 K. A. Lomashvili, S. Cobbs, R. A. Hennigar, K. I. Hardcastle and W. C. O’Neill, *J. Am. Soc. Nephrol.*, 2004, **15**, 1392–1401.
- 54 G. S. Getz, C. A. Reardon, G. S. Getz and C. A. Reardon, *Arterioscler. Thromb. Vasc. Biol.*, 2012, **32**, 1104–1115.
- 55 G. Lo Sasso, W. K. Schlage, S. Boué, E. Veljkovic, M. C. Peitsch and J. Hoeng, *J. Transl. Med.*, 2016, **14**, 146.
- 56 S. Gargiulo, M. Gramanzini and M. Mancini, *Int. J. Mol. Sci.*, 2016, 17.
- 57 K. S. Meir and E. Leitersdorf, *Arterioscler. Thromb. Vasc. Biol.*, 2004, **24**, 1006–1014.
- 58 J. Jawien, *Curr. Pharm. Biotechnol.*, 2012, **13**, 2435–2439.

- 59 Y. T. Lee, H. Y. Lin, Y. W. F. Chan, K. H. C. Li, O. T. L. To, B. P. Yan, T. Liu, G. Li, W. T. Wong, W. Keung and G. Tse, *Lipids Health Dis.*, 2017, **16**, 12.
- 60 Y. Ma, C. C. Malbon, D. L. Williams and F. E. Thorngate, *PLoS One*, 2008, **3**, e2503.
- 61 R. Wallin, N. Wajih, G. Todd Greenwood and D. C. Sane, *Med. Res. Rev.*, 2001, **21**, 274–301.
- 62 R. Villa-Bellosta and W. C. O’Neill, *Kidney Int.*, 2018, **0**.
- 63 S. N. Rampersad, *Sensors (Switzerland)*, 2012, **12**, 12347–12360.
- 64 A. N. Kapustin, J. D. Davies, J. L. Reynolds, R. McNair, G. T. Jones, A. Sidibe, L. J. Schurgers, J. N. Skepper, D. Proudfoot, M. Mayr and C. M. Shanahan, *Circ. Res.*, 2011, **109**, e1-12.
- 65 M. Murshed and M. D. McKee, *Curr. Opin. Nephrol. Hypertens.*, 2010, **19**, 359–365.
- 66 M. Abedin, Y. Tintut and L. L. Demer, *Arterioscler. Thromb. Vasc. Biol.*, 2004, **24**, 1161–1170.
- 67 D. Zhu, N. C. W. Mackenzie, J. L. Millan, C. Farquharson and V. E. Macrae, *J. Mol. Endocrinol.*, 2014, **52**, 77–85.
- 68 L. Cui, D. A. Houston, C. Farquharson and V. E. MacRae, *Bone*, 2016, **87**, 147–158.
- 69 D. Zhu, P. W. F. Hadoke, J. Wu, A. T. Vesey, D. A. Lerman, M. R. Dweck, D. E. Newby, L. B. Smith and V. E. MacRae, *Sci. Rep.*, 2016, **6**, 24807.
- 70 Y.-K. Lee, J. Song, S.-B. Lee, K.-M. Kim, S.-H. Choi, C.-K. Kim, R. Z. LeGeros and K.-N. Kim, *J. Biomed. Mater. Res.*, 2004, **69A**, 188–195.
- 71 K. Hiura, K. Sumitani, T. Kawata, K. Higashino, M. Okawa, T. Sato, Y. Hakeda and M. Kumegawa, *Endocrinology*, 1991, **128**, 1630–1637.
- 72 S. C. Verberckmoes, V. Persy, G. J. Behets, E. Neven, A. Hufkens, H. Zebger-Gong, D. Müller, D. Haffner, U. Querfeld, S. Bohic, M. E. De Broe and P. C. D’Haese, *Kidney Int.*, 2007, **71**, 298–303.
- 73 R. I. Grant, D. A. Hartmann, R. G. Underly, A. A. Berthiaume, N. R. Bhat and A. Y. Shih, *J. Cereb. Blood Flow Metab.*, 2017.
- 74 J. Hu, C. Xie, H. Ma, B. Yang, P. X. Ma and Y. E. Chen, *PLoS One*, 2012, **7**, e35580.

- 75 S. R. Arridge, *Inverse Probl.*, 1999, 15, R41–R93.
- 76 J. Sharpe, *Rev. Lit. Arts Am.*, 2004, 6, 209–228.

# Chapter 4- Human Tissue and Potential Biomarkers for Plaque Vulnerability

## 4.1 Carotid and coronary plaques

Atherosclerotic cardiovascular disease accounts for the vast majority of deaths worldwide. Despite decades of investment in delivering effective medical therapy, the prevalence of atherosclerotic cardiovascular disease continues to increase. Carotid plaques are found in vessels in the neck that supply oxygen to the brain while coronary plaques are located on vessels on the surface of the heart that supply blood to the heart.

Even though they have different characteristics (*Table 4.1*); carotid plaques have a thicker fibrous cap, higher chance of plaque haemorrhage, lower erosion rate and higher percentage of calcified nodules, recent evidence suggests that the pathophysiology is broadly similar in the two vascular beds with similar risk factors and stages of plaque development.<sup>1-5</sup> Indeed, a strong connection between the extent of coronary atherosclerosis and the progression of carotid atherosclerosis, as well the stabilizing effect that calcium deposits have on both carotid and coronary arteries has been reported.<sup>6,7</sup>



Table 4.1: Differences between coronary and carotid artery disease.

	<b>Coronary artery disease</b>	<b>Carotid artery disease</b>
<b>Risk factors</b>	Hypertension, smoking, diabetes, hypercholesterolemia	Smoking, hypertension, hypercholesterolemia
<b>Age of formation</b>	<40 years	Men >40 years Women post-menopause
<b>Shear stress</b>	Complex effect on arteries because of anatomical differences i.e. curvature, flow	Mainly in the carotid bifurcation area
<b>Symptomatic mechanism of the disease</b>	Acute thrombosis	Acute thrombosis, stroke
<b>Severe angiographic stenosis</b>	Results in myocardial infarction	Frequently results in stroke
<b>Small plaques</b>	Often symptomatic, lipid rich	Rarely symptomatic, intimal hyperplasia
<b>Large occluding plaques</b>	Fibrotic, stable	Ulcerated, lipid rich, unstable
<b>Thrombus</b>	Main cause of occlusion	Rare cause of occlusion, usually small intramural thrombi
<b>Plaque ulceration</b>	Thrombus related, acute event	Chronic, small microemboli on the surface, rarely acute event
<b>Calcification</b>	In 5-10%	In 50-60%

## 4.2 Rodent vs human models

Animal models, especially rodents have been used to investigate the pathology of cardiovascular diseases, however, studying atherosclerosis using rodent models has several limitations. One of the most prominent restrictions is in contrast to human plaques, rodent plaques do not rupture and therefore do not reflect plaque instability very well. Another difference between human and rodent models is that differently from human, rodents receive a high cholesterol diet increasing their level of cholesterol in the serum, this is not normally seen in patients with atherosclerotic plaques.<sup>12-18</sup> Other differences arise in the immune system and gene expression where T cells and monocyte markers are fairly different between the two species.<sup>13,14,19</sup> Another major limitation is the location of the plaque within the species, in rodent models plaques occur mainly in the carotid artery and are not normally seen in the coronary arteries.<sup>12,15,20</sup> Due to these key differences between rodent and human models, it is crucial that human plaque tissue is analysed and assessed in order to understand disease progression, pathogenesis and prevention, in parallel to animal studies.

### 4.3 Early detection of calcification, PET and Fluorescein-BP

Calcification is a key feature of coronary atherosclerotic plaques and, in particular, the burden of calcification correlates with the future risk of cardiovascular events. Large population studies, such as the MESA study,<sup>8</sup> have highlighted an inverse correlation with coronary artery calcium density with low density calcium conferring the highest risk of cardiovascular events.<sup>9</sup>

As such, there is increasing interest in identifying markers of early micro-calcification that may better improve risk stratification and downstream management of patients with cardiovascular disease.<sup>10</sup> Early coronary calcification can be detected with positron emission tomography using the radiotracer Na<sup>18</sup>F.<sup>11</sup> However PET has limited spatial resolution and cannot be used in conjunction with existing invasive imaging techniques. Developing alternatives techniques to identify micro-calcification with improved spatial resolution and potential translation in to the cardiac catheterisation laboratory is an important research goal with the potential to improve cardiovascular risk prediction.

A fluorescent dye, Fluorescein-BP (**55**), has been developed to detect HAP. Both probe components, alendronate (**26**) and Fluorescein (**54**) are FDA approved and this therefore makes the Fluorescein-BP (**55**) probe particularly attractive for human translation as a method for the detection of vascular calcification.

Fluorescence spectroscopy can provide higher spatial resolution than PET and therefore is able to afford better anatomical information on the plaque and its stability. Moreover the fluorescent signal can potential be detected with modern invasive coronary catheters. Building on cell and *ex vivo* mouse models (Chapter 3) which have provided exciting and promising results, the translation of the Fluorescein-BP probe(**55**) to detect HAP in human vascular tissue is essential.

### 4.4 Selectivity of Na<sup>18</sup>F PET tracer

In Chapter 2, the ability of Fluorescein-BP (**55**) to bind to specific calcium compounds was determined. Fluorescein-BP (**55**) exhibited high specificity towards HAP in comparison to other calcium compounds (CaOx, CaPi and CaPyr) analysed as well as greater selectivity in comparison to the Alizarin S stain. The selectivity of the Na<sup>18</sup>F tracer for HAP, CaPi, CaOx and CaPyr was quantified and compared with the discrimination of Fluorescein-BP. Calcium minerals (HAP, CaOx, CaPi and CaPyr) were incubated in Na<sup>18</sup>F for 20 minutes after which unbound tracer was removed by a series of centrifugation steps and the solid particles were subsequently imaged using PET/CT. Similarly to Fluorescein-BP (**55**), Na<sup>18</sup>F shows no

selectivity towards CaOx and CaPyr, however it was found to bind to both HAP and CaPi nonetheless showing stronger affinity for HAP (Figure 4.1). These results show the benefit of imaging with a probe such as Fluorescein-BP (55) due to its high affinity for HAP in comparison to other minerals which compares favourably with current methods of staining (Alizarin S and von Kossa) and imaging (PET).

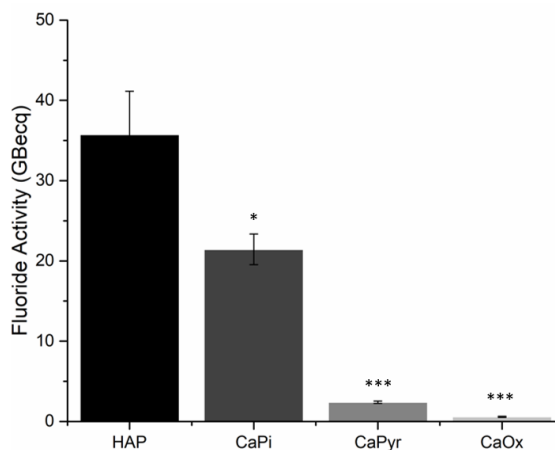


**Figure 4.1: Selectivity of  $^{18}\text{F}$ -NaF PET tracer towards calcium minerals.** Calcium minerals were incubated with  $^{18}\text{F}$ -NaF for 20 minutes after which un-bound tracer was removed and the solid particles were analysed by PET/CT. Data shown is from at least 3 repeats and shown as the mean  $\pm$  S.E.M. \*  $p < 0.05$ , \*\*  $p < 0.01$ , \*\*\*  $p < 0.001$  compared to HAP.

#### 4.5 PET/CT and Fluorescein-BP imaging of *ex vivo* coronary plaques

We next compared Fluorescein-BP (55) binding to the detection of vascular calcification on computed tomography and  $\text{Na}^{18}\text{F}$  PET in 8 samples of human coronary tissues (7 affected by calcific atherosclerotic disease and 1 control tissue which was free of atherosclerosis). All tissue samples were initially assessed using PET/CT scans followed by sectioning of the tissue as required to allow appropriate fluorescence images to be obtained. A representative sample is shown in Figure 4.2. PET/CT imaging showed both areas of macro-calcification, as detected by CT (Figure 4.2 B), and areas of micro-calcification, as detected by  $\text{Na}^{18}\text{F}$  PET (Figure 4.2 C). Samples from both areas were sectioned and stained (Figure 4.2 D-K). The images show that Fluorescein-BP probe (55) was able to bind to both macro- and micro-calcification and co-localizes with Alizarin S staining (Figure 4.2 E and I).

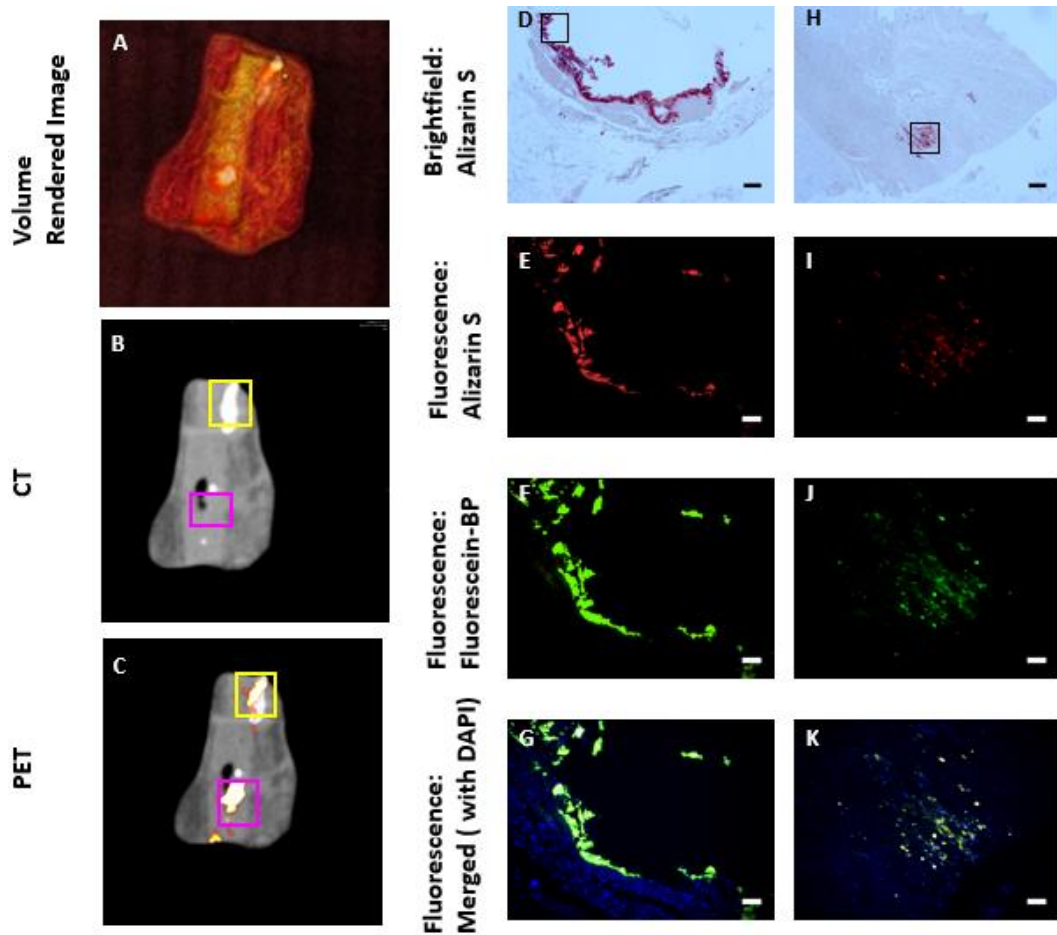


**Figure 4.2: Imaging of calcified coronary tissue.** (A) Volume rendered image; (B) CT image; (C) PET image, with  $\text{Na}^{18}\text{F}$  tracer, of vascular tissue. Yellow and purple boxes indicate the areas selected for tissue sectioning where brightfield and fluorescence images of calcification were taken. (D, E, F, G) Brightfield and fluorescence (Alizarin S, Fluorescein-BP, DAPI) images of tissue in area in the yellow box presenting area of high CT activity. (H, I, J, K) Brightfield and Fluorescence (Alizarin S, Fluorescein-BP, DAPI) images of tissue in area in the purple box presenting area of high PET activity. Sections were incubated with Fluorescein-BP (1  $\mu\text{M}$ , 2 hours), Alizarin S (2%, 10 minutes) and DAPI (500 nM, 5 minutes) and subsequently imaged. Scale bars = 0.2 cm for brightfield and 100  $\mu\text{m}$  for fluorescence.

The control tissue sample (Figure 4.3), where there was no evidence of atheroma, displaced neither increased PET/CT activity (Figure 4.3 B) signal nor fluorescence staining (Figure 4.3 C-F).

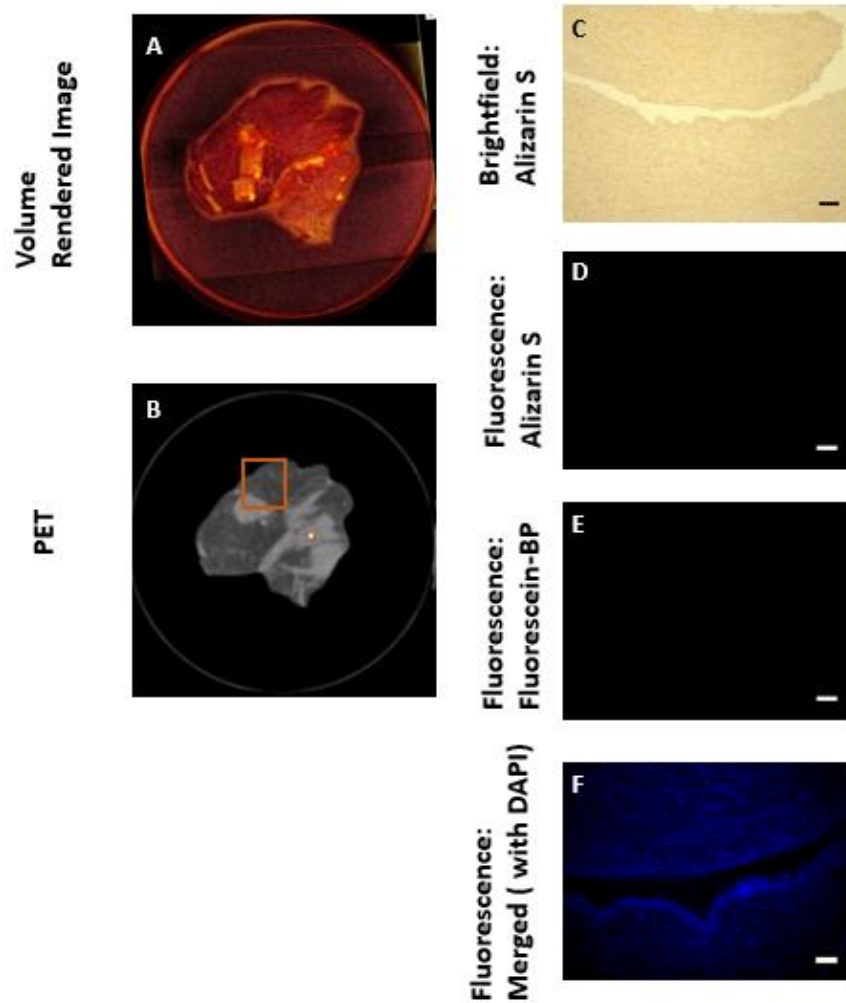


**Figure 4.3: Imaging of coronary tissue without atheromatous plaque.** (A) Volume rendered image; (B) PET image, with  $\text{Na}^{18}\text{F}$  tracer, of vascular tissue. Orange box indicates the area selected for tissue sectioning where Brightfield and Fluorescence images of calcification were taken. (C, D, E, F). Sections were incubated with Fluorescein-BP (1  $\mu\text{M}$ , 2 hours), Alizarin S (2%, 10 minutes) and DAPI (500 nM, 5 minutes) and subsequently imaged. Scale bars = 0.2 cm for brightfield and 100  $\mu\text{m}$  for fluorescence.

#### 4.6 Fluorescein-BP imaging of *ex vivo* carotid plaques

Fluorescein-BP (55) imaging studies were repeated with *ex vivo* carotid plaque tissues from patients that were admitted for a carotid endarterectomy following a recent stroke or transient ischaemic attack. The samples were embedded, sectioned and stained using both Alizarin S and Fluorescein-BP (55). A representative sample was selected and stained using both Alizarin S (Figure 4.4 A and C) and Fluorescein-BP (55) (Figure 4.4 B and D). These results once more show the ability of Fluorescein-BP (55) to stain areas of plaque calcification that co-localised with the Alizarin S stain. Indeed Fluorescein-BP staining was observed in both areas

of macro- (Figure 4.4 A and B), and micro-calcification (Figure 4.4 C and D) confirming the observations in the rodent models reported in Chapter 3 and in the coronary samples.

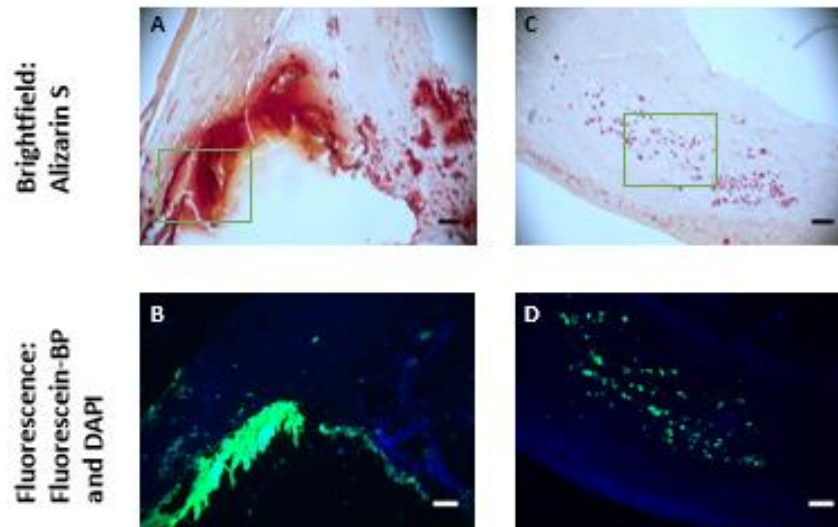


**Figure 4.4: Determination of calcification in human carotid tissue.** (A, C) Alizarin S staining of carotid tissue. Green boxes indicate the areas where Fluorescence images of calcification were taken. (B, D) Fluorescence (Fluorescein-BP, DAPI) images of tissue. Sections were incubated with Fluorescein-BP (1  $\mu$ M, 2 hours) and DAPI (500 nM, 5 minutes) and subsequently imaged. Scale bars = 0.2 cm for brightfield and 100  $\mu$ m for fluorescence.

The coronary and carotid samples provide sections with both macro and micro calcification, in stable and unstable plaques, all of which can be detected using Fluorescein-BP (55) showing the reproducibility of the probe on different types of calcified samples. Another advantage of the Fluorescein-BP (55) probe is the lack of background staining which could lead to false positives. By contrast the control sample which was free from atheromatous plaque and calcification did not demonstrate any staining while areas with micro and macro deposits fluoresced. Although this might be the case when using Alizarin S on sections that are highly calcified, when staining sections with micro-calcification, often the stain appears very weak and not visible under the microscope.

#### 4.7 Comparison of PET and Alizarin S with the upregulation of osteogenic markers

Recently, Osteopontin (OPG) and Osteoprotegerin (OPN) have been reported to detect early stage calcification in blood plasma. OPN and OPG (Figure 4.5) are two of the many bone regulatory proteins that have been shown to be present in atherosclerotic plaques *in vitro* and seem to be expressed by vascular cells *in vivo*.<sup>21-23</sup>

OPG is a cytokine of the tumour necrosis factor receptor and acts as an inhibitor of the RANKL-RANK interaction.<sup>22,24,25</sup> By doing so it prevents the proliferation and differentiation of osteoclast and leads to bone resorption.<sup>22,24,26-28</sup> OPG deletion results in a significant increase in aortic medial calcification which suggests the protective role of OPG against atherosclerotic calcification.<sup>25,27,29</sup> Recent studies showed that plasma levels of OPG were increasingly high in patients with acute coronary syndrome in comparison to those with stable angina or normal arteries; as a result, OPG may be a marker of onset atherosclerosis and plaque stability.<sup>22,24,26,27</sup>

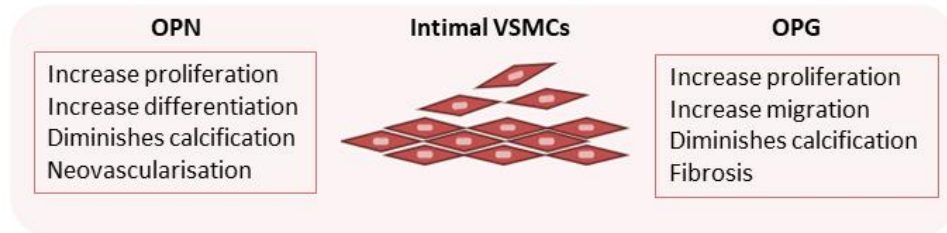


**Figure 4.5: Role of OPG and OPN on VSMCs.**

OPN is a multifunctional glycoprotein which is implicated in a range of acute and chronic inflammatory processes and has been shown to act as an inhibitor of calcification.<sup>25,26,30,31</sup> Recent studies have suggested that OPN antagonizes the macrophage mediated pathologic mineralization process by inhibiting osteoclast formation and increasing the expression of macrophage-derived inflammatory molecules.<sup>31</sup> Recent studies have shown that the OPN protein is upregulated in atherosclerotic plaques and is higher in patients with cardiovascular disease than in the ones without, especially in lesions with active calcification where it increases with increase of disease severity.<sup>24,26,31</sup>

Both OPG and OPN have been shown to have the potential to be used as early stage detection of unstable plaques, however, no reports are available in the literature showing the correlation between these biomarkers and Na<sup>18</sup>F PET activity. Here, tissues that exhibit Na<sup>18</sup>F PET activity as well as no activity (*Figure 4.6*), were analysed for OPG and OPN and linked to Alizarin S images. Na<sup>18</sup>F/CT analysis was categorised into tissue with Na<sup>18</sup>F signal present/absent and/or increased CT attenuation (>1000 CT units) present/absent. Examples of the range of Na<sup>18</sup>F activity are shown in *Figure 4.6* where samples display no Na<sup>18</sup>F/CT activity PET-CT- (*Figure 4.6 A*), high PET activity with little or no CT signal PET+CT- (*Figure 4.6 B, C* – two different samples) and a sample with high CT signal and Na<sup>18</sup>F signal PET+CT+ (*Figure 4.6 D*).

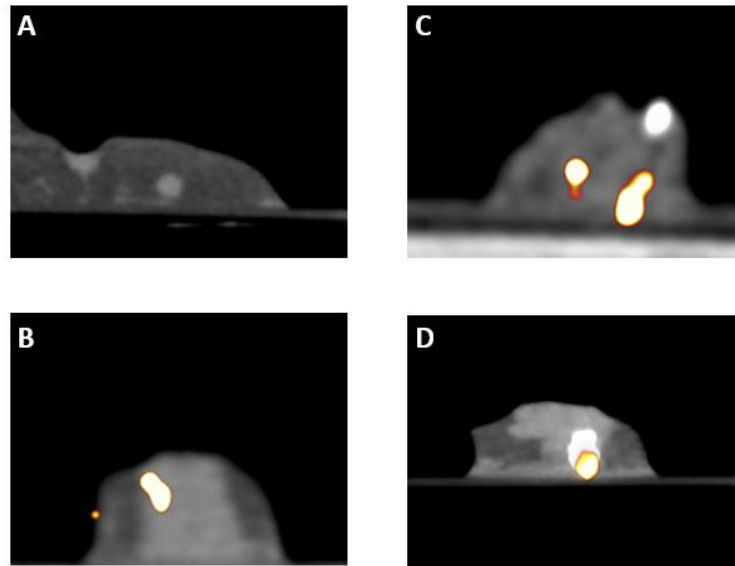


**Figure 4.6: PET/CT images of coronary tissue.** Negative control sample not displaying any type of calcification PET-CT- (A), 2 calcified samples displaying high level of Na<sup>18</sup>F PET tracer uptake PET+CT- (B, C) and positive control sample displaying high CT signal PET+CT+ (D).

While the intensity of Na<sup>18</sup>F activity did not correlate with fluorescence signal obtained from the Fluorescein-BP (55) probe, macroscopic calcium deposits had a higher fluorescent signal (Figure 4.2 F and Figure 4.4 B) in comparison with microscopic deposits (Figure 4.2 J and Figure 4.4 D). OPG and OPN were only present in areas of with Na<sup>18</sup>F signal.

All tissue samples were initially assessed using PET/CT scans (Figure 4.6) followed by sectioning of the tissue as required to allow appropriate sections to be taken and subsequently analysed by immunohistochemistry (IHC). IHC revealed that, uncalcified tissue (Figure 4.7 A, E, I), PET-CT-, does not stain for Alizarin S, which was expected, and neither OPG and OPN staining was visible. When looking at a PET+CT+ sample (Figure 4.6 D and Figure 4.7 D, H, L), Alizarin S staining was present around the arterial wall indicating the presence of calcification, however, when OPG and OPN staining was carried out no staining was visible. This supports previous findings on the lack of OPG and OPN expression in the blood of patients with normal arteries or stable angina.<sup>24,30</sup> However, when analysing two PET+CT- samples (Figure 4.6 B and C and Figure 4.7 B, C, F, G, J, K) these show higher levels of OPG and OPN in comparison to the controls confirming that these two proteins are highly expressed in unstable coronary arteries. On closer inspection, OPG and OPN localized in different locations within the PET active samples. While OPN signal was found in regions of high Na<sup>18</sup>F activity, OPG expression was evident in the peripheral margin surrounding the micro-calcification.



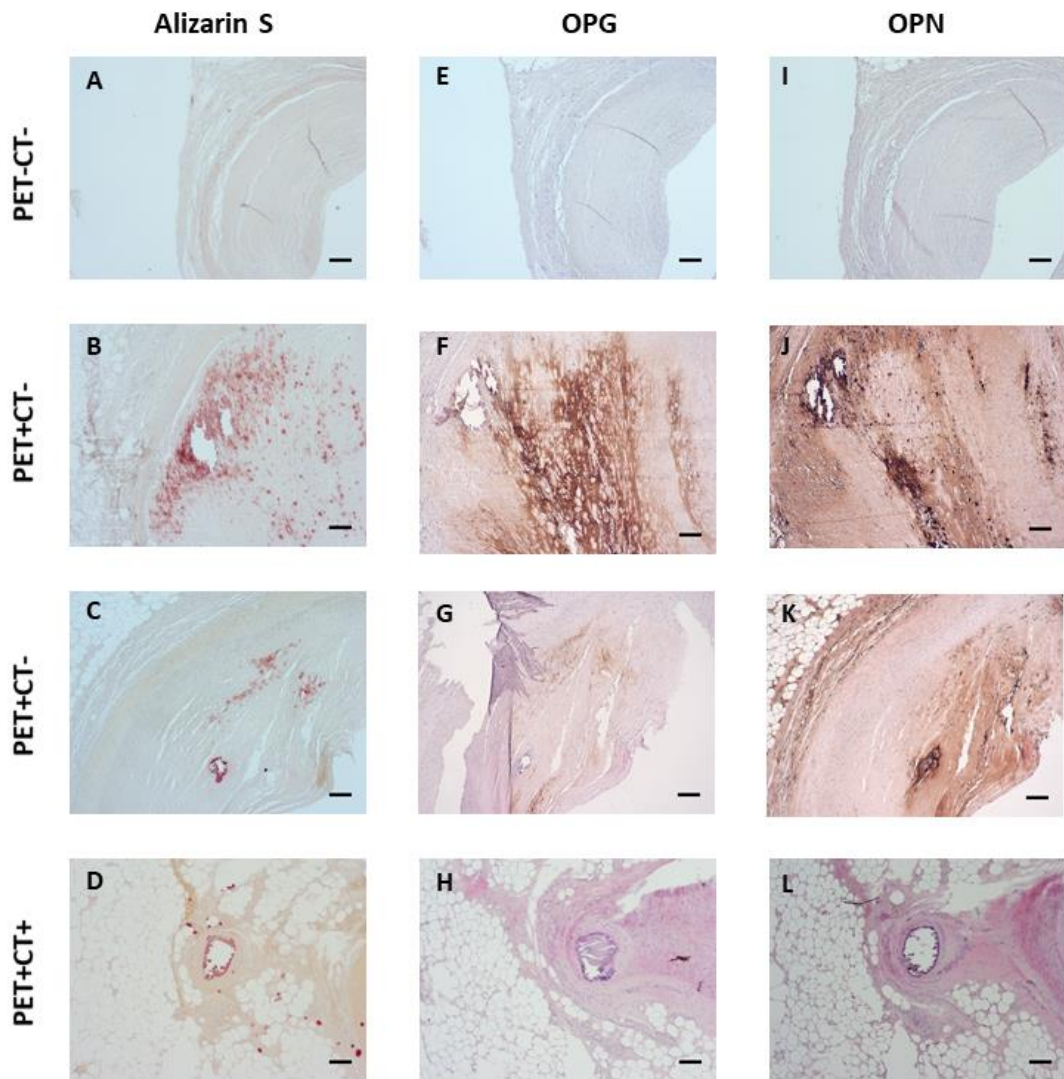


**Figure 4.7: Alizarin S staining, OPG and OPN immunohistochemistry of coronary tissue.** (A, E, I) control sample PET-CT-, non-calcified; (B, F, J) PET active sample 1, showing active/unstable calcification; (C, G, K) 2 PET+CT- samples, showing active/unstable calcification; (D, H, L) PET+CT+, showing inactive/stable calcification. (A, B, C, D) Alizarin S staining of coronary tissue. (E, F, G, H) OPG IHC, (I, J, K, L) OPN IHC. IHC analysis performed with Vectastain ABC kit (mouse IgG) where all antibodies were anti-human mouse clones (1:100 dilution). All IHC were counterstained with H&E. Scale bars = 0.2 cm. IGG controls shown in Appendix 3.

#### 4.8 Comparison of Alizarin S with the upregulation of osteogenic markers

OPG and OPN IHC on carotid specimens was carried out to determine whether the staining pattern was similar to that observed in coronary tissue. In these samples Alizarin S and OPN appear to co localize in most areas (Figure 4.8 A, B, E, F) while OPG staining is focussed in the surrounding areas (Figure 4.8 A, B, E, F), suggesting that OPG might play a protective

role in vascular calcification. This theory is supported by animal studies whereby a positive association between OPG levels in serum and clinical cardiovascular disease severity has been demonstrated.<sup>29,32</sup>

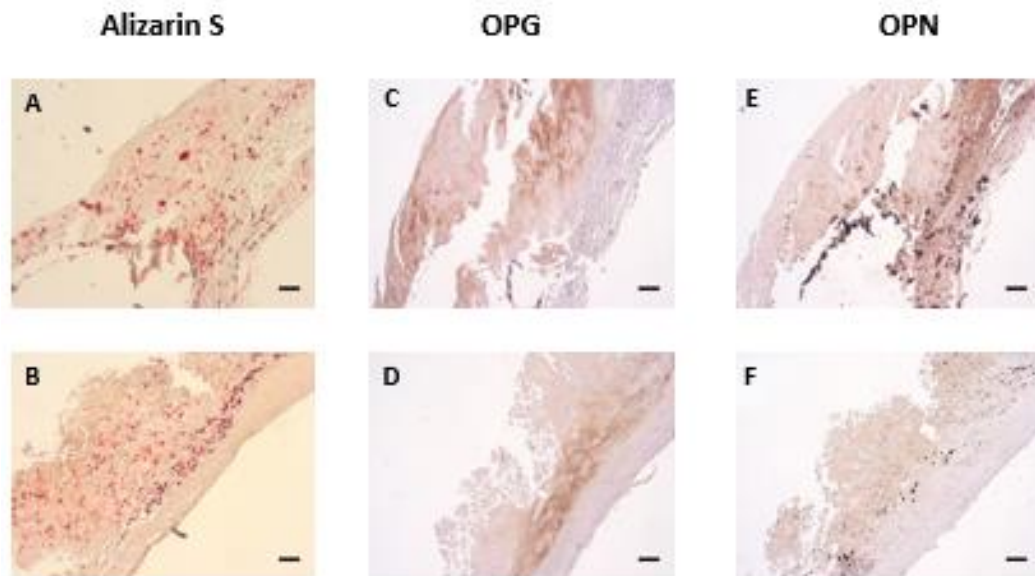


**Figure 4.8: Alizarin S staining, OPG and OPN immunohistochemistry of carotid tissues.** (A, B) Alizarin S staining of carotid tissue. (C, D) OPG IHC, (E, F) OPN IHC. IHC analysis performed with Vectastain ABC kit (mouse IgG) where all antibodies were anti-human mouse clones (1:100 dilution). All IHC were counterstained with H&E. Scale bars = 0.2 cm. IGG controls shown in Appendix 3.

#### 4.9 Comparison of Fluorescein-BP, OPG and OPN on coronary plaques

From data shown in Figure 4.2 and Figure 4.4 it is evident that Fluorescein-BP (55) can be used to detect both macro- and micro-calcification without discriminating between the disease activity. In fact, in contrast to the Na<sup>18</sup>F PET signal, the Fluorescein-BP probe (55) shows a stronger signal when binding to samples with macro-calcification in comparison to micro-calcification. However, this does not imply that the probe is not able to detect submicron calcification deposits as when analysing these samples a fluorescent signal is obvious. On the other hand, from data shown in Figure 4.7 and Figure 4.8 it is apparent that OPG and OPN are biomarkers for active disease and localize in areas with high Na<sup>18</sup>F PET signal. These sets of data raise an important clinical question; does Fluorescein-BP (55) co-localize in the same regions as OPG and OPN staining? To answer this question, tissue sequential sections that were previously analysed for Fluorescein-BP (55) staining, were treated for OPG and OPN IHC and were examined side by side (Figure 4.9). It is apparent that, Fluorescein-BP (55) OPG and OPN co-localize in the same area. OPG shows a very faint stain around the

calcification nodule while Fluorescein-BP (55) and OPN staining around the same nodule as well as staining some smaller deposits.

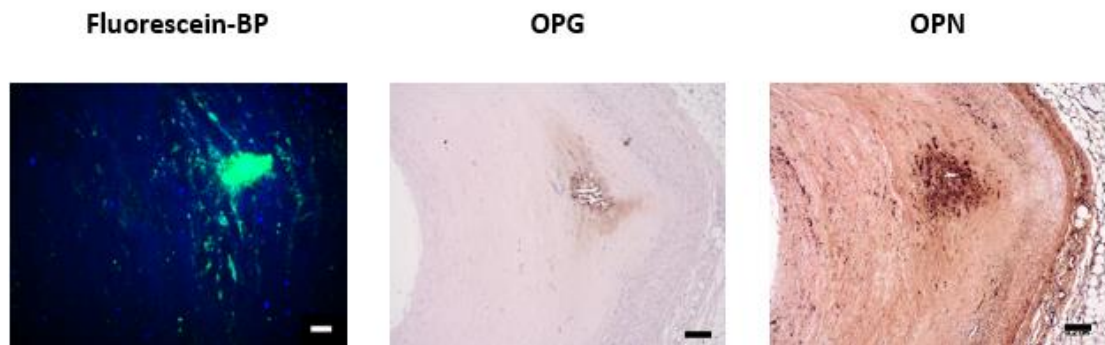


**Figure 4.9: Fluorescein-BP staining, OPG and OPN immunohistochemistry of carotid tissues.** (A) Fluorescein-BP (55) staining of carotid tissue: sections are incubated with Fluorescein-BP (1  $\mu$ M, 2 hours) and DAPI (500 nM, 5 minutes) and subsequently imaged. (B) OPG IHC, (C) OPN IHC. IHC analysis performed with Vectastain ABC kit (mouse IgG) where all antibodies were anti-human mouse clones (1:100 dilution). All IHC were counterstained with H&E. Scale bars = 100  $\mu$ m for fluorescence, 0.2 cm for brightfield.

These results are indicative that Fluorescein-BP (55) can be used to detect areas of active calcification to the same extent as OPG and OPN, but in contrast to the IHC, Fluorescein-BP (55) can also be used to detect areas of calcification which do not show any activity and are stable.

#### 4.10 Conclusion

Building and extending upon results from Chapter 3, here, it was demonstrated that Fluorescein-BP (55) is a highly sensitive and specific marker of hydroxyapatite in vascular coronary and carotid human tissue. Fluorescein-BP (55) has been compared to one of the current gold standard techniques for identifying calcification, Alizarin S, and has been shown to co-localize in the same areas. When applied to tissue presenting both macro- and micro-calcification, Fluorescein-BP (55) shows binding to both types of vascular calcification which is not otherwise possible using one stand-alone technique, eg. PET/CT.

Vascular calcification in atherosclerotic plaques contains high concentrations of crystalline HAP.<sup>33</sup> Within the arterial walls, extracellular vesicles containing hydroxyapatite are released from lipid-rich macrophages and apoptotic smooth muscle cells which increase the plaque structural stress and corresponding risk of fibroatheromatous cap fracture.<sup>34</sup> The inflammatory environment driving the production of HAP deposition is associated with a tendency to destabilise plaques and results in clinical cardiovascular events.<sup>35,36</sup> Recent clinical trials have focused attention on the vital role that early calcification plays in carotid, aortic aneurysmal

and coronary artery disease and hence there is a clinical imperative to better understand the mechanisms governing early calcification in the vascular wall.<sup>35-37</sup> The ability to differentiate calcium derivatives in regions of calcification, specifically by detecting hydroxyapatite, will facilitate the division of unstable and stable cardiovascular phenotypes in future clinical trials.

Moreover, OPG and OPN could also be used as biomarkers for unstable cardiovascular phenotypes as they have been shown to be present in increasing concentrations in tissue showing micro-calcification in comparison to sections which are atherosclerotic free or have stable macro-calcification which do not stain for either protein. However, limited data is available showing: 1) the relationship between OPG and calcification; as well as 2) the relationship between PET-active vascular tissue, OPG and OPN. These studies are only the beginning of understanding the mechanism behind the role of OPG in protecting and inhibiting vascular calcification suggesting that more data is required before any valid explanation could be presented.

Comparing Fluorescein-BP (**55**) with OPG and OPN IHCs reveals that all three can be used to detect areas of active calcification to the same degree; however in contrast to the IHC, Fluorescein-BP (**55**) also detects stable calcific lesions. This notably aids the field of cardiovascular research as up to now, a range of imaging tools are required to visualise both macro- and micro-calcification, however, the application of Fluorescein-BP (**55**) allows for only one technique to be used, which can elucidate calcific structures and differentiate between the different sizes of the calcification. This could allow for a more accurate definition of the cut-off point for macro and micro-calcification compared to that provided by both PET and CT.

#### 4.11 References

- 1 F. Sigala, E. Oikonomou, A. S. Antonopoulos, G. Galyfos and D. Tousoulis, *Curr. Opin. Pharmacol.*, 2018, **39**, 9–18.
- 2 M. Slevin, Q. Wang, M. A. Font, A. Luque, O. Juan-Babot, J. Gaffney, P. Kumar, S. Kumar, L. Badimon and J. Krupinski, *Pathobiology*, 2008, **75**, 209–25.
- 3 M. Kanadaşı, M. Çayli, M. Şan, K. Aikimbaev, C. C. Alhan, M. Demir and M. Demirtaş, *Angiology*, 2006, **57**, 585–592.
- 4 L. Saba, C. Yuan, T. S. Hatsukami, N. Balu, Y. Qiao, J. K. DeMarco, T. Saam, A. R. Moody, D. Li, C. C. Matouk, M. H. Johnson, H. R. Jäger, M. Mossa-Basha, M. E. Kooi, Z. Fan, D. Saloner, M. Wintermark, D. J. Mikulis and B. A. Wasserman, *Am. J.*

- Neuroradiol.*, 2018, **39**, E9–E31.
- 5 J. F. Polak, R. Tracy, A. Harrington, A. E. H. Zavodni and D. H. O’Leary, *J. Am. Soc. Echocardiogr.*, 2013, **26**, 548–555.
- 6 J. C. Grotta, F. M. Yatsu, L. C. Pettigrew, H. Rhoades, P. Bratina, D. Vital, R. Alam, R. Earls and C. Picone, *Neurology*, 1989, **39**, 1325–1331.
- 7 K. R. Nandalur, A. D. Hardie, P. Raghavan, M. J. Schipper, E. Baskurt and C. M. Kramer, *Stroke*, 2007, **38**, 935–40.
- 8 D. E. Bild, D. A. Bluemke, G. L. Burke, R. Detrano, A. V. Diez Roux, A. R. Folsom, P. Greenland, D. R. Jacobs, R. Kronmal, K. Liu, J. C. Nelson, D. O’Leary, M. F. Saad, S. Shea, M. Szklo and R. P. Tracy, *Am. J. Epidemiol.*, 2002, **156**, 871–881.
- 9 M. H. Criqui, J. B. Knox, J. O. Denenberg, N. I. Forbang, R. L. McClelland, T. E. Novotny, V. Sandfort, J. Waalen, M. J. Blaha and M. A. Allison, *JACC Cardiovasc. Imaging*, 2017, **10**, 845–854.
- 10 J. M. Tarkin, F. R. Joshi, N. K. Rajani and J. H. Rudd, *Future Cardiol.*, 2015, **11**, 115–131.
- 11 M. R. Dweck, N. A. Boon and D. E. Newby, *J. Am. Coll. Cardiol.*, 2012, **60**, 1854–1863.
- 12 M. von Scheidt, Y. Zhao, Z. Kurt, C. Pan, L. Zeng, X. Yang, H. Schunkert and A. J. Lusis, *Cell Metab.*, 2017, **25**, 248–261.
- 13 C. Erbel, D. Okuyucu, M. Akhavanpoor, L. Zhao, S. Wangler, M. Hakimi, A. Doesch, T. J. Dengler, H. A. Katus and C. A. Gleissner, *J. Vis. Exp.*, 2014, 1–6.
- 14 J. F. Bentzon and E. Falk, *Curr. Opin. Lipidol.*, 2010, **21**, 434–440.
- 15 Y. T. Lee, H. Y. Lin, Y. W. F. Chan, K. H. C. Li, O. T. L. To, B. P. Yan, T. Liu, G. Li, W. T. Wong, W. Keung and G. Tse, *Lipids Health Dis.*, 2017, **16**, 12.
- 16 T. Hampton, *Circulation*, 2017, **135**, 1757–1758.
- 17 B. Emini Veseli, P. Perrotta, G. R. A. De Meyer, L. Roth, C. Van der Donckt, W. Martinet and G. R. Y. De Meyer, *Eur. J. Pharmacol.*, 2017, **816**, 3–13.
- 18 C. O’Rourke, G. Shelton, J. D. Hutcheson, M. F. Burke, T. Martyn, T. E. Thayer, H. R. Shakartzi, M. D. Buswell, R. E. Tainsh, B. Yu, A. Bagchi, D. K. Rhee, C. Wu, M.

- Derwall, E. S. Buys, P. B. Yu, K. D. Bloch, E. Aikawa, D. B. Bloch and R. Malhotra, *J. Vis. Exp.*, 2016, e54017–e54017.
- 19 Y. V Bobryshev, E. A. Ivanova, D. A. Chistiakov, N. G. Nikiforov and A. N. Orekhov, *Biomed Res. Int.*, 2016, **2016**, 9582430.
- 20 Y. C. Chen and K. Peter, *Atherosclerosis*, 2015, **241**, 595–596.
- 21 O. Phan, O. Ivanovski, I. G. Nikolov, N. Joki, J. Maizel, L. Louvet, M. Chasseraud, T. Nguyen-Khoa, B. Lacour, T. B. Drücke and Z. A. Massy, *Nephrol. Dial. Transplant.*, 2008, **23**, 82–90.
- 22 B. Znorko, E. Oksztulska-Kolanek, M. Michałowska, T. Kamiński and K. Pawlak, *Adv. Med. Sci.*, 2017, **62**, 52–64.
- 23 Y. Nitschke, G. Weissen-Plenz, R. Terkeltaub and F. Rutsch, *J. Cell. Mol. Med.*, 2011, **15**, 2273–2283.
- 24 S. M. Venuraju, A. Yerramasu, R. Corder and A. Lahiri, *J. Am. Coll. Cardiol.*, 2010, **55**, 2049–2061.
- 25 O. Gungor, I. Kocyigit, M. I. Yilmaz and S. Sezer, *Semin. Dial.*, 2018, **31**, 72–81.
- 26 M. Abedin, Y. Tintut and L. L. Demer, *Arterioscler. Thromb. Vasc. Biol.*, 2004, **24**, 1161–1170.
- 27 C. Pérez De Ciriza, A. Lawrie and N. Varo, *Int. J. Endocrinol.*, 2015, 2015, 564934.
- 28 K. A. Lomashvili, S. Cobbs, R. A. Hennigar, K. I. Hardcastle and W. C. O’Neill, *J. Am. Soc. Nephrol.*, 2004, **15**, 1392–1401.
- 29 A. Van Campenhout and J. Golledge, *Atherosclerosis*, 2009, **204**, 321–329.
- 30 M. Bjerre, S. H. Pedersen, R. Møgelvang, S. Lindberg, J. S. Jensen, S. Galatius and A. Flyvbjerg, *Eur. J. Prev. Cardiol.*, 2013, **20**, 922–929.
- 31 Q. Ge, C.-C. Ruan, Y. Ma, X.-F. Tang, Q.-H. Wu, J.-G. Wang, D.-L. Zhu and P.-J. Gao, *Sci. Rep.*, 2017, **7**, 40253.
- 32 S. Morony, Y. Tintut, Z. Zhang, R. C. Cattley, G. Van, D. Dwyer, M. Stolina, P. J. Kostenuik and L. L. Demer, *Circulation*, 2008, **117**, 411–420.
- 33 D. Carlstorm, B. Engfeldt, A. Engstrom and N. Ringertz, *Lab. Invest.*, 1953, **2**, 325–35.

- 34 A. Kelly-Arnold, N. Maldonado, D. Laudier, E. Aikawa, L. Cardoso and S. Weinbaum, *Proc. Natl. Acad. Sci.*, 2013, **110**, 10741–10746.
- 35 A. T. Vesey, W. S. A. Jenkins, A. Irkle, A. Moss, G. Sng, R. O. Forsythe, T. Clark, G. Roberts, A. Fletcher, C. Lucatelli, J. H. F. Rudd, A. P. Davenport, N. L. Mills, R. Al-Shahi Salman, M. Dennis, W. N. Whiteley, E. J. R. van Beek, M. R. Dweck and D. E. Newby, *Circ. Cardiovasc. Imaging*, 2017, **10**, e004976.
- 36 N. V Joshi, I. Toor, A. S. V Shah, K. Carruthers, A. T. Vesey, S. R. Alam, A. Sills, T. Y. Hoo, A. J. Melville, S. P. Langlands, W. S. A. Jenkins, N. G. Uren, N. L. Mills, A. M. Fletcher, E. J. R. van Beek, J. H. F. Rudd, K. A. A. Fox, M. R. Dweck and D. E. Newby, *J. Am. Heart Assoc.*, 2015, **4**, e001956.
- 37 R. O. Forsythe, M. R. Dweck, O. M. B. McBride, A. T. Vesey, S. I. Semple, A. S. V. Shah, P. D. Adamson, W. A. Wallace, J. Kaczynski, W. Ho, E. J. R. van Beek, C. D. Gray, A. Fletcher, C. Lucatelli, A. Marin, P. Burns, A. Tambyraja, R. T. A. Chalmers, G. Weir, N. Mitchard, A. Tavares, J. M. J. Robson and D. E. Newby, *J. Am. Coll. Cardiol.*, 2018, **71**, 513–523.

# Chapter 5- Chemical Composition of Vascular Calcification Deposits

## 5.1 Raman spectroscopy

Spectroscopy is the study the interactions of radiation with matter and is a field that encompasses a wide range of techniques. Raman spectroscopy is based on the interaction of light and matter and was initially observed by C.V. Raman in 1928.<sup>1-3</sup> Raman and Krishnan hypothesized that an energy transfer, similar to the one that takes place during X-ray spectroscopy, should take place when electromagnetic radiation is scattered by atoms or molecules.<sup>3-5</sup>

When a photon of light interacts with a molecule, it allows the molecule to transit to a virtual energy state, and although this transition is short lived, this increase in energy means that the molecule is at a higher energy state (*Figure 5.1*).<sup>2</sup> The molecule can then relax back in two manners:

- to the initial ground state in a single step by releasing the same amount of energy as that of the incoming photon. This process is called Rayleigh (or elastic) scattering.<sup>2-4,6</sup> When this occurs, no energy is transferred to the molecule and therefore the process does not yield any information.
- to a different ground state when the molecule releases a different quantum of energy to that of the incident photon. This process is called Raman (inelastic) scattering and can be divided into two further processes; Stokes and anti-Stokes scattering.<sup>4,6,7</sup> Stokes scattering occurs when energy is transferred to the molecule from the incident photon while anti-Stokes scattering occurs when the molecule loses some energy to the scattered photon which is then greater than the energy of the incident photon.<sup>1,3,4,6,7</sup>



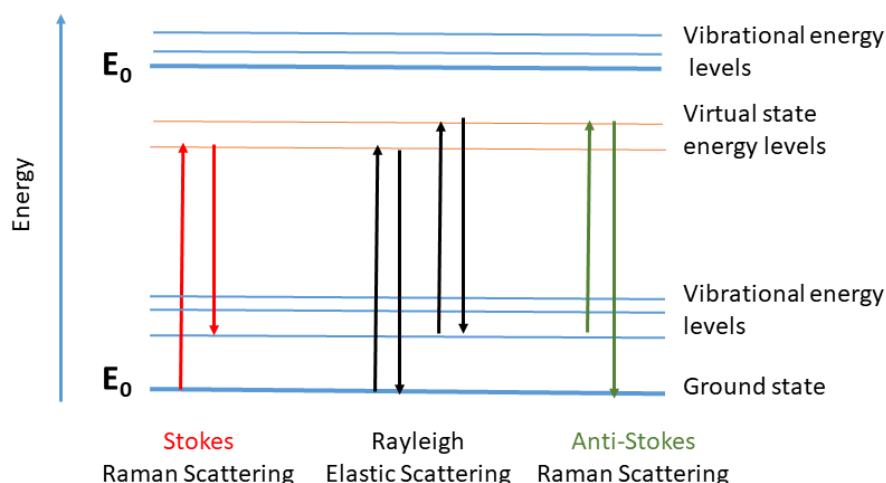


**Figure 5.1: Diagram of energetic transitions involved in Raman scattering.** Rayleigh scattering is elastic; the incident photon is of the same energy as the scattered photon. Raman scattering is inelastic; in Stokes scattering, the incident photon is of greater energy than the scattered photon, while in anti-Stokes scattering, the scattered photon is of greater energy of the incident photon.

Stokes scattering is most commonly observed, however the signal is inherently weak with only 1 in  $10^7$  photons undergoing Raman scattering.<sup>1,7-9</sup> To obtain Raman scattering, a laser is used to provide coherent, monochromatic light for molecule excitation. A diffractive spectrometer based on a reflective grating is then used to disperse the light onto highly sensitive detectors which will eventually generate a spectrum.<sup>1,10</sup> A simplified schematic of a microscope for Raman spectroscopy is shown below (Figure 5.2).

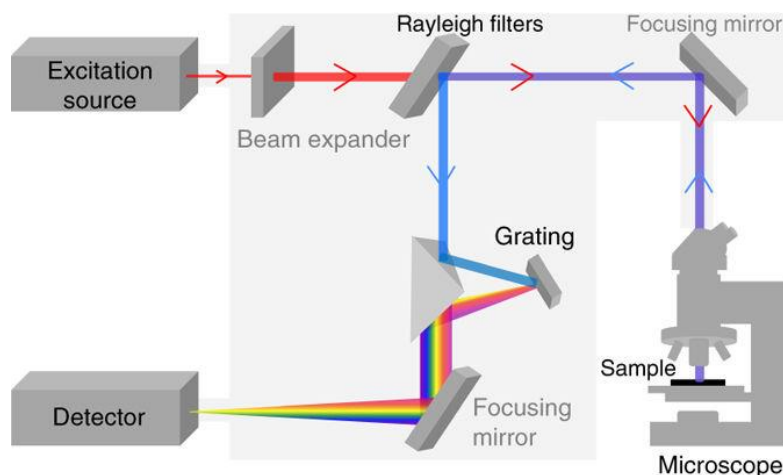


**Figure 5.2: Overview of Raman microscope system for Spontaneous Raman Spectroscopy.** Figure reproduced with permission.<sup>8</sup>

For a molecule to be able to produce Raman scattering it requires a change in the polarizability of its bonds during a vibration. Raman inactive or forbidden molecular vibrations will not

generate Raman scattering.<sup>11</sup> A typical Raman spectrum is a plot of intensity of the scattered light (in AU) relative to the frequency of the scattered light (in wavenumbers). Specific bonds will vibrate at unique wavenumbers and therefore each molecule will have a characteristic spectroscopic fingerprint.<sup>9,12</sup> Raman can be applied to a wide range of samples; from solids, to cells and tissues; very little preparation is required and spectra are easily obtained within seconds.

## 5.2 Raman spectroscopy of biological samples

Raman spectroscopy has become increasingly popular in recent years as a tool to characterize and analyse cells and tissues, as well as a diagnostic tool for diseases both *in vitro* and *in vivo*.<sup>1,8,12–15</sup> This is due to it being label-free, safe and non-invasive. It relies on the inherent scattering nature of all biomolecules and can be used to detect specific extra- and intracellular structures such as proteins, lipids and nucleic acids with submicron spatial resolution in both living and fixed systems, allowing for characterization and comparison of biologically interesting samples without alteration (*Figure 5.3*).<sup>5,12,16–18</sup>

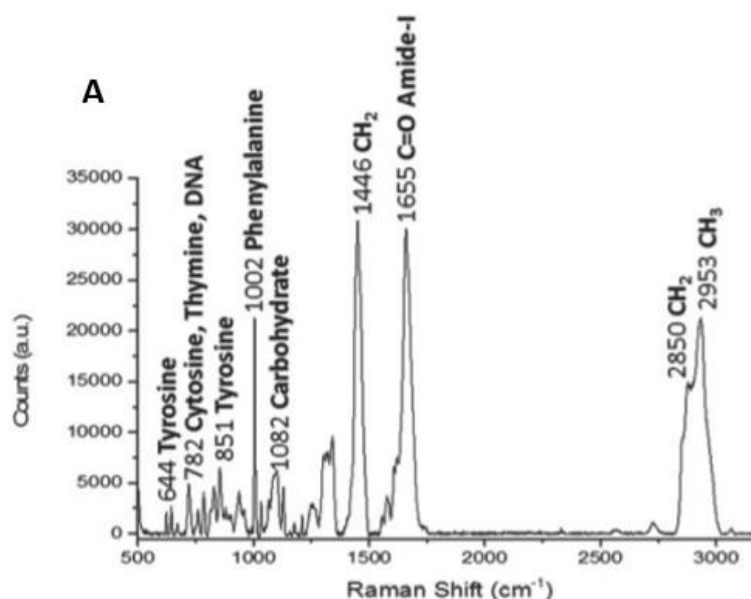


**Figure 5.3 Raman spectra of SKBR3 cells by Raman microscopy.** Spontaneous Raman spectrum of SKBR3 cell pellet measured using 785 nm excitation. Key bands are indicted. Figure reproduced with permission.<sup>15</sup>

Current analytical techniques most frequently used to assess the morphology of samples involve disrupting the very process under investigation, for example immunohistochemistry and immunofluorescence. There is a need for a non-destructive, non-invasive technique that is capable of analysing samples at a biomolecular level.<sup>1,19–21</sup> Raman spectroscopy has been

established in the recent years as a powerful laboratory technique, and recently *in vivo* clinical trials indicate its potential for biomolecular characterisation and diagnosis.<sup>22-24</sup> It could prove particularly crucial in diagnosing disease early in the pathogenesis as it can be used to detect chemical alterations before morphological changes appear.

### 5.3 Raman spectroscopy of mineralized vascular tissue

CaPi rich solid mineral species associated with vascular calcification have been commonly compared to those found during the development of bone and tooth, leading to a number of hypotheses as to potential precursors.<sup>12,25</sup> The most commonly proposed precursors to bone HAP are ACP, brushite, octacalcium phosphate (OCP),  $\beta$ -tricalcium phosphate ( $\beta$ TCP) and whitlockite, a magnesium substituted  $\beta$ TCP (WTK) (*Table 5.1*). These species all have a distinct Raman signal, and are yet to be fully characterized in cardiovascular systems.<sup>25</sup>

*Table 5.1: Inorganic CaPi-rich phases and their corresponding Raman signals.*

<b>Inorganic CaPi-rich phases</b>	<b>Formula</b>	<b>Raman Signal <math>V_1 PO_4^{3-} (cm^{-1})</math></b>	<b>Ref.</b>
<b>ACP</b>	$Ca_xHy(PO_4)_z \cdot nH_2O$ n=3-4.5; 15-20% H <sub>2</sub> O	955	26
<b>HAP</b>	$Ca_5(PO_4)_3(OH)$	960-963	5,12,21,25,27
<b>OCP</b>	$Ca_8(HPO_4)_2(PO_4)_4 \cdot 5H_2O$	957	26
<b><math>\beta</math>TCP</b>	$\beta-Ca_3(PO_4)_2$	970	21,26
<b>WTK</b>	$Ca_9(MgFe)(PO_4)_6PO_4H$	973	5

Raman spectroscopy has previously been used for the characterization of the atherosclerotic plaque.<sup>18,20,21,27,28</sup> Latterman *et al.* imaged the cross section of atherosclerotic plaques from rabbits with high-cholesterol diet-induced disease and provided detailed characterization of the lipidic component of the tissue.<sup>18,20,27,28</sup> Other groups have developed fibre-optic techniques using miniaturized Raman probes to aid the diagnosis of atherosclerosis *in vivo*.<sup>18,21,29</sup> Recently, calcification has also gained a lot of attention and both vascular and valve calcification have been studied extensively, not only using Raman, but with other imaging techniques.<sup>5,18,27,30,31</sup> Raman spectroscopy has been used for its powerful ability to analyse the inorganic mineral structures in biological tissue by having a high sensitivity to changes in the crystallinity and atom substitution of biological apatite. Building on previous work, in this chapter, calcified vascular cell monolayers, *ex vivo* rat aortic tissue and human vascular tissue

will be analysed. This allows for information, which is complementary to the results provided by fluorescence, to be obtained. In particular it allows for the assessment of the crystallinity of the calcium species, in order to shed further light on the calcification process. Additionally, a comparison of Raman spectroscopy with PET/CT images will be carried out to improve understanding of the binding of the Na<sup>18</sup>F PET tracer to the calcified plaques.

## 5.4 Raman on Calcium species

Spontaneous Raman spectroscopy is able to distinguish peaks that are at 1 cm<sup>-1</sup> apart allowing for an accurate characterisation of more subtle spectral features such as minor changes in the shape or position of a peak thus allowing analysis of phenomena such as crystallinity and polymorphism. In order to determine the chemical composition of cardiovascular calcification, the Raman fingerprint of known calcium phosphate species was analysed. Literature reports the presence of five potential calcium minerals in vascular tissue; with HAP being the only mineral present in cellular models and ACP, OCP,  $\beta$ TCP and WTK present in vascular tissue and valves.<sup>25,26,32</sup> Raman spectra of synthetic, non-biogenic, commercial minerals were obtained on the InVia Renishaw microscope using a 785 nm laser, and are reported below (*Figure 5.4*). This allowed for a direct comparison between the minerals as well as aiding in the subsequent determination of the mineral phase present in both cell and human models.

When analysing mixtures of different minerals, such as ACP and HAP, two distinct peaks are visible (*Figure 5.4*), looking closely at the mixture of 3:7 ACP:HAP, one major peak with a side peak were visible suggesting that the two compounds could be distinguished when analysed together. Using Origin, peak fitting of the spectrum was performed and clearly showed the distinct two peaks at 955 and 960 cm<sup>-1</sup>, it was also possible to analyse the area under the two fitted peaks which in this instance accounted for 25% ACP and 75% HAP which is only slightly different from the experimental mixture produced, indicating that this technique can be used to analyse mixture and can fairly accurately report the ratios of compounds present in the solid mix.

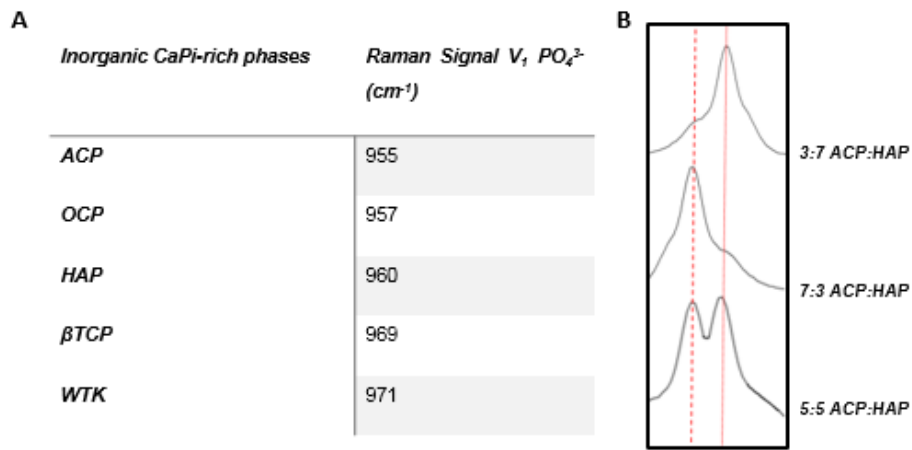


**Figure 5.4: Phosphate ( $\nu_1$ ) Raman signal of different calcium species (A) and spectra of ACP:HAP mixtures (B).** Values and spectra obtained using an InVia Renishaw microscope with a 785 nm laser. Red dashed line indicative of ACP, red dotted line indicative of HAP.

## 5.5 Raman analysis on calcified cell pellet

Calcification can occur in a wide range of tissues, spanning from soft tissues to vascular tissues.<sup>33–35</sup> In the field of vascular biology, calcification can occur at different locations, and therefore different cell models are required to study the specific molecular biology and pathways behind the disease.<sup>36,37</sup>

An example of a cell phenotype present in vascular tissues is the primary vascular smooth muscle cell (VSMC) which is one of the cellular components of the normal blood vessel wall. VSMCs provide structural integrity and regulate the diameter of the vessel by contracting and relaxing in response to vasoactive stimuli. In contrast to skeletal and muscle cells, VSMCs are not terminally differentiated and can change their phenotype in response to environmental change to become calcifying osteoblastic cells, thereby facilitating the production of extracellular matrix components.<sup>36–39</sup> VSMCs are the principal cell type that are involved in vascular calcification and are primarily used to study calcification in conditions such as atherosclerosis and chronic kidney disease (CKD).<sup>36,38,40</sup>

Calcified rat VSMC cell pellets were analysed by Raman spectroscopy (Figure 5.5). Cells were cultured for 7 days under two different conditions: control and calcifying media (1.4 mM Ca and 2.4 mM Pi). The cell monolayer was then treated with trypsin to allow the cells to be collected in the form of a pellet for Raman analysis.

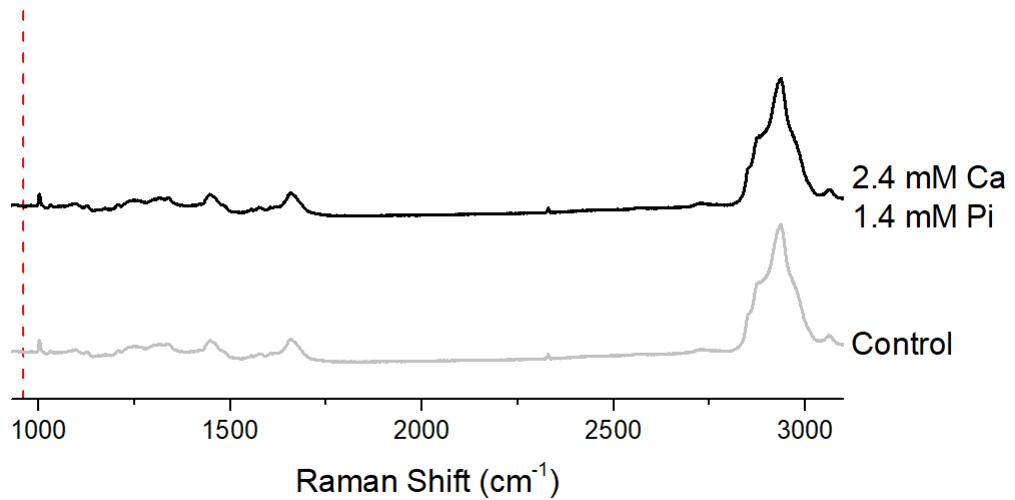


**Figure 5.5: Spontaneous Raman spectra of VSMC cell pellets.** Calcified and control VSMCs cell pellet. Raman spectroscopy of cell monolayers obtained using Renishaw InVia, 785 nm laser, 30 s, 100%. Spectra are offset for clarity and normalized to the phenylalanine peak ( $1003\text{ cm}^{-1}$ ). Spectra are a representative of at least three repeats. Red dashed line indicative of  $960\text{ cm}^{-1}$  HAP value.

Spectra obtained from Raman analysis of the cell pellet showed the most common cellular peaks; phenylalanine, amide bonds and lipid (Table 5.2). However, when the cell monolayer was cultured in calcium and phosphate enriched media, which should induce calcification, no peak corresponding to calcium mineralisation was observed amongst the other signals.

**Table 5.2: Raman shift of common cell features**

<b>Peak position (<math>\text{cm}^{-1}</math>)</b>	<b>Major Assignments</b>
<b>855</b>	C-C stretch
<b>875</b>	C-C stretch
<b>960</b>	Hydroxyapatite $\text{PO}_4^{3-}$ symmetric stretch
<b>1003</b>	Phenylalanine
<b>1032</b>	Proline
<b>1128</b>	C-N
<b>1206</b>	Hydroxyproline
<b>1247-1270</b>	Protein amide III band
<b>1595-1720</b>	Amide I (C=O stretching mode of proteins/ C=C of lipids)
<b>2880</b>	$\text{CH}_2$ , lipids
<b>2940</b>	$\text{CH}_3$ , proteins

The lack of calcium mineral deposited in the cell pellet is due to the collection process employed. When cells undergo treatment with trypsin and pelleted, the extracellular matrix disintegrates and releases the calcification crystals which have been deposited on the

extracellular matrix, resulting in an absence of a peak corresponding to the calcium mineral. This was confirmed by incubating the cells with Fluorescein-BP (55), which as reported in Figure 2.16 shows selectivity towards HAP and binds to calcium mineral deposits when incubated with cells as seen in Chapter 3. After incubation with Fluorescein-BP (55) the cell monolayers were washed to remove any unbound probe and subsequently underwent treatment with trypsin, pelleted and fluorescence analysis was performed on the supernatant. The supernatant should contain all the extracellular matrix content and therefore also the bound Fluorescein-BP (55) would consequently provide a strong fluorescence signal. Figure 5.6 illustrates this as it shows that the supernatant of the calcified cell monolayers has a fluorescence signal of 75 AU which is comparable to the intensity of the same concentration of Fluorescein-BP (55) in media alone without cells. In contrast, the supernatant of the control does not present any fluorescence signal as unbound probe was removed in the washing step. This proves that, when the cell monolayer undergoes trypsinisation and pelleting, the calcium mineral, which has been deposited on the ECM, is removed from the cell bulk (pellet) and is present in the supernatant instead (Figure 5.6). It is apparent that the fluorescence intensity of the supernatant of the calcified cell monolayer and of the media alone are not equivalent; this could be due to small amounts of Fluorescein-BP (55) entering the cells and binding to calcium minerals present in the matrix vesicles.

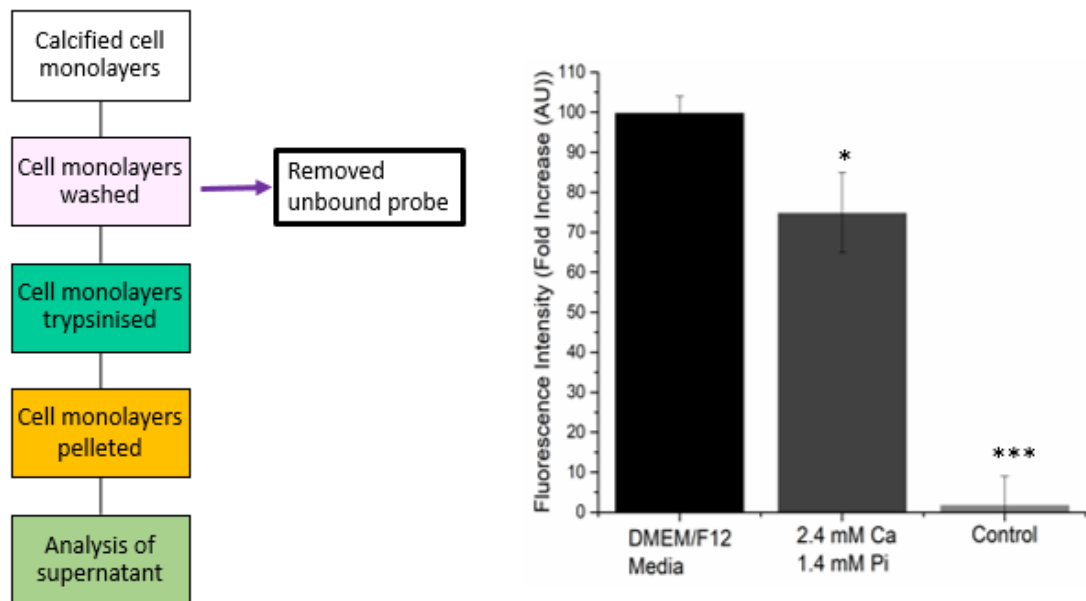


**Figure 5.6: Fluorescence signal of the supernatant of pelleted VSMCs incubated with Fluorescein-BP (55).** VSMCs are grown to confluence and then transferred to either control media or calcification media (2.4 mM Ca and 1.4 mM Pi) for 7 days, changing media on alternate days. Once calcified, cells were incubated with Fluorescein-BP (1  $\mu$ M, 2 hours) and then centrifuged. Pellet and supernatant were separated and the supernatant was analysed using a Fluoromax-3. Data shows is an average of three independent results and are shown as the mean  $\pm$  S.E.M. \* $P < 0.05$ , \*\* $P < 0.01$ , \*\*\* $P < 0.001$ .

## 5.6 Raman analysis of calcified cell monolayer

Another way of obtaining Raman spectra of calcified primary cells or cell lines is to analyse the cell monolayer directly. This can be done by seeding and calcifying the cells on Raman-inactive substrates such as CaF<sub>2</sub> slides. In comparison to glass or plastic, CaF<sub>2</sub> slides do not produce any Raman signal and therefore do not mask the Raman spectrum of the cell monolayer. Rat VSMCs were seeded on CaF<sub>2</sub> slides that had previously been autoclaved, and the cells were incubated with either control media or calcification media, (2.4 mM Ca and 1.4 mM Pi), for 7 days. On day 7, the monolayer was fixed and subsequently analysed by Raman spectroscopy. In contrast to the cell pellet, the calcified rat VSMC monolayer grown on CaF<sub>2</sub> slides shows the appearance of a peak at 960 cm<sup>-1</sup> which is absent in the control (*Figure 5.7*), corresponding to HAP.

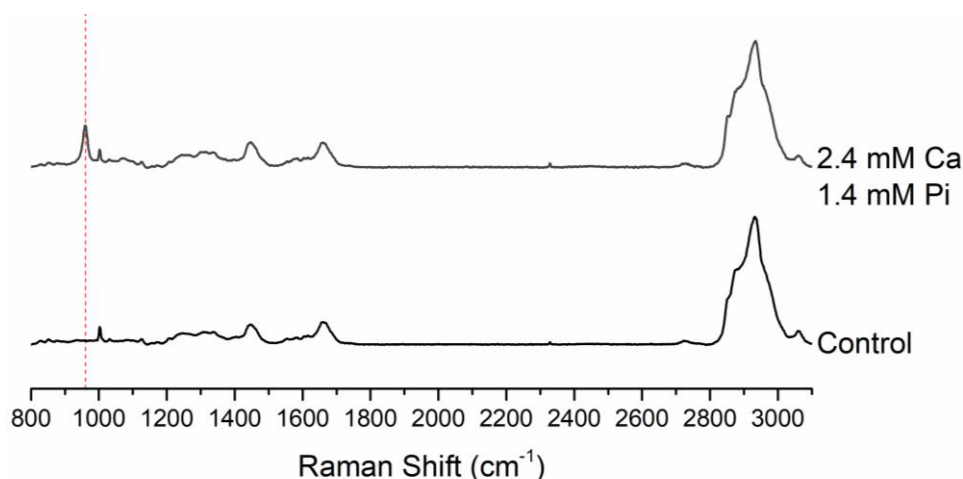


**Figure 5.7:** Spontaneous Raman spectra of rat VSMC monolayer grown on CaF<sub>2</sub> Raman slides. Cells were seeded and then incubated with either control media or calcifying media (2.4 mM Ca and 1.4 mM Pi). Cells were incubated with media for 7 days changing media on alternate day. Raman spectroscopy of cell monolayer obtained using Renishaw InVia, 785 nm laser, 30 s, 100%. Spectra are offset for clarity and normalized to the phenylalanine peak (1003 cm<sup>-1</sup>). Spectra are a representative of at least three repeats. Red dashed line indicative of 960 cm<sup>-1</sup> peak (HAP).

Previously, in section 5.2.2, VSMCs were discussed as an example of cell phenotype present in vascular tissue. Another important cell phenotype used to study vascular calcification is the primary valve interstitial cell (VICS); these cells are the most prevalent cells in the heart valve and are thought to be responsible for maintaining the structural integrity of the valve.<sup>41,42</sup> In contrast to the VSMCs, VICS are used to study conditions such as aortic valve stenosis, due to calcification of the valve leaflets. Together with atherosclerosis, aortic valve stenosis is one of the most common causes of cardiovascular disease.<sup>43,44</sup> Aside from primary cells, cell lines



can also be used to study vascular calcification. In general, cell lines offer a reliable, convenient and economical system in which to investigate vascular calcification *in vitro*.<sup>39,45</sup> An example of this is the MOVAS-1 cell line which exhibits a smooth muscle cell phenotype, and has been previously employed to investigate the VSMC cell cycle.<sup>45</sup>

Primary rat VSMCs, primary rat VICs and MOVAS-1 cells were cultured, calcified and analysed by Raman spectroscopy. The HAP peak, at 960 cm<sup>-1</sup>, was present in all phenotypes. The cell monolayers were cultured under different calcification conditions (2.7 mM Ca and 2.4 mM Pi; 2.4 mM Ca and 1.4 mM Pi), and overall these studies showed that with increasing concentrations of calcification media, there was an increase in the intensity of the 960 cm<sup>-1</sup> peak. ACP or OCP were not observed in any of the cell monolayers, suggesting that within the 7 days incubation period, the calcium phosphate deposited by the cell has been converted to HAP.

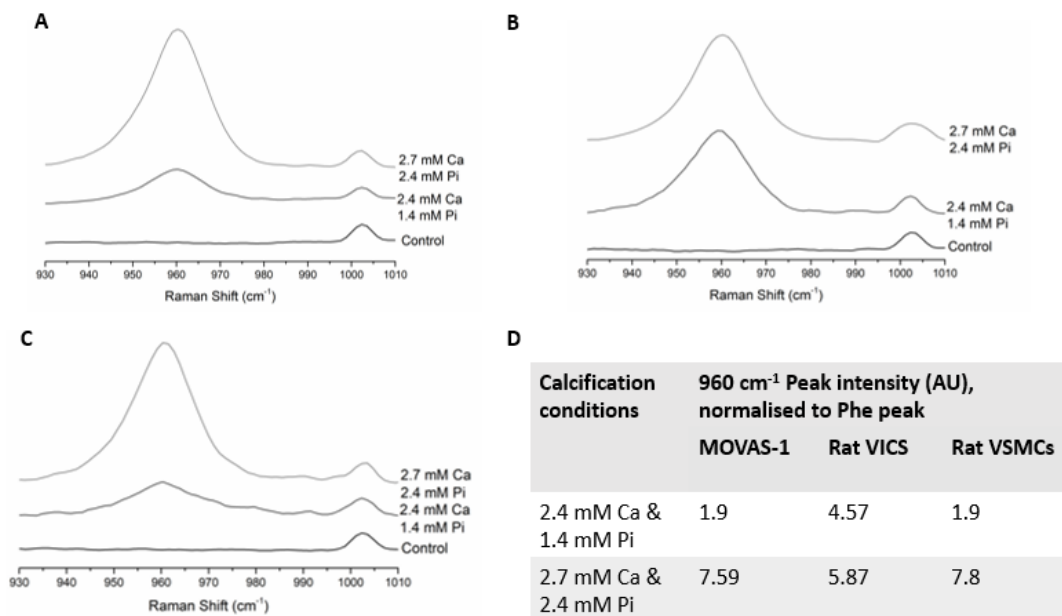


**Figure 5.8: Static Raman spectra of different vascular cell monolayers.** MOVAS-1 (A), primary rat VICs (B), primary rat VSMCs (C) were grown on CaF<sub>2</sub> slides and incubated with either control or calcifying media (2.4 mM Ca and 1.4 mM Pi or 2.7 mM Ca and 2.4 mM Pi) for 7 days with media change on alternating days. On day 7, cells were fixed with 10% NBF (15 minutes) and then imaged using Renishaw InVia, laser 785 nm, 30 s, 100% laser power. Images are representative of at least three repeats. Spectra are offset for clarity and normalized to the phenylalanine peak (1003 cm<sup>-1</sup>). (D) Table reporting the peak intensity for HAP at both concentration for MOVAS-1, rat VICs and rat VSMCs.

Both MOVAS-1 and rat VSMCs show a 4-fold increase in the intensity of the HAP peak between the two calcification conditions (2.4 mM Ca and 1.4 mM P<sub>i</sub> or 2.7 mM Ca and 2.4 mM P<sub>i</sub>) (Figure 5.8), while the rat VICs seem to calcify just as efficiently when using either

set of conditions (Figure 5.8). Upon closer inspection, it is apparent that MOVAS-1 and rat VSMCS are more prone to calcification, when using 2.7 mM Ca and 2.4 mM P<sub>i</sub> as indicated by a higher intensity HAP peak, in comparison to the rat VICS. This might be due to the fact that VSMCs (primary and cell line) are more predisposed to a change in phenotype and therefore allow for accelerated migration, proliferation and production of extracellular matrix components.

The MOVAS-1 cell line was selected due to its convenient and economical nature to address whether the HAP peak was observed in the same area as the Alizarin S staining. As mentioned in chapter 3, Alizarin S is one of the most commonly used techniques to stain calcium.<sup>46</sup> This experiment showed that the calcium staining by Alizarin S co-localised with calcium imaging by Raman; with Raman spectroscopy being able to elucidate the type of calcium present as HAP (Figure 5.9).

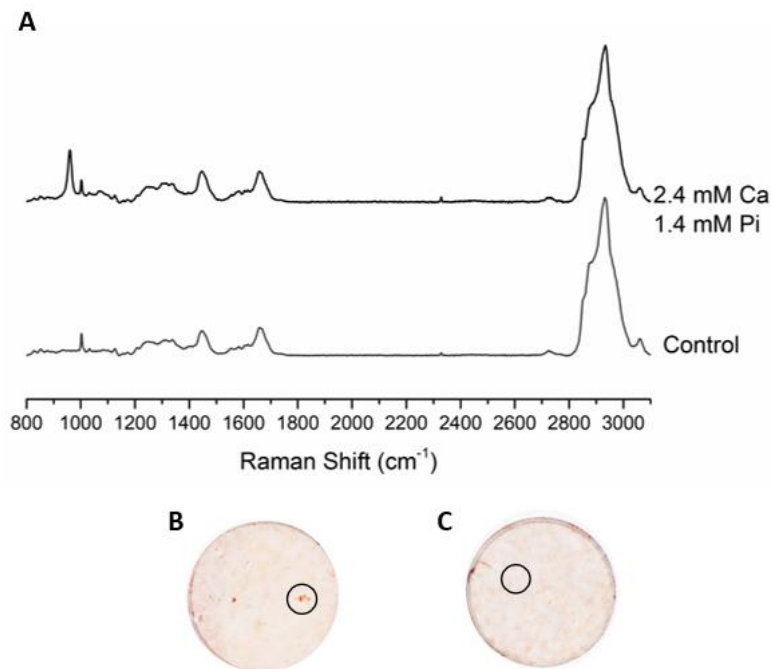


**Figure 5.9: Full spontaneous Raman spectrum for MOVAS-1 (A) and Alizarin S staining (B, C).** Cells grown on CaF<sub>2</sub> slides and incubated with either control (A, C) or calcifying media (2.4 mM Ca and 1.4 mM Pi) (A, B) for 7 days with changing media on alternate days. On day 7, cells were fixed with 10% NBF (15 minutes) and then imaged using Renishaw InVia, laser 785 nm, 30 s, 100% laser power. Following Raman imaging, the monolayer was then incubated with 2% Alizarin S (5 minutes), washed three times with water and then imaged. Black circles are indicative of the area imaged by Raman spectroscopy. Images are representative of at least three repeats. Spectra are offset for clarity and normalized to the phenylalanine peak (1003 cm<sup>-1</sup>).

## 5.7 Raman analysis on calcified aortic rings

As mentioned in Chapter 3, cell cultures are of limited use in the study of calcification as they lack the architecture and matrix of normal vessels.<sup>47</sup> Cultured aortae can provide complementary information that bridges the gap between traditional cell culture and animal models.<sup>47,48</sup> Rat aortae were cultured in 3 mM  $P_i$  enriched media and then analysed by Raman spectroscopy. A range of methods were explored in order to obtain a clean and noise free Raman spectrum (*Figure 5.10*).

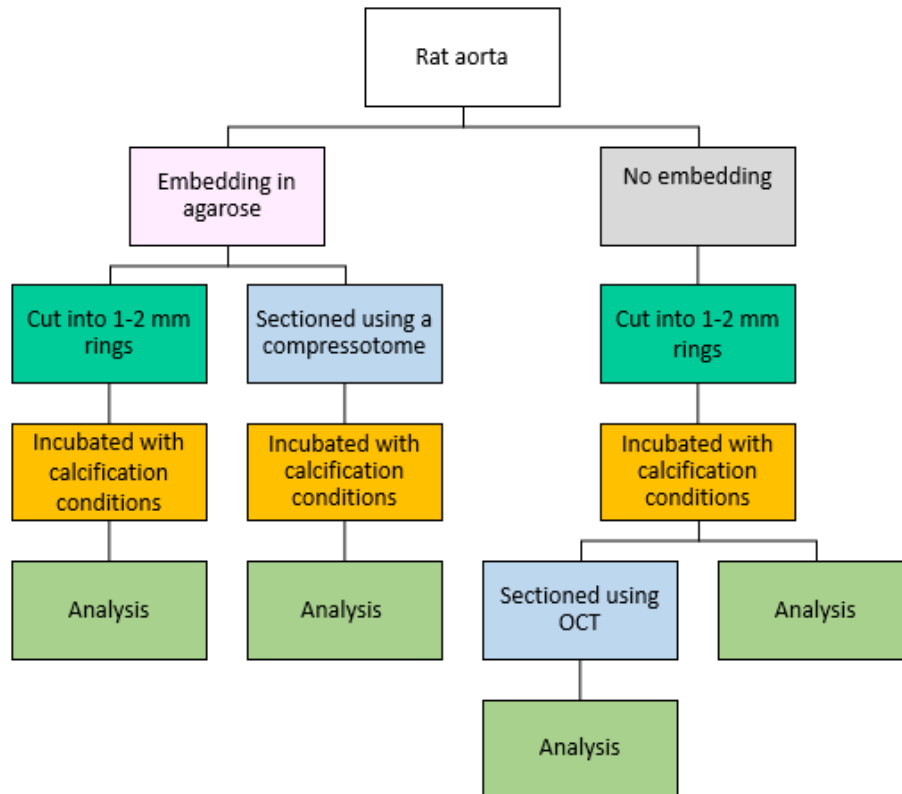


*Figure 5.10: Flowchart showing the methods explored for rat aorta culture and analysis.*

Aortae from wild type rats were dissected and either embedded in agarose or not. The aortae were embedded in low melting agarose. Once solidified, the embedded sections were sectioned using a compressotome (from which 10  $\mu\text{m}$  sections were obtained) or cut into 1-2 mm rings. The agarose embedded rings and sections were then cultured in 3 mM  $P_i$  enriched media for 7 days. Once calcified, the sections were fixed, followed by removal of agarose upon gentle heating. In a second experiment, the non embedded aorta were cut into 1-2 mm rings and then calcified in 3 mM  $P_i$  enriched media after which they were either analysed as rings or cryo-sectioned in optimal cutting temperature (OCT) medium and analysed as sections.

When analysed by Raman spectroscopy, both embedded and non-embedded aortic rings and OCT samples gave a higher background signal in comparison to the agarose sections and therefore the latter were selected for further analysis. Gentle heating allowed for the majority of the agarose to be dissolved and washed off, however, a small amount was present when the aortae were analysed. Nonetheless, the remains of agarose had no impact on the HAP peak, which, as for the peak observed in cell models was visualised at  $960\text{ cm}^{-1}$  (Figure 5.11 A). The peak at  $960\text{ cm}^{-1}$  only appears in the calcified sample and is not present in the control; within the calcified sample the signal is obtained in the medial layer of the aorta which is consistent with the fluorescence signal obtained from the Fluorescein-BP (55) in Chapter 3. The peak found in the calcified samples co-localizes with the Alizarin S stain (Figure 5.11 B-C) carried out on the rings and correspondingly there was no staining present in the control sample (Figure 5.11 C). Once again, the Raman signal for HAP was mainly present in the medial layer of the aorta (Figure 5.11 B).

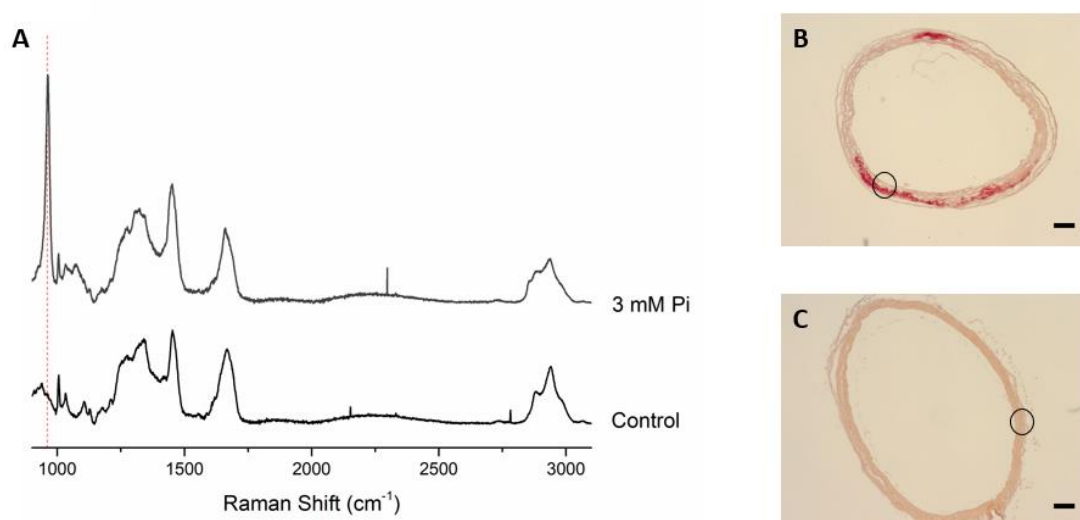


**Figure 5.11: Raman and Alizarin on aortic ring sections.** (A) Raman spectra of calcified and control aortic ring sections. Raman spectroscopy of cell monolayer obtained using Renishaw InVia, 785 nm laser, 30 s, 100%. Spectra are offset for clarity and normalized to the phenylalanine peak ( $1003\text{ cm}^{-1}$ ). Red dashed line indicative of the  $960\text{ cm}^{-1}$  peak (HAP). (B) Alizarin of aortic ring calcified at 3 mM Pi for 7 days (C) Alizarin S of aortic ring cultured in control media for 7 days. Black circles indicate areas where the Raman spectra were taken. Spectra and images are representative of at least three repeats. Scale bars = 0.1 cm.

## 5.8 Raman on calcified human samples analysis and comparison to PET/CT

Rodent models offer the possibility of investigating the pathology of cardiovascular disease however, as mentioned in Chapter 4, they have several limitations. For this reason, the ability to analyse and assess human tissues is key in understanding disease progression and prevention. Human tissue samples were obtained from a collaboration with a PhD student, Alastair Moss, MD, in Marc Dweck's group (UoE). Samples which had been collected during autopsy from victims of sudden death (Appendix 2), were imaged by PET/CT using Na<sup>18</sup>F PET tracer and divided into three categories (Table 5.3). The tissue was subsequently processed and embedded in paraffin wax prior to Raman analysis.

**Table 5.3: Study patient population.** Tissue samples are divided into three groups: No PET/CT activity, CT active and PET active.

<b>Number of samples</b>	<b>No PET/CT activity</b>	<b>CT activity</b>	<b>PET activity</b>
1	4	3	

PET/CT imaging using Na<sup>18</sup>F has been reported as a novel tool for vascular disease diagnosis.<sup>49,50</sup> Na<sup>18</sup>F can be used to identify areas of micro-calcification that are associated with an unstable plaque phenotype, and which are beyond the resolution of CT. Indeed, Na<sup>18</sup>F PET is currently being explored as a method for detecting high risk coronary plaques and improving cardiovascular risk prediction (clinicaltrials.gov NCT02278211).<sup>49-51</sup>

Embedding samples in paraffin wax comes with its disadvantages as paraffin's Raman spectrum has peaks in the regions of amide I, III and in other areas in the low wavenumber regions which overlap with signals obtained from tissue samples. Recent literature reported that, when paraffin embedded, tissues require at least 30 minutes in xylene and ethanol to completely remove the paraffin.<sup>52</sup> However, there is a fine balance between removal of paraffin and deterioration of tissue structure, as xylene can interfere with the lipid peaks.<sup>52</sup> The report mentioned that there are computational methods such as independent component analysis (ICA), partial least square (PLS) and independent component partial least square (IC-PLS) that would allow the removal of paraffin peaks. However, for the purpose of this study, and the interest in the spectral window around 940-1010 cm<sup>-1</sup> which displays no paraffin bands, no computational tools were required.

The vascular tissue obtained was embedded, sectioned and subsequently placed on CaF<sub>2</sub> slides. Once dried, the slides were placed in xylene for 15 minutes followed by dehydration in ethanol.

As soon as they were dehydrated the sections were ready for imaging and did not require additional processing. Sections from tissue presenting no calcium or fluoride signal (control, *Figure 5.12 A, D*), high calcium signal (CT active, *Figure 5.12 C, F*) as well as high fluoride signal (PET active, *Figure 5.12 B-E*) were selected in order to address whether there were any differences in the apatite crystallinity and/or any molecular substitution in the structure.

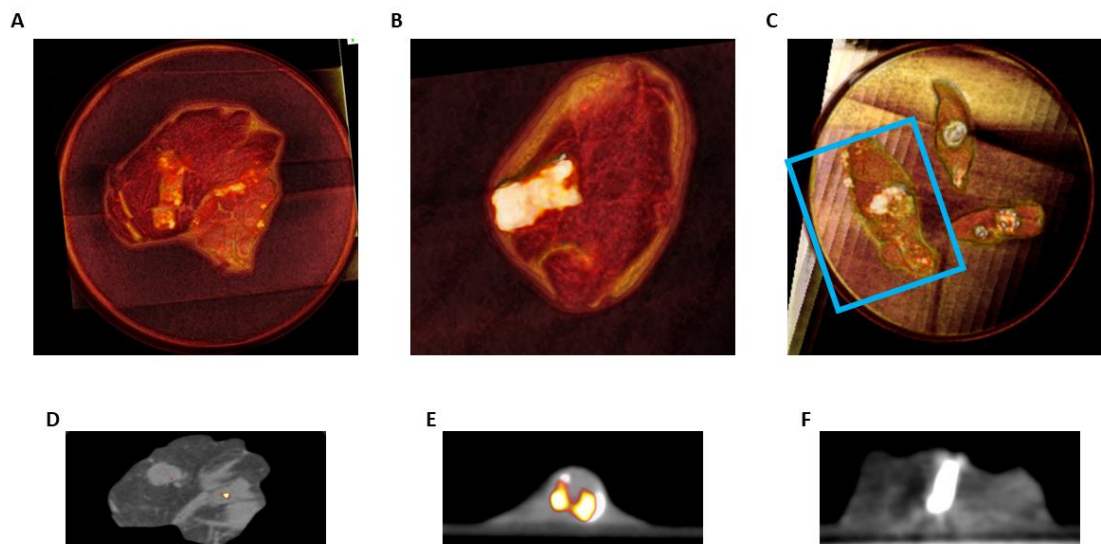


**Figure 5.12** PET/CT activity of the different tissue classes. (A-C) volume rendered image of the tissue. (D-F) close up of the tissue. (A, D) tissue which shows no PET/CT activity, (B,E) tissue that presents PET activity and (C,F) tissue that shows CT activity only. Blue box indicative of which tissue was selected in image C.

Spectra from tissues with high calcium signal, and little to no fluoride signal, displayed macroscopic HAP (*Figure 5.13 D*). Around the plaque and plaque rupture area, however they also displayed the presence of another apatite species, WTK (*Figure 5.13 C*). WTK has been analysed by Raman spectroscopy and has been reported to be present in vascular tissue by You *et al.*<sup>5</sup> in early 2018. Analysis of 4 samples presenting high CT activity showed areas of WTK surrounding the larger HAP macrocalcification. When peak fitting, on Origin, what appeared to be the WTK spectrum obtained from the highly calcified tissue which did not display any fluoride signal, it was apparent that there were two overlapping peaks which belong to HAP and WTK (*Figure 5.13 F*). When analysing the area under the curves, there appears to be a 30:70 ratio between HAP and WTK.

Spectra from tissue reporting high fluoride signal on the other hand, showed no WTK (*Figure 5.13 B*) but microscopic HAP deposits. The Raman analysis was followed by Alizarin S staining which showed that this commonly used stain was unable to discriminate between the two calcium species (as reported in Chapter 2).

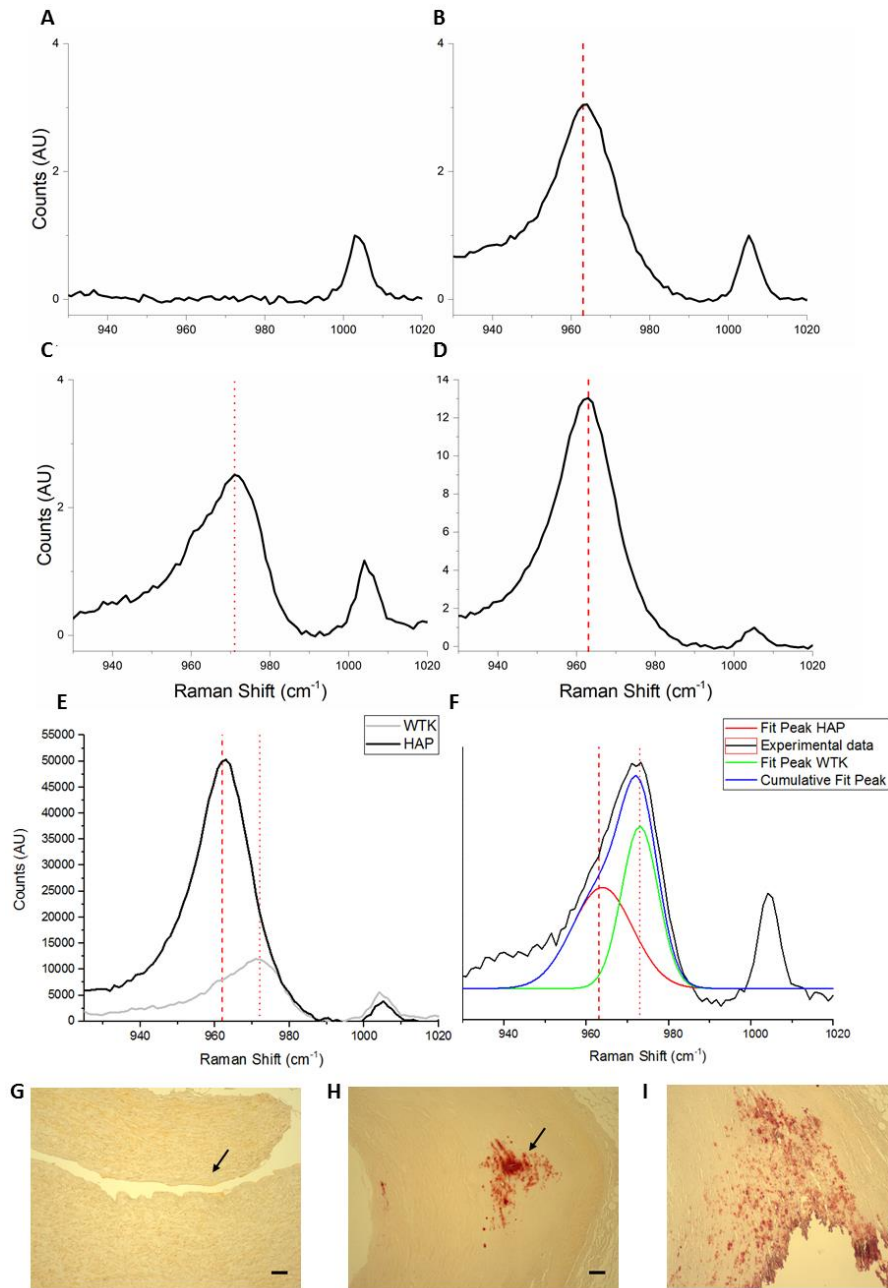


**Figure 5.13 Raman spectroscopy (A-F) and Alizarin S staining (G-I) analysis of control, PET active and CT active vascular tissue.** Tissue was embedded in paraffin wax and sectioned into 5  $\mu\text{m}$  sections and placed on  $\text{CaF}_2$  slides. Sections were dehydrated using xylene and ethanol washes and then imaged using Renishaw InVia, laser 785 nm, 60 s, 100% laser power. Following Raman imaging, the monolayer was incubated with 2% Alizarin S (5 minutes), washed three times with water and then imaged. Arrows are indicative of the location imaged by Raman spectroscopy, black areas where no HAP or HAP was found while purple arrow indicates area where WTK was found. (A) and (G) represent Raman spectrum and Alizarin S image of control sample, (B) and (H) represent PET active sample while (C, D) and (I) represent CT active sample. (E) Represents overlaid WTK and HAP spectra obtained from CT active sample (C, D), while (F) shows the peak fitted analysis of the WTK experimental spectrum showing the presence of both HAP and WTK. Red dotted line are indicative of the  $970\text{ cm}^{-1}$  peak (WTK), red dashed line representative of the  $960\text{ cm}^{-1}$  peak (HAP). Scale bars = 0.2 cm.

However, one of the three PET active samples, in contrast to the other two, exhibited small amounts of WTK around areas where larger calcification deposits were visible (spectrum not shown). This sample belonged to a patient who had diabetes mellitus which would explain the presence of high levels of magnesium in the body and therefore the substituted apatites.

The presence of WTK has been reported previously in patients with uraemia and end-stage renal disease, where nanocrystals analysis showed the presence of both HAP and WTK.<sup>53,54</sup> In patients presenting with uraemia, WTK had been described as a preliminary stage in soft tissue calcification prior to HAP deposition, however, the number of studies investigating WTK is subordinate to those reporting HAP and ACP in uremic vascular calcification,<sup>53,55</sup> while in end-stage renal disease studies, WTK has been described in advanced conditions.<sup>54</sup> Surprisingly, before 2010, WTK had rarely been reported to be a component of vascular calcification.

The WTK studies resulted in the development of novel models to address the role of magnesium in cell studies. In some cell-based models, magnesium is shown to have a protective role in living organisms.<sup>56</sup> Other literature also illustrates how magnesium significantly reduces calcification both in bovine as well as human primary VSMCs, in addition to downregulating known pro-calcification markers and upregulating anti-calcification markers towards restoring more physiological conditions.<sup>56,57</sup> Louvet *et al.* were one of the first groups to show the inhibitory effect that magnesium has on hydroxyapatite formation and precipitation. Their *in vitro* work showed that magnesium was able to stabilize amorphous calcium phosphate and inhibit the formation of HAP by forming WTK.<sup>32,56,57</sup>

Louvet's analysis elucidates the potential role of WTK around areas of macrocalcification in the analysed CT active samples. However, when WTK and HAP (*Figure 5.14*) and CaPi, CaOx, CaPyr (*Chapter 4, Figure 4.2*) were analysed by PET/CT, no fluoride uptake was observed for both CaOx and CaPyr, but no difference was observed between the uptake by WTK, CaPi and HAP, indicating that Na<sup>18</sup>F uptake is not specific to HAP and therefore cannot give any anatomical information on the morphology of the crystals in the vascular tissue. On the other hand, Raman spectroscopy is able to distinguish between the species and is therefore able to provide additional information that PET lacks.



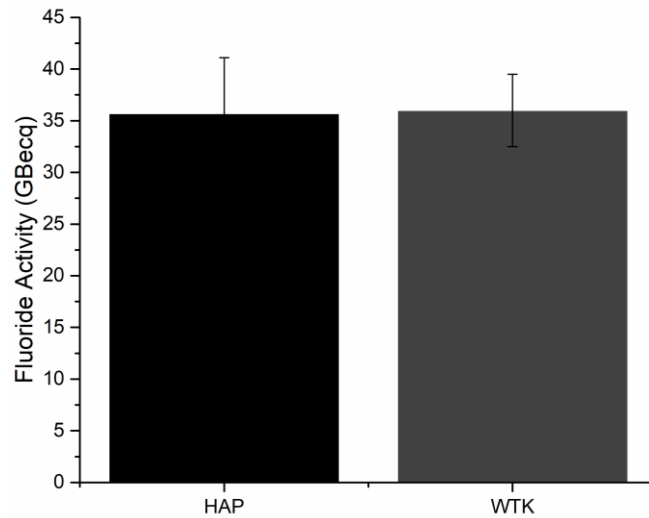


**Figure 5.14: HAP and WTK incubation with  $Na^{18}F$ .** HAP and WTK were incubated with  $Na^{18}F$  for 20 minutes and then scanned using PET/CT scanner. Data shown is an average of three independent results and are shown as the mean  $\pm$  S.E.M.

## 5.9 Conclusion

Raman spectroscopy has been a useful tool in the study of vascular calcification to address the specific nature of the mineral phase for both *in vitro* and *ex vivo* models. In cell models, calcium and phosphate enriched media promotes the deposition of hydroxyapatite. It is surprising that no other species is detectable, especially ACP, a precursor of HAP. But this could be due to the immediate conversion, during fixation, of any ACP to HAP as the latter is more thermodynamically stable.<sup>53,58</sup> Interestingly, the level of calcification is different for different primary cells. This could be due to the VSMCs being more prone to a change in phenotype, and therefore extracellular matrix component production, however, in order to validate this, additional studies employing immunofluorescence targeting cytoskeleton markers are required. These studies would help elucidate whether VSMCs are more prone to phenotypical change when compared to VICs. In *ex vivo* human tissue models, HAP was not the only mineral observed. WTK co-existed with HAP in tissue samples which showed high CT activity but not in tissue with high PET activity. However, due to the limited number of samples no definite conclusion can be made as to whether WTK was present due to a tolerance mechanism of the cells to inhibit HAP production, or whether it was caused by the disease or diet. Additional studies, with a larger sample population, and more detailed medical charts on the tissue provenance are required to address the active role of WTK in vascular calcification caused by atherosclerosis.

## 5.10 References

- 1 K. J. I. Ember, M. A. Hoeve, S. L. McAughtrie, M. S. Bergholt, B. J. Dwyer, M. M. Stevens, K. Faulds, S. J. Forbes and C. J. Campbell, *npj Regen. Med.*, 2017, **2**, 12.
- 2 A. Smekal, *Naturwissenschaften*, 1923, **11**, 873–875.
- 3 C. V. Raman and K. S. Krishnan, *Nature*, 1928, **121**, 501–502.
- 4 H. A. Szymanski, *Raman Spectroscopy : Theory and Practice*, Springer US, 1967.
- 5 A. Y. F. You, M. S. Bergholt, J. P. St-Pierre, W. Kit-Anan, I. J. Pence, A. H. Chester, M. H. Yacoub, S. Bertazzo and M. M. Stevens, *Sci. Adv.*, 2017, **3**, e1701156.
- 6 G. Bruno, *Raman Eff. A Unified Treat. Theory Raman Scatt. by Mol.*, 2002, **8**, 31–48.
- 7 D. A. Long, *The Raman Effect*, John Wiley & Sons, Ltd, Chichester, UK, 2002.
- 8 H. J. Butler, L. Ashton, B. Bird, G. Cinque, K. Curtis, J. Dorney, K. Esmonde-white, N. J. Fullwood, B. Gardner, P. L. Martin-Hirsch, M. J. Walsh, M. R. Mcainsh, N. Stone and F. L. Martin, *Nat. Protoc.*, 2016, **11**, 664–687.
- 9 M. D. Morris and G. S. Mandair, *Clin. Orthop. Relat. Res.*, 2011, **469**, 2160–9.
- 10 A. Downes and A. Elfick, *Sensors*, 2010, **10**, 1871–1889.
- 11 D. A. Long, in *The Raman Effect*, John Wiley & Sons, Ltd, Chichester, UK, pp. 85–152.
- 12 M. B. Peres, L. Silveira, R. A. Zângaro, M. T. T. Pacheco and C. A. Pasqualucci, *Lasers Med. Sci.*, 2011, **26**, 645–655.
- 13 S. Wachsmann-Hogiu, T. Weeks and T. Huser, *Chemical analysis in vivo and in vitro by Raman spectroscopy-from single cells to humans*, Elsevier Current Trends, 2009, vol. 20.
- 14 K. Kong, C. Kendall, N. Stone and I. Notingher, *Adv. Drug Deliv. Rev.*, 2015, **89**, 121–134.
- 15 W. J. Tipping, M. Lee, A. Serrels, V. G. Brunton and A. N. Hulme, *Chem. Soc. Rev.*, 2016, **45**, 2075–2089.
- 16 E. Gentleman, R. J. Swain, N. D. Evans, S. Boonrungsiman, G. Jell, M. D. Ball, T. A. V. Shean, M. L. Oyen, A. Porter and M. M. Stevens, *Nat. Mater.*, 2009, **8**, 763–770.
- 17 L.-P. Choo-Smith, H. G. M. Edwards, H. P. Endtz, J. M. Kros, F. Heule, H. Barr, J. S. Robinson, H. A. Bruining and G. J. Puppels, *Biopolymers*, 2002, **67**, 1–9.
- 18 H. P. Buschman, G. Deinum, J. T. Motz, M. Fitzmaurice, J. R. Kramer, A. Van Der Laarse, A. V Brusckke and M. S. Feld, *Cardiovasc. Pathol.*, 2001, **10**, 69–82.
- 19 P. Matousek, E. R. C. Draper, A. E. Goodship, I. P. Clark, K. L. Ronayne and A. W. Parker, *Appl. Spectrosc.*, 2006, **60**, 758–763.

- 20 A. Lattermann, C. Matthäus, N. Bergner, C. Beleites, B. F. Romeike, C. Krafft, B. R. Brehm and J. Popp, *J. Biophotonics*, 2013, **6**, 110–121.
- 21 K. Czamara, J. Natarska, P. Kapusta, M. Baranska and A. Kaczor, *Analyst*, 2015, **140**, 2164–2170.
- 22 R. J. Swain and M. M. Stevens, *Biochem. Soc. Trans.*, 2007, **35**, 544–549.
- 23 I. Notingher and L. L. Hench, *Expert Rev. Med. Devices*, 2006, **3**, 215–234.
- 24 M. M. Kerssens, P. Matousek, K. Rogers and N. Stone, *Analyst*, 2010, **135**, 3156–61.
- 25 C. Delogne, P. V. Lawford, S. M. Habesch and V. A. Carolan, *J. Microsc.*, 2007, **228**, 62–77.
- 26 M. Pilarczyk, K. Czamara, M. Baranska, J. Natarska, P. Kapusta, A. Undas and A. Kaczor, *J. Raman Spectrosc.*, 2013, **44**, 1222–1229.
- 27 R. Manoharan, J. J. Baraga, M. S. Feld and R. P. Rava, *J. Photochem. Photobiol. B Biol.*, 1992, **16**, 211–233.
- 28 C. Liu, S. Boydston-White, A. Weisberg, W. Wang, L. A. Sordillo, A. Perotte, V. P. Tomaselli, P. P. Sordillo, Z. Pei, L. Shi and R. R. Alfano, *J. Biomed. Opt.*, 2016, **21**, 127006.
- 29 O. Tzang, K. Kfir, E. Flaxer, O. Cheshnovsky and S. Einav, *Cardiovasc. Eng. Technol.*, 2011, **2**, 228–233.
- 30 J. S. Lee, J. D. Morrisett and C.-H. Tung, *Atherosclerosis*, 2012, **224**, 340–7.
- 31 S. J. Gadaleta, E. P. Paschalis, F. Betts, R. Mendelsohn and A. L. Boskey, *Calcif. Tissue Int.*, 1996, **58**, 9–16.
- 32 S. C. Verberckmoes, V. Persy, G. J. Behets, E. Neven, A. Hufkens, H. Zebger-Gong, D. Müller, D. Haffner, U. Querfeld, S. Bohic, M. E. De Broe and P. C. D’Haese, *Kidney Int.*, 2007, **71**, 298–303.
- 33 M. Abedin, Y. Tintut and L. L. Demer, *Arterioscler. Thromb. Vasc. Biol.*, 2004, **24**, 1161–1170.
- 34 A. S. Black and I. O. Kanat, *J. Foot Surg.*, **24**, 243–50.
- 35 G. Luo, P. Ducey, M. D. McKee, G. J. Pinero, E. Loyer, R. R. Behringer and G. Karsenty, *Nature*, 1997, **386**, 78–81.
- 36 R. P. Metz, J. L. Patterson and E. Wilson, *Vascular smooth muscle cells: Isolation, culture, and characterization*, Humana Press, Totowa, NJ, 2012, vol. 843.
- 37 S. Lim and S. Park, *BMB Rep.*, 2014, **47**, 1–7.
- 38 A. Rudijanto, *Acta Med. Indones.*, **39**, 86–93.
- 39 MacRae, *Int. J. Mol. Med.*, 2011, **27**, 663–8.
- 40 C. M. Shanahan, M. H. Crouthamel, A. Kapustin and C. M. Giachelli, *Circ. Res.*, 2011,

- 109, 697–711.
- 41 A. C. Liu, V. R. Joag and A. I. Gotlieb, *Am. J. Pathol.*, 2007, 171, 1407–1418.
- 42 N. M. Rajamannan, F. J. Evans, E. Aikawa, K. J. Grande-Allen, L. L. Demer, D. D. Heistad, C. A. Simmons, K. S. Masters, P. Mathieu, K. D. O'Brien, F. J. Schoen, D. A. Towler, A. P. Yoganathan and C. M. Otto, *Circulation*, 2011, **124**, 1783–91.
- 43 A. Rutkovskiy, A. Malashicheva, G. Sullivan, M. Bogdanova, A. Kostareva, K. O. Stensløyken, A. Fiane and J. Vaage, *J. Am. Heart Assoc.*, 2017, **6**, e006339.
- 44 N. T. Lam, T. J. Muldoon, K. P. Quinn, N. Rajaram and K. Balachandran, *Integr. Biol. (Camb)*, 2016, **8**, 1079–1089.
- 45 T. Afroze, L. L. Yang, C. Wang, R. Gros, W. Kalair, A. N. Hoque, I. N. Mungrue, Z. Zhu and M. Husain, *AJP Cell Physiol.*, 2003, **285**, C88–C95.
- 46 H. Paul, A. J. Reginato and H. R. Schumacher, *Arthritis Rheum.*, 1983, **26**, 191–200.
- 47 T. Akiyoshi, H. Ota, K. Iijima, B. K. Son, T. Kahyo, M. Setou, S. Ogawa, Y. Ouchi and M. Akishita, *Atherosclerosis*, 2016, **244**, 51–58.
- 48 K. A. Lomashvili, S. Cobbs, R. A. Hennigar, K. I. Hardcastle and W. C. O'Neill, *J. Am. Soc. Nephrol.*, 2004, **15**, 1392–1401.
- 49 A. Irkle, A. T. Vesey, D. Y. Lewis, J. N. Skepper, J. L. E. Bird, M. R. Dweck, F. R. Joshi, F. A. Gallagher, E. A. Warburton, M. R. Bennett, K. M. Brindle, D. E. Newby, J. H. Rudd and A. P. Davenport, *Nat. Commun.*, 2015, **6**, 7495.
- 50 M. R. Dweck, M. K. Doris, M. Motwani, P. D. Adamson, P. Slomka, D. Dey, Z. A. Fayad, D. E. Newby and D. Berman, *Nat. Rev. Cardiol.*, 2016, **13**, 533–548.
- 51 P. D. Adamson, A. T. Vesey, N. V. Joshi, D. E. Newby and M. R. Dweck, *Cardiovasc. Diagn. Ther.*, 2015, **5**, 150–155.
- 52 P. Meksiarun, M. Ishigaki, V. A. C. Huck-Pezzei, C. W. Huck, K. Wongravee, H. Sato and Y. Ozaki, *Sci. Rep.*, 2017, **7**, 44890.
- 53 G. Schlieper, A. Aretz, S. C. Verberckmoes, T. Kruger, G. J. Behets, R. Ghadimi, T. E. Weirich, D. Rohrmann, S. Langer, J. H. Tordoir, K. Amann, R. Westenfeld, V. M. Brandenburg, P. C. D'Haese, J. Mayer, M. Ketteler, M. D. McKee and J. Floege, *J. Am. Soc. Nephrol.*, 2010, **21**, 689–696.
- 54 D. C. Fischer, G. J. Behets, O. W. Hakenberg, M. Voigt, B. A. Vervaet, S. Robijn, G. Kundt, W. Schareck, P. C. D'Haese and D. Haffner, *Calcif. Tissue Int.*, 2012, **90**, 465–472.
- 55 R. Lagier and C.-A. Baud, *Pathol. - Res. Pract.*, 2003, **199**, 329–335.
- 56 L. Louvet, J. Buchel, S. Steppan, J. Passlick-Deetjen and Z. A. Massy, *Nephrol. Dial. Transplant.*, 2013, **28**, 869–878.

- 57 L. Louvet, D. Bazin, J. Büchel, S. Steppan, J. Passlick-Deetjen and Z. A. Massy, , DOI:10.1371/journal.pone.0115342.
- 58 S. Boonrunsiman, E. Gentleman, R. Carzaniga, N. D. Evans, D. W. McComb, A. E. Porter and M. M. Stevens, *Proc. Natl. Acad. Sci.*, 2012, **109**, 14170–14175.

## Chapter 6- Conclusion and Future Work

In chapter 1 we discussed the importance of detecting vulnerable atherosclerotic plaques and how the limitations of the current imaging modalities available to study CVD is lacking in valuable patient diagnosis and positive outcomes. The only available technique that has shown to somewhat detect vulnerable plaques is PET with the use of Na<sup>18</sup>F bone marker. However, the understanding of the mode of action this probe and why it binds to vulnerable plaques and not stable ones is yet to be understood.

We dealt with this problem, in chapter 2, by synthesising a range of fluorescent probes to study the PET tracer as well as to look directly at the vulnerable plaques, mainly the HAP protective layer. Three fluoride specific optical probes were synthesised, two based on the cyanoacrylate motif and one based on rhodamine. Their selectivity towards anions, specifically, fluoride was tested and only the rhodamine-based probe showed selectivity. However, unfortunately the concentration required to activate the rhodamine-based probe was too high in comparison to the MBq amount of Na<sup>18</sup>F which is used in humans.

The other way of assessing vulnerable plaques is by using fluorescent probes conjugated to HAP selective molecules. A number of fluorophores were explored (Cy5.5, Cy7 and fluorescein) and were either reacted with alendronate, an FDA approved BPs, or a HAP-selective peptide. Selectivity tests to address whether the probes were selective to HAP and would not interact with any other calcium minerals were performed and showed that only the alendronate conjugated fluorophore was selective for HAP while the HAP selective peptide, although conjugated to a different fluorophore, would interact with all species equally. Ideally, both alendronate and HAP selective peptide should have been coupled to the same fluorophore to be certain that the alendronate was more selective. Their binding was also compared to Alizarin S, the gold standard stain for HAP, which showed that the alendronate conjugate was more selective than Alizarin S as the latter interacted in a similar fashion to the HAP selective peptide indicating the significant opportunity that the alendronate probe could provide in the detection of HAP.

Fluorescein-BP (**55**) was then used in cell and *ex vivo* studies. Toxicity studies and localization studies were carried out first and showed that at the concentration used the probe does not cause cell apoptosis. Confocal imaging of the MOVAS-1 cell monolayer confirmed what had previously been reported, the probe was localizing between cells in the extracellular matrix

where the HAP crystals were depositing. Comparative studies with the calcium leaching assay as well as Alizarin S stain showed that in both condition-specific and temporal studies of CVD, the Fluorescein-BP is less time consuming and more sensitive than both assays which could allow the probe to be used for high-throughput multi-well analysis of calcification. Fluorescein-BP was also able to detect calcification in MC3T3 cells showing the versatility of the probe and the potential to use to study other diseases that involve HAP deposition.

Fluorescein-BP was also used on *ex vivo* WT aortic sections as well as *ApoE*<sup>-/-</sup> mouse sections and in both instances shows to bind to intraplaque calcification. *ApoE*<sup>-/-</sup> are genetically modified mice that have been fed on a high fat diet and therefore should present symptoms and plaque morphology similar to the ones found in humans. Upon closer inspection of the intraplaque calcification, two different types of deposits were visible. Larger macrocalcification and smaller microcalcification were both detected using Fluorescein-BP while Von Kossa was only able to detect the larger deposits suggesting that this probe can be used as a tool to study early detection of calcification.

Animal models have provided a good tool to investigate the pathology of CVD however, there are key limitations when studying the disease using rodents. For this reason, in chapter 4 calcified coronary and carotid human tissue were also assessed. Coronary and carotid tissue, calcified and control samples, were sectioned and stained with Fluorescein-BP and Alizarin S. With these samples, we demonstrated that Fluorescein-BP is a highly sensitive and specific biomarker for HAP in human tissue and when compared to Alizarin S co-localizes in the same area. When compared to the current techniques used in the clinic to detect calcification, PET and CT, Fluorescein-BP is able to detect both type of stable and unstable calcification which neither PET nor CT can do, suggesting that the probe could have a potential application in the clinic to detect early stage vulnerable calcification. Biomarkers that only detect early stage calcification could also have a role in early diagnosis of CVD. In chapter 4, OPG and OPN as two potential markers were assessed on both carotid and coronary vascular tissue and both are present in high concentrations in vulnerable tissue while go undetected in control or stable vascular tissue.

In the last chapter, chapter 5, we looked at using Raman spectroscopy to detect calcification in vascular tissue. Throughout the thesis the biggest focus has been on the detection of HAP which has a strong characteristic Raman peak at 960 cm<sup>-1</sup>. Studies to address whether this peak was present in calcified cell models, *ex vivo* sections and human sections were carried out showing that, in both cells and *ex vivo* sections, the characteristic peak at 960 cm<sup>-1</sup> is present and its intensity increases with increasing degree of calcification. However, when assessing

human tissue, a different peak at  $973\text{ cm}^{-1}$ , WTK, appears in areas that are stained with Alizarin S. This peak nevertheless, only appears in tissue samples that have stable phenotype and not present in vulnerable plaques. Various assumptions have been made on the role of WTK in cell and tissue models but additional studies are required to determine its actual role in vascular tissue.

In this thesis we discussed the development of a highly fluorescent probe for the detection of HAP *in vitro* and with the potential of *in vivo* applications. The probe has shown to be more selective than the current techniques which are used in the lab and the clinic with Alizarin S stain and Von Kossa binding to any calcium or any phosphate respectively and with  $\text{Na}^{18}\text{F}$  PET/CT not being able to distinguish between WTK and HAP. The probe has shown to have great sensitivity *in vitro* and *ex vivo* mouse and human vascular tissue. The probe is synthesised with two low cost reagents which have been approved by the FDA, making the translatability of this probe from the bench to humans easier. Future *in vivo* studies in mouse and humans are required and might be enabled by intravascular administration of the Fluorescein-BP probe using catheters fitted with a confocal endomicroscope probe. This would negate the need for use of costly NIR dye, such as Osteosense, as endomicroscope probes do not require the fluorophore to be detectable through the skin.



# Chapter 7- Materials and Methods

## 7.1 Synthesis

### 7.1.1 General Information

All non-aqueous reactions were carried out under an atmosphere of dry nitrogen using oven-dried glassware that was cooled under a dry nitrogen atmosphere. Unless otherwise noted, starting materials and reagents were obtained from commercial suppliers and were used without further purification. Toluene, THF, MeCN, MeOH and DCM were dried and purified by passage through activated alumina columns using a Glass Contour Solvent Purification System. Saturated aqueous solutions of inorganic salts are represented as (volume, sat. aq.). On resin chemistry was performed on functionalised 1% DVB cross-linked chloromethyl polystyrene with a loading capacity of 1.75 mmol g<sup>-1</sup> and performed using SPE tubes, draining to a vacuum box and agitation on a Stuart B2 tube spinner at 20 rpm.

For peptide synthesis, all amino acids and resins were purchased from either Novasyn (Merck) or Sigma-Aldrich. All amino acids were *N*-Fmoc protected and side chains were protected with Boc (Lys); *O*<sup>t</sup>Bu (Ser); Pbf (Arg). All peptides were synthesised on Rink Amide AM PS resin with a loading capacity of 0.69 mmol g<sup>-1</sup>. Synthesis of peptides was performed manually using SPE tubes, draining to a vacuum box and agitation on a Stuart B2 tube spinner at 20 rpm, while monitoring of coupling steps was performed using tandem chloranil and TNBS testing

<sup>1</sup>H and <sup>13</sup>C NMR spectra were obtained on Bruker instruments at the stated frequency using TMS as a reference and residual solvent as an internal standard. Infra-red spectra were recorded neat on a Shimadzu IRAffinity-1. Electrospray (ESI) mass spectra were obtained on a Bruker micrOTOF II instrument. ESI-MS was performed in positive ion as well as negative ion mode on a liquid chromatography-ion trap mass spectrometer. Mass to charge ratios (*m/z*) of all parent (molecular) ions ([M]<sup>+/-</sup>) and their intensities are reported, followed by (major) fragment or adduct ions and their intensities. UV/VIS absorption spectra were measured at room temperature with a Shimadzu UV-1800 spectrometer with a 1.0 cm glass cell. The scanning speed was set to fast with a sampling interval of 0.1. The scan mode was set to repeats with 5 scans for each sample. Fluorescence spectra were measured using a Horiba Fluoromax-

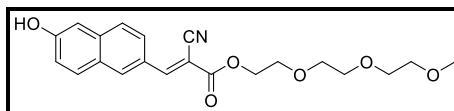
3 spectrometer, scanning the necessary range by 0.50 nm increments, 0.50 seconds integration time and each spectrum reported as an average of 5 scans.

Melting points were determined on a Gallenkamp Electrothermal Melting Point apparatus and are uncorrected. Flash chromatography was carried out using Merck Kieselgel 60 (Merck 9385) under positive pressure unless stated otherwise. Eluent compositions are quoted as v/v ratios. Preparative reverse phase HPLC was conducted on a Waters® 600 (225  $\mu$ L) system using a 486 tuneable absorbance detector recording at 210 nm equipped with a Phenomenex® Luna C18(2), 5  $\mu$ m, 250  $\times$  21.2 mm column using H<sub>2</sub>O (0.1% TFA) and acetonitrile (0.1% TFA) as eluent at a flow rate of 18 mL min<sup>-1</sup>.

Raman imaging was carried out using an InVia Renishaw Microscope with a 785 nm laser excitation source which was used to excite the sample through a 50, N.A. 0.75 objective. The total data acquisition was performed during 30 s for spectra with a 50% laser power using the WiRE software. All the spectra acquired were background subtracted using a background correction algorithm present on WiRE software.

### 7.1.2 Fluoride sensor

#### 2-cyano-3-(6-hydroxy-2-naphthalenyl)-1-2-[2-(2-methoxyethoxy)ethoxy]ethyl ester (**3**)

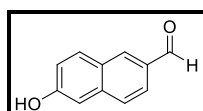


A solution of 6-hydroxy-2-naphthaldehyde (**6**) (100 mg, 0.50 mmol, 1 eq) in THF (6 mL) was added to a mixture of 2-(2-(2-methoxyethoxy)ethoxy)-ethyl 2-cyanoacetate (**7**) (130 mg, 0.50 mmol, 1 eq) and DMAP (10.0 mg, 0.10 mmol, 0.2 eq). The reaction was stirred at 60 °C for 24 h. When the reaction was complete (checked by TLC), it was cooled to rt and then concentrated *in vacuo*. Purification by column chromatography (50% EtOAc in hexane) gave the title compound **3** as yellow solid (160 mg, 72%)

**R<sub>f</sub>** (EtOAc:hexane, 1:1) = 0.36; **mp** 135-137 °C, lit<sup>1</sup> 137-138 °C; **IR** (solid, cm<sup>-1</sup>): 3304 (O-H), 2218 (C≡N), 1697 (C=O), 1622 (C=C), 1589 (C=C), 1110 (C-O-C); **<sup>1</sup>H NMR** (500 MHz, CDCl<sub>3</sub>)  $\delta$  8.07 (1H, s, *CHCCN*), 8.02 (1H, s, *ArH*), 7.98 (1H, dd, *J* = 8.8, 1.8 Hz, *ArH*), 7.79 (1H, d, *J* = 8.6 Hz, *ArH*), 7.69 (1H, d, *J* = 8.8 Hz, *ArH*), 7.19 – 7.16 (1H, m, *ArH*), 7.16 (1H, s, *ArH*), 4.48–4.46 (2H, m, COOCH<sub>2</sub>), 3.89–3.86 (2H, m, COOCH<sub>2</sub>CH<sub>2</sub>), 3.81–3.78 (2H, m, CH<sub>2</sub>), 3.74 (2H, dd, *J* = 5.8, 2.8 Hz, CH<sub>2</sub>), 3.69–3.66 (2H, m, CH<sub>2</sub>), 3.55 – 3.53 (2H, m, CH<sub>2</sub>), 3.32 (3H, s, OCH<sub>3</sub>); **<sup>13</sup>C NMR** (126 MHz, CDCl<sub>3</sub>)  $\delta$  162.89 (CN), 156.99 (C=O), 154.83 (=CH), 137.27 (Ar C), 134.42 (Ar CH), 131.71 (Ar CH), 127.90 (Ar C), 127.40 (Ar CH),

126.61 (Ar C), 126.05 (Ar CH), 119.49 (Ar CH), 115.90 (Ar C), 109.88 (Ar CH), 100.14 (C), 71.89 (CH<sub>2</sub>), 70.81 (CH<sub>2</sub>), 70.66 (CH<sub>2</sub>), 70.59 (CH<sub>2</sub>) 68.86 (CH<sub>2</sub>), 65.61 (CH<sub>2</sub>), 59.00 (CH<sub>3</sub>); *m/z* (ESI+, H<sub>2</sub>O:MeOH): 386 ([M+H]<sup>+</sup>, 95%), 266 (100), 222 (90). <sup>1</sup>H and <sup>13</sup>C spectroscopic data in good agreement with literature.<sup>1</sup>

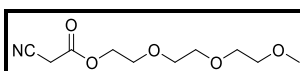
### 6-Hydroxy-2-naphthaldehyde (6)



AlCl<sub>3</sub> (1 g, 7.5 mmol, 3 eq) was added to a solution of 6-methoxy-2-naphthaldehyde (**8**) (500 mg, 2.6 mmol, 1 eq) in chlorobenzene (15 mL) and the reaction mixture was heated under reflux at 130 °C for 4 hours. The reaction was followed by TLC and when completed, the solution was cooled to rt. The mixture was added to HCl (20 ml; 5 N aq.) and was extracted with chloroform (20 mL). The organic layer was then concentrated under reduced pressure. Purification by column chromatography (15% EtOAc in hexane) gave the phenol **6** as a yellow oil (0.10 g, 20%).

**R<sub>f</sub>** (EtOAc:hexane, 15:85) = 0.25; <sup>1</sup>H NMR (500 MHz, CDCl<sub>3</sub>) δ 10.06 (1H, s, CHO), 8.23 (1H, s, ArH), 7.89 (1H, bd, *J*=8.9, 0.7 Hz, ArH), 7.88 (1H, dd, *J*=8.6, 1.6 Hz, ArH), 7.73 (1H, d, *J*=8.6 Hz, ArH), 7.17 (1H, dd, *J*=8.9, 2.5 Hz ArH), 7.16 (1H, d, *J*=2.5 Hz, ArH); <sup>13</sup>C NMR (126 MHz, CDCl<sub>3</sub>) δ 191.98 (CHO), 156.24 (Ar C), 138.20 (Ar C), 134.50 (Ar CH), 132.45 (Ar C), 131.78 (Ar CH), 128.96 (Ar C), 127.44 (Ar CH), 123.74 (Ar CH), 118.96 (Ar CH), 109.99 (Ar CH); *m/z* (ESI+, H<sub>2</sub>O:MeOH): 173 ([M+H]<sup>+</sup>, 80%), 102 (100%). <sup>1</sup>H and <sup>13</sup>C spectroscopic data in good agreement with literature.<sup>2</sup>

### 2-(2-(2-methoxyethoxy)ethoxy)-ethyl 2-cyanoacetate (7)

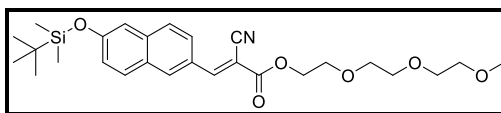


Triethylene glycol monomethyl ether (**10**) (500 mg, 3.00 mmol, 1 eq) and DMAP (2 mg, 0.02 mmol, 0.06 mol% eq) were added to DCM (10 mL). The solution was added dropwise to a solution of cyanoacetic acid (**9**) (310 mg, 3.65 mmol, 1.2 eq) which was previously dissolved

in DCM (5 ml) and the mixture stirred at 0 °C for 10 minutes. To this solution DCC (755 mg, 3.60 mmol, 1.2 eq) was added and the reaction mixture was stirred at 0 °C for 6 hours. The reaction mixture was allowed to warm to rt and diluted with DCM (30 mL). DCU was then removed by filtration. The solution was dried (MgSO<sub>4</sub>) and concentrated under reduced pressure. Purification by column chromatography (100% Et<sub>2</sub>O) gave the cyanoacetate **7** white solid (0.36 g, 86%).

**R<sub>f</sub>** (Et<sub>2</sub>O, 100%) = 0.47; **mp** 150 °C; **IR** (solid, cm<sup>-1</sup>) 1745 (C=O), 1257 (C-O); **<sup>1</sup>H NMR** (500 MHz, CDCl<sub>3</sub>) δ 4.38-4.35 (2H, m, COOCH<sub>2</sub>), 3.75-3.73 (2H, m, COOCH<sub>2</sub>CH<sub>2</sub>O), 3.68-3.63 (6H, m, 3 × CH<sub>2</sub>O), 3.57-3.53 (2H, m, CH<sub>2</sub>O), 3.50 (2H, s, CH<sub>2</sub>CN), 3.38 (3H, s, OCH<sub>3</sub>); **<sup>13</sup>C NMR** (126 MHz, CDCl<sub>3</sub>) δ 163.01 (C=O), 112.91 (CN), 71.95 (CH<sub>2</sub>), 70.70 (CH<sub>2</sub>), 70.62 (CH<sub>2</sub>), 70.61 (CH<sub>2</sub>), 68.52 (CH<sub>2</sub>), 65.82 (CH<sub>2</sub>), 59.04 (CH<sub>3</sub>), 24.69 (CH<sub>2</sub>); **m/z** (ESI+, H<sub>2</sub>O:MeOH): 485 ([2M+Na]<sup>+</sup>, 100%), 254 ([M+Na]<sup>+</sup>, 65), <sup>1</sup>H and <sup>13</sup>C spectroscopic data in good agreement with literature.<sup>3</sup>

**2-cyano-3-(6-tert-butyltrimethylsilyloxy-2-naphthalenyl)-2-[2-(2-methoxyethoxy)ethoxy]ethyl ester (**4**)**

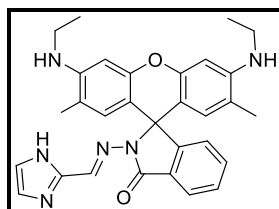


2-Cyano-3-(6-hydroxy-2-naphthalenyl)-2-[2-(2-methoxyethoxy)ethoxy]ethyl ester (**3**) (0.070 g, 0.20 mmol, 1 eq), TBDMS-Cl (0.075 g, 0.50 mmol, 1.1 eq) and imidazole (0.050 g, 0.70 mmol, 4 eq) were stirred in DMF (5 mL) at rt for 1 hour. The reaction mixture was then diluted with ether (15 mL) and subsequently washed with water (3 × 15 mL). Purification by column chromatography (50% EtOAc in hexane) gave the silyl derivative **4** as a yellow oil (0.090 g, 44%).

**R<sub>f</sub>** (EtOAc:hexane, 1:1) = 0.4; **IR** (neat, cm<sup>-1</sup>): 2218 (C≡N), 1728 (C=O), 1622 (C=C), 1583 (C=C), 1571 (C=C); **<sup>1</sup>H NMR** (500 MHz, CDCl<sub>3</sub>) δ 8.36 (1H, s, CHCCN), 8.32 (1H, brs, ArH), 8.14 (1H, dd, *J* = 8.7, 1.7 Hz, ArH), 7.84 (1H, d, *J* = 8.8 Hz, ArH), 7.76 (1H, d, *J* = 8.7 Hz, ArH), 7.21 (1H, d, *J* = 2.2 Hz, ArH), 7.15 (1H, dd, *J* = 8.8, 2.2 Hz, ArH), 4.50–4.46 (2H, m, COOCH<sub>2</sub>), 3.87–3.82 (2H, m, CH<sub>2</sub>), 3.76–3.72 (2H, m, CH<sub>2</sub>), 3.69–3.66 (4H, m, 2 × CH<sub>2</sub>), 3.57–3.54 (2H, m, CH<sub>2</sub>), 3.38–3.36 (3H, m, OCH<sub>3</sub>), 1.03 (9H, s, SiC(CH<sub>3</sub>)<sub>2</sub>C(CH<sub>3</sub>)<sub>3</sub>), 0.30–0.26 (6H, m, SiC(CH<sub>3</sub>)<sub>2</sub>C(CH<sub>3</sub>)<sub>3</sub>); **<sup>13</sup>C NMR** (126 MHz, CDCl<sub>3</sub>) δ 163.00 (CN), 156.81 (C=O), 155.41 (=CH), 137.29 (Ar C), 134.40 (Ar CH), 131.29 (Ar CH), 128.41 (Ar C), 127.85 (Ar CH), 126.95 (Ar C), 125.83 (Ar CH), 123.47 (Ar CH), 115.92 (Ar C), 115.04 (Ar CH), 100.91

(C), 71.97 (CH<sub>2</sub>), 70.85 (CH<sub>2</sub>), 70.66 (CH<sub>2</sub>), 70.22 (CH<sub>2</sub>), 68.80 (CH<sub>2</sub>), 65.63 (CH<sub>2</sub>), 59.04 (CH<sub>3</sub>), 25.65 (3 × CH<sub>3</sub>), 18.14 (C), -3.92 (2 × CH<sub>3</sub>); *m/z* (ESI+, H<sub>2</sub>O:MeOH): 522 ([M+Na]<sup>+</sup>, 100%), 500 (10).

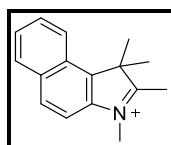
### Imidazole bearing Rhodamine 6G (5)



Rhodamine 6G (0.5 g, 1.12 mmol, 1 eq) was dissolved in MeOH (10 mL). To this solution, hydrazine hydrate (0.625 ml, 0.02 mol, 20 eq) was added dropwise. The mixture was heated under reflux until the red colour disappeared. The solution was cooled to room temperature, poured into distilled water (100 mL) and left stirring overnight. A white solid formed which was removed by filtration and dried *in vacuo* to give Rhodamine 6G hydrazine. Without further purification the next step was carried out. Rhodamine 6G hydrazine (0.4 g, 0.94 mmol, 1 eq) and 2-formyl imidazole (0.4 g, 0.94 mmol, 1 eq) were added to ethanol (10 mL). The mixture was heated under reflux overnight in the presence of catalytic amount of acetic acid. The reaction mixture was cooled to room temperature which resulted in the precipitation of a colourless solid. Further purification was carried out by column chromatography (10% EtOAc in DCM) to obtain the imidazole bearing rhodamine **5** as a colourless solid. (0.39 g, 78 %)

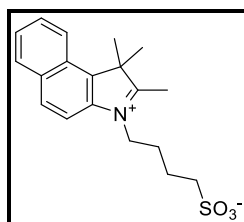
**R<sub>f</sub>** (EtOAc:DCM, 1:9) = 0.85; **mp** 340 °C; **IR** (solid, cm<sup>-1</sup>) 1707 (C=O), 1618 (N-H), 1332 (C-N), 1259 (C-O); **<sup>1</sup>H NMR** (500 MHz, Chloroform-*d*) δ 11.27 (1H, s, NH), 8.03 – 7.93 (1H, m, ArH), 7.81 (1H, s, ArH), 7.46 (2H, m, 2 × ArH), 7.09 – 7.01 (2H, m, 2 × ArH), 6.98 (1H, s, NCH), 6.38 (2H, s, 2 × ArH), 6.30 (2H, s, 2 × ArH), 3.49 (2H, s, 2 × NH), 3.19 (4H, q, *J* = 7.2 Hz, 2 × NHCH<sub>2</sub>CH<sub>3</sub>), 1.86 (6H, s, CH<sub>3</sub>), 1.30 (6H, t, *J* = 7.2 Hz, 2 × NHCH<sub>2</sub>CH<sub>3</sub>); **<sup>13</sup>C NMR** (126 MHz, Chloroform-*d*) δ 166.14 (C=O), 153.34 (C=N), 150.95 (2 × Ar C), 147.84 (2 × Ar C), 144.41 (Ar C), 134.85 (Ar CH), 134.09 (Ar CH), 130.20 (Ar CH), 128.33 (Ar CH), 127.01 (Ar CH), 126.86 (Ar C), 123.60 (Ar CH), 123.49 (Ar CH), 118.22 (2 × Ar C), 117.67 (Ar CH), 97.28 (2 × Ar CH), 78.3 (C), 65.9 (C=N), 38.31 (2 × CH<sub>2</sub>), 16.73 (1 × CH<sub>3</sub>), 14.76 (2 × CH<sub>3</sub>); *m/z* (ESI+, H<sub>2</sub>O:MeOH): 507 ([M+Na]<sup>+</sup>, 100%). <sup>1</sup>H and <sup>13</sup>C spectroscopic data in good agreement with literature.<sup>4</sup>

## 7.1.3 Cy dye building blocks

**1,1,2,3-tetramethyl-1*H*-benz[*e*]indolium (31)**

1,1,2-Trimethyl-1*H*-benz[*e*]indole (**36**) (250 mg, 0.42 mmol, 1 eq) was stirred in 1,2-dichlorobenzene (5 mL). To this, MeI (500 mg, 3.8 mmol, 3.1 eq) was added and the reaction was stirred under reflux at 110 °C for 24 h under argon. When complete, the reaction was cooled to rt. The solvent was removed under reduced pressure and the resultant solid was triturated with ether (20 mL) which was removed by decantation after the mixture was centrifuged to give the desired product as a white solid. (0.25 g, 99%)

**mp** 220-221 °C, lit<sup>5</sup> 199 °C; **IR** (solid, cm<sup>-1</sup>) 1581 (C=C), 1524 (C=C); **<sup>1</sup>H NMR** (500 MHz, DMSO-*d*<sub>6</sub>) δ 8.33 (1H, dd, *J* = 8.4, 1.1 Hz, *ArH*), 8.29 (1H, d, *J* = 8.9 Hz, *ArH*), 8.21 (1H, dd, *J* = 8.2, 1.3 Hz, *ArH*), 8.06 (1H, d, *J* = 8.9 Hz, *ArH*), 7.78 (1H, ddd, *J* = 8.4, 6.9, 1.4 Hz, *ArH*), 7.72 (1H, ddd, *J* = 8.1, 6.9, 1.3 Hz, *ArH*), 4.05 (3H, s, NCH<sub>3</sub>), 2.83 (3H, s, NCCCH<sub>3</sub>), 1.72 (6H, s, NCC(CH<sub>3</sub>)<sub>2</sub>); **<sup>13</sup>C NMR** (126 MHz, DMSO-*d*<sub>6</sub>) δ 139.94 (Ar C), 137.02 (Ar C), 133.53 (Ar C), 131.02 (Ar CH), 130.23 (Ar CH), 128.87 (Ar CH), 127.63 (Ar CH), 123.88 (Ar CH), 113.59 (Ar CH), 55.74 (Ar C), 35.47 (CH<sub>3</sub>), 21.76 (2 × CH<sub>3</sub>), 14.32 (CH<sub>3</sub>); ***m/z*** (ESI+, H<sub>2</sub>O:MeOH): 224 ([M]<sup>+</sup>, 100%), 209 (80). <sup>1</sup>H and <sup>13</sup>C spectroscopic data in good agreement with literature.<sup>6</sup>

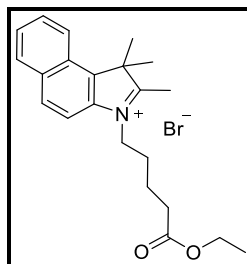
**1,1,2-Trimethyl-3-(4-sulfobutyl)- 1*H*-Benz[*e*]indolium (32)**

1,1,2-Trimethyl-1*H*-benz[*e*]indole (**36**) (1.00 g, 4.80 mmol, 1 eq) was dissolved in 1,2-dichlorobenzene (20 mL) to give a golden solution. 1,4-Butane sultone (1.86 g, 13.7 mmol,

2.8 eq) was added and the mixture was stirred at 120 °C overnight to give a brown solution. Upon cooling a solid separated which was removed by filtration and triturated with ether (20 mL) which was removed by decantation after the mixture was centrifuged. The product was subsequently dried under ambient conditions to give indolium **21** as a grey powder. (1.66 g, 98%)

**mp** 242-247 °C, lit<sup>7</sup> 263 °C; **IR** (solid, cm<sup>-1</sup>) 1637 (C=C), 1585 (C=C), 1469 (S=O), 1164 (S=O), 1161 (C=N); **<sup>1</sup>H NMR** (500 MHz, CDCl<sub>3</sub>) δ 7.70 (2H, d, *J* = 8.8 Hz, *ArH*), 7.65 (1H, d, *J* = 8.6 Hz, *ArH*), 7.59 (1H, d, *J* = 8.9 Hz, *ArH*), 7.31 (1H, m, *ArH*), 7.23 (1H, m, *ArH*), 4.28-4.23 (2H, m, NCH<sub>2</sub>), 2.52 (3H, s, CH<sub>3</sub>CN), 2.46-2.36 (2H, m, CH<sub>2</sub>SO<sub>3</sub><sup>-</sup>), 1.83 (2H, m, NCH<sub>2</sub>CH<sub>2</sub>), 1.56 (2H, m, NCH<sub>2</sub>CH<sub>2</sub>CH<sub>2</sub>), 1.36 (6H, s, NCCH(CH<sub>3</sub>)<sub>2</sub>); **<sup>13</sup>C NMR** (126 MHz, DMSO-*d*<sub>6</sub>) δ 197.55 (CN), 139.12 (Ar C), 137.40 (Ar C), 133.53 (Ar C), 131.17 (Ar CH), 130.21 (Ar CH), 128.83 (Ar CH), 127.92 (Ar C), 127.70 (Ar CH), 123.87 (Ar CH), 113.95 (Ar CH), 55.93 (C), 50.61 (CH<sub>2</sub>), 48.16 (CH<sub>2</sub>), 26.70 (CH<sub>2</sub>), 22.18 (CH<sub>2</sub>), 22.08 (2 × CH<sub>3</sub>), 14.13 (CH<sub>3</sub>); ***m/z*** (ESI+, H<sub>2</sub>O:MeOH): 368 ([M+Na]<sup>+</sup>, 80%) 346 ([M+H]<sup>+</sup>, 100%). <sup>1</sup>H and <sup>13</sup>C spectroscopic data in good agreement with literature.<sup>8</sup>

### 3-(5-Ethoxy-5-oxopentyl)-1,1,2-trimethyl-1*H*-Benz[*e*]indolium bromide (**34**)

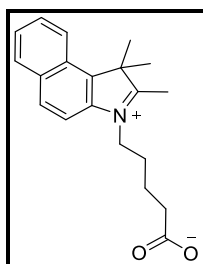


1,1,2-Trimethyl-1*H*-benz[*e*]indole (**36**) (1.00 g, 4.80 mmol, 1 eq) was dissolved in MeCN (20 mL). Ethyl 5-bromovalerate (2.09 g, 10.0 mmol, 2 eq) and KI (85.0 mg, 0.50 mmol, 0.1 eq) were added and the reaction was stirred under reflux at 80 °C for 4 days. The solvent was removed under reduced pressure and the resultant solid was triturated with ether (20 mL) which was removed by decantation after the mixture was centrifuged. The solid was dried under ambient conditions to give the blue indolium salt **34** (1.58 g, 82%).

**mp** 185-190 °C; **IR** (solid, cm<sup>-1</sup>) 1722 (C=O), 1635 (C=C), 1580 (C=C), 1163 (C=N); **<sup>1</sup>H NMR** (500 MHz, CDCl<sub>3</sub>) δ 8.32-8.16 (4H, m, *ArH*), 7.85-7.41 (2H, m, *ArH*) 4.95 (2H, t, *J* = 7.7 Hz, NCH<sub>2</sub>), 4.09 (2H, q, *J* = 7.1 Hz, COOCH<sub>2</sub>), 3.24 (3H, s, CH<sub>3</sub>CN), 2.44 (2H, t, *J* = 6.8 Hz, CH<sub>2</sub>CO<sub>2</sub>Et), 2.14-2.04 (2H, m, NCH<sub>2</sub>CH<sub>2</sub>), 1.89 (6H, s, C(CH<sub>3</sub>)<sub>2</sub>), 1.86-1.81 (2H, m,

$\text{CH}_2\text{CH}_2\text{CO}_2\text{Et}$ ), 1.22 (3H, t,  $J = 7.1$  Hz,  $\text{COOCH}_2\text{CH}_3$ );  $^{13}\text{C}$  NMR (126 MHz,  $\text{CDCl}_3$ )  $\delta$  195.22 (CN), 172.77 (C=O), 137.13 (Ar C), 133.76 (Ar C), 131.51 (Ar C), 130.14 (Ar CH), 128.70 (Ar CH), 127.92 (Ar C), 127.70 (Ar CH), 122.79 (Ar CH), 122.34 (Ar CH), 112.35 (Ar CH), 60.64 ( $\text{CH}_2$ ), 55.90 (C), 49.66 ( $\text{CH}_2$ ), 33.02 ( $\text{CH}_2$ ), 27.32 ( $\text{CH}_2$ ), 22.72 ( $2 \times \text{CH}_3$ ), 21.88 ( $\text{CH}_2$ ), 16.16 ( $\text{CH}_3$ ), 14.19 ( $\text{CH}_3$ );  $m/z$  (ESI+,  $\text{H}_2\text{O}:\text{MeOH}$ ): 338 ( $[\text{M}]^+$ , 100%), 210 (30). Spectroscopic  $^1\text{H}$  and  $^{13}\text{C}$  spectroscopic data in good agreement with literature.<sup>8</sup>

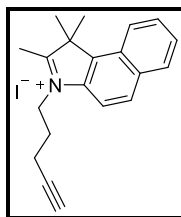
### 3-(4-Carboxybutyl)-1,1,2-trimethyl-1H-benz[e]indolium (33)



3-(5-Rthoxy-5-oxopentyl)-1,1,2-trimethyl-1H-benz[e]indolium salt (**34**) (0.98 g, 2.9 mmol, 1 eq) was suspended in HCl (20 mL; 5 N aq) and heated under reflux at 90 °C overnight to afford a yellow solution with a little blue precipitate. The precipitate was removed by filtration and the yellow solution was concentrated under *vacuum* to afford a yellow oil (quant.).

**IR** (neat,  $\text{cm}^{-1}$ ) 2926 (O-H), 1712 (C=O), 1633 (C=C), 1581 (C=C), 1171 (C=N);  **$^1\text{H}$  NMR** (500 MHz, MeOD)  $\delta$  8.21 – 8.17 (1H, m, ArH), 8.10 (1H, dd,  $J = 8.9, 2.7$  Hz, ArH), 8.02 (1H, dd,  $J = 8.2, 0.5$  Hz, ArH), 7.88 (1H, d,  $J = 8.9$  Hz, ArH), 7.67-7.60 (1H, m, ArH), 7.59 – 7.55 (1H, m, ArH), 4.53 (2H, td,  $J = 7.8, 1.7$  Hz,  $\text{CH}_2\text{N}$ ), 2.39 – 2.26 (2H, m,  $\text{CH}_2\text{COOH}$ ), 2.00 – 1.88 (2H, m,  $\text{NCH}_2\text{CH}_2$ ), 1.71 (6H, bs,  $\text{NCCH}(\text{CH}_3)_2$ ), 1.60-1.56 (2H, m,  $\text{NCH}_2\text{CH}_2\text{CH}_2$ );  **$^{13}\text{C}$  NMR** (126 MHz, MeOD)  $\delta$  198.22 (CN), 175.35 (C=O), 139.98 (Ar C), 138.93 (Ar C), 135.36 (Ar C), 132.63 (Ar CH), 131.25 (Ar CH), 129.91 (Ar CH), 129.33 (Ar C) 128.92 (Ar CH), 124.58 (Ar CH), 113.94 (Ar CH), 61.80 (C), 48.91 ( $\text{CH}_2$ ), 33.92 ( $\text{CH}_2$ ), 28.48 ( $\text{CH}_2$ ), 22.99 ( $\text{CH}_2$ ), 22.58 ( $2 \times \text{CH}_3$ ), 20.65 ( $\text{CH}_3$ );  $m/z$  (ESI+,  $\text{H}_2\text{O}:\text{MeOH}$ ): 324 ( $[\text{M}]^+$ , 100%), 210 (10).  $^1\text{H}$  and  $^{13}\text{C}$  spectroscopic data in good agreement with literature.<sup>7</sup>

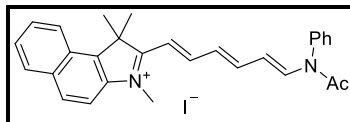


**1-(4-Pentynyl)-2,3,3-trimethylbenz[e]indolium iodide (35)**

Potassium iodide (1.19 g, 6.9 mmol, 2.2 eq) was suspended in MeCN (2 mL), followed by 5-chloro-1-pentyne (0.38 g, 3.1 mmol, 1 eq) and stirred at 50 °C. After 10 minutes 2,3,3-trimethylbenz[e]indole (**36**) (0.5 g, 2.4 mmol, 1 eq) was added and the reaction stirred for 24 hours under reflux. The reaction was then cooled to rt, diluted with DCM (15 mL) and washed with H<sub>2</sub>O (3 × 20 mL). The organic layer was dried over magnesium sulfate, filtered and the solvent was removed *in vacuo*. The solid was dissolved in the minimum amount of DCM and precipitated using Et<sub>2</sub>O. The remaining solid was removed by filtration, washed with Et<sub>2</sub>O and dried *in vacuo*. The indolium salt **35** was obtained as a green solid (0.72 g, 72%).

**mp** 140-142 °C; **IR** (solid, cm<sup>-1</sup>): 3203 (C≡C-H), 2358 (C≡C), 1581 (C=C), 1521 (C=C); **<sup>1</sup>H NMR** (500 MHz, CDCl<sub>3</sub>) δ 8.15 (1H, d, *J* = 8.9 Hz, *ArH*), 8.12 (1H, d *J* = 8.4 Hz, *ArH*), 8.09 (1H, d, *J* = 8.4, *ArH*), 7.93 (1H, d, *J* = 8.9 Hz, *ArH*), 7.77 (1H, dd, *J* = 8.3, 6.8, *ArH*), 7.71 (1H, dd, *J* = 8.3, 6.8 Hz, *ArH*), 5.05 (2H, t, *J* = 7.5 Hz, NCH<sub>2</sub>CH<sub>2</sub>), 3.32 (3H, s, NCCCH<sub>3</sub>), 2.55 (2H, td, *J* = 6.6, 2.5 Hz, CH<sub>2</sub>CCH), 2.35 (2H, qn, *J* = 6.6 Hz, CH<sub>2</sub>CH<sub>2</sub>C≡CH), 2.15 (1H, t, *J* = 2.5 Hz, CH<sub>2</sub>CCH), 1.92 (6H, s, NCC(CH<sub>3</sub>)<sub>2</sub>); **<sup>13</sup>C NMR** (126 MHz, CDCl<sub>3</sub>) δ 196.14 (CN), 138.33 (Ar C), 137.12 (Ar C), 133.80 (Ar C), 131.64 (Ar CH), 130.18 (Ar CH), 128.75 (Ar CH), 127.92 (Ar C), 127.76 (Ar CH), 122.83 (Ar CH), 112.57 (Ar CH), 82.01 (C), 71.22 (CH), 56.03 (C), 48.99 (CH<sub>2</sub>), 26.82 (CH<sub>2</sub>), 22.89 (2 × CH<sub>2</sub>), 16.82 (CH<sub>3</sub>), 16.23 (CH<sub>2</sub>); ***m/z*** (ESI+, H<sub>2</sub>O:MeOH) 276 ([M]<sup>+</sup>, 100%). <sup>1</sup>H and <sup>13</sup>C spectroscopic data in good agreement with literature.<sup>9</sup>

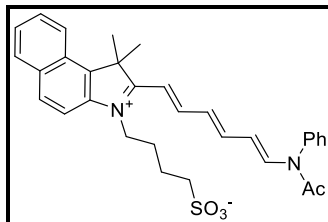
**2-[(1E,3E,5E)-6-(Acetylphenylamino)-1,3,5-hexatrien-1-yl]-1,1,3-trimethyl-1H-benz[e]indolium iodide (38)**



1,1,2,3-Tetramethyl-1H-benz[e]indolium iodide (**31**) (120 mg, 0.28 mmol, 1 eq) and glutaconaldehyde dianil hydrochloride salt (**37**) (70.0 mg, 0.31 mmol, 1.1 eq) were added to a round bottom flask containing acetic acid (3 mL) and acetic anhydride (3 mL). The reaction mixture was stirred at 120 °C for 2.5 hours. The solvent was removed *in vacuo* and the resulting solid was triturated with EtOAc:H<sub>2</sub>O (20 mL, 1:1) which was removed by decantation after the mixture was centrifuged to give a dark purple solid **38** (52 mg, 40%).

**mp** 200-202 °C; **IR** (solid, cm<sup>-1</sup>) 1681 (C=O), 1548 (C=C), 1504 (C=C); **<sup>1</sup>H NMR** (500 MHz, DMSO-*d*<sub>6</sub>) δ 8.33-7.32 (12H, m, 9 × ArH & 3 × =CH), δ 7.28 (1H, d, *J* = 14.2 Hz, =CH), 7.02-6.99 (1H, t, *J* = 7.4 Hz, ArH), 6.90 (1H, d, *J* = 15.3 Hz, =CH), 6.58 (1H, dd, *J* = 15.3, 11.1 Hz, ArH), 5.27 (1H, dd, *J* = 14.2, 11.5 Hz, =CH), 4.01 (3H, s, CH<sub>3</sub>), 2.04 (3H, s, CH<sub>3</sub>), 1.92 (6H, s, 2 × CH<sub>3</sub>); **<sup>13</sup>C NMR** (126 MHz, DMSO-*d*<sub>6</sub>) δ 181.51 (CN), 168.72 (C=O), 154.34 (CH), 150.59 (CH), 139.98 (Ar C), 139.80 (Ar C), 138.71 (Ar C), 137.61 (Ar C), 133.31 (Ar C), 131.21 (Ar CH), 130.82 (Ar CH), 130.46 (Ar CH), 129.87 (CH), 129.80 (Ar CH), 129.11 (CH), 129.04 (Ar CH), 128.76 (Ar CH), 127.25 (Ar CH), 123.51 (Ar CH), 123.42 (Ar CH), 119.44 (Ar CH), 113.45 (CH), 112.89 (Ar CH), 112.78 (CH), 53.42 (C) 34.43 (CH<sub>3</sub>), 25.94 (2 × CH<sub>3</sub>), 24.49 (CH<sub>3</sub>); ***m/z*** (ESI+, H<sub>2</sub>O:MeOH): 421 ([M]<sup>+</sup>, 100%). <sup>1</sup>H and <sup>13</sup>C spectroscopic data in good agreement with literature.<sup>6</sup>

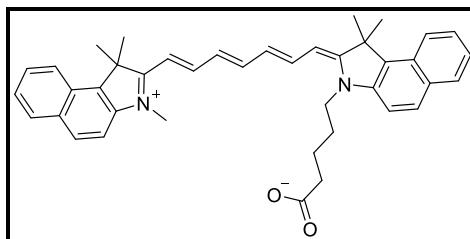
**2-[6-(Acetylphenylamino)-1,3,5-hexatrien-1-yl]-1,1-dimethyl-3-(4-sulfobutyl)-1H-benz[e]indolium (39)**



Glutaconaldehyde dianyl hydrochloride salt (**37**) (475 mg, 1.65 mmol, 1.1 eq) was added to a solution of 1,1,2-trimethyl-3-(4-sulfobutyl)-1H-benz[e]indolium (**32**) (512 mg, 1.47 mmol, 1 eq) in acetic acid (4.5 mL) and acetic anhydride (4.5 mL) and was stirred at 120 °C for 3 hours. The solvent was removed under reduced pressure and the resultant solid was triturated with EtOAc:H<sub>2</sub>O (20 mL, 1:1) which was removed by decantation after the mixture was centrifuged to give the title compound **39** (0.31 g, 40%).

**mp** 260-263 °C; **IR** (solid, cm<sup>-1</sup>) 1685 (C=O), 1544 (C=C), 1492 (SO<sub>3</sub><sup>-</sup>); **<sup>1</sup>H NMR** (500 MHz, MeOD) δ 8.37 (1H, d, *J* = 8.1 Hz, ArH), 8.30–8.23 (2H, m, ArH & =CH), 8.20 (1H, d, *J* = 8.9 Hz, ArH), 8.14 (1H, d, *J* = 8.7 Hz, =CH), 7.95 (1H, d, *J* = 8.9 Hz, ArH), 7.81–7.76 (1H, m, ArH), 7.71–7.61 (4H, m, 3 × ArH & =CH), 7.48 (1H, dd, *J* = 14.3, 11.5 Hz, ArH), 7.43–7.37 (2H, m, ArH & =CH), 7.04 (1H, d, *J* = 15.1 Hz, =CH), 6.67 (1H, dd, *J* = 14.3, 11.2 Hz, ArH), 5.44 (1H, dd, *J* = 13.7, 11.5 Hz, & =CH), 4.64–4.59 (2H, m, NCH<sub>2</sub>), 2.92 (2H, t, *J* = 7.0 Hz, CH<sub>2</sub>SO<sub>3</sub><sup>-</sup>), 2.17 (6H, s, 2 × CH<sub>3</sub>), 2.06 (3H, s, CH<sub>3</sub>), 2.05–2.00 (4H, m, CH<sub>2</sub>CH<sub>2</sub>CH<sub>2</sub>CH<sub>2</sub>SO<sub>3</sub><sup>-</sup>); **<sup>13</sup>C NMR** (126 MHz, MeOD) δ 181.70 (C=N), 169.99 (C=O), 155.07 (CH), 150.42 (CH), 138.48 (Ar C), 137.91 (Ar C), 133.61 (Ar C), 131.20 (Ar CH), 130.27 (2 × Ar CH), 129.88 (2 × CH), 129.43 (Ar CH), 128.38 (Ar CH), 128.36 (Ar CH), 128.02 (Ar CH), 127.39 (Ar C), 126.75 (Ar CH), 123.74 (Ar C), 122.61 (Ar CH), 119.80 (Ar CH), 113.42 (CH), 112.06 (Ar CH), 111.89 (CH), 53.38 (C), 49.81 (CH<sub>2</sub>), 48.22 (CH<sub>2</sub>), 45.83 (CH<sub>2</sub>), 26.63 (CH<sub>2</sub>), 25.28 (3 × CH<sub>3</sub>); ***m/z*** (ESI+, H<sub>2</sub>O:MeOH): 565 ([M+Na]<sup>+</sup>, 100%), 543 ([M+H]<sup>+</sup>, 40). <sup>1</sup>H and <sup>13</sup>C spectroscopic data in good agreement with literature.<sup>8</sup>

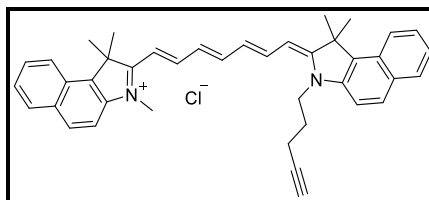
## 7.1.4 Solution phase approach

**4-(2-(1E,3E,5E,7Z)-7-(3-(4-Carboxybutyl)-1,1-dimethyl-1H-benzo[e]indol-2(3H)-ylidene)hepta-1,3,5-trienyl)-1,1-dimethyl-1H-benzo[e]indolinium-3-yl (42)**

3-(4-Carboxybutyl)-1,1,2-trimethyl-1H-benz[e]indolinium (**33**) (5.0 mg, 0.01 mmol, 1.2 eq) was added to a solution of 2-[(1E,3E,5E)-6-(acetylphenylamino)-1,3,5-hexatrien-1-yl]-1,1,3-trimethyl-1H-benz[e]indolinium (**38**) (6.0 mg, 0.01 mmol, 1 eq) in anhydrous pyridine (5 mL) and stirred at rt for 24 hours. The reaction mix was triturated with ether and the solid was filtered off, washed with ether and dried *in vacuo*. Column chromatography (0-2 % MeOH/DCM) gave compound **42** as a green solid (6.02 mg, 75%).

**mp** 234-236 °C; **IR** (solid,  $\text{cm}^{-1}$ ) 3394 (OH), 2922 (CH), 1666 (C=O);  **$^1\text{H NMR}$**  (601 MHz, MeOD)  $\delta$  8.28 (2H, d,  $J = 8.5$  Hz, ArH), 8.09 - 8.04 (5H, m,  $3 \times \text{ArH}$  &  $2 \times =\text{CH}$ ), 7.92 (1H, dd,  $J = 20.7, 8.6$  Hz, =CH), 7.71 - 7.64 (4H, m, 4 ArH), 7.51 - 7.54 (2H, m, =CH), 7.48 - 7.33 (1H, m, =CH), 6.66 - 6.64 (2H, m, ArH), 6.47 - 6.34 (2H, m, ArH & =CH), 4.29 (2H, t,  $J = 7.6$ ,  $\text{NCH}_2\text{CH}_2\text{CH}_2\text{CH}_2\text{COOH}$ ) 3.76 (3H, s,  $\text{CH}_3$ ), 2.32 (2H, t,  $J = 7.1$  Hz,  $\text{NCH}_2\text{CH}_2\text{CH}_2\text{CH}_2\text{COOH}$ ), 2.02 (12H, s,  $4 \times \text{CH}_3$ ), 1.95 - 1.90 (2H, m,  $\text{NCH}_2\text{CH}_2\text{CH}_2\text{CH}_2\text{COOH}$ ), 1.84 - 1.79 (2H, m,  $\text{NCH}_2\text{CH}_2\text{CH}_2\text{CH}_2\text{COOH}$ );  **$^{13}\text{C NMR}$**  (151 MHz, MeOD)  $\delta$  194.06 (C=O), 178.97 (CN), 173.15 (CN), 149.63 (CH), 140.60 (Ar C), 140.33 (Ar C), 133.63 (Ar C), 131.91 ( $2 \times \text{Ar C}$ ), 131.85 ( $2 \times \text{Ar C}$ ), 130.44 (Ar CH), 130.36 (Ar CH), 129.93 ( $3 \times \text{Ar CH}$ ), 129.55 (CH), 128.13 ( $4 \times \text{Ar CH}$ ), 127.56 (Ar CH), 126.60 (CH), 124.73 (Ar CH), 122.18 (Ar CH), 122.15 (Ar CH), 111.02 (CH), 110.98 (Ar C), 110.11 (CH), 103.56 (CH), 103.21 (Ar CH) 50.81 (C), 48.11 (C), 43.88 ( $\text{CH}_2$ ), 36.16 ( $\text{CH}_2$ ), 30.73 ( $\text{CH}_3$ ), 26.42 ( $\text{CH}_2$ ), 25.90 ( $4 \times \text{CH}_3$ ), 23.20 ( $\text{CH}_2$ );  **$m/z$**  (ESI+,  $\text{H}_2\text{O}:\text{MeOH}$ ): 595 ( $[\text{M}]^+$ , 100%).  $^1\text{H}$  and  $^{13}\text{C}$  spectroscopic data in good agreement with literature.<sup>10</sup>

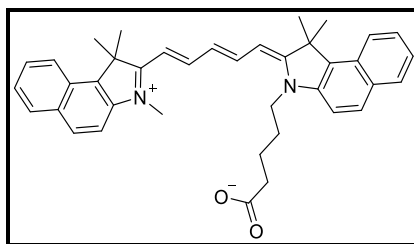
**4-(2-(1E,3E,5E,7Z)-7-(3-(4-Pentynyl)-1,1-dimethyl-1H-benzo[e]indol-2(3H)-ylidene)hepta-1,3,5-trienyl)-1,1-dimethyl-1H-benzo[e]indolinium-3-yl chloride(43)**



1-(4-Pentynyl)-2,3,3-trimethylbenzo[e]indolinium indole (**35**) (30 mg, 0.1 mmol, 1.2 eq) was added to a solution of 2-[(1E,3E,5E)-6-(acetylphenylamino)-1,3,5-hexatrien-1-yl]-1,1,3-trimethyl-1H-benzo[e]indolinium chloride (**38**) (38 mg, 0.09 mmol, 1 eq) in anhydrous pyridine (5 mL) and stirred at rt for 24 hours. Column chromatography (0-2 % MeOH/DCM) provided the title product **43** as a green solid (300 mg, 69%).

**mp** 207 °C; **IR** (solid,  $\text{cm}^{-1}$ ) 2929 (C≡C-H), 2113 (C≡C), 1666 (C=C);  **$^1\text{H}$  NMR** (500 MHz, MeOD)  $\delta$  8.25 (2H, t,  $J = 9.5$  Hz, ArH & =CH), 8.09 – 7.94 (5H, m,  $3 \times$  ArCH & =CH), 7.68 – 7.56 (5H, m, 4 ArH & 1 =CH), 7.54 – 7.40 (3H, m, =CH), 6.66 – 6.56 (2H, m, ArH), 6.44 – 6.32 (2H, m, ArH & =CH), 4.31 (2H, t,  $J = 6.7$  Hz, NCH<sub>2</sub>), 3.77 (3H, s, NCH<sub>3</sub>), 2.53 (1H, t,  $J = 2.6$  Hz, C≡CH), 2.43 (2H, td,  $J = 6.7, 2.6$  Hz, CH<sub>2</sub>C≡CH), 2.08 – 2.05 (2H, m, CH<sub>2</sub>CH<sub>2</sub>C≡CH), 2.01 (12H, s,  $4 \times$  CH<sub>3</sub>);  **$^{13}\text{C}$  NMR** (126 MHz, MeOD)  $\delta$  174.52 (CN), 172.30 (CN), 151.13 (CH), 150.95 (Ar CH), 139.84 (Ar C), 133.63 (Ar C), 133.23 (Ar C), 133.00 (Ar C), 132.12 (Ar C), 131.83 (Ar C), 130.30 (Ar CH), 130.26 (Ar CH), 129.72 (Ar CH), 129.70 (Ar C), 128.09 (Ar C), 127.31 (CH), 127.25 (CH), 125.70 (Ar CH), 125.35 (Ar CH), 124.73 (CH), 124.41 (CH), 121.93 (Ar CH), 121.85 (Ar CH), 110.47 ( $2 \times$  Ar CH), 110.32 ( $2 \times$  Ar CH), 103.74 (Ar CH), 102.40 (CH), 82.45 (C), 69.93 (≡CH), 53.40 (C), 42.38 (CH<sub>2</sub>), 35.54 (C), 30.43 (CH<sub>3</sub>), 26.28 ( $2 \times$  CH<sub>3</sub>), 26.15 (CH<sub>2</sub>), 26.07 ( $2 \times$  CH<sub>3</sub>), 15.18 (CH<sub>2</sub>);  **$m/z$**  (ESI+, H<sub>2</sub>O:MeOH): 561 ([M]<sup>+</sup>, 100%), 318 (100).  $^1\text{H}$  and  $^{13}\text{C}$  spectroscopic data in good agreement with literature.<sup>10</sup>

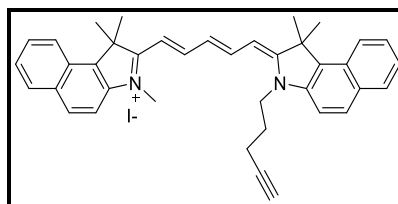
**4-(2-(1E,3E,5E)-5-(3-(4-Carboxybutyl)-1,1-dimethyl-1H-benzo[e]indol-2(3H)-ylidene)penta-1,3-dienyl)-1,1-dimethyl-1H-benzo[e]indolinium-3-yl (46)**



1,2,3,3-Tetramethylbenz[e]indolium iodide (**31**) (0.51 g, 2.2 mmol, 1 eq) and malondialdehyde bis(phenylimine)monohydrochloride (0.73 g, 4.37 mmol, 1.1 eq) in acetic acid (5 mL) was heated at reflux under argon. After 30 min the reaction was cooled to rt and a solution of 3-(4-carboxybutyl)-1,1,2-trimethyl-1H-benz[e]indolium (**33**) (0.82 g, 2.41 mmol, 1.1 eq) in anhydrous pyridine (5 mL) was added and the reaction stirred at rt for 24 hours. The reaction mix was precipitated with ether and the solid filtered off, washed with ether and dried *in vacuo*. Column chromatography (0-2 % MeOH/DCM) provided the title compound **33** as a red-gold solid (0.65 g, 70%).

$\lambda_{\text{abs}}/\lambda_{\text{em}}$  665/693;  $\Phi$  0.68;  $\epsilon$  150,000 M<sup>-1</sup>cm<sup>-1</sup>; **mp** 190 °C; **IR** (solid, cm<sup>-1</sup>) 3311 (OH), 2924 (CH), 1660 (C=O), 1479 (C=C), 1436 (C=C); **<sup>1</sup>H NMR** (500 MHz, DMSO-*d*<sub>6</sub>)  $\delta$  12.08 (1H, s, COOH), 8.50 – 8.37 (2H, m, ArH & =CH), 8.26-8.24 (2H, m, ArH), 8.16 – 7.97 (4H, m, ArH), 7.74 (2H, dd, *J* = 8.9, 4.2 Hz, ArH), 7.69-6.67 (2H, m, ArH & =CH), 7.53-7.50 (2H, m, ArH), 6.61 (1H, t, *J* = 12.3 Hz, =CH), 6.40 – 6.32 (2H, m, ArH =CH), 4.24 (2H, t, *J* = 7.3 Hz, NCH<sub>2</sub>CH<sub>2</sub>CH<sub>2</sub>CH<sub>2</sub>COOH), 3.73 (3H, s, NCH<sub>3</sub>), 2.30 (2H, t, *J* = 7.2 Hz, NCH<sub>2</sub>CH<sub>2</sub>CH<sub>2</sub>CH<sub>2</sub>COOH), 1.96 (12H, s, 4 × CH<sub>3</sub>), 1.76 (2H, m, NCH<sub>2</sub>CH<sub>2</sub>CH<sub>2</sub>CH<sub>2</sub>COOH), 1.64 (2H, m, NCH<sub>2</sub>CH<sub>2</sub>CH<sub>2</sub>CH<sub>2</sub>COOH); **<sup>13</sup>C NMR** (126 MHz, DMSO-*d*<sub>6</sub>)  $\delta$  174.78 (CN), 174.64 (CO) 173.99 (CN), 158.51 (Ar C), 158.14 (Ar C), 153.35 (CH), 153.32 (Ar CH), 140.89 (Ar C), 140.24 (Ar C), 133.51 (Ar C), 131.81 (Ar CH), 131.73 (Ar CH), 130.76 (Ar CH), 130.67 (Ar CH), 130.41 (Ar CH), 128.20 (CH), 128.09 (Ar CH), 128.00 (Ar CH), 126.00 (CH), 125.24 (Ar CH), 122.65 (Ar CH), 122.59 (CH), 118.41 (Ar C), 112.09 (Ar CH), 103.66 (Ar CH), 102.28 (CH), 43.33 (CH<sub>2</sub>), 33.37 (CH<sub>2</sub>), 31.67 (CH<sub>3</sub>), 26.96 (2 × CH<sub>3</sub>), 26.85 (CH<sub>2</sub>), 26.80 (2 × CH<sub>3</sub>), 21.82 (CH<sub>2</sub>); ***m/z*** (ESI+, H<sub>2</sub>O:MeOH): 569 ([M]<sup>+</sup>, 100%). <sup>1</sup>H and <sup>13</sup>C spectroscopic data in good agreement with literature.<sup>10</sup>

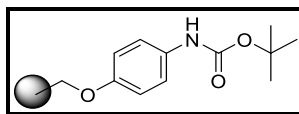
**4-(2-(*1E,3E,5E*)-5-(3-(4-Pentynyl)-1,1-dimethyl-1*H*-benzo[*e*]indol-2(3*H*)-ylidene)penta-1,3-dienyl)-1,1-dimethyl-1*H*-benzo[*e*]indolinium-3-yl (47)**



1,2,3,3-Tetramethylbenzo[*e*]indolinium iodide (**31**) (1.42 g, 3.98 mmol, 1 eq) and malondialdehyde bis(phenylimine)monohydrochloride (1.13 g, 4.37 mmol, 1.1 eq) in acetic acid (5 mL) was heated at reflux under argon. After 30 min the reaction was cooled to rt and a solution of 1-pentynyl-2,3,3-trimethylbenzo[*e*]indolinium iodide (**35**) (1.76 g, 4.37 mmol, 1.1 eq) in anhydrous pyridine (5 mL) was added and the reaction stirred at rt for 24 hours. The reaction mix was precipitated with ether and the solid filtered off, washed with ether and dried in vacuo. Column chromatography (0-2 % MeOH/DCM) provided compound **47** as a red-gold solid (1.78 g, 71%).

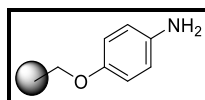
$\lambda_{\text{abs}}/\lambda_{\text{em}}$  665/690;  $\Phi$  0.70;  $\epsilon$  90,000 M<sup>-1</sup>cm<sup>-1</sup>; **mp** 170 °C; **IR** (solid, cm<sup>-1</sup>): 3059 (C≡C-H), 2115 (C≡C), 1634 (C=C), 1581 (C=C); **<sup>1</sup>H NMR** (500 MHz, DMSO-*d*<sub>6</sub>)  $\delta$  8.51 – 8.42 (2H, m, ArH & =CH), 8.29 – 8.24 (2H, m, ArH), 8.12 – 8.05 (4H, m, 3 × ArH & =CH), 7.77 (1H, d, *J* = 8.9 Hz, ArH), 7.73 (1H, d, *J* = 8.9 Hz, ArH), 7.72-7.60 (2H, m, ArH & =CH), 7.55 -7.52 (2H, m, ArH), 6.61 (1H, t, *J* = 12.3 Hz, =CH), 6.39 - 6.30 (2H, m, ArH & =CH), 4.27 (2H, t, *J* = 7.5 Hz, NCH<sub>2</sub>), 3.76 (3H, s, NCH<sub>3</sub>), 2.99 (1H, t, *J* = 2.6 Hz, CH<sub>2</sub>C≡CH), 2.38 (2H, td, *J* = 7.5, 2.6 Hz, CH<sub>2</sub>C≡CH), 1.98 (6H, s, 2 × CH<sub>3</sub>), 1.97 (6H, s, 2 × CH<sub>3</sub>), 1.97 – 1.92 (2H, m, NCH<sub>2</sub>CH<sub>2</sub>); **<sup>13</sup>C NMR** (126 MHz, DMSO-*d*<sub>6</sub>)  $\delta$  175.24 (CN), 173.72 (CN), 153.73 (CH), 152.98 (Ar CH), 140.83 (Ar C), 140.22 (Ar C), 133.73 (Ar C), 133.33 (Ar C), 131.88 (Ar C), 131.69 (Ar C), 130.75 (Ar CH), 130.60 (Ar CH), 130.41 (Ar CH), 128.24 (Ar C), 128.19 (CH), 128.13 (CH), 127.96 (Ar CH), 125.96 (Ar CH), 125.34 (Ar CH), 125.15 (Ar CH), 122.68 (CH), 122.57 (Ar CH), 118.53 (Ar C), 112.14 (Ar CH), 111.75 (Ar CH), 104.00 (Ar CH), 102.83 (CH), 84.01 (C), 72.66 (≡CH), 51.28 (C), 51.08 (C), 42.99 (CH<sub>2</sub>), 31.16 (CH<sub>3</sub>), 27.31 (2 × CH<sub>3</sub>), 27.09 (2 × CH<sub>3</sub>), 26.65 (CH<sub>2</sub>), 15.74 (CH<sub>2</sub>); ***m/z*** (ESI+, H<sub>2</sub>O:MeOH): 535 ([M+]<sup>+</sup>, 100%). <sup>1</sup>H and <sup>13</sup>C spectroscopic data in good agreement with literature.<sup>10</sup>

## 7.1.5 On resin approach

**(4-hydroxyphenyl)carbamic acid *tert*-butyl ester PS (50)**

N-Boc-4-hydroxyaniline (**49**) (1.25 g, 6.00 mmol, 30 eq), Cs<sub>2</sub>CO<sub>3</sub> (1.95 g, 6.00 mmol, 30 eq) and KI (30.0 mg, 2.0 mmol, 1 eq) were added to acetone (25 mL). To this solution 1% DVB cross linked chloromethyl PS (1.00 g, 1.95 mmol, 10 eq) was added and the mixture was stirred at 70 °C for 16 hours. The resin was washed with H<sub>2</sub>O (4 × 25 mL) followed by DMF (4 × 25 mL), DCM (4 × 25 mL) and Et<sub>2</sub>O (4 × 25 mL). The resin was then dried under reduced pressure to give a beige resin. (2.24 g)

**IR** (solid, cm<sup>-1</sup>) 1724 (C=O), 1598 (C=C), 1512 (C=C).

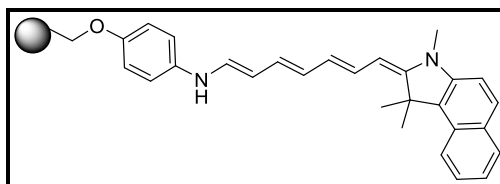
**4-aminophenol PS (51)**

(4-hydroxyphenyl)carbamic acid *tert*-butyl ester PS (**50**) (20.0 mg, 0.03 mmol, eq) is shaken at rt with 20% TFA in DCM (0.3 mL) for 2 hours. The resin is then isolated by filtration and washed with DCM (2 × 10 mL). The resin is then shaken with 10% TEA in DCM (0.3 mL) for 15 minutes, filtered, washed with DCM (4 × 10 mL) and then dried. Keiser and TNBS tests carried out showed removal of Boc group took place. (18 mg)

**IR** (solid, cm<sup>-1</sup>) 1672 (NH<sub>2</sub>), 1510 (C=C), 1492 (C=C)



**2-[(1E,3E,5E)-6-(acetylphenylamino)-1,3,5-hexatrien-1-yl]-1,1,3-trimethyl-1H-Benz[e]indolium PS (52)**



2-[(1E,3E,5E)-6-(acetylphenylamino)-1,3,5-hexatrien-1-yl]-1,1,3-trimethyl-1H-Benz[e]indolium (**31**) (50.0 mg, 0.12 mmol, 1 eq) and 4-aminophenol PS 51) (70.0 mg, 0.13 mmol, 1eq) were shaken in DCM (3 mL) for 2 hours. The resin was then washed with DMF (3 × 10 mL), DCM (3 × 10 mL) and dried under reduced pressure to give a dark purple resin. (0.11 g)

**IR** (solid, cm<sup>-1</sup>) 1631 (C=C), 1600 (C=C).

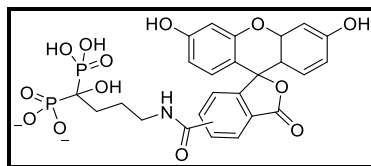
**4-(2-(1E, 3E, 5E, 7Z)-7-(3-(R)-1,1-dimethyl-1H-benzo[e]indol-2(3H)-ylidene)hepta-1,3,5-trienyl)-1,1-dimethyl-1H-benzo[e]indolinium-3-yl (42 or 43)**

R= 4- carboxybutyl (**33**) or 4-pentynyl (**34**)

2-[(1E,3E,5E)-6-(acetylphenylamino)-1,3,5-hexatrien-1-yl]-1,1,3-trimethyl-1H-Benz[e]indolium PS (**38**) (65.0 mg, 0.12 mmol, 1 eq), 3-(4-carboxybutyl)-1,1,2-trimethyl- 1H-Benz[e]indolium (**33**) or 1-(4-pentynyl)-2,3,3-trimethylbenz[e]indolium indole (**34**) (5.0 mg, 0.01 mmol, 0.1 eq) or were shaken with pyridine (0.47 mL) and acetic anhydride (0.11 mL) for 3 hours. The resin was then washed with DMF (3 ×10 mL), DCM (3 × 10 mL) and the filtrate was collected. The filtrate was dried under reduced pressure to give a green solid. (61 mg, 64% and 59 mg, 60%)

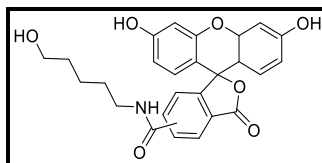
## 7.1.6 Fluorescein compounds

## Fluorescein-Alendronate (55)



Sodium alendronate (34 mg, 1 mmol, 5 eq; Alfa Aesar) was dissolved in  $\text{NaHCO}_3$  (1 mL, sat. aq.). Fluorescein (5/6) NHS ester (10 mg, 0.2 mmol, 1 eq; Thermo Fisher) dissolved in DMF (0.1 mL) was added to the solution and the reaction mixture was stirred for 2 days at room temperature in the dark. The solution was acidified with TFA (10% v/v aq.) and purified by RP HPLC [isocratic 80/20  $\text{H}_2\text{O}$  (+0.1% v/v TFA)/MeCN (+0.1% v/v TFA)] to yield the fluorescein-BP conjugate as an orange solid (34 mg, 50%).

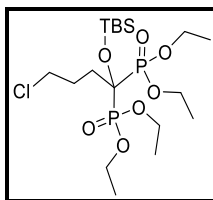
$\lambda_{\text{abs}}/\lambda_{\text{em}}$  491/515;  $\Phi$  0.83;  $\epsilon$  41,400  $\text{M}^{-1}\text{cm}^{-1}$ ; mp 240 °C; IR (solid,  $\text{cm}^{-1}$ ) 1700 (C=O), 1635 (C=O), 1538 (N-H), 1271 (P=O), 1116 (C-N);  $^1\text{H NMR}$  (601 MHz,  $\text{DMSO-}d_6$ )  $\delta$  10.13 (2H, br s, OH isomer 1+2) 8.85 (0.6H, t,  $J = 5.7$  Hz, NH isomer 1), 8.72 (0.4H, t,  $J = 5.9$  Hz, NH isomer 2), 8.47 (0.6H, d,  $J = 1.5$  Hz, ArH isomer 1), 8.26 (0.6H, dd,  $J = 8.0, 1.5$  Hz, ArH isomer 1), 8.19 (0.4H, dd,  $J = 8.1, 1.4$  Hz, ArH isomer 2), 8.07 (0.4H, d,  $J = 8.1$  Hz, ArH isomer 2), 7.70 (0.4H, s, ArH isomer 2), 7.37 (0.6H, d,  $J = 8.0$  Hz, ArH isomer 1), 6.69 (2H, dd,  $J = 5.3, 2.3$  Hz, ArH isomer 1+2), 6.63 – 6.53 (4H, m, ArH isomer 1+2) 3.30 (1.2H, q,  $J = 6.5$  Hz,  $\text{NCH}_2$  isomer 1), 3.17 (0.8H, q,  $J = 6.4$  Hz,  $\text{NCH}_2$  isomer 2), 2.01-1.70 (4H, m,  $\text{CH}_2\text{CH}_2$  isomer 1+2);  $^{13}\text{C NMR}$  (151 MHz,  $\text{DMSO-}d_6$ )  $\delta$  168.69 (C=O), 168.55 (C=O), 164.86 (C=O), 164.67 (C=O), 160.06 (2  $\times$  Ar C), 155.02 (Ar C), 153.17 (Ar C), 152.32 (2  $\times$  Ar C), 152.30 (2  $\times$  Ar C), 141.35 (Ar C), 136.96 (Ar C), 135.16 (Ar CH), 129.85 (ArCH), 129.74 (2  $\times$  ArCH), 129.66 (2  $\times$  ArCH), 128.55 (Ar C), 126.92 (Ar C), 125.27 (Ar CH), 124.66 (Ar CH), 123.72 (Ar CH), 122.73 (Ar CH), 113.21 (2  $\times$  Ar CH), 113.16 (2  $\times$  Ar CH), 109.67 (2  $\times$  Ar C), 109.60 (2  $\times$  Ar C), 102.73 (2  $\times$  Ar CH), 83.75 (C), 83.72 (C), 72.60 (t,  $^1J_{\text{CP}} = 148$  Hz, C), 41.99 (t,  $^2J_{\text{CP}} = 21$  Hz,  $\text{CH}_2$ ), 41.65 (t,  $^2J_{\text{CP}} = 21$  Hz,  $\text{CH}_2$ ), 31.13 ( $\text{CH}_2$ ), 24.06 ( $\text{CH}_2$ );  $^{31}\text{P NMR}$  (202 MHz,  $\text{DMSO-}d_6$ )  $\delta$  20.21;  $m/z$  (ESI+,  $\text{H}_2\text{O}:\text{MeOH}$ ): 630 ( $[\text{M}+\text{Na}]^+$ , 10%), 608 ( $[\text{M}+\text{H}]^+$ , 100).

**Fluorescein-amino-1-pentanol (72)**

Prepared following the method of Gavin *et al.*<sup>1</sup> 5-amino-1-pentanol (34 mg, 1 mmol, 5 eq) was dissolved in NaHCO<sub>3</sub> (1 mL, sat. aq.). Fluorescein (5/6) NHS ester (10 mg, 0.2 mmol, 1 eq) dissolved in DMF (0.1 mL) was added to the solution and the reaction mixture was stirred for 2 days at room temperature in the dark. The solution was acidified with TFA (10% v/v aq.) and purified by RP HPLC [isocratic 80/20 H<sub>2</sub>O (+0.1% v/v TFA)/MeCN (+0.1% v/v TFA)] to yield the fluorescein-OH conjugate as an orange solid (5 mg, 34%).

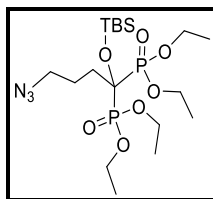
$\lambda_{\text{abs}}/\lambda_{\text{em}}$  491/517;  $\Phi$  0.87;  $\epsilon$  38,400 M<sup>-1</sup>cm<sup>-1</sup>; **mp** 227 °C; **IR** (solid, cm<sup>-1</sup>): 3410 (OH), 1624 (C=O), 1498 (N-H), 1106 (C-N); **<sup>1</sup>H NMR** (601 MHz, DMSO-*d*<sub>6</sub>)  $\delta$  10.11 (2H, br s, OH isomer 1+2), 8.80 (0.6H, t, *J* = 6.5 Hz, NH isomer 1), 8.66 (0.4H, d, *J* = 6.5 Hz, NH isomer 2), 8.46 (0.6H, d, *J* = 6.6 Hz, ArH isomer 1), 8.25 (0.6H, t, *J* = 7.5 Hz, ArH isomer 1), 8.17 (0.4H, t, *J* = 7.5 Hz, ArH isomer 2), 8.08 (0.4H, t, *J* = 7.6 Hz, ArH isomer 2), 7.67 (0.4H, d, *J* = 6.5 Hz, ArH isomer 2), 7.37 (0.6H, t, *J* = 7.6 Hz, ArH isomer 1), 6.70 (2H, br s, ArH isomer 1+2), 6.63 – 6.52 (4H, m, ArH isomer 1+2), 3.42-3.32 (2H, m, CH<sub>2</sub>OH isomer 1+2), 3.32 (1.2H, m, NCH<sub>2</sub> isomer 1), 3.19 (0.8H, t, *J* = 6.8 Hz, NCH<sub>2</sub> isomer 2), 1.56 (1.2H, m, CH<sub>2</sub> isomer 1), 1.49-1.21 (4.8H, m, 2 x CH<sub>2</sub> isomer 1+2 + CH<sub>2</sub> isomer 2); **<sup>13</sup>C NMR** (126 MHz, DMSO-*d*<sub>6</sub>)  $\delta$  168.69 (CO), 168.53 (CO), 164.95 (CO), 164.77 (CO), 160.09 (2 x Ar C), 155.04 (Ar C), 153.15 (Ar C), 152.31 (2 x Ar C), 141.31 (Ar C), 136.90 (Ar C), 135.15 (Ar CH), 129.85 (Ar CH), 129.72 (2 x Ar CH), 129.63 (2 x Ar CH), 128.59 (Ar C), 126.92 (Ar C), 125.32 (Ar CH), 124.68 (Ar CH), 123.68 (Ar CH), 122.67 (Ar CH), 113.23 (2 x Ar CH), 113.16 (2 x Ar CH), 109.66 (2 x Ar C), 109.59 (2 x Ar C), 102.75 (2 x Ar CH), 102.73 (2 x ArCH), 83.78 (C), 61.11 (CH<sub>2</sub>), 61.03 (CH<sub>2</sub>), 39.86 (CH<sub>2</sub>), 32.71 (CH<sub>2</sub>), 32.68 (CH<sub>2</sub>), 29.35 (CH<sub>2</sub>), 29.28 (CH<sub>2</sub>), 23.51 (CH<sub>2</sub>); ***m/z*** (ESI+, H<sub>2</sub>O:MeOH): 558 (5%), 462 ([M+H]<sup>+</sup>, 100).

## 7.1.7 Azide alendronate synthesis

**Tetraethyl (4-chloro-1-*tert*-butyldimethylsilyl-1,1-butanediyl)bisphosphonate (61)**

Triethyl phosphite (0.29 g, 1.7 mmol, 1 eq) was added dropwise to 4-chlorobutyl chloride (0.25 g, 1.8 mmol, 1 eq) at 0 °C. The resulting mixture was allowed to reach rt after which it was stirred at rt for another 15 minutes. DCM (5 mL) was subsequently added followed by diethyl phosphite (0.27 g, 1.9 mmol, 1 eq) and DMAP (0.21 g, 1.7 mmol, 1 eq). The reaction mixture was then stirred at rt for 2 h after which *tert*-butyldimethylsilyl chloride (0.29 g, 1.92 mmol, 1 eq) was added and the mixture was stirred overnight. The reaction mixture was washed with HCl (2 × 20 mL; 0.1 M aq), dried over magnesium sulphate and then concentrated under reduced pressure. Further purification by column chromatography (5 % EtOAc in hexane) to obtain the product as a clear oil (0.21 g, 25%).

**IR** (neat,  $\text{cm}^{-1}$ ) 1246 (P=O), 1020 (O-Si), 964 (P-OR);  **$^1\text{H NMR}$**  (500 MHz,  $\text{CDCl}_3$ )  $\delta$  4.19-4.30 (m, 8H, 4 ×  $\text{OCH}_2\text{CH}_3$ ), 3.56 (t,  $J = 6.0$  Hz, 2H,  $\text{ClCH}_2\text{CH}_2\text{CH}_2$ ), 2.14 – 2.25 (m, 4H,  $\text{ClCH}_2\text{CH}_2\text{CH}_2$ ), 1.37 (t,  $J = 7.1$  Hz, 12H, 4 ×  $\text{OCH}_2\text{CH}_3$ ), 0.93 (s, 9H,  $\text{C}(\text{CH}_3)_3$ ), 0.22 (s, 6H, 2 ×  $\text{CH}_3$ );  **$^{13}\text{C NMR}$**  (126 MHz,  $\text{CDCl}_3$ )  $\delta$  77.73 (t,  $^1J_{\text{PC}} = 156.8$  Hz, C), 62.89 ( $^2J_{\text{CP}} = 19.4$  Hz, 4 ×  $\text{CH}_2$ ), 45.56 ( $\text{CH}_2$ ), 33.55 ( $\text{CH}_2$ ), 27.16 ( $\text{CH}_2$ ), 25.85 (3 ×  $\text{CH}_3$ ), 19.02 (C), 16.47 (4 ×  $\text{CH}_3$ ), -2.54 (2 ×  $\text{CH}_3$ );  **$^{31}\text{P NMR}$**  (202 MHz,  $\text{CDCl}_3$ )  $\delta$  20.51;  **$m/z$**  (EI+,  $\text{H}_2\text{O}:\text{MeOH}$ ): 439 ( $[\text{C}^{35}\text{ClM}^{\text{tBu}}]^+$ , 100%), 437 ( $[\text{C}^{37}\text{ClM}^{\text{tBu}}]^+$ , 55).  $^1\text{H}$ ,  $^{13}\text{C}$  and  $^{31}\text{P}$  spectroscopic data in good agreement with literature.<sup>11</sup>

**Tetraethyl (4-azide-1-*tert*-butyldimethylsilyl-1,1-butanediyl)-bisphosphonate (56)**

Sodium azide (0.37 g, 1.0 mmol, 5 eq) was added to tetraethyl-(4-chloro-1-*tert*-butyldimethylsilyl-1,1-butanediyl)bispophosphate (**58**) (0.57 g, 6.0 mmol, 1 eq) in DMF (10 mL) and the reaction mixture was stirred at 75 °C for 3 hours. The mixture was then cooled to rt and combined with H<sub>2</sub>O (30 mL) and DCM (30 mL). The layers were separated and the organic fraction was further washed with H<sub>2</sub>O (2 × 50 mL). The solution was dried over magnesium sulfate and concentrated in *vacuo* to give a pale yellow oil (0.47 g, 82 %).

**IR** (neat, cm<sup>-1</sup>) 2096 (N<sub>3</sub>); 1247 (P=O); **<sup>1</sup>H NMR** (500 MHz, CDCl<sub>3</sub>) δ 4.27 – 4.19 (8H, m, 4 × OCH<sub>2</sub>CH<sub>3</sub>), 3.29 (2H, t, *J* = 6.5 Hz, N<sub>3</sub>CH<sub>2</sub>), 2.19 – 2.08 (2H, m, N<sub>3</sub>CH<sub>2</sub>CH<sub>2</sub>), 2.05 – 1.94 (2H, m, N<sub>3</sub>CH<sub>2</sub>CH<sub>2</sub>CH<sub>2</sub>), 1.37 (12H, t, *J* = 7.0 Hz, 4 × OCH<sub>2</sub>CH<sub>3</sub>), 0.93 (9H, s, SiC(CH<sub>3</sub>)<sub>3</sub>), 0.23 (6H, s, Si(CH<sub>3</sub>)<sub>2</sub>); **<sup>13</sup>C NMR** (126 MHz, CDCl<sub>3</sub>) δ 77.21 (t, <sup>1</sup>J<sub>PC</sub> 150.1 Hz, C) 63.01 (d, <sup>2</sup>J<sub>CP</sub> = 20.6 Hz, 4 × CH<sub>2</sub>), 51.90 (CH<sub>2</sub>), 33.23 (CH<sub>2</sub>), 25.80 (3 × CH<sub>3</sub>), 23.74 (d, <sup>3</sup>J<sub>CP</sub> = 5.7 Hz, CH<sub>2</sub>), 19.02 (C), 16.45 (4 × CH<sub>3</sub>), -2.60 (2 × CH<sub>3</sub>); ***m/z*** (ESI+, H<sub>2</sub>O:MeOH) 524 ([M+Na]<sup>+</sup>, 100%), 410 (40). <sup>1</sup>H, <sup>13</sup>C and <sup>31</sup>P spectroscopic data in good agreement with literature.<sup>11</sup>

### 7.1.8 Peptide synthesis

#### HAP Selective peptide (67)

Ac-Ser-Val-Ser-Val-Gly-Met-Lys-Pro-Ser-Pro-Arg-Pro-Gly-Gly-Gly-Lys(N<sub>3</sub>)-Ac

Produced using Rink Amide AM Resin (500 mg, 0.345 mmol), standard Fmoc SPPS protocols described below and RP HPLC ([isocratic 60/40 H<sub>2</sub>O (+0.1% v/v TFA)/MeCN (+0.1% v/v TFA)] to give a colourless solid (180 mg, 51%).

**IR** (solid, cm<sup>-1</sup>) 3273 (OH), 2962 (C-H), 2098 (N<sub>3</sub>), 1624 (C=O), 1527 (CH), 1431 (CH); **m/z** (ESI+, H<sub>2</sub>O:MeOH) 826 ([M+2Na]<sup>2+</sup>, 100%), 815 ([M+H+Na]<sup>2+</sup>, 80), 805 ([M+2H]<sup>2+</sup>, 40).

#### Standard Procedure for Solid Phase peptide synthesis

##### *Method A – Swelling*

Rink amide AM resin (150 mg, 104 μmol, 690 μmol g<sup>-1</sup>) was placed in an empty reservoir (6 mL) and swelled in DCM (5 mL) for 30 minutes, before washing the resin with DMF (3 × 4 mL) and DCM (3 × 4 mL).

##### *Method B – Fmoc Deprotection*

A solution of piperidine (20% in DMF, 4 mL) was added to the resin and the mixture was agitated for 10 minutes, the solution was drained into a vacuum box and washed with DMF (3 × 4 mL) and DCM (3 × 4 mL), before repeating the process again. Method C was used to check for successful deprotection.

##### *Method C – Chloranil Test*

To verify a successful coupling or deprotection, a chloranil test was used to check for the presence or absence of primary or secondary amines. Chloranil test requires two solutions; Solution A acetaldehyde (2% in DMF) and Solution B chloranil (2% in DMF). The test was carried out by placing a small number of beads in an Eppendorf tube and adding 5-6 drops of each solution. The mixture was then agitated for 5 minutes. If free amines were present the beads would turn blue and if no free amines were present no colour change would be observed on the beads.

##### *Method D – Coupling of Amino acids*

The appropriate amino acid (3 eq) was pre-activated by dissolving it with Oxyma (3 eq) in DMF (1 mL), the solution was agitated for 3 minutes whereupon DCC (3 eq) was added and

the solution was agitated for a further 2 min. The highly activated complex was then added to the resin and agitated for 40 minutes. Once the coupling was complete the solution was drained and the resin was washed with DMF (3 × 4 mL) and DCM (3 × 4 mL). Method C was then used to check for complete coupling.

#### *Method E – Capping*

Once the final amino acid was successfully coupled, the peptide was acetylated by agitating the resin with a solution of Ac<sub>2</sub>O (20 eq), DIPEA (20 eq) in DMF (1 mL) for 40 minutes. Method C was used to check for complete acetylation.

#### *Method F – Cleavage*

After successfully capping of the peptide, the resin was washed with DMF (3 x 4 mL), DCM (5 × 4 mL) and dried under vacuum. Peptide cleavage was carried out by agitating the resin in TFA:H<sub>2</sub>O:EDT:TIS (94:2.5:2.5:1).

The TFA liquor was collected in a Falcon tube (50 mL) and the resin was washed with more of the cocktail liquor (5 × 3 mL) before concentrating the solution under a stream of N<sub>2</sub>. Cold Et<sub>2</sub>O (20 mL) was then added to the precipitate and the solution was sonicated before being centrifuged at 3500 rpm for 2 minutes, the supernatant was decanted, and the process was repeated again for up to a maximum of 4 times. The precipitated crude peptide was then lyophilized by dissolving it in H<sub>2</sub>O and MeCN.

#### **Cy5.5-HAP selective peptide (71)**

Cy5.5 (**47**) (100 mg, 0.96 mmol, 1.2 eq) and HAP selective peptide (**67**) (130 mg, 0.84 mmol, 1 eq) were dissolved in DMF (10 mL). To this Cu(MeCN)<sub>4</sub>BF<sub>4</sub> (10 mol %) was added. The reaction was left stirring for 24 hours at rt in the dark. The solution was concentrated under reduced pressure and purified by RP HPLC [isocratic 65/35 H<sub>2</sub>O (+0.1% v/v TFA)/MeCN (+0.1% v/v TFA)] to yield a blue solid (150 mg, 90%).

$\lambda_{\text{abs}}/\lambda_{\text{em}}$  660/695;  $\Phi$  0.73;  $\epsilon$  110,000 M<sup>-1</sup>cm<sup>-1</sup>; **IR** (solid, cm<sup>-1</sup>): 3410 (OH), 3000 (NH), 2924 (CH), 1654 (C=O), 1436 (CH), 1406 (CH); *m/z* (ESI+, H<sub>2</sub>O:MeOH) 1075 ([M+2H]<sup>2+</sup>, 10%), 715 ([M+3H]<sup>3+</sup>).

### 7.1.9 Incorporation of probes in calcium minerals

#### **Fluorescein-BP (42), Cy-Pep (53) and Alizarin S incorporation in calcium minerals**

Aqueous suspension of calcium species (HAP, CaOx, CaPi, CaPyr, Sigma Aldrich and Fisher Scientific) (50 mg) were incubated with either Fluorescein-BP (**42**) (5  $\mu$ M) or CyPep (**53**) (5  $\mu$ M) or Alizarin S (1%) for 2 hours. Unbound probe was removed after a series of centrifugation steps and washing steps which involved: resuspension of the solid in H<sub>2</sub>O (3  $\times$  15 minutes). Fluorescence analysis of the combined aqueous extracts was performed using Synergy HT Multi Mode Microplate reader at 488 nm (Fluorescein-BP), 530 nm (Alizarin S) and using Fluoromax-3 at 630 nm (Cy-Pep).

#### **Na<sup>18</sup>F incorporation in calcium minerals**

Aqueous suspension of calcium species (HAP, CaOx, CaPi, CaPyr, WTK Sigma Aldrich and Fisher Scientific) (50 mg) were incubated with Na<sup>18</sup>F solution (100kBq/mL) for 20 minutes. Unbound probe was removed after a series of centrifugation steps and three washing steps which involved: resuspension of the solid in H<sub>2</sub>O. Calcium solids were scanned using high-resolution micro-positron emission tomography and non-contrast computed tomography [50kVp tube voltage, 300msec exposure time] (Mediso nanoScan PET/CT).

#### **Fluorescein-BP (55), Cy-Pep (71) and Alizarin S incorporation in calcium mineral phantoms**

Calcium species (HAP, CaOx, CaPi, CaPyr (50 mg) were suspended in 2% agarose in H<sub>2</sub>O (2 mL) and left to set. Upon hardening, agarose phantoms were incubated with either Fluorescein-BP (**55**) (5  $\mu$ M) or CyPep (**71**) (5  $\mu$ M) or Alizarin S (1%) for 2 hours. Phantoms were subsequently washed with H<sub>2</sub>O (3  $\times$  5 minutes) and then imaged using Zeiss Axiovert 25 inverted microscope (Fluorescein-BP and Cy-Pep) or photographed (Alizarin S).



## 7.2 Biology

### 7.2.1 General procedures

Chemicals used were purchased from Sigma-Aldrich, and tissue culture media and buffers were purchased from Thermo Fisher unless otherwise specified. All animals were culled by cervical dislocation in accordance with the Home Office Schedule 1 guidelines in the U.K. The dissections took place in a ventilated hood and all tools were sterilised by autoclaving prior to dissection.

### 7.2.2 Tissue culture

Wash buffer consisted of Hank's Balanced Salt Solution (HBSS, Life Technologies) containing 1% gentamicin (Life Technologies). For cell detachment, TrypLE Express Enzyme (Life Technologies), a trypsin replacement, was used. Cell culture media consisted of Dulbecco's Modified Eagle Media F-12 (DMEM/F, Life Technologies) or Minimum Essential Media ( $\alpha$ -MEM, Life Technologies) containing 1% gentamicin and 10% heat inactivated foetal bovine serum (FBS, Life Technologies) which was sterilised by passing through a 0.22  $\mu$ m filter. All tissue culture procedures were completed in a ventilated tissue culture hood to ensure sterile conditions, at 37°C in 95% air/5% CO<sub>2</sub>.

#### 7.2.2.1 Cell types

Primary mouse VSMC and rat aortic VICs were obtained from either 5 week old male Sprague Dawley rats or C57BL6 mice (Charles River Laboratories). The mouse VSMC cell line (MOVAS-1) previously described by Afroze,<sup>12</sup> was purchased from ATCC, was stored at a density of  $2.7 \times 10^6$ /mL and frozen to -150 °C until needed. MOVAS-1 is a cell line isolated from aortic smooth muscle tissue which had been immortalized with SV40 large T antigen which has been employed previously to investigate the VSMC cell cycle.<sup>12-15</sup> MC3T3 cell line, was purchased from ATCC and stored at a density of  $2.7 \times 10^6$ /mL and frozen to -150 °C until needed. The MC3T3 is an osteoblast precursor cell line derived from mouse calvaria and has been widely used to study bone biology.<sup>16,17</sup> When required, the cells were warmed to 37 °C in a water bath and immediately added to 20 mL of DMEM/F (MOVAS-1) or  $\alpha$ -MEM (MC3T3) cultured media. The cell suspension was then centrifuged at 670 g for 5 minutes to remove any cell debris and DMSO which had been used in the freezing media. The cell pellet was then re-suspended in culture media and transferred to a T175 flask to propagate.

### 7.2.2.2 Primary mouse VSMC isolation and culture

Primary aortic VSMCs were isolated from five week old mice (Charles River Laboratories) as previously described.<sup>18-20</sup> Mice were euthanized by cervical dislocation the aorta was then dissected and the adventitia removed. After washing with HBSS the aorta was cut longitudinally to expose the endothelial layer. Eight aortae were pooled together and incubated for 10 minutes at 37 °C in 1 mg/mL trypsin to remove any remaining adventitia and endothelium. Aortae were washed and incubated overnight at 37 °C in  $\alpha$ -MEM culture media. Tissues were then washed and then incubated in 100  $\mu$ L Collagenase type II (425 UI/mL, Worthington Biochemical Corporation) for 4 hours at 37 °C. The resulting cell suspension was centrifuged at 320 g for 5 minutes. VSMC pellets were resuspended in  $\alpha$ -MEM culture media and cultured for two passages in T25 tissue culture flasks (Corning) coated with 0.25  $\mu$ g/cm<sup>2</sup> laminin to promote maintenance of the contractile differentiation state.<sup>21</sup>

### 7.2.2.3 Primary rat VIC isolation and culture

Primary aortic VICs were isolated from aortic valve leaflets, dissected from the hearts of 5 weeks old male Sprague Dawley rats (Charles River Laboratories) as previously described.<sup>22</sup> The animal was placed supine, and the abdomen skin, ribcage, fatty tissue and lungs removed to expose the heart. The latter was extracted and placed in cold HBSS until all dissections were complete. To extract the heart valves, cardiac muscle was trimmed to expose the aorta and the aortic root. The artery was then cut open and the valve leaflets were carefully dissected. To clean and release the VICs from the leaflets, the following digestions were performed. The leaflets were centrifuged at 100 g, for 1 minute to pellet and remove HBSS and then digested in 100  $\mu$ L of Collagenase type II (425 U/mL) for 5 minutes at 37 °C to release valve endothelial cells (VECs). Following digestions, the leaflets were subjected to another 30 seconds centrifugation at 100 g. The supernatant, which contained the digested VECs, was discarded subsequently. A wash with 500  $\mu$ L of HBSS was applied to rinse off any remaining VECs and the leaflets were pelleted with a 30 seconds 100 g centrifugation. The supernatant was discarded. To digest the VICs, the leaflets were incubated with 100  $\mu$ L of Collagenase II (425 U/mL) for 2 hours, at 37 °C. At the end of the incubation, VICs were removed from the leaflets by forceful pipetting. The VICs were spun at 670 g for 5 minutes and relocated to a suitable sized flask, T75, and left to propagate.

### 7.2.2.4 Cell expansion and calcification

Cells were cultured until 90-100% confluent, at which point culture media was replaced as necessary. For cell expansion, the culture media was initially removed, and the monolayer was rinsed with HBSS. For cell detachment, the HBSS was discarded and the monolayer was

incubated at 37 °C for 3-5 minutes in the presence of TypLE. The reaction was deactivated by adding double the volume of culture media. The cells were then pelleted at 670 g for 5 minutes. The supernatant was discarded, and the cells were re-suspended in 1 mL of fresh culture media and transferred to a suitable sized flask with pre-warmed culture media. To count the number of viable cells, a haemocytometer was used. The cells were then transferred to a new flask and left to propagate until 90-100% confluent.

For calcification experiments, cells were seeded and then were left to propagate at 37 °C, in a humidified incubator.

#### 7.2.2.5 Aortae isolation and culture

Aortic rings were dissected from eight-week-old Fischer rats. Rats were euthanized by cervical dislocation; the aorta was then dissected, and the adventitia removed. After washing with HBSS the aortae were cut into ~4 mm thick rings and cultured in  $\alpha$ -MEM culture media.

#### 7.2.2.6 ApoE<sup>-/-</sup> Mice

Male atherosclerosis-prone apolipoprotein E-deficient (ApoE<sup>-/-</sup>) mice were obtained from Dr Hadoke. Mice started a high cholesterol diet (D12336,<sup>23-25</sup> Research Diets, Inc. Cholesterol: 1.25%) at 12-14 weeks old and were kept on the diet for 12 weeks. The mice were subsequently culled and aortic arch harvested for further investigations. Tissue was section into 5  $\mu$ m sections. For OPT imaging, ApoE<sup>-/-</sup> mice were culled at age of 15 months, thoracic aorta were carefully dissected and fixed in 10% NBF.

#### 7.2.2.7 Induction of calcification

Cells were seeded in culture medium for 2 days and then switched to calcification medium, which was prepared by adding; 1 M inorganic phosphate (P<sub>i</sub>, mixture of NaH<sub>2</sub>PO<sub>4</sub> and Na<sub>2</sub>HPO<sub>4</sub>, pH=7.4) and 1M CaCl<sub>2</sub> (Ca). Cells were always compared to the control, DMEM/F contains 1.05 mM of Ca and 0.95 mM of Pi while  $\alpha$ -MEM contains 1.8 mM of Ca and 1.01 mM Pi.

For MOVAS-1, cells were grown in DMEM/F culture media to confluence before treatment with DMEM/F calcification medium; phosphate alone (3 mM and 5 mM) or phosphate and calcium rich (1.4 mM Pi and 2.4 mM Ca or, 2.5 mM Pi and 2.7 mM Ca). Cells were incubated for 7 days and the medium was changed every 2-3 days.

For VICS, cells were grown in DMEM/F culture media to confluence before treatment with DMEM/F calcification medium; phosphate and calcium rich (1.4 mM Pi and 2.4 mM Ca or, 2.5 mM Pi and 2.7 mM Ca). Cells were incubated for 7 days and the medium was changed every 2-3 days.

For VSMCs, cells were grown in  $\alpha$ -MEM culture media until confluent and switched to  $\alpha$ -MEM calcification medium; phosphate rich (1.8 mM, 2.6 mM and 3 mM). Cells were incubated for 7 days and the medium was changed every 2-3 days.

For MC3T3, cells were grown in  $\alpha$ -MEM culture media switched to  $\alpha$ -MEM calcification medium, which was prepared by adding 2.5 mM  $\beta$ -glycerophosphate ( $\beta$ -GP) and 50  $\mu$ g/ml ascorbic acid (aa). Cells were incubated for 21 days in 95% air/5% CO<sub>2</sub> and the medium was changed every 2-3 days.

For aortic rings, rings were cultured in  $\alpha$ -MEM culture media. After 1 day, the media was changed to  $\alpha$ -MEM calcifying media of the following P<sub>i</sub> concentrations; 1.8 mM, 2.6 mM, 3 mM for 7 days with media change on alternative days.

## 7.2.3 Imaging of cell and tissue cultures

### 7.2.3.1 Tissue processing and embedding

Tissue was either embedded in wax or in OCT. For OCT,<sup>26</sup> sectioned into 5  $\mu$ m thick slices and placed on slides. For waxed samples, NBF fixed tissues were slowly dehydrated, following a technique previously described,<sup>20</sup> using a series of alcohol incubations as follows: PBS (2  $\times$  5 minutes), followed by EtOH (70%, 1 h), EtOH (4  $\times$  95% for 1 hour), EtOH (100%, 1 hour), EtOH:xylene (50:50 1 hour), xylene (2  $\times$  1 hour) and transferred into wax embedding cassettes in paraffin wax at 60 °C for 4 hour. The wax blocks were embedded in plastic moulds and trimmed using an Ernst Leitz AG microtome to expose sample surface. The paraffin wax-embedded samples were then cooled on ice for 30 minutes and sectioned at 4  $\mu$ m thickness. They were then floated in a 40 °C water bath for 1 minute before carefully transferring onto electrostatically charged slides. The slides were dried overnight at 37 °C.

### 7.2.3.2 Staining with Fluorescein-BP

Culture media was removed, and the cell monolayer was subsequently washed with HBSS then incubated with appropriate media containing Fluorescein-BP (**42**) (1  $\mu$ M) for 2 hours.

For staining with Fluorescein-BP (**42**) alone; the media was then discarded, and the cell monolayer was washed with HBSS (2  $\times$  2 mL), fixed with 10% NBF for 15 minutes and washed with phosphate buffer saline (PBS, 2  $\times$  2 mL) and with H<sub>2</sub>O (1  $\times$  2 mL).

For dual imaging with Cell Mask Orange; monolayers were washed with HBSS (2  $\times$  2 mL) and fresh HBSS containing Cell Mask Orange (0.5x, Life Technologies) was added for 5 minutes. Monolayers were washed with HBSS (2  $\times$  2 mL), fixed with 10% neutral-buffered formalin (NBF, CellPath) for 15 minutes and subsequently washed with PBS (2  $\times$  2 mL) and

H<sub>2</sub>O. Glass coverslips were mounted onto slides with Prolong Gold Anti-Fade Reagent (Life Technologies).

For dual imaging with DAPI; monolayers were subsequently washed with HBSS (2 × 2 mL). Monolayer was incubated with DAPI (300 nM, Life Technologies) for 5 minutes followed by washing with HBSS (2 × 2 mL), fixed and mounted as described above.

For *ApoE*<sup>-/-</sup> Mice Sections, WT rats and human sections; sections were de-waxed in xylene and incubated with Fluorescein-BP (1 μM) for 2 hours, washed in H<sub>2</sub>O (2 × 500 μL) followed by incubation with 2% Alizarin S (250 μL) for 5 minutes. Sections were washed in H<sub>2</sub>O (3 × 500 μL) and subsequently incubated with DAPI (500 nM) for 5 minutes. Sections were washed with H<sub>2</sub>O (1 × 500 μL) and then mounted as described above.

Fluorescence images were captured using a Leica DMBL-2 upright fluorescent microscope and/or Zeiss Confocal LSM 710 and/or Leica DMRB fluorescence microscope. Fluorescence intensity detected on Synergy HT Multi Mode Microplate reader at 488 nm.

#### 7.2.3.3 Alizarin S staining

For the cell monolayers, cells were fixed with 10% NBF for 15 minutes before washing with PBS (2 × 2 mL). The cells were then stained with 2% Alizarin Red (500 μL) for 10 minutes at rt, supernatant discarded and the cell monolayer was subsequently washed with H<sub>2</sub>O (3 × 2 mL).

For the aortic rings, after Fluorescein-BP (**42**) rings were fixed with 10% NBF for 15 minutes then permeabilised with 1% KOH for 1 hour followed by overnight staining with 0.00005% Alizarin S in 1% potassium hydroxide (KOH). Residual Alizarin S was removed by washing H<sub>2</sub>O (3 × 2 mL).

For human tissue, sections were de-waxed in xylene and stained with 2% Alizarin red for 5 minutes, washed with H<sub>2</sub>O (3 × 500 μL) and dehydrated to visualize calcium deposition.

#### 7.2.3.4 Von Kossa staining

For *ApoE*<sup>-/-</sup> and human tissues; sections were de-waxed in xylene and stained with 1% silver nitrate (150 μL) under a UV lamp for 20 minutes.<sup>27</sup> Sections were rinsed with H<sub>2</sub>O (3 × 500 μL) then incubated with 5% sodium thiosulfate (150 μL) for 5 minutes. Subsequently, sections were washed with H<sub>2</sub>O (2 × 500 μL) and then counterstained with 0.1% neutral red (150 μL) for 2 minutes. Sections were dehydrated, with three changes of absolute ethanol and cleared with three changes of xylene and mounted using DePex. Images were obtained using a Nikon Ni1 Brightfield microscope.

### 7.2.3.5 Immunofluorescence on aortic rings

5 µm rat aortae sections on slides were incubated with Tris-Buffered Saline and Tween 20 (TBS/T) for 15 minutes then permeabilised with 0.1% Triton-X in 1x TBS for 30 minutes at rt. Sections were washed with TBS/T (3 × 500 µL; 5 minutes per wash) and then incubated with blocking buffer (TBS/T and 5% BSA, 200 µl) for 1 hour. After 1 hour, the blocking buffer was removed by washing with TBS/T (3 × 500 µL; 5 minutes per wash), slides were then incubated with anti- $\alpha$ -smooth muscle action ( $\alpha$ -SMA, 1:100, 200 µL)<sup>28</sup> and CD31 (1:100, 200 µL)<sup>26</sup> overnight at 4 °C. Negative control consisted of the same concentration of IgG from the same animal species as primary antibody. On day 2, after washing with TBS/T (3 × 500 µL; 5 minutes per wash), sections were incubated with Alexa Fluor® 496 goat-anti-rabbit antibody (1:250, 200 µL, Thermo Fisher) in blocking buffer for 1 hour in the dark. Following removal of excess antibody with TBS/T (3 × 500 µL; 5 minutes per wash) sections are then incubated with DAPI (300nM) for 5 minutes, washed with TBS/T (1 × 500 µL; 2 minutes per wash) and mounted with ProLong Gold Antifade. Care was taken to remove any air bubbles and the slides were left to dry for 24 hours at 4 °C before imaging. Fluorescence signal was detected under a Leica DMRB fluorescence microscope.

### 7.2.3.6 OPT imaging of *ApoE*<sup>-/-</sup> Mice

The aorta were washed in PBS for 3 hour and then immediately immersed in Fluorescein-BP (1 µM) overnight. The aorta were washed in PBS (1 × for 1 hour) and then processed for OPT imaging. Aorta were embedded in a 1% solution of low-melting agarose and then dehydrated three times in 100% ethanol overnight. Once the aortae were completely dehydrated, ethanol was replaced with BABB solution and clear for 2 days. The embedded aortae were then glued on a mount and left to dry for 2 hour. Specimens are then scanned using an OPT scanner.

### 7.2.3.7 Immunohistochemistry (IHC) of human tissue

IHC was performed using the Vectastain ABC Kit (mouse IgG) (Vector Labs, Peterborough, UK) according to manufacturer's instructions. Before IHC sections were de-waxed in xylene. Immunohistochemical analysis of OPN (1:00 dilution, anti-human mouse clone OPN (AKm2A1), Santa Cruz Biotechnology) or OPG (1:00 dilution, anti-human mouse clone OPG (E-10), Santa Cruz Biotechnology),<sup>29</sup> was conducted after heat-induced epitope retrieval using a 10 mM citrate buffer (pH 6) for 1 hour at 70 °C. Endogenous peroxidase was blocked by soaking in 0.3% H<sub>2</sub>O<sub>2</sub> in TBS/T at rt for 30 minutes, followed by non-specific antibody blocking with serum for another 30 minutes. Sections were then incubated with the specific primary anti-human antibodies overnight at 4 °C. All incubation steps were followed by washing in TBS/T. The sections were then washed in TBS/T and then incubated with diluted

biotinylated secondary antibody (1:100) for 30 minutes at rt. After washing in TBS/T for 5 minutes, the sections were then incubated for 30 minutes with ABC reagent (avidin and horse radish peroxidase (HPR)). The reaction was developed using premixed 3,3'-diaminobenzidine (DAB; 0.06% DAB, 0.1% hydrogen peroxide, in PBS) solution (Vector Labs) until the desired stain intensity developed (5 minutes). The sections were rinsed and counterstained with haematoxylin and eosin (H&E).<sup>27</sup> Dehydration through graded alcohols, cleared using xylene in a Leica Autostainer XL and then mounted in DePex. IgG Control sections were incubated with mouse IgG (1:100) in place of OPN or OPG or RUNX-2 antibody. Images were obtained using a Nikon Ni1 Brightfield microscope.

#### 7.2.3.8 PET/CT analysis human tissue

Atherosclerotic layers of left main coronary arteries were obtained with ethical approval and informed relative authorisation from the next of kin at autopsy from victims of sudden death (National Health Service South East Scotland 14/SS/1090). The tissue was immediately frozen at -80 °C. Thawed non-decalcified coronary artery specimens were incubated for 20 minutes in <sup>18</sup>F-sodium fluoride 100kBq/mL solution (10.5MBq <sup>18</sup>F-NaF in 99.5mL 0.9% NaCl). Samples were washed in 10mLs 0.9% NaCl (2 × 5 minutes) to remove unbound <sup>18</sup>F-fluoride. Coronary artery specimens were scanned using high-resolution micro-positron emission tomography and non-contrast computed tomography [50kVp tube voltage, 300msec exposure time] (Mediso nanoScan PET/CT). After whole specimen imaging, the coronary arteries were fixed in 10% buffered formaldehyde before being dehydrated, embedded in paraffin wax and sectioned (5 µm thickness).<sup>30</sup>

### 7.2.4 Biochemical assays

#### 7.2.4.1 Calcium leaching assay

Initially, the culture media was discarded, and the cells were washed with PBS. The cell monolayer was incubated with an appropriate volume of 0.6M HCl and left to leach for 24 hours at 4 °C. Subsequently, a Calcium Assay Kit (Randox) was used to measure the calcium deposition in the cells. The assay depends on a binding mechanism between *O*-cresolphthalein complexone and calcium ions in an alkaline media. A negative control (0.6 M of HCl) and a calcium standard are required to determine the calcium concentration. 5.5 µL of standard, negative control and the sample were added to a 96-well plate, in duplicate. 250 µL of 1:1 ratio of 2-amino-2-methyl-propan-1-ol (R1) and *O*-cresolphthalein complexone, 8-Hydroxyquinoline, HCl (R2) were added to each well. The ODs were determined on a Synergy HT Multi Mode Microplate reader at 570 nm. Calcium concentration of each sample was determined using the following equation:

$$\text{Concentration} \left( \frac{\text{mmol}}{\text{L}} \right) = \left( \frac{\text{sample OD}}{\text{standard OD}} \right) * \text{standard concentration} \left( \frac{\text{mmol}}{\text{L}} \right)$$

Calcium concentration was then standardised using total protein concentration described below.

#### 7.2.4.2 Protein Concentration Assay

The cellular proteins were denatured using 0.1M NaOH + 0.1% sodium dodecyl sulphate (SDS). Protein content of the cell was measured using Bio-Rad DC protein assay. Bovine  $\gamma$ -globulin protein standards (0.125 - 2 mg/mL) were prepared in the solution: 0.1 M NaOH + 0.1% SDS. 5  $\mu$ L of sample or standards were transferred to a 96-well plate, in duplicate. To each well, 25  $\mu$ L of alkaline copper tartrate solution and 200  $\mu$ L of dilute folin reagent were added. The plate was incubated at rt for 20 minutes. The optical densities (OD) were obtained on a Synergy HT Multi Mode Microplate reader at 690 nm. The protein concentration was resolved from the standard curve.

#### 7.2.4.3 Alamar Blue assay

All wells were washed with HBSS (2  $\times$  2 mL) and then incubated Alamar Blue (10  $\mu$ L per 100  $\mu$ L of media, Life Technologies) for 4 hours. Results were recorded using Synergy HT Multi Mode Microplate reader at 570 nm.

### 7.2.5 Raman Spectroscopy

#### 7.2.5.1 Raman on cell pellet

MOVAS-1 cells were grown, in a T75 flask, in DMEM/F culture media to confluence (day 0) and switched to calcification medium or control media. On day 7, MOVAS-1 monolayer was washed with PBS (3  $\times$  2 mL) after which the monolayer was incubated with TrypLE Express Enzyme (1 mL) for 2 minutes at 37 °C. DMEM/F culture media (10 mL) was added and the cells were centrifuged at 100 g, for 5 minutes. The supernatant was removed and the pellet was washed with PBS (10 mL). The pellet was resuspended in PBS and subsequently centrifuged again. The supernatant was discarded and the pellet kept in PBS (100  $\mu$ L) until imaging. Raman imaging was carried out using a InVia Renishaw Microscope with a 785 nm laser excitation source which was used to excite the sample through a 50, N.A. 0.75 objective. The total data acquisition was performed during 30 s for spectra with a 50% laser power using the WiRE software. All of the spectra acquired were background subtracted using a background correction algorithm present on WiRE software. For the purpose of this work, all peaks were normalised the phenylalanine which should not be altered in the presence or absence of calcification media.



## 7.2.5.2 Raman assessment of cell monolayer

MOVAS-1, VICS, mouse VSMCs were grown and calcified on CaF<sub>2</sub> slides as described under the induction of calcification section. On day 7, the monolayers were fixed in 10% NBF for 15 minutes and then imaged. Raman imaging was carried out in the same manner as mentioned under the cell pellet section.

## 7.2.5.3 Raman analysis of agarose embedded aortic rings

Aortic rings were dissected from eight-week-old Fischer rats. Rats were euthanized by cervical dislocation; the aorta was then dissected, and the adventitia removed. After washing with HBSS the aortae were filled and embedded in 8 % UltraPure™ Low Melting Point Agarose. The aortae were then cut into 10 μm sections using a VF-300-07 Compressotome™ (Precisionary) and subsequently cultured in α-MEM. The agarose rings were calcified for 7 days and then fixed in 10 % NBF for 15 minutes. The agarose was subsequently removed upon gentle heating in PBS to allow for Raman imaging. The conditions used for Raman imaging were the same as mentioned under the cell pellet section.

## 7.2.5.4 Raman on human Sections

Sections were de-waxed in xylene (15 minutes), EtOH (100%, 15 minutes), EtOH (95%, 15 minutes), followed by EtOH (70%, 15 minutes). Stored at rt until imaging using the Renishaw InVia, 785 nm laser, 60 second, 100% laser power. Spectra obtained were subtracted from paraffin spectra using the same parameters mentioned above.

## 7.3 References

- 1 R. Liu, Y. Gao, Q. Zhang, X. Yang, X. Lu, Z. Ke, W. Zhou and J. Qu, *New J. Chem.*, 2014, **38**, 2941.
- 2 S. Ghosh, M. A. Alam, A. Ganguly, S. Dalapati and N. Guchhait, *Inorganica Chim. Acta*, 2015, **429**, 39–45.
- 3 W. M. Chang, M. Dakanali, C. C. Capule, C. J. Sigurdson, J. Yang and E. A. Theodorakis, *ACS Chem. Neurosci.*, 2011, **2**, 249–255.
- 4 G. Sivaraman and D. Chellappa, *J. Mater. Chem. B*, 2013, **1**, 5768.
- 5 J. Wang, W. F. Cao, J. H. Su, H. Tian, Y. H. Huang and Z. R. Sun, *Dye. Pigment.*, 2003, **57**, 171–179.
- 6 M. Lopalco, E. N. Koini, J. K. Cho and M. Bradley, *Org. Biomol. Chem.*, 2009, **7**, 856–9.

- 7 H. Langhals, A. Varja, P. Laubichler, M. Kernt, K. Eibl and C. Haritoglou, *J. Med. Chem.*, 2011, **54**, 3903–3925.
- 8 D. M. Mizrahi, O. Ziv-Polat, B. Perlstein, E. Gluz and S. Margel, *Eur. J. Med. Chem.*, 2011, **46**, 5175–83.
- 9 M. Gerowska, L. Hall, J. Richardson, M. Shelbourne and T. Brown, *Tetrahedron*, 2012, **68**, 857–864.
- 10 K. Kiyose, K. Hanaoka, D. Oushiki, T. Nakamura, M. Kajimura, M. Suematsu, H. Nishimatsu, T. Yamane, T. Terai, Y. Hirata and T. Nagano, *J. Am. Chem. Soc.*, 2010, **132**, 15846–8.
- 11 T. Eisner, Charles University, Prague, 2014.
- 12 T. Afroze, L. L. Yang, C. Wang, R. Gros, W. Kalair, A. N. Hoque, I. N. Mungrue, Z. Zhu and M. Husain, *AJP Cell Physiol.*, 2003, **285**, C88–C95.
- 13 MacRae, *Int. J. Mol. Med.*, 2011, **27**, 663–8.
- 14 J. A. Chalmers, T. A. Martino, N. Tata, M. R. Ralph, M. J. Sole and D. D. Belsham, *Am. J. Physiol. Regul. Integr. Comp. Physiol.*, 2008, **295**, R1529-38.
- 15 T. Afroze and M. Husain, *J. Biol. Chem.*, 2000, **275**, 9062–9069.
- 16 Y.-K. Lee, J. Song, S.-B. Lee, K.-M. Kim, S.-H. Choi, C.-K. Kim, R. Z. LeGeros and K.-N. Kim, *J. Biomed. Mater. Res.*, 2004, **69A**, 188–195.
- 17 K. Hiura, K. Sumitani, T. Kawata, K. Higashino, M. Okawa, T. Sato, Y. Hakeda and M. Kumegawa, *Endocrinology*, 1991, **128**, 1630–1637.
- 18 D. Zhu, N. C. W. Mackenzie, J. L. Millán, C. Farquharson and V. E. MacRae, *PLoS One*, 2011, **6**, e19595.
- 19 D. Zhu, N. A. Rashdan, K. E. Chapman, P. W. Hadoke and V. E. MacRae, *Vascul. Pharmacol.*, 2016, **86**, 87–93.
- 20 M. J. Berridge, P. Lipp and M. D. Bootman, *Nat. Rev. Mol. Cell Biol.*, 2000, **1**, 11–21.
- 21 K. A. Johnson, M. Polewski and R. A. Terkeltaub, *Circ. Res.*, 2008, **102**, 529–537.
- 22 L. Cui, N. A. Rashdan, D. Zhu, E. M. Milne, P. Ajuh, G. Milne, M. H. Helfrich, K. Lim, S. Prasad, D. A. Lerman, A. T. Vesey, M. R. Dweck, W. S. Jenkins, D. E. Newby, C. Farquharson and V. E. Macrae, *J. Cell. Physiol.*, 2017, **232**, 2985–2995.

- 23 F. Usui, H. Kimura, T. Ohshiro, K. Tatsumi, A. Kawashima, A. Nishiyama, Y. ichiro Iwakura, S. Ishibashi and M. Takahashi, *Biochem. Biophys. Res. Commun.*, 2012, **420**, 72–77.
- 24 A. E. Jääskeläinen, S. Seppälä, T. Kakko, U. Jaakkola and J. Kallio, *Neuropeptides*, 2013, **47**, 67–73.
- 25 D. Weiss, J. J. Kools and W. R. Taylor, *Circulation*, 2001, **103**, 448–54.
- 26 P. Menon and E. A. Fisher, in *Methods in Molecular Biology*, NIH Public Access, 2015, vol. 1339, pp. 131–148.
- 27 W. Bloch and Y. Korkmaz, in *Practical Methods in Cardiovascular Research*, Springer-Verlag, Berlin/Heidelberg, 2005, pp. 485–499.
- 28 U. Raaz, I. N. Schellinger, E. Chernogubova, C. Warnecke, Y. Kayama, K. Penov, J. K. Hennigs, F. Salomons, S. Eken, F. C. Emrich, W. H. Zheng, M. Adam, A. Jagger, F. Nakagami, R. Toh, K. Toyama, A. Deng, M. Buerke, L. Maegdefessel, G. Hasenfuß, J. M. Spin and P. S. Tsao, *Circ. Res.*, 2015, **117**, 513–24.
- 29 K. D. O’Brien, J. Kuusisto, C. E. Reichenbach, Dennis D. Ferguson, Marina Giachelli, Cecilia Charles E. Alpers and C. M. Otto, *Circulation*, 1995, **92**, 2163–2168.
- 30 A. Irkle, A. T. Vesey, D. Y. Lewis, J. N. Skepper, J. L. E. Bird, M. R. Dweck, F. R. Joshi, F. A. Gallagher, E. A. Warburton, M. R. Bennett, K. M. Brindle, D. E. Newby, J. H. Rudd and A. P. Davenport, *Nat. Commun.*, 2015, **6**, 7495.



# Chapter 8- Abbreviations

#	number
$\mu\text{M}$	micro molar
$^{18}\text{F}$ -FDG	fluorodeoxyglucose
$^{18}\text{F}$ -NaF	sodium fluoride
2D	two dimensional
3D	three dimensional
AA	ascorbic acid
$\text{Ac}_2\text{O}$	acetic anhydride
ACP	amorphous calcium phosphate
ALK	alkaline phosphate
<i>ApoE</i> <sup>-/-</sup>	apolipoprotein E knockout mouse
AU	arbitrary units
BL	basal lamina
BMP	bone matrix protein
Boc	<i>tert</i> -butyloxycarbonyl
BP	bisphosphonate
Ca	calcium
CAC	coronary artery calcium scoring
$\text{CaCO}_3$	calcium carbonate
$\text{CaOx}$	calcium oxalate
CaPi	calcium phosphate
CaPyr	calcium pyrophosphate

CD31	platelet endothelial cell adhesion molecule-1
CKD	chronic kidney disease
CT	computed tomography
CVD	cardiovascular disease
Cy	cyanine dye
DCB	dichlorobenzene
DCC	N,N'-dicyclohexylcarbodiimide
DCM	dichloromethane
DCU	dicyclohexylurea
DMAP	4-dimethylaminopyridine
DMF	dimethylformamide
DTT	1,4-dithiothreitol
DVB	divinylbenzene
EC	endothelial cells
ECM	extracellular matrix
EDCI	1-Ethyl-3-(3-dimethylaminopropyl)carbodiimide
ENPP1	ectonucleotide pyrophosphatase/phosphodiesterase 1
Et <sub>2</sub> O	diethyl ether
FAM	Fluorescein
FC	foam cells
FDA	Food and Drug Administration
f-HAP	fluorinated hydroxyapatite
G	glycine
GFP	green fluorescent protein
h	hour

HAP	hydroxyapatite
HCl	hydrochloric acid
ICA	independent component analysis
IF	immunofluorescence
IGG	immunoglobulin G
IHC	immunohistochemistry
IR	infrared
IVUS	intravascular ultrasonography
K	lysine
K <sub>i</sub>	inhibitory constant
KI	potassium iodide
<i>LDLR</i> <sup>-/-</sup>	low density lipoprotein receptor deficient mouse
LOD	limit of detection
M	methionine
M	molar
Mac	macrophages
MC3T3	mouse calvaria osteoblast precursor cell line
Me	methyl
MeCN	acetonitrile
MeI	methyl iodide
MeOH	methanol
MESA	multi-ethnic study of atherosclerosis
MGP	Matrix Gla Protein
MLp	modified lipoproteins
mM	millimolar

MMP	Matrix Metalloproteinases
Mon	blood monocytes
MOVAS-1	mouse vascular smooth muscle cells
MRI	magnetic resonance imaging
MW	microwave
N	normal
n	number of replicates
NaN <sub>3</sub>	sodium azide
NBF	neutral buffer formalin
NHS	<i>n</i> -hydroxysuccinimide
NIR	near infrared
NIRF	near-infrared fluorescence
NIRS	near-infrared spectroscopy
°C	degrees Celsius
OCP	octacalcium phosphate
OCT	optimal cutting temperature
OCT	optical coherence tomography
OPG	Osteoprotegerin
OPN	Osteopontin
OPT	optical projection tomography
P	proline
P	P-value
P <sub>2</sub> -Et	phosphazene base
PET	positron emission tomography
P <sub>i</sub>	phosphate



PLS	partial least squares
pM	pico molar
PS	polystyrene
R	arginine
S	serine
S.E.M.	standard error mean
Sat.	saturated
SPPS	solid phase peptide synthesis
Sulfo	sulfonated
TBAF	tetrabutylamminium fluoride
TBDMS-Cl	<i>tert</i> -butyldimethylsilyl chloride
TFA	trifluoroacetic acid
THF	tetrahydrofuran
UV	ultraviolet
V	valine
VECs	vascular endothelial cells
VICs	vascular interstitial cells
VIS	visible
VSMCs	vascular smooth muscle cells
WT	wild type
WTK	whitlockite
$\alpha$ -SMA	alpha-smooth muscle actin
$\beta$ -GP	$\beta$ -glycerolphosphate
$\beta$ -TCP	beta-tricalcium phosphate
$\epsilon$	extinction coefficient

$\lambda_{\text{abs}}$	absorption wavelength
$\lambda_{\text{Em}}$	emission wavelength
$\lambda_{\text{Ex}}$	excitation wavelength
$\Phi$	quantum yield

# Chapter 9- Permissions

## 1.1 Chapter 1

Figure 1.3 and 1.6

4/26/2018	RightsLink Printable License
<b>WOLTERS KLUWER HEALTH, INC. LICENSE TERMS AND CONDITIONS</b>	
	Apr 26, 2018
<hr/>	
<p>This Agreement between Alisia Sim ("You") and Wolters Kluwer Health, Inc. ("Wolters Kluwer Health, Inc.") consists of your license details and the terms and conditions provided by Wolters Kluwer Health, Inc. and Copyright Clearance Center.</p>	
License Number	4336420931557
License date	Apr 26, 2018
Licensed Content Publisher	Wolters Kluwer Health, Inc.
Licensed Content Publication	Circulation Research
Licensed Content Title	Noninvasive Molecular Imaging of Disease Activity in Atherosclerosis
Licensed Content Author	Marc R. Dweck, Elena Aikawa, David E. Newby, Jason M. Tarkin, James H.F. Rudd, Jagat Narula, Zahi A. Fayad
Licensed Content Date	Jul 8, 2016
Licensed Content Volume	119
Licensed Content Issue	2
Type of Use	Dissertation/Thesis
Requestor type	Individual
Portion	Figures/table/illustration
Number of figures/tables/illustrations	1
Figures/tables/illustrations used	figure 3
Author of this Wolters Kluwer article	No
Title of your thesis / dissertation	Detection of calcification in atherosclerotic plaques using optical imaging
Expected completion date	Sep 2018
Estimated size(pages)	180
Requestor Location	Alisia Sim Kings Building, Joseph Black Building University of Edinburgh  Edinburgh, MIDLOTHIAN EH89PL United Kingdom Attn: Alisia Sim
Publisher Tax ID	EU826013006
Billing Type	Invoice
Billing Address	Alisia Sim Kings Building, Joseph Black Building University of Edinburgh  Edinburgh, United Kingdom EH89PL Attn: Alisia Sim
Total	0.00 USD
Terms and Conditions	
<b><u>Wolters Kluwer Terms and Conditions</u></b>	
<a href="https://s100.copyright.com/AppOispatchServlet">https://s100.copyright.com/AppOispatchServlet</a>	
	1/3

Figure 1.7

4/26/2018	RightsLink Printable License
<b>SPRINGER NATURE LICENSE TERMS AND CONDITIONS</b>	
	Apr 26, 2018
<hr/>	
<p>This Agreement between Alisia Sim ("You") and Springer Nature ("Springer Nature") consists of your license details and the terms and conditions provided by Springer Nature and Copyright Clearance Center.</p>	
License Number	4336430716605
License date	Apr 26, 2018
Licensed Content Publisher	Springer Nature
Licensed Content Publication	Springer eBook
Licensed Content Title	Morphology of Atherosclerotic Lesions
Licensed Content Author	Maya Simionescu, Anca V. Sima
Licensed Content Date	Jan 1, 2012
Type of Use	Thesis/Dissertation
Requestor type	academic/university or research institute
Format	print
Portion	figures/tables/illustrations
Number of figures/tables/illustrations	1
Will you be translating?	no
Circulation/distribution	<501
Author of this Springer Nature content	no
Title	Detection of calcification in atherosclerotic plaques using optical imaging
Instructor name	n/a
Institution name	n/a
Expected presentation date	Sep 2018
Portions	Fig2.1
Requestor Location	Alisia Sim Kings Building, Joseph Black Building University of Edinburgh  Edinburgh, MIDLOTHIAN EH89PL United Kingdom Attn: Alisia Sim
Billing Type	Invoice
Billing Address	Alisia Sim Kings Building, Joseph Black Building University of Edinburgh  Edinburgh, United Kingdom EH89PL Attn: Alisia Sim
Total	0.00 USD
Terms and Conditions	
<p><b>Springer Nature Terms and Conditions for RightsLink Permissions</b>  <b>Springer Customer Service Centre GmbH (the Licensor) hereby grants you a non-exclusive, world-wide licence to reproduce the material and for the purpose and</b></p>	
<a href="https://s100.copyright.com/AppDispatchServlet">https://s100.copyright.com/AppDispatchServlet</a>	
1/3	

Figure 1.9


4/26/2018	RightsLink Printable License
<b>BMJ PUBLISHING GROUP LTD. LICENSE TERMS AND CONDITIONS</b>	
	Apr 26, 2018
<hr/>	
<p>This Agreement between Alisia Sim ("You") and BMJ Publishing Group Ltd. ("BMJ Publishing Group Ltd.") consists of your license details and the terms and conditions provided by BMJ Publishing Group Ltd. and Copyright Clearance Center.</p>	
License Number	4336430460755
License date	Apr 26, 2018
Licensed Content Publisher	BMJ Publishing Group Ltd.
Licensed Content Publication	Heart Asia
Licensed Content Title	The invasive assessment of coronary atherosclerosis and stents using optical coherence tomography: a clinical update
Licensed Content Author	Muhammad Asrar ul Haq, Jamie Layland, Vivek Mutha, Peter Barlis
Licensed Content Date	Jan 1, 2013
Licensed Content Volume	5
Licensed Content Issue	1
Type of Use	Dissertation/Thesis
Requestor type	Individual
Format	Print
Portion	Figure/table/extract
Number of figure/table/extracts	2
Description of figure/table/extracts	Figure 1 and Figure 2
Will you be translating?	No
Circulation/distribution	200
Title of your thesis / dissertation	Detection of calcification in atherosclerotic plaques using optical imaging
Expected completion date	Sep 2018
Estimated size(pages)	180
Requestor Location	Alisia Sim Kings Building, Joseph Black Building University of Edinburgh  Edinburgh, MIDLOTHIAN EH89PL United Kingdom Attn: Alisia Sim
Publisher Tax ID	GB674738491
Billing Type	Invoice
Billing Address	Alisia Sim Kings Building, Joseph Black Building University of Edinburgh  Edinburgh, United Kingdom EH89PL Attn: Alisia Sim
Total	0.00 GBP
Terms and Conditions	
<hr/>	
<a href="https://s100.copyright.com/AppDispatchServlet">https://s100.copyright.com/AppDispatchServlet</a>	1/4

Figure 1.10

4/26/2018	RightsLink Printable License
<b>OXFORD UNIVERSITY PRESS LICENSE TERMS AND CONDITIONS</b>	
	Apr 26, 2018
<hr/>	
<p>This Agreement between Alisia Sim ("You") and Oxford University Press ("Oxford University Press") consists of your license details and the terms and conditions provided by Oxford University Press and Copyright Clearance Center.</p>	
License Number	4336431069492
License date	Apr 26, 2018
Licensed content publisher	Oxford University Press
Licensed content publication	European Heart Journal
Licensed content title	Imaging of coronary atherosclerosis by computed tomography
Licensed content author	Achenbach, Stephan; Raggi, Paolo
Licensed content date	May 19, 2010
Type of Use	Thesis/Dissertation
Institution name	
Title of your work	Detection of calcification in atherosclerotic plaques using optical imaging
Publisher of your work	n/a
Expected publication date	Sep 2018
Permissions cost	0.00 USD
Value added tax	0.00 USD
Total	0.00 USD
Title	Detection of calcification in atherosclerotic plaques using optical imaging
Instructor name	n/a
Institution name	n/a
Expected presentation date	Sep 2018
Portions	figure 1
Requestor Location	Alisia Sim Kings Building, Joseph Black Building University of Edinburgh  Edinburgh, MIDLOTHIAN EH89PL United Kingdom Attn: Alisia Sim
Publisher Tax ID	GB125506730
Billing Type	Invoice
Billing Address	Alisia Sim Kings Building, Joseph Black Building University of Edinburgh  Edinburgh, United Kingdom EH89PL Attn: Alisia Sim
Total	0.00 USD
Terms and Conditions	
<hr/>	
<a href="https://s100.copyright.com/AppDispatchServlet">https://s100.copyright.com/AppDispatchServlet</a>	1/3

Figure 1.12

4/26/2018 Copyright Clearance Center



Note: Copyright.com supplies permissions but not the copyrighted content itself.

1  
PAYMENT

2  
REVIEW

**3  
CONFIRMATION**

### Step 3: Order Confirmation

**Thank you for your order!** A confirmation for your order will be sent to your account email address. If you have questions about your order, you can call us 24 hrs/day, M-F at +1.855.239.3415 Toll Free, or write to us at info@copyright.com. This is not an invoice.

**Confirmation Number: 11713903**  
**Order Date: 04/26/2018**

**Payment Information**

Alisia Sim  
s1434748@sms.ed.ac.uk  
+44 7765132756  
Payment Method: n/a

If you paid by credit card, your order will be finalized and your card will be charged within 24 hours. If you choose to be invoiced, you can change or cancel your order until the invoice is generated.

---

#### Order Details

**Cardiovascular diagnosis and therapy**

<p><b>Order detail ID:</b> 71145550 <b>Order License Id:</b> 4336430061486 <b>ISSN:</b> 2223-3652 <b>Publication Type:</b> Journal <b>Volume:</b> <b>Issue:</b> <b>Start page:</b> <b>Publisher:</b> AME Publishing Company</p>	<p><b>Permission Status:</b> <span style="color: green;">✔</span> <b>Granted</b> <b>Permission type:</b> Republish or display content <b>Type of use:</b> Thesis/Dissertation</p> <p><b>Requestor type:</b> Academic Institution</p> <p><b>Format:</b> Print</p> <p><b>Portion:</b> image/photo</p> <p><b>Number of images/photos requested:</b> 1</p> <p><b>The requesting person/organization:</b> Alisia Sim</p> <p><b>Title or numeric reference of the portion(s):</b> Chapter 1 figure 1.12</p> <p><b>Title of the article or chapter the portion is from:</b> Introduction</p> <p><b>Editor of portion(s):</b> n/a</p> <p><b>Author of portion(s):</b> n/a</p> <p><b>Volume of serial or monograph:</b> n/a</p>
---	--

<https://www.copyright.com/printCol/ConfirmPurchase.do?operation=defaultOperation&confirmNum=11713903&showTCCitation=TRUE>
1/5

Figure 1.13

4/26/2018	RightsLink Printable License
<b>SPRINGER NATURE LICENSE TERMS AND CONDITIONS</b>	
Apr 26, 2018	
<hr/>	
<b>This Agreement between Alisia Sim ("You") and Springer Nature ("Springer Nature") consists of your license details and the terms and conditions provided by Springer Nature and Copyright Clearance Center.</b>	
License Number	4336430231393
License date	Apr 26, 2018
Licensed Content Publisher	Springer Nature
Licensed Content Publication	Nature Reviews Cardiology
Licensed Content Title	PET imaging of inflammation in atherosclerosis
Licensed Content Author	Jason M. Tarkin, Francis R. Joshi, James H. F. Rudd
Licensed Content Date	Jun 10, 2014
Licensed Content Volume	11
Licensed Content Issue	8
Type of Use	Thesis/Dissertation
Requestor type	academic/university or research institute
Format	print
Portion	figures/tables/illustrations
Number of figures/tables/illustrations	1
High-res required	no
Will you be translating?	no
Circulation/distribution	<501
Author of this Springer Nature content	no
Title	Detection of calcification in atherosclerotic plaques using optical imaging
Instructor name	n/a
Institution name	n/a
Expected presentation date	Sep 2018
Portions	Chapter 1, Figure 1.13
Requestor Location	Alisia Sim Kings Building, Joseph Black Building University of Edinburgh  Edinburgh, MIDLOTHIAN EH89PL United Kingdom Attn: Alisia Sim
Billing Type	Invoice
Billing Address	Alisia Sim Kings Building, Joseph Black Building University of Edinburgh  Edinburgh, United Kingdom EH89PL Attn: Alisia Sim
Total	0.00 USD
<a href="https://s100.copyright.com/AppDispatchServlet">https://s100.copyright.com/AppDispatchServlet</a>	
1/3	



## 1.2 Chapter 2

Figure 2.4

05/06/2018	RightsLink Printable License
<b>ROYAL SOCIETY OF CHEMISTRY LICENSE TERMS AND CONDITIONS</b>	
Jun 05, 2018	
<hr/>	
This Agreement between Alisia Sim ("You") and Royal Society of Chemistry ("Royal Society of Chemistry") consists of your license details and the terms and conditions provided by Royal Society of Chemistry and Copyright Clearance Center.	
License Number	4362510629583
License date	Jun 05, 2018
Licensed Content Publisher	Royal Society of Chemistry
Licensed Content Publication	New Journal of Chemistry
Licensed Content Title	A fluorescent probe based on hydroxynaphthalene 2-cyanoacrylate: fluoride ion detection and its bio-imaging in live cells
Licensed Content Author	Ruiyuan Liu, Ya Gao, Qianbing Zhang, Xiaodong Yang, Xinwei Lu, Zhiyong Ke, Wenqiang Zhou, Jinqing Qu
Licensed Content Date	Mar 4, 2014
Licensed Content Volume	38
Licensed Content Issue	7
Type of Use	Thesis/Dissertation
Requestor type	academic/educational
Portion	figures/tables/images
Number of figures/tables/images	1
Format	print
Distribution quantity	10
Will you be translating?	no
Order reference number	
Title of the thesis/dissertation	Detection of calcification in atherosclerotic plaques using optical imaging
Expected completion date	Sep 2018
Estimated size	180
Requestor Location	Alisia Sim Kings Building, Joseph Black Building University of Edinburgh  Edinburgh, MIDLOTHIAN EH89PL United Kingdom Attn: Alisia Sim
Billing Type	Invoice
Billing Address	Alisia Sim Kings Building, Joseph Black Building University of Edinburgh  Edinburgh, United Kingdom EH89PL Attn: Alisia Sim
<b>Total</b>	0,00 USD

<https://s100.copyright.com/AppDispatchServlet>

1/4

Figure 2.5

<b>ROYAL SOCIETY OF CHEMISTRY LICENSE TERMS AND CONDITIONS</b>	
	Jun 05, 2018
This Agreement between Alisia Sim ("You") and Royal Society of Chemistry ("Royal Society of Chemistry") consists of your license details and the terms and conditions provided by Royal Society of Chemistry and Copyright Clearance Center.	
License Number	4362510790838
License date	Jun 05, 2018
Licensed Content Publisher	Royal Society of Chemistry
Licensed Content Publication	Journal of Materials Chemistry B
Licensed Content Title	Rhodamine based sensor for naked-eye detection and live cell imaging of fluoride ions
Licensed Content Author	Gandhi Sivaraman, Duraisamy Chellappa
Licensed Content Date	Aug 21, 2013
Licensed Content Volume	1
Licensed Content Issue	42
Type of Use	Thesis/Dissertation
Requestor type	academic/educational
Portion	figures/tables/images
Number of figures/tables/images	1
Format	print
Distribution quantity	10
Will you be translating?	no
Order reference number	
Title of the thesis/dissertation	Detection of calcification in atherosclerotic plaques using optical imaging
Expected completion date	Sep 2018
Estimated size	180
Requestor Location	Alisia Sim Kings Building, Joseph Black Building University of Edinburgh  Edinburgh, MIDLOTHIAN EH89PL United Kingdom Attn: Alisia Sim
Billing Type	Invoice
Billing Address	Alisia Sim Kings Building, Joseph Black Building University of Edinburgh  Edinburgh, United Kingdom EH89PL Attn: Alisia Sim
<b>Total</b>	<b>0.00 USD</b>

<https://s100.copyright.com/AppDispatchServlet>

1/4

Figure 2.9

4/26/2018	RightsLink Printable License
<b>BMJ PUBLISHING GROUP LTD. LICENSE TERMS AND CONDITIONS</b>	
Apr 26, 2018	
<hr/>	
<b>This Agreement between Alisia Sim ("You") and BMJ Publishing Group Ltd. ("BMJ Publishing Group Ltd.") consists of your license details and the terms and conditions provided by BMJ Publishing Group Ltd. and Copyright Clearance Center.</b>	
License Number	4336440476427
License date	Apr 26, 2018
Licensed Content Publisher	BMJ Publishing Group Ltd.
Licensed Content Publication	British Journal of Ophthalmology
Licensed Content Title	Fluorescein angiography and optical coherence tomography concordance for choroidal neovascularisation in multifocal choroiditis
Licensed Content Author	Athanasios I Kotsolis, Frank A Killian, Ioannis D Ladas, Lawrence A Yannuzzi
Licensed Content Date	Nov 1, 2010
Licensed Content Volume	94
Licensed Content Issue	11
Type of Use	Dissertation/Thesis
Requestor type	Individual
Format	Print
Portion	Figure/table/extract
Number of figure/table/extracts	1
Description of figure/table/extracts	figure 1
Will you be translating?	No
Circulation/distribution	200
Title of your thesis / dissertation	Detection of calcification in atherosclerotic plaques using optical imaging
Expected completion date	Sep 2018
Estimated size(pages)	180
Requestor Location	Alisia Sim Kings Building, Joseph Black Building University of Edinburgh  Edinburgh, MIDLOTHIAN EH89PL United Kingdom Attn: Alisia Sim
Publisher Tax ID	GB674738491
Billing Type	Invoice
Billing Address	Alisia Sim Kings Building, Joseph Black Building University of Edinburgh  Edinburgh, United Kingdom EH89PL Attn: Alisia Sim
Total	0.00 GBP
Terms and Conditions	
<a href="https://s100.copyright.com/AppDispatchServlet">https://s100.copyright.com/AppDispatchServlet</a>	
1/4	

Figure 2.12

4/26/2018	RightsLink Printable License
<b>JOHN WILEY AND SONS LICENSE TERMS AND CONDITIONS</b>	
Apr 26, 2018	
<hr/>	
<b>This Agreement between Alisia Sim ("You") and John Wiley and Sons ("John Wiley and Sons") consists of your license details and the terms and conditions provided by John Wiley and Sons and Copyright Clearance Center.</b>	
License Number	4336440144213
License date	Apr 26, 2018
Licensed Content Publisher	John Wiley and Sons
Licensed Content Publication	Advanced Materials
Licensed Content Title	Identification of a Highly Specific Hydroxyapatite-binding Peptide using Phage Display
Licensed Content Author	Matthew L. Becker, Eric J. Amis, Scott K. Stanley, et al
Licensed Content Date	May 15, 2008
Licensed Content Volume	20
Licensed Content Issue	10
Licensed Content Pages	7
Type of use	Dissertation/Thesis
Requestor type	University/Academic
Format	Print
Portion	Figure/table
Number of figures/tables	1
Original Wiley figure/table number(s)	fig 3
Will you be translating?	No
Title of your thesis / dissertation	Detection of calcification in atherosclerotic plaques using optical imaging
Expected completion date	Sep 2018
Expected size (number of pages)	180
Requestor Location	Alisia Sim Kings Building, Joseph Black Building University of Edinburgh  Edinburgh, MIDLOTHIAN EH89PL United Kingdom Attn: Alisia Sim
Publisher Tax ID	EU826007151
Total	0.00 GBP
Terms and Conditions	
<b>TERMS AND CONDITIONS</b>	
This copyrighted material is owned by or exclusively licensed to John Wiley & Sons, Inc. or one of its group companies (each a "Wiley Company") or handled on behalf of a society with which a Wiley Company has exclusive publishing rights in relation to a particular work (collectively "WILEY"). By clicking "accept" in connection with completing this licensing transaction, you agree that the following terms and conditions apply to this transaction (along with the billing and payment terms and conditions established by the Copyright	
<a href="https://s100.copyright.com/AppDispatchServlet">https://s100.copyright.com/AppDispatchServlet</a>	1/4

## 1.3 Chapter 3

5/21/2018

RightsLink Printable License

**WOLTERS KLUWER HEALTH, INC. LICENSE  
TERMS AND CONDITIONS**

May 21, 2018

This Agreement between Alisia Sim ("You") and Wolters Kluwer Health, Inc. ("Wolters Kluwer Health, Inc.") consists of your license details and the terms and conditions provided by Wolters Kluwer Health, Inc. and Copyright Clearance Center.

License Number	4353580635687
License date	May 21, 2018
Licensed Content Publisher	Wolters Kluwer Health, Inc.
Licensed Content Publication	Circulation
Licensed Content Title	Osteogenesis Associates With Inflammation in Early-Stage Atherosclerosis Evaluated by Molecular Imaging In Vivo
Licensed Content Author	Elena Aikawa,Matthias Nahrendorf,Jose-Luiz Figueiredo,Filip K. Swirski,Timur Shtatland,Rainer H. Kohler,Farouc A. Jaffer,Masanori Aikawa,Ralph Weissleder
Licensed Content Date	Dec 11, 2007
Licensed Content Volume	116
Licensed Content Issue	24
Type of Use	Dissertation/Thesis
Requestor type	Individual
Portion	Figures/table/illustration
Number of figures/tables/illustrations	1
Figures/tables/illustrations used	Figure 2
Author of this Wolters Kluwer article	No
Title of your thesis / dissertation	Detection of calcification in atherosclerotic plaques using optical imaging
Expected completion date	Sep 2018
Estimated size(pages)	180
Requestor Location	Alisia Sim Kings Building, Joseph Black Building University of Edinburgh  Edinburgh, MIDLOTHIAN EH89PL United Kingdom Attn: Alisia Sim
Publisher Tax ID	EU826013006
Billing Type	Invoice
Billing Address	Alisia Sim Kings Building, Joseph Black Building University of Edinburgh  Edinburgh, United Kingdom EH89PL Attn: Alisia Sim
Total	0.00 GBP
Terms and Conditions	

<https://s100.copyright.com/AppDispatchServlet>

1/3

## 1.4 Chapter 5

Figure 5.2

04/05/2018 RightsLink Printable License

**SPRINGER NATURE LICENSE  
TERMS AND CONDITIONS**

May 04, 2018

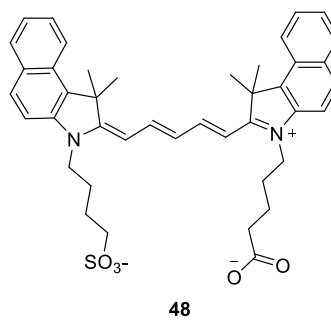
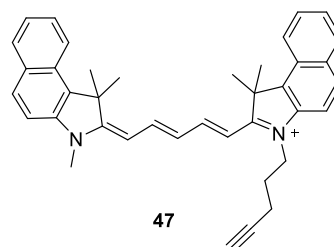
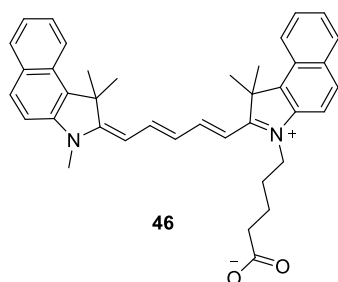
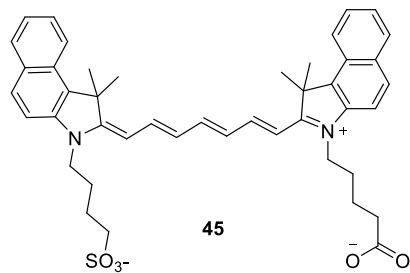
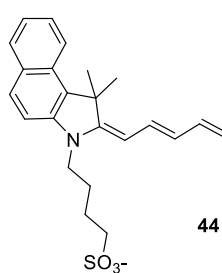
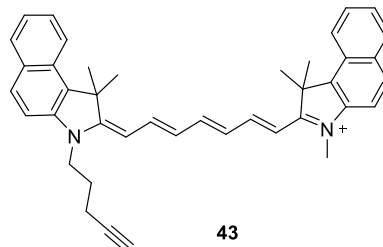
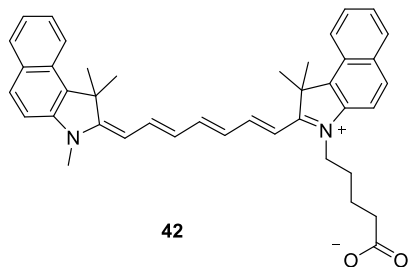
---

This Agreement between Alisia Sim ("You") and Springer Nature ("Springer Nature") consists of your license details and the terms and conditions provided by Springer Nature and Copyright Clearance Center.

License Number	4341811454965
License date	May 04, 2018
Licensed Content Publisher	Springer Nature
Licensed Content Publication	Nature Protocols
Licensed Content Title	Using Raman spectroscopy to characterize biological materials
Licensed Content Author	Holly J Butler, Lorna Ashton, Benjamin Bird, Gianfelice Cinque, Kelly Curtis et al.
Licensed Content Date	Mar 10, 2016
Licensed Content Volume	11
Licensed Content Issue	4
Type of Use	Thesis/Dissertation
Requestor type	academic/university or research institute
Format	print
Portion	figures/tables/illustrations
Number of figures/tables/illustrations	1
High-res required	no
Will you be translating?	no
Circulation/distribution	<501
Author of this Springer Nature content	no
Title	Detection of calcification in atherosclerotic plaques using optical imaging
Instructor name	n/a
Institution name	n/a
Expected presentation date	Sep 2018
Portions	Figure 3
Requestor Location	Alisia Sim Kings Building, Joseph Black Building University of Edinburgh  Edinburgh, MIDLOTHIAN EH89PL United Kingdom Attn: Alisia Sim
Billing Type	Invoice
Billing Address	Alisia Sim Kings Building, Joseph Black Building University of Edinburgh

<https://s100.copyright.com/AppDispatchServlet> 1/3

# Appendix 1- Cyanine dyes



## Appendix 2- Patient information

### Appendix 2.1 Coronary tissue samples

Ethics code: National Health Service South East Scotland 14/SS/1090

Patient information:

<b>Patient</b>	<b>Date of post mortem</b>	<b>Age</b>	<b>Gender</b>	<b>Cause of death (1,2)</b>
<b>1</b>	23/08/2016	46	M	Ischaemic heart disease
<b>2</b>	16/11/2016	49	M	Ischaemic heart disease (1) Coronary artery atherosclerosis (2)
<b>3</b>	18/01/2017	49	F	Complications of alcohol toxicity
<b>4</b>	28/02/2017	71	F	Ischaemic and hypertensive heart disease (1) Diabetes mellitus (2)
<b>5</b>	11/05/2017	50	M	Haemopericardium (1) Dissection of thoracic aorta (2)
<b>6</b>	24/05/2017	67	M	n/a
<b>7</b>	07/06/2017	48	M	n/a
<b>8</b>	27/09/2016	57	M	Ischaemic heart disease

### Appendix 2.2: Carotid tissue samples

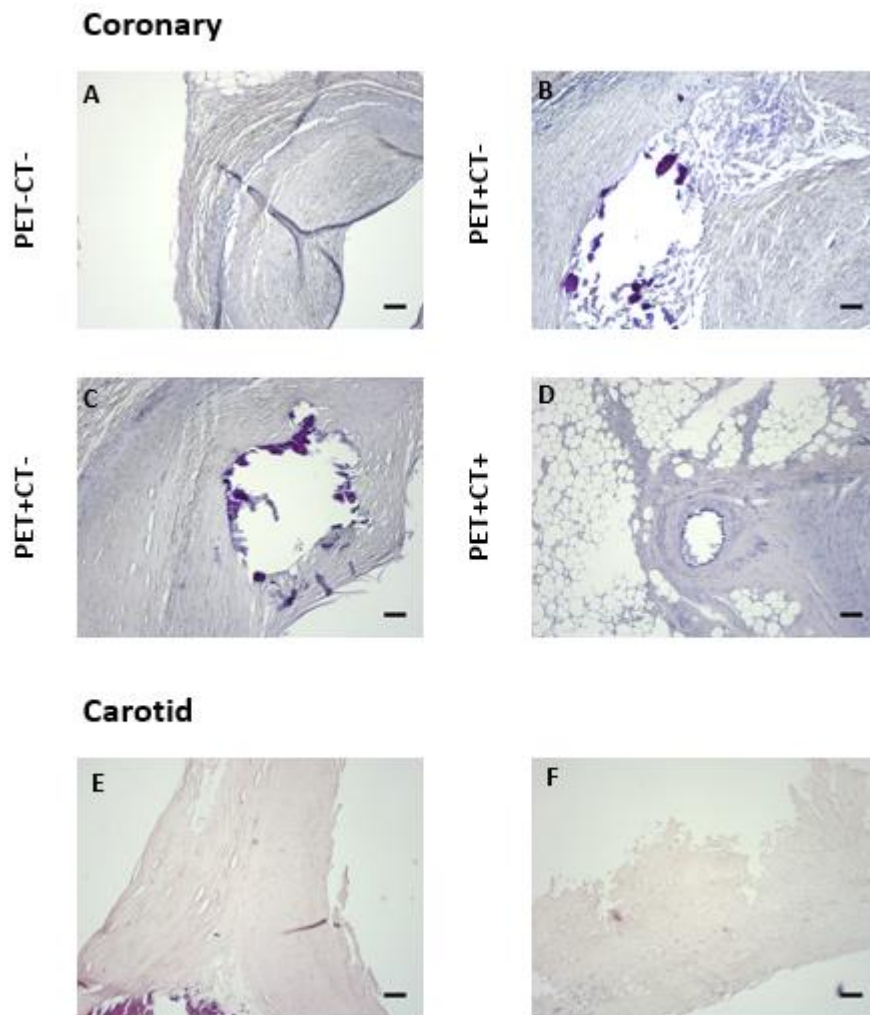
Ethics code: Lothian NRS Bioresources 15/ES/0094

Patient information:

<b>Patient</b>	<b>Date of Surgery</b>	<b>Age</b>	<b>Gender</b>	<b>PMH</b>
<b>1</b>	23/6/17	74	M	Myocardial infarction, pleural plaques, COPD, severe left ventricular systolic dysfunction, aortic stenosis
<b>2</b>	17/10/17	54	M	COPD, smoking
<b>3</b>	20/10/17	71	M	Pancreatic cancer, hypertension, hypercholesterolaemia



## Appendix 3- IGG control



*Appendix 3 Figure 1: IGG control of coronary (A, B, C, D) and carotid (E, F) arteries. IHC analysis performed with Vectastain ABC kit (mouse IgG) where all antibodies were anti-human mouse clones (1:100 dilution). All IHC were counterstained with H&E. Scale bars = 0.2 cm.*

## Appendix 4- Staining solutions

### Wiegert's Iron Haematoxylin

Haematoxylin (1 gr) was dissolved in 95% alcohol (100 mL). 29% Ferric Chloride in H<sub>2</sub>O (4 mL) was dissolved in distilled H<sub>2</sub>O (95 mL) containing HCl (conc., 1 mL). The haematoxylin solution was combined to the Ferric Chloride solution in a 1:1 ratio.

### 1% Acetic H<sub>2</sub>O

Acetic acid (glacial, 1 mL) was dissolved in distilled H<sub>2</sub>O (99 mL).

### 2% Alizarin Red

Alizarin Red (2.00 g) was dissolved in distilled H<sub>2</sub>O (100 mL). The pH was adjusted to 4.1-4.3.

### 1% Silver nitrate solution

Silver nitrate (1.00 g) was dissolved in distilled H<sub>2</sub>O (100 mL).

### 5% Sodium thiosulfate solution

Sodium thiosulfate (5.00 g) was dissolved in distilled H<sub>2</sub>O (100 mL).

### 0.1% Nuclear fast red solution

Aluminium sulfate (5.00 g) was dissolved in distilled H<sub>2</sub>O (100 mL). The solution was stirred and subsequently nuclear fast red (0.10 g) is added.

### 2% Acidic H<sub>2</sub>O

HCl (conc., 1 mL) was added to 70% ethanol (99 mL).